

Geological Survey of Denmark and Greenland (GEUS)  
Department for Petrology and Economic Geology  
Øster Voldgade 10  
DK-1350 Copenhagen K  
Denmark

Report by: Stefanie Lode, Björn Heincke, Nynke T. Keulen

**Compilation of data acquired by optical microscopy and automated quantitative mineralogy combined with scanning electron microscopy (AQM-SEM) of thin-sections from the Qullissat bore hole FP94-4-5 and correlation to petrophysical measurements**

\*Contact person:

Stefanie Lode	stefanie.lode@ntnu.no
(former now inactive stlo@geus.dk)	
Nynke Keulen	ntk@geus.dk

## Table of Contents

<b>1)</b>	<b>INTRODUCTION AND METHODOLOGIES .....</b>	<b>5</b>
1.1.	SUMMARY OF RESULTS - MINERALOGY .....	8
1.1.1	<i>Native iron / cohenite</i> .....	12
1.1.2	<i>Graphite</i> .....	13
1.1.3	<i>Magnetite</i> .....	14
1.1.4	<i>Pyrrhotite</i> .....	14
1.1.5	<i>NiFe-phosphides, pentlandite, and other Cu-Fe-sulphides</i> .....	14
1.1.6	<i>Potential indicator minerals</i> .....	14
1.1.7	<i>Primary basaltic minerals and pheno- and xenocrysts</i> .....	14
1.1.8	<i>Other sulphides, oxides, phosphates, carbonates, Au</i> .....	15
1.1.9	<i>Microtextures</i> .....	15
1.2	CORRELATION OF MINERALOGY AND PETROPHYSICAL PROPERTIES (FIG. 3A) .....	15
1.3	DEFINITION OF MINERALS / MINERAL LIST .....	16
1.4.	LEGEND FOR AQM MINERAL MAPS .....	17
<b>2)</b>	<b>RESULTS .....</b>	<b>18</b>
2.1.	FP94-4-5_049.50 SUMMARY .....	18
2.2.	FP94-4-5_049.50 SEM-BSE/EDS .....	18
2.3.	FP94-4-5_049.50 MICROSCOPY .....	19
2.4.	FP94-4-5_049.50 AQM-SEM .....	20
2.5.	FP94-4-5_054.80 SUMMARY .....	21
2.6.	FP94-4-5_054.80 SEM-BSE/EDS .....	21
2.7.	FP94-4-5_054.80 MICROSCOPY .....	23
2.8.	FP94-4-5_054.80 AQM-SEM .....	25
2.9.	FP94-4-5_066.26 SUMMARY .....	27
2.10.	FP94-4-5_066.26 SEM-BSE/EDS .....	27
2.11.	FP94-4-5_066.26 MICROSCOPY .....	29
2.12.	FP94-4-5_066.26 AQM-SEM .....	31
2.13.	FP94-4-5_075.90 SUMMARY .....	33
2.14.	FP94-4-5_075.90 SEM-BSE/EDS .....	33
2.15.	FP94-4-5_075.90 MICROSCOPY .....	35
2.16.	FP94-4-5_075.90 AQM-SEM .....	37
2.17.	FP94-4-5_087.13 SUMMARY .....	38
2.18.	FP94-4-5_087.13 SEM-BSE/EDS .....	38
2.19.	FP94-4-5_087.13 MICROSCOPY .....	39
2.20.	FP94-4-5_087.13 AQM-SEM .....	40
2.21.	FP94-4-5_095.40 SUMMARY .....	41
2.22.	FP94-4-5_095.40 SEM-BSE/EDS .....	41
2.23.	FP94-4-5_095.40 MICROSCOPY .....	42
2.24.	FP94-4-5_095.40 AQM-SEM .....	44
2.25.	FP94-4-5_103.68 SUMMARY .....	45
2.26.	FP94-4-5_103.68 SEM-BSE/EDS .....	45
2.27.	FP94-4-5_103.68 MICROSCOPY .....	46
2.28.	FP94-4-5_103.68 AQM-SEM .....	48
2.29.	FP94-4-5_110.90 SUMMARY .....	49
2.30.	FP94-4-5_110.90 SEM-BSE/EDS .....	49
2.31.	FP94-4-5_110.90 MICROSCOPY .....	51
2.32.	FP94-4-5_110.90 AQM-SEM .....	53

2.33.	FP94-4-5_121.80 SUMMARY .....	54
2.34.	FP94-4-5_121.80 SEM-BSE/EDS .....	54
2.35.	FP94-4-5_121.80 MICROSCOPY .....	56
2.36.	FP94-4-5_121.80 AQM-SEM .....	58
2.37.	FP94-4-5_126.30 SUMMARY .....	59
2.38.	FP94-4-5_126.30 SEM-BSE/EDS .....	59
2.39.	FP94-4-5_126.30 MICROSCOPY .....	60
2.40.	FP94-4-5_126.30 AQM-SEM .....	62
2.41.	FP94-4-5_127.45 SUMMARY .....	63
2.42.	FP94-4-5_127.45 SEM-BSE/EDS .....	63
2.43.	FP94-4-5_127.45 MICROSCOPY .....	64
2.44.	FP94-4-5_127.45 AQM-SEM .....	65
2.45.	FP94-4-5_127.98 SUMMARY .....	66
2.46.	FP94-4-5_127.98 SEM-BSE/EDS .....	66
2.47.	FP94-4-5_127.98 MICROSCOPY .....	68
2.48.	FP94-4-5_127.98 AQM-SEM .....	70
2.49.	FP94-4-5_131.60 SUMMARY .....	71
2.50.	FP94-4-5_131.60 SEM-BSE/EDS .....	71
2.51.	FP94-4-5_131.60 MICROSCOPY .....	72
2.52.	FP94-4-5_131.60 AQM-SEM .....	75
2.53.	FP94-4-5_142.42 SUMMARY .....	76
2.54.	FP94-4-5_142.42 SEM-BSE/EDS ELEMENT MAP .....	76
2.55.	FP94-4-5_142.42 MICROSCOPY .....	78
2.56.	FP94-4-5_142.42 AQM-SEM .....	79
2.57.	FP94-4-5_153.20 SUMMARY .....	80
2.58.	FP94-4-5_153.20 SEM-BSE/EDS ELEMENT MAPS .....	80
2.59.	FP94-4-5_153.20 MICROSCOPY .....	83
2.60.	FP94-4-5_153.20 AQM-SEM .....	85
2.61.	FP94-4-5_159.70 SUMMARY .....	86
2.62.	FP94-4-5_159.70 SEM-BSE/EDS .....	86
2.63.	FP94-4-5_159.70 MICROSCOPY .....	87
2.64.	FP94-4-5_159.70 AQM-SEM .....	89
2.65.	FP94-4-5_170.47 SUMMARY .....	90
2.66.	FP94-4-5_170.47 SEM-BSE/EDS .....	90
2.67.	FP94-4-5_170.47 MICROSCOPY .....	91
2.68.	FP94-4-5_170.47 AQM-SEM .....	93
2.69.	FP94-4-5_177.40 SUMMARY .....	94
2.70.	FP94-4-5_177.40 SEM-BSE/EDS .....	94
2.71.	FP94-4-5_177.40 MICROSCOPY .....	96
2.72.	FP94-4-5_177.40 AQM-SEM .....	97
2.73.	FP94-4-5_183.87 SUMMARY .....	98
2.74.	FP94-4-5_183.87 SEM-BSE/EDS .....	98
2.75.	FP94-4-5_183.87 MICROSCOPY .....	100
2.76.	FP94-4-5_183.87 AQM-SEM .....	101
2.77.	FP94-4-5_187.55 SUMMARY .....	102
2.78.	FP94-4-5_187.55 SEM-BSE/EDS .....	102
2.79.	FP94-4-5_187.55 MICROSCOPY .....	104
2.80.	FP94-4-5_187.55 AQM-SEM .....	107
2.81.	FP94-4-5_190.54 SUMMARY .....	108
2.82.	FP94-4-5_190.54 SEM-BSE/EDS .....	108
2.83.	FP94-4-5_190.54 MICROSCOPY .....	109



2.84.	FP94-4-5_190.54 AQM-SEM .....	111
2.85.	FP94-4-5_200.58 SUMMARY.....	112
2.86.	FP94-4-5_200.58 SEM-BSE/EDS .....	112
2.87.	FP94-4-5_200.58 AQM-SEM .....	113
2.88.	FP94-4-5_215.70 SUMMARY.....	114
2.89.	FP94-4-5_215.70 SEM-BSE/EDS .....	114
2.90.	FP94-4-5_215.70 AQM-SEM .....	115
<b>3.</b>	<b>CONCLUSIONS.....</b>	<b>116</b>
<b>4.</b>	<b>ACKNOWLEDGEMENTS .....</b>	<b>116</b>
<b>5.</b>	<b>REFERENCES.....</b>	<b>117</b>
<b>5.</b>	<b>APPENDIX .....</b>	<b>117</b>

## 1) Introduction and methodologies

Focus of this project is the identification, quantification, and characterisation of mineral phases present in samples of the borehole FP94-4-5 located a few kilometers south of the abandoned village Qullissat at northern Disko Island (UTM22N coordinates: 7772427N, 423818E), West Greenland Basalt Province. The exploration bore hole FP94-4-5 targeted a highly conductive anomaly that was identified by an airborne EM-survey (Olshefsky & Jerome, 1993). The vertical borehole had a total depth of 270.5 m and intersected the complete fine-crystalline volcanic succession (depths: 58.1–190.5 m) but also intercepted sedimentary rocks stratigraphically above and below that targeted volcanic succession. The borehole was part of a diamond drilling project that was initiated by the mineral exploration company Falconbridge Greenland A/S in March 1994 to investigate a Palaeocene (62-61 Ma) sediment-contaminated volcanic succession of the Asuk Member, Vaigat Formation, for Ni-Cu-PGE mineralization (Olshefsky et al., 1995, Pedersen et al., 2017,2018). The contamination of the Asuk Member magma by carbonaceous sediments (marine mudstones, deltaic shales and coal seams) resulted in strongly reduced conditions enabling the formation of native iron, as well as graphite, Ni-Fe-phosphides and Ni-Cu-sulphides (Pedersen et al., 2017,2018; Stensgaard et al., 2018).

The presence of magnetic and conductive minerals, such as native iron, pyrrhotite, graphite, and magnetite, in the volcanic rocks makes it enormously difficult to assign observed magnetic and conductive anomalies to the available geophysical surveys (Olshefsky & Jerome, 1993, Heincke et al., 2020). To determine type and amount of these and other mineral phases that potentially influence conductive and magnetic properties, a mineralogical study on systematically selected samples from FP94-4-5 was undertaken and compared with petrophysical data measured on the same sample intervals. For this purpose, the GEUS scientists Björn H. Heincke, Lotte M. Larsen, and Asger K. Pedersen, together with the student Ethan Barnes, selected in total 23 samples from core depths ranging from 49.50 to 215.70 m (typically in intervals of ~10 m, but in areas of major changes in lithology in shorter intervals; see Table 1). The samples cover the volcanic succession and sedimentary rocks above and below. Prior to the mineralogical investigations, the samples were sent to the petrophysical lab of the Finnish Geological Survey (GTK), Espoo, for measurements of the magnetic (induced and remanent magnetisation, inclination, and declination) and electromagnetic (resistivity and induced polarization) properties, as well as densities. Results of the petrophysical measurements are attached in Appendix\_A. Subsequently, samples from the same selected intervals were sent to Precision Petrographics Ltd., Canada, for thin section preparation. Due to the fissility of the shales, those two samples were prepared as polished epoxy pucks.

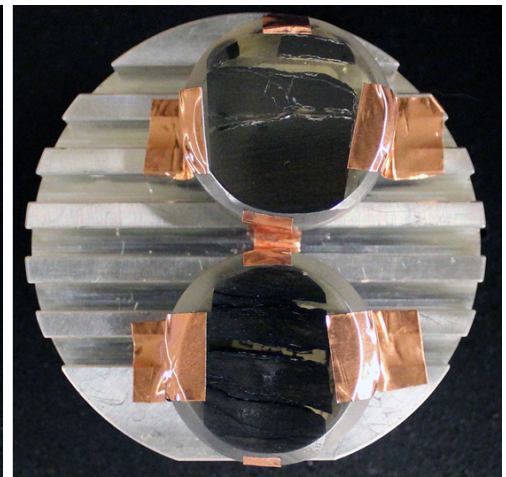
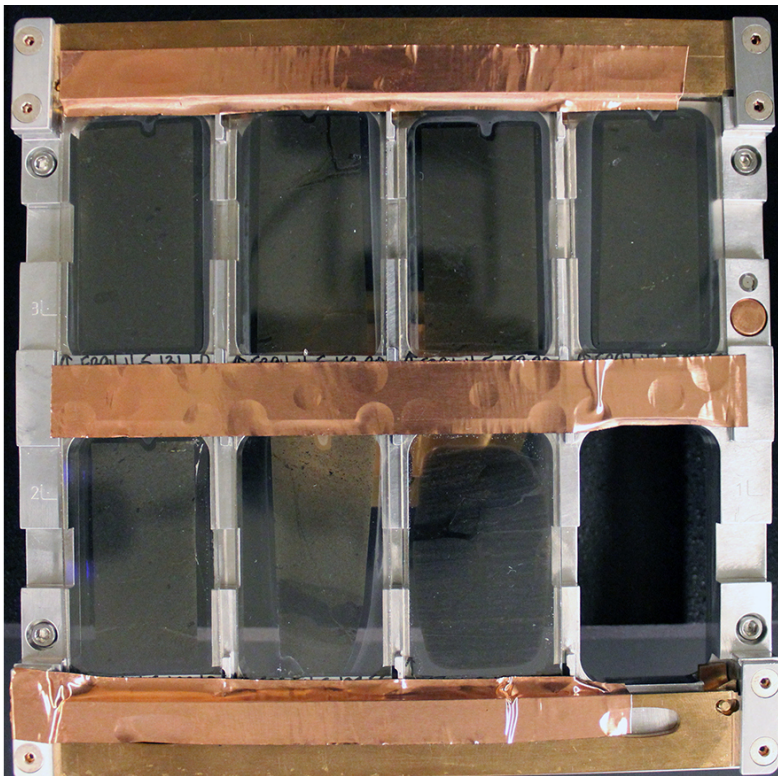
On all thin sections, optical and electron microscopy was performed and acquired at the Geological Survey of Denmark and Greenland (GEUS) using transmitted and reflected microscopy, manual qualitative scanning electron microscope (SEM) microanalysis, including energy dispersive X-ray spectroscopy (EDS), backscatter electron (BSE) imaging, and automated quantitative mineralogy (AQM-SEM) for generating mineral maps and modal mineral data. The SEM laboratory at GEUS hosts a ZEISS Sigma 300VP Field Emission SEM that is equipped with 2 Bruker Xflash 6|30

129 eV EDS detectors and ZEISS Mineralogic Software. The optical microscope is a ZEISS AxioScope 40. Results of the mineralogical measurements are attached in Appendix\_B and Appendix\_C.

**FP94-4-5 Core depth [m] Rocktype**

1)	049.50	Sandstone
2)	054.80	?Taxite (Lapilli tuff breccia)
3)	066.26	Basalt
4)	075.90	Basalt
5)	087.13	Basalt
6)	095.40	Basalt
7)	103.63	Basalt
8)	110.90	Basalt
9)	121.80	Basalt
10)	126.30	Basalt
11)	127.45	Basalt
12)	127.98	Basalt
13)	131.60	Basalt
14)	142.42	Basalt
15)	153.20	Basalt
16)	159.70	Basalt
17)	170.47	Basalt
18)	177.40	Basalt
19)	183.87	Basalt
20)	187.55	Basalt
21)	190.54	Siltstone-sandstone
22)	200.58	Shale
23)	215.70	Shale

**Table 1.** List of sampled intervals for petrophysical and mineralogical investigations.



**Fig. 1.** Left: Thin-section holder with seven of the Qullissat FP94-4-5 samples (131.60, 153.20, 159.70, 170.47, 177.40, 187.55, 190.54) and two epoxy pucks (200.58 (top) and 215.70 (bottom) prepared for SEM investigations. Thin-sections are standard size (26x46 mm) and pucks 2.5 cm, both are polished and coated with 10 nm carbon.

Optical microscopy in transmitted light was performed to investigate the mineralogy of the sedimentary and basaltic rocks, pheno- and xenocrysts in the basaltic rocks, as well as identify glassy phases and micro-textures. Reflected light microscopy enables the identification of the opaque phase, such as graphite, sulphides, metal oxides, phosphides, and native iron and their textural relationships.

In AQM-SEM, energy dispersive X-ray spectra (EDS) are collected systematically covering a high-resolution grid in the analyzed mineral grains, whereby each individual EDS spectrum identifies a mineral phase based on the contained element wt%. The step size of this high-resolution grid of EDS spectra is flexible and can be adjusted from a few hundreds of nanometer to micrometer-scale in a manner of best fit for the grain size of the sample and the specific focus of the research. Due to the fine-crystalline basaltic rocks and fine-grained shale samples, a step size of 0.5  $\mu\text{m}$  and 1.8  $\mu\text{m}$  was chosen to ensure the detection of the various mineral and glassy phases, and other detrital and later-stage diagenetic minerals, and to reduce the effects of beam interaction of sample material. Only the coarser grained sandstone @049.50 was analysed with a step size of 1.8  $\mu\text{m}$ .

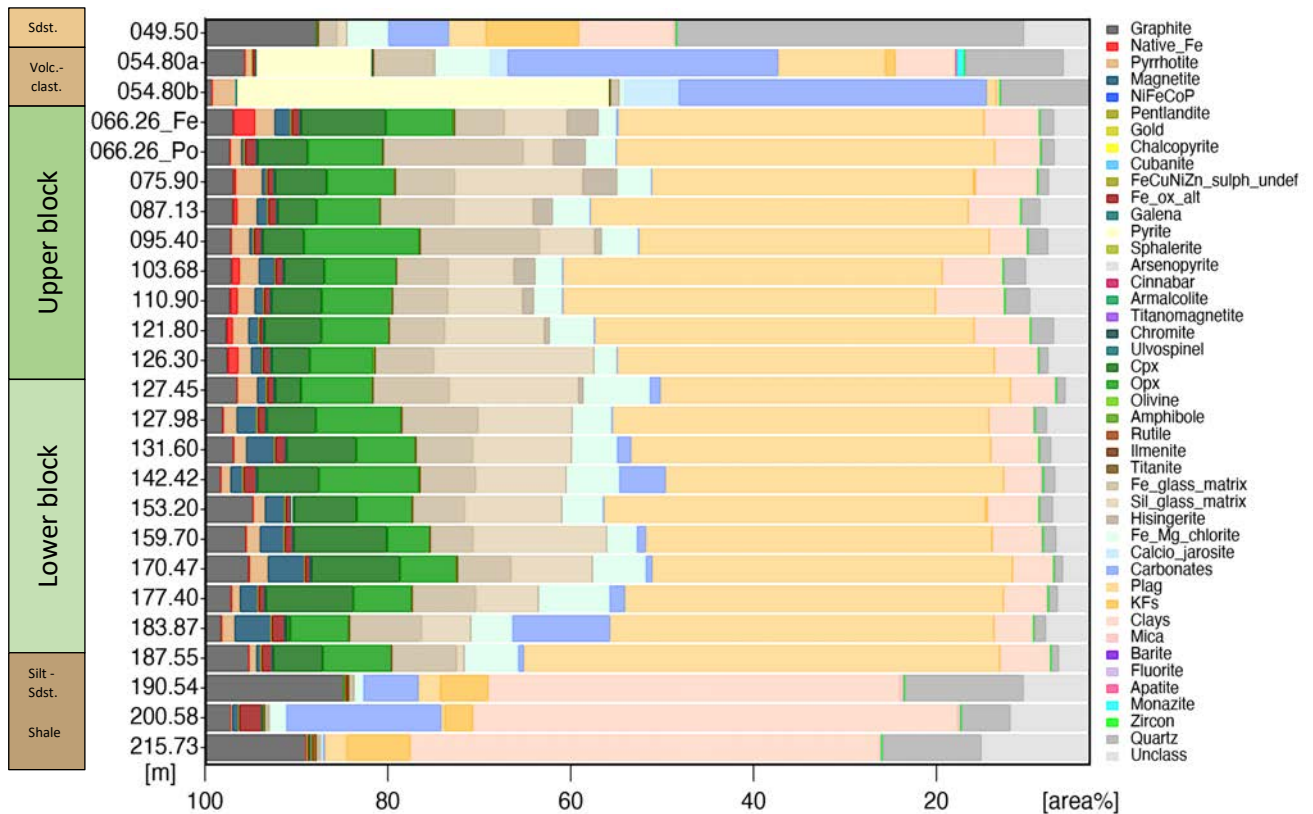
An important role in such automated mineralogical studies is the definition of a mineral list containing the minerals present in the investigated samples, as the AQM software (ZEISS, Mineralogic) requires this information to classify each mineral based on the analyzed EDS spectra. The mineral list is generated prior to the automated run and optimized after the run, allowing to add missing mineral phases. Quality assurance and quality control protocols are applied by running duplicate analyses to ensure reliable data procurement. Each mineral phase is given a certain colour resulting in a false-colour mineral map of the analyzed sample area. In addition to the mineral maps, backscattered electron (BSE) micrographs of the analyzed area are acquired automatically by the AQM software. For each of the samples, a representative area within the thin section was selected for AQM-SEM analyses. For each of the analyzed area of a sample, mineral and BSE maps are produced, as well as data tables for quantitative modal mineralogy (bulk mineralogy). A summary table and bulk mineralogy figure is compiled for all samples of FP94-4-5 presenting modal mineralogy data systematically over the covered core depth (Table 2, Figure 2).

Additionally, mineralogical data is compared with the petrophysical data and presented in Figure 3.

Electron backscatter diffraction (EBSD) analyses on a few samples was suggested as optional additional measurements to test whether pyrrhotite *sensu strictu* is distinguishable from troilite (part of the pyrrhotite group, i.e., pyrrhotite *sensu lato*). According to Ramdohr (1975), these forms of pyrrhotite commonly occur in various proportions together in one grain and therefore, a distinction using EBSD would be difficult. Furthermore, to detect variations in the amounts of troilite vs pyrrhotite *s.str.* in a meaningful matter in respect to the petrophysical data, all 23 samples would have to be analysed using EBSD, or other suitable method, which would require extensive sample preparation and analysis time. Due to these uncertainties and time intense sample preparation it therefore was chosen not to perform any EBSD analyses.

### 1.1. Summary of results - mineralogy

The analyzed samples from the Qullissat borehole FP94-4-5 cover the core depths 49.50 to 215.70 m ranging from the upper carbonaceous sandstone interval, a volcanoclastic breccia, which possibly represents a taxite, over the volcanic succession to the lower carbonaceous sedimentary rocks (silty shale and shale). Based on the magnetic properties, the volcanic succession was subdivided into an upper basaltic block and a lower basaltic block. These units are distinguishable using automated mineralogy (Figs. 2, 3).



**Fig. 2.** Bulk mineralogy of the analyzed samples of FP94-4-5 given in area%. Variations in mineralogy of the different lithological units are illustrated in following figure. Individual carbonates and silicates were measured, but grouped here for better visualisation. Appendices B and C contain all measured individual minerals.

**Note:** Colour coding of the legend of minerals shown in this figures does not correspond exactly to the colours of the legend for the AQM-SEM analyses.



Table 2 – part 1

Min_area%	049.50	054.80a	054.80b	066.26_Fe	066.26_Po	075.90	087.13	095.40	103.68	110.90	121.80	126.30
Density_D	2140.224	2204.620		2785.068		2803.064	2781.090	2773.548	2780.661	2774.518	2788.102	2800.971
Susceptibility_K	129.634	1552.955		20092.728		23907.614	27571.934	32936.751	34295.546	34708.298	47537.108	44361.260
Remanence_J	117.035	1823.164		405.446		431.355	217.195	367.069	1100.045	351.584	609.107	272.044
Graphite	12.17701	4.43776	0.82845	3.10501	2.74082	3.11751	3.08945	2.87051	2.90046	2.76615	2.37637	2.47708
Native iron				2.38626	0.07467	0.28066	0.47194	0.07611	0.92767	0.81543	0.68529	1.17852
Pyrrhotite	0.01016	0.77454	2.59128	2.09499	1.12207	2.81393	2.07858	1.89232	2.03737	1.82096	1.66322	1.37513
Fe-ox (magn)	0.00260	0.00111	0.00872	1.86751	0.41432	0.58743	1.25267	0.49069	1.81576	1.01979	1.21400	1.24687
Ni-Fe(+/-Co)P	0.00000	0.00000	0.00000	0.01061	0.00195	0.01530	0.03424	0.01608	0.02780	0.02044	0.02337	0.04382
Pentlandite				0.00111	0.00059	0.00026	0.00007	0.00059	0.00007	0.00007		
Gold	0.00007	0.00007										
Chalcopyrite	0.00003			0.00085	0.00091	0.00059			0.00013		0.00007	
Cubanite	0.00003		0.00716	0.01230	0.00475	0.00332	0.00078	0.00065	0.00046	0.00013	0.00072	0.00013
Fe-Cu(+/-Ni+/-Zn)-sulph_undef.							0.00046	0.00104	0.00052	0.00026	0.00065	0.00020
Fe-ox (altered)	0.01491	0.43223	0.01361	0.98783	1.36725	0.79681	0.98333	0.92676	0.90840	0.80299	0.49818	0.92852
Galena											0.00007	0.00007
Pyrite(+/-As+Ni+Co)	0.01600	12.68542	40.80729	0.01094	0.00859	0.02311	0.01087	0.01771	0.00638	0.00866	0.00618	0.00697
Sphalerite												
Arsenopyrite									0.00007			
Cinnabar	0.00007	0.00026	0.00052			0.00020	0.00026	0.00052	0.00007	0.00013	0.00026	0.00013
Armalcolite								0.00013			0.00007	0.00020
Titanomagnetite				0.00007	0.00039	0.00163	0.00046	0.00026	0.00020	0.00013	0.00091	0.00326
Chromite	0.00239			0.00182	0.00026			0.00020				
Ulvo-spinel	0.00003	0.00059		0.00130	0.00566	0.00410	0.00078	0.00059	0.00007	0.00033	0.00202	0.00560
Cpx	0.06083	0.06973	0.00905	9.29928	5.50651	5.69258	4.30814	4.54167	4.44329	5.51458	6.27259	4.20931
Opx	0.00827	0.03574	0.01966	7.35964	8.22122	7.41178	6.97585	12.59798	7.91322	7.78958	7.45319	6.91849
Olivine	0.00038	0.01816	0.02611	0.18639	0.04212	0.01745	0.01432	0.15684	0.01152	0.00632	0.00547	0.20332
Amphibole (ferrohornblende)												
Rutile	0.10938	0.00241	0.00117	0.02246	0.02318	0.10514	0.00241	0.00117		0.00007	0.00905	0.05990
Ilmenite	0.02192	0.00977	0.00104	0.00299	0.02109	0.00378	0.00098	0.00026	0.00007	0.00007	0.00423	0.00970
Titanite	0.00082	0.00013		0.00156	0.00163	0.00039	0.00020	0.00026				0.00208
Fe-glass (matrix)	2.00055	6.53802	0.96250	5.41673	15.26380	6.48535	8.04733	13.03177	5.65384	6.01608	6.01868	6.38802
Siliceous_glass (matrix)	1.11573	0.20215	0.00007	6.78145	3.22318	13.90632	8.56712	5.93509	7.09206	8.10846	10.83548	17.54036
Hisingerite	0.01870			3.51660	3.61361	3.83027	2.21862	0.87181	2.40625	1.30072	0.66797	
Fe-Mg-chlorite	4.47369	5.94648	0.52480	1.93600	3.34095	3.79772	4.11660	4.05059	2.97572	3.17559	4.85508	2.52168
Calcio-jarosite		1.91517	5.94108									
Carbonates	6.63881	29.64596	33.72318	0.20690	0.03639	0.01348	0.03177	0.00710	0.07298	0.01484	0.06484	0.00964
Plag	4.01707	11.66510	1.06289	39.98698	41.37096	35.12298	41.29368	38.31914	41.47396	40.74408	41.49421	41.20026
KFs	10.19314	1.14108	0.00000	0.05814	0.02500	0.27728	0.01960	0.01204	0.02207	0.02598	0.01992	0.04401
Clays	10.33453	6.45130	0.43730	5.99857	4.98854	6.64564	5.70111	4.14258	6.62806	7.52734	6.07051	4.70807
Mica	0.33790	0.24395	0.00007	0.07018	0.00007	0.15579	0.05846	0.06953	0.00000	0.04336	0.07865	0.13965
Barite		0.00020			0.04876		0.00736		0.03757			
Fluorite									0.00052			
Apatite	0.00352	0.00078		0.00749	0.01452	0.00026	0.00130	0.00866	0.00020	0.00260	0.00026	0.02077
Monazite		0.91660										
Zircon	0.00127											
Quartz	38.00859	10.78997	9.68275	1.54967	1.45645	1.21693	2.10299	2.19323	2.43652	2.73040	2.54434	1.00710
Unclass	10.41120	6.07520	3.29447	7.11745	7.05951	7.67122	8.60827	7.76589	10.20677	9.74447	7.13418	7.75111

Table 2 – part 1. Summary of results for the samples 049.50 – 126.30 analysed by AQM-SEM at GEUS.

Note:

Sample 054.80 is very heterogeneous in texture and composition and accordingly, two representative areas (\_a and \_b) were analysed

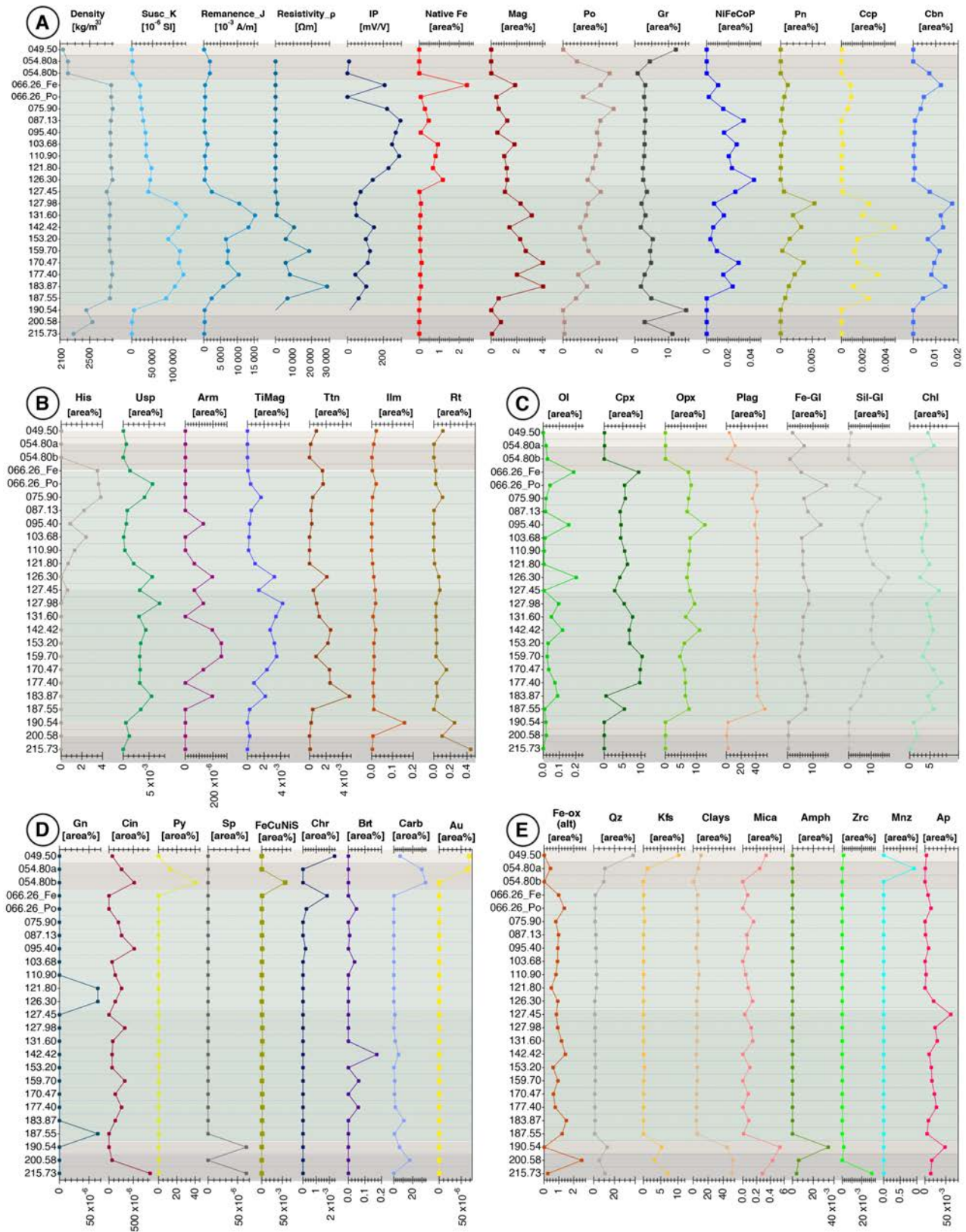
Sample 066.26 appeared to have two intermingled flows of slightly different composition, one contained more preserved large droplets of native Fe and the other was more pyrrhotite-dominated with smaller preserved native Fe occurrences. Also here two representative areas (066.26\_Fe and 066.26\_Po) were analysed.

Table 2 – part 2

Min_area%	127.45	127.98	131.60	142.42	153.20	159.70	170.47	177.40	183.87	187.55	190.54	200.58	215.73
Density_D	2725.021	2766.966	2767.411	2762.102	2760.658	2766.826	2793.513	2797.433	2774.772	2767.659	2452.201	2533.931	2281.230
Susceptibility_K	40157.875	106588.632	129741.580	112016.882	87933.190	115853.190	113211.805	124267.395	103756.663	82728.507	5126.230	598.320	132.800
Remanence_J	2410.873	10560.212	15244.205	13296.736	6618.125	7189.429	7055.956	10390.641	5822.831	2371.546	264.707	289.116	175.111
Graphite	3.57773	1.97598	3.15318	1.77435	5.28444	4.52409	4.80313	2.91250	1.80267	4.86335	15.22624	2.90111	11.12936
Native iron	0.01081	0.08444	0.05636	0.02624	0.05072	0.05182	0.11712	0.04766	0.08457	0.01022	0.00020		
Pyrrhotite	2.09284	1.38848	1.27734	0.95853	1.20313	1.41810	1.94382	0.84303	1.33066	0.72402	0.00007	0.07559	0.07721
Fe-ox (magn)	1.07051	2.29596	3.16208	1.43288	2.26712	2.69766	4.03210	2.01413	4.04720	0.58047	0.00990	0.75469	0.07018
Ni-Fe(+/-Co)P	0.02656	0.00677	0.01592	0.00605	0.00345	0.00944	0.02956	0.01536	0.02402	0.00000	0.00000	0.00000	0.00000
Pentlandite	0.00052	0.00534	0.00195	0.00326	0.00143	0.00026	0.00365	0.00221	0.00130	0.00072			
Gold													
Chalcopyrite	0.00013	0.00254	0.00195	0.00495	0.00150	0.00124	0.00150	0.00339	0.00111	0.00247			
Cubanite	0.00736	0.01732	0.01226	0.01328	0.00651	0.01172	0.00938	0.00807	0.01426	0.00436			
Fe-Cu(+/-Ni+/-Zn)-sulph_undef.	0.00078	0.00137	0.00148	0.00072	0.00059	0.00059	0.00111	0.00156	0.00072	0.00130	0.00000	0.00000	0.00000
Fe-ox_(altered)	0.83223	0.92474	1.18632	1.44355	0.61198	0.94193	0.63040	0.76159	1.50221	1.21764	0.01628	2.54440	0.25378
Galena										0.00007			
Pyrite(+/-As+Ni+Co)	0.04082	0.03236	0.02834	0.02611	0.28652	0.03034	0.03470	0.01953	0.01367	0.02376	0.00007	0.11322	0.20365
Sphalerite											0.00007		0.00007
Arsenopyrite													
Cinnabar		0.00033	0.00008	0.00007	0.00007	0.00033	0.00013	0.00026	0.00013			0.00007	0.00085
Armalcolite	0.00007	0.00013	0.00020	0.00020	0.00026	0.00026	0.00013	0.00020	0.00020				
Titanomagnetite	0.00137	0.00423	0.00343	0.00273	0.00326	0.00352	0.00234	0.00078	0.00215	0.00026		0.00026	
Chromite													
Ulvospinel	0.00319	0.00703	0.00304	0.00436	0.00339	0.00319	0.00326	0.00319	0.00547	0.00339	0.00052	0.00117	
Cpx	2.83555	5.40020	7.65614	6.76999	6.87741	10.23516	9.71048	9.60020	4.9538	5.45397	0.00690	0.00020	0.00195
Opx	7.84160	9.31016	6.48653	10.93691	6.08633	4.68411	6.15052	6.37552	6.39798	7.55898	0.03874	0.05247	0.00124
Olivine	0.00586	0.09531	0.05058	0.11908	0.03099	0.02487	0.03405	0.07227	0.08809	0.00964	0.01634	0.01940	0.00104
Amphibole (ferrohornblende)											0.03457	0.00592	0.00391
Rutile	0.07324	0.02799	0.02592	0.03040	0.03437	0.02721	0.15299	0.03333	0.04076	0.00150	0.25020	0.09987	0.44473
Ilmenite	0.01654	0.01855	0.00609	0.01882	0.01074	0.01133	0.01211	0.00645	0.00905	0.01009	0.15801	0.00573	0.00326
Titanite	0.00046	0.00085	0.00117	0.00254	0.00221	0.00078	0.00241	0.00247	0.00482	0.00039	0.00020		0.00007
Fe-glass_(matrix)	8.28854	8.28854	6.19863	6.03470	5.65404	4.67194	5.83652	6.92344	7.84681	7.08522	0.48880	0.35996	0.29909
Siliceous_glass_(matrix)	14.09271	10.31374	10.80526	9.92858	10.65579	14.62793	8.91243	6.86973	5.41022	0.84538	0.11367	0.13926	0.20527
Hisingerite	0.60462												
Fe-Mg-chlorite	7.23841	4.27363	4.95853	5.79147	4.45215	3.27279	5.80638	7.74896	4.49512	5.87370	0.98184	1.83952	0.23346
Calcio-jarosite									0.02064				
Carbonates	1.17858	0.12897	1.54181	5.08607	0.13893	0.99284	0.71009	1.68568	10.67409	0.62734	6.00605	16.95299	0.18919
Plag	38.31393	41.15632	39.31534	36.95059	41.66719	37.84746	39.38750	41.39967	42.00397	52.06074	2.36165	0.34336	2.35332
KFs	0.01055	0.02331	0.04293	0.02389	0.28210	0.06009	0.04082	0.02624	0.00775	0.00065	5.29688	3.12871	6.99525
Clays	4.89954	4.87253	5.12153	4.15684	5.56868	5.46100	4.44980	4.81374	4.28099	5.56999	44.93034	52.93984	51.29408
Mica	0.02852	0.12148	0.14309	0.00000	0.10013	0.00000	0.07943	0.00000	0.08724	0.01068	0.53743	0.43053	0.28392
Barite				0.17181		0.06217		0.06009					
Fluorite													
Apatite	0.06224	0.02428	0.02943	0.01003	0.01510	0.01667	0.02279	0.02741	0.00827	0.00488	0.04831	0.01634	0.01380
Monazite													
Zircon											0.002		0.030
Quartz	0.962	1.303	1.272	1.293	1.472	1.437	0.940	0.995	1.297	0.851	13.012	5.388	10.838
Unclass	5.882	7.894	7.441	6.977	7.228	6.873	6.139	6.727	8.001	6.604	10.464	11.887	15.073

Table 2 – part 2. Summary of results for the samples 127.45 – 215.73 analysed by AQM-SEM at GEUS.

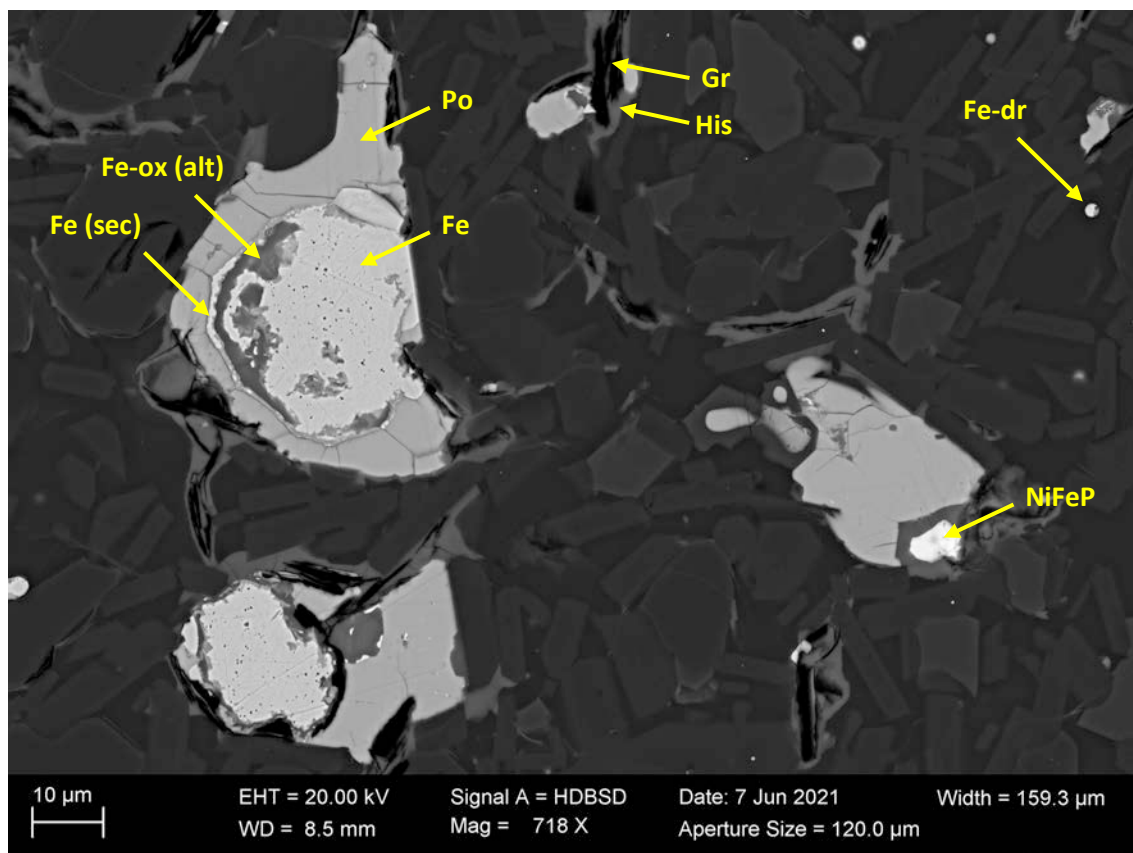
**Fig. 3 (next page). A:** Measured petrophysical parameters (density, susceptibility [K], remanence [J], resistivity [ $\rho$ ], and induced polarization [IP]) in correlation with magnetic/conductive minerals (native iron [Fe], magnetite [Mag], pyrrhotite [Po], graphite [Gr]), Ni-Cu minerals. Note: no resistivity and IP measurements for sedimentary rocks due to fracturing. **B:** Potential indicator minerals: Amorphous phase hisingerite [His] and titanium phases ulvöspinel [Usp], armalcolite [Arm], titanomagnetite [TiMag], titanite [Ttn], ilmenite [Ilm], and rutile [Rt]. **C:** Basaltic primary and xenolite/phenocryst minerals, such pyroxene [Opx, Cpx], plagioclase [Pl], olivine [Ol], as well as Fe-Mg-chlorite [Chl] as alteration product and glassy matrix phases [Fe-Gl, Sil-Gl]. **D:** Other observed sulphides galena [Gn], cinnabar [Cin], pyrite [Py], sphalerite [Sp], FeCuNi-sulphides [FeCuNiS], chromite, barite, carbonates [Carb], and gold [Au]. **E:** Detrital minerals quartz [Qz], K-feldspar [Kfs], mica, amphibole [Amph], zircon [Zrc], monazite [Mnz], and apatite [Ap], as well as alteration minerals, such as clays and Fe-oxide [Fe-ox(alt)].



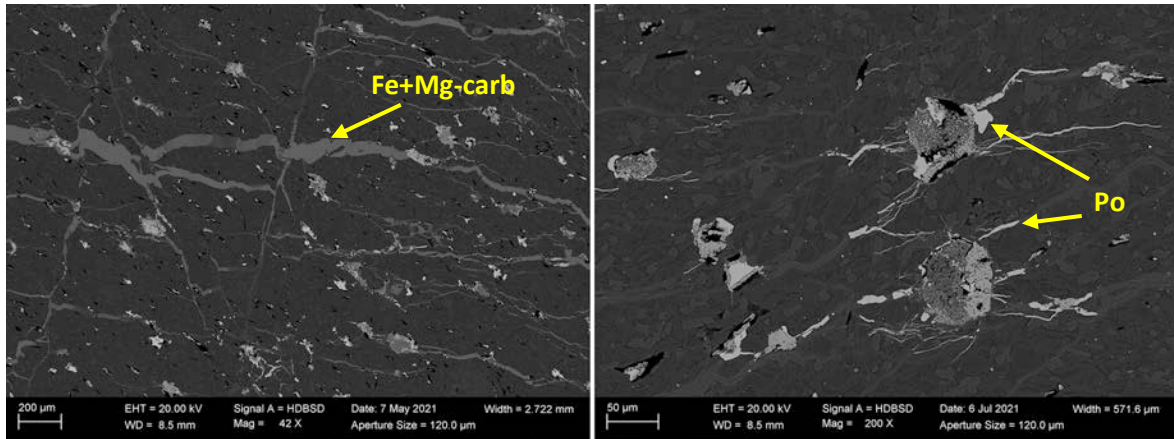
### 1.1.1 Native iron / cohenite

Native iron is predominantly preserved in the upper basaltic block (Fig. 3A) and commonly occurs as larger rounded to subrounded to irregular shaped droplets, commonly with a rim of magnetite and/or an low-density Fe-oxide alteration phase. The subrounded to irregular native Fe occurrences are most commonly within a few tens of  $\mu\text{m}$ , but can range up to a few hundred  $\mu\text{m}$  in size. Furthermore, native Fe is also present as micron-sized droplets (Fig. 4) within the matrix and outer zones of pheno- and xenocrysts (plagioclase, orthopyroxene). Only very little native Fe was observed in the lower basaltic block (177.40; Figs. 5, 6). Frequently, a 'cleaner' appearing secondary Fe phase is forming a thin rim or patch around the native Fe and/or Fe-oxide phase, which possibly represents cohenite.

Cohenite was observed and reported in previous Disko samples from this area (e.g., Pedersen, 1981). Due to the carbon coating, a quantification of the C in cohenite ( $\text{Fe}_3\text{C}$ ) using EDS is difficult, and therefore, also the distinction of native Fe and  $\text{Fe}_3\text{C}$ . Both of the above described texturally different Fe phases have the same Fe-contents when performing EDS spot analyses. Nevertheless, it is possible that EDS as method to analyse the composition is not able to sufficiently detect the differences between cohenite and native Fe and that this secondary Fe is in fact cohenite. A similar rim-texture is described and measured (electron microprobe analysis) as cohenite from an Fe-bearing sample from the Hammersdal complex, NW Disko (Ulff-Møller, 1977). Due to the uncertainty, the term secondary Fe 'Fe (sec)' is used to distinguish this phase from native Fe.



**Fig. 4.** Backscatter electron micrograph of native iron [Fe] with characteristic spongy texture preserved as few tens of  $\mu\text{m}$ -sized subrounded droplets and as micron-sized droplets in the matrix [Fe-dr], as well as a 'cleaner' appearing secondary rim of Fe. Associated mineral phases are pyrrhotite [Po], Fe-oxide [Fe-ox], Ni-Fe-phosphide [NiFeP], graphite [Gr], hisingerite [His]. Upper basaltic block (087.13).



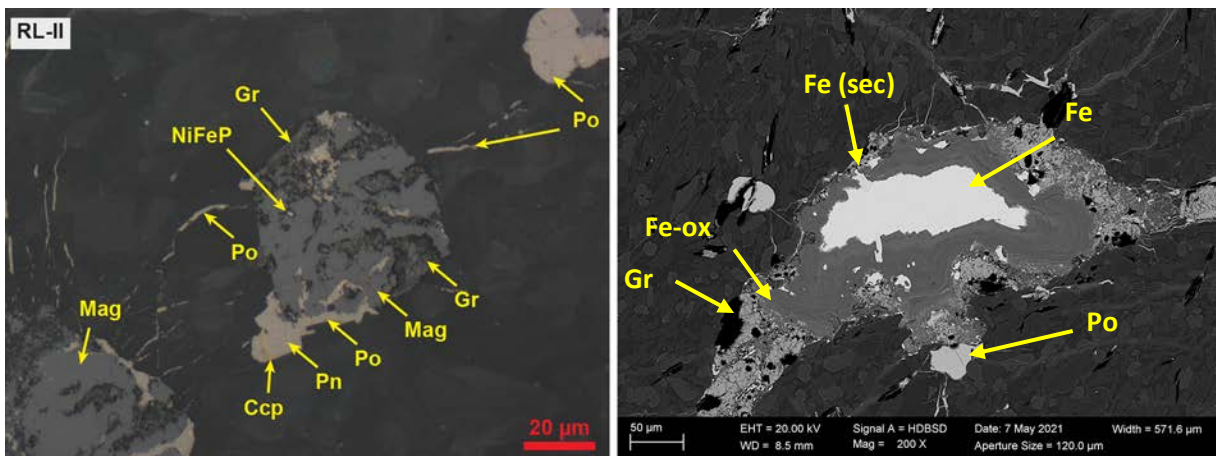
**Fig. 5.** Backscatter electron micrograph of lower block samples (left: 187.55, right: 183.87) with carbonate-filled conjugate sets of faults and remobilized pyrrhotite. Native Fe is not preserved.

### 1.1.2 Graphite

Graphite is present in the upper and lower basaltic blocks. The upper block has more constant quantities of graphite, whereas the lower block has more varying graphite contents and a minor increase in the lower half of the lower block.

A significant difference in the association of the graphite of the upper to the lower block is observable: graphite in the upper basaltic block always occurs with amorphous hydrated Fe-silicate hisingerite that is coating/enveloping the graphite (Fig. 4). Hisingerite is phasing out towards the contact to the lower block (Fig. 3B) and not present (Figs. 5, 6).

Both, the upper and lower sedimentary units, are carbonaceous with various organic matter components and semi-amorphous graphitic carbon. More detailed descriptions are given in the section of these units. Carbonaceous matter in the sedimentary and volcanoclastic units is classified as 'Graphite' in the AQM-SEM analyses, as a distinction between the various organic matter and graphite phases cannot be done by AQM only.



**Fig. 6.** Left: Reflected light micrograph of a lower block sample (183.87) with magnetite [Mag] in association with graphite [Gr], NiFe-phosphide [NiFeP], and pyrrhotite [Po]. Pyrrhotite also occurs remobilized in fractures and contains pentlandite [Pn] flames and chalcopyrite [Ccp] inclusions. Right: Rare observed native Fe in lower block (177.40). Strongly altered alteration rims of Fe-oxide [Fe-ox] indicate that the Fe likely is only preserved due to its large size. Also preserved the second Fe phase [Fe (sec)].

### 1.1.3 Magnetite

Magnetite is present in both, the upper and lower basaltic blocks, whereas the lower block has higher amounts of magnetite (Fig. 3A, 6). In the upper block it commonly is forming a rim around native Fe, whereas in the lower block it occurs as larger subrounded minerals (Fig. 6).

### 1.1.4 Pyrrhotite

Pyrrhotite is present in both, the upper and lower basaltic blocks, although the upper block contains moderately more pyrrhotite than the lower one (Fig. 3A). It commonly is associated with native Fe and Fe-oxide phases and often with graphite. Pyrrhotite in the lower block more frequently contains chalcopyrite (or other CuFe-sulphide phases) and pentlandite flames (Fig. 6) than those occurring in the upper block (Fig. 4). Locally, secondary covellite is forming at the margins of the pyrrhotite.

### 1.1.5 NiFe-phosphides, pentlandite, and other Cu-Fe-sulphides

NiFe-phosphides occur in schreibersite composition, but also as more Ni-rich undefined NiP phases, locally with measureable Co-enrichment. Pentlandite flames and chalcopyrite (and minor cubanite) occur within pyrrhotite, predominantly in the lower basaltic block, whereas NiFe-phosphides show moderately higher detected quantities in the upper block (Fig. 3A).

### 1.1.6 Potential indicator minerals

Potential indicator minerals represent minerals that occur predominantly or exclusively in one of the basaltic blocks. Hisingerite occurs in the upper block only, and accordingly, may serve as indicator mineral to identify the native iron bearing upper basaltic block. Ulvöspinel, armalcolite, titanomagnetite, and titanite do not exclusively but predominantly occur in the lower basaltic block, and enrichments of these as a group may serve as indicator minerals for the lower basaltic block (Fig. 3B).

### 1.1.7 Primary basaltic minerals and pheno- and xenocrysts

The basaltic groundmass consists of euhedral plagioclase microlite laths and subhedral to anhedral orthopyroxene (enstatite and intermediate Fe-Mg Opx composition) and clinopyroxene (predominantly diopside, minor hedenbergite and augite composition). The intersertal matrix mainly consists of a K-bearing siliceous glass phases and an Fe-rich siliceous glass phase. The latter may represent palagonitic composition, however, only in the vug space of the volcanoclastic sample (054.80), a typical palagonitic texture could be observed. The K-bearing high silica glass in the matrix is atypical for mafic to ultramafic rocks, but likely to be a result of the assimilation of the sedimentary units.

The xenolite/phenocryst minerals consist predominantly of orthopyroxene and plagioclase, commonly oscillatory zoned with micron-sized Fe-droplets dispersed in an outer rim and frequently with serrated dissolution embayments. Size of xeno- and phenocryst varies, but can reach up to few mm in size. Olivine is only preserved in very minor amounts as relict cores within orthopyroxene.

No significant difference in these minerals can be observed between the two basaltic blocks. Only clinopyroxene appears slightly enriched in the lower block (Fig. 3C).

### 1.1.8 Other sulphides, oxides, phosphates, carbonates, Au

Pyrite occurs predominantly as colloform melnikovit-pyrite in the volcanoclastic (possibly taxite) sample (054.80) and commonly in association with rhythmically zoned carbonates with varying compositions between the different layers. This samples also contained small amounts of another undefined FeCuNi-sulphide. Carbonates consist mainly of siderite and ankerite, with varying amounts of Fe-Mg±Mn±Ca. Interestingly, locally, gold was detected in traces within those carbonates. Carbonates occur as a main phase as cement in the upper and lower sedimentary and volcanoclastic unit but also in the lower basaltic block as late-stage fracture fill. Sphalerite occurs as accessory mineral in the lower sedimentary units. Cinnabar was detected throughout the complete succession as accessory mineral and chromite as accessory mineral in the upper sedimentary unit and in the upper half of the upper block (Fig. 3D).

### 1.1.9 Microtextures

The plagioclase microlites and sometimes also the phenocrysts, sulphides, and graphite often show signs of flow foliation-related, locally also shearing-related, alignment in the upper block. The lower block frequently is cross-cut by conjugate sets of faults/joints and sheared, whereby the groundmass minerals are often shear-foliated and larger minerals/pheno-xenocrysts have shear sense indicators with pressure shadow mineralisation (Figs. 5, 6). The joints and fractures in the lower block are commonly rhythmically filled with Fe-Mg±Mn±Ca carbonates, similarly in composition as those in the 054.80 volcanoclastic rock. Shearing and related oxidation represents a possibly cause that native Fe mostly is not preserved, with the exception of the large but strongly altered native Fe in 177.40 (Fig. 6). Pyrrhotite is commonly remobilized into small fractures and veinlets surrounding the main mineral (Figs. 5, 6).

## 1.2 Correlation of mineralogy and petrophysical properties

The petrophysical properties magnetic susceptibility, remanence, as well as the electrical properties (resistivity and IP) clearly show a distinction between the upper and lower basaltic blocks (Fig. 3A). The density is slightly higher in the upper block, but remains mostly constant within each block. The lower block has a strong increase in both, magnetic susceptibility and remanence, which correlates with increased occurrences of magnetite and not with native Fe. This is in disagreement with a former hypothesis that native Fe strongly contributes to the overall magnetisation. Higher amounts of native Fe, however, correlate with higher measured conductivities. Similarly, pyrrhotite appears slightly enriched in the more conductive upper block samples. Resistivity is clearly more pronounced in the lower 2/3 of the lower block, which may relate to the lack (or very minor occurrences) of native Fe and/or to the strongly fractured and carbonate -filled nature of this part of the volcanic succession. Graphite appears not to have any significant influence on any of the magnetic or electric properties. This was unexpected, as graphite commonly is described as main source of conductivities in rocks. However, a plausible explanation is that graphite occurs in random orientations and disseminated within the volcanic rocks, and not as continuous carbonaceous layer within a sedimentary rock. The exact role of the disseminated nature of the main conductive

minerals (native Fe, pyrrhotite, and graphite) and other potentially minor conductive minerals on the IP effect is remains unresolved and further studies would be advised.

Cohenite is a strongly magnetitic mineral (Ramdohr, 1975) and in literature reported to be associated with native Fe on Disko (Ulff-Møller, 1977; Pedersen, 1981); however, if the second Fe phase observed in this study represents cohenite, it is not abundant enough to influence the magnetic properties and/or to compensate the reduced magnetisation in the upper block due to the lower amount of magnetite.

### 1.3 Definition of minerals / mineral list

Native iron is defined as individual mineral phase, locally contains traces of Co.

Schreibersite (Fe,Ni)<sub>3</sub>P is one of the Ni-Fe-phosphide varieties present in the samples. Some deviate from the stoichiometric composition of schreibersite, and additional phosphide varieties were added to the mineral list accordingly. One NiFeP-phase contained Co.

Graphite was recognized as mineral phase by reflected and transmitted light microscopy and for AQM-SEM defined primarily based on the grey scale and accordingly, could be quantified as individual mineral phase. In the sedimentary units, this 'graphite' classification comprises graphitic carbon and other organic matter phases.

Pyrrhotite is given as 'pyrrhotite', previous studies by L. Melchior and A.K. Pedersen suggest that it includes troilite, which belongs to the pyrrhotite group and accordingly 'pyrrhotite' as name was chosen. Pyrrhotite commonly contains pentlandite flames and chalcopyrite inclusions. Due to the small grain size, it is not always possible to fully distinguish the Fe-Cu-Ni-sulphides and when not fitting into a stoichiometric class, undefined Fe-Cu-Ni-sulphide minerals were added to the mineral list to indicate their presence.

Based on reflected light petrography, the Fe-oxide was identified as magnetite, and was defined as such when stoichiometrically close to the magnetite composition. Additionally, an Fe-oxide alteration product of native Fe was observed as a lower than magnetite density mineral phase, which may represent goethite or another alteration Fe-oxide phase. As distinction from magnetite, a classification 'Fe-oxide (altered)' was added. Hematite was not observed in reflected light microscopy.

A range of Fe-Mg-Ca±Mn-carbonates were detected and distinguished, as they may have exploration implications (e.g., Au trace occurrences).







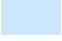






















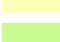

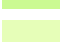


























Glasses occur in the matrix and/or as amygdale-fill and are subdivided into a 'siliceous matrix (glass)' phase, which contains high Si contents (~40-45wt%), that consistently also contains Al (5-9 wt%), and K (2-4 wt%), two Fe-bearing glass phases 'Fe-siliceous matrix (glass)' and 'Fe-siliceous matrix (glass)\_2', as well as an Fe-bearing amorphous mineral phase commonly coating graphite in the



upper block basalts that could be identified as hisingerite. Recognition as glass/amorphous mineral phase is based on optical microscopy.

Other mineral classifications with the add-on ‘altered’ were added to some of the minerals to allow a broader characterisation of the respective mineral, when having slight alteration rims or when bordering to other minerals (e.g., silicates), since the beam interaction at the border particles will detect some elements from the neighbouring minerals. Manual investigations ensured that the classification is still correct and that the ‘altered’ category just indicates that the composition is broader defined than in the main mineral classification.

#### 1.4. Legend for AQM mineral maps

 Schreibersite	 Gold	 Opx	 Fe-rich clay
 Ni-Fe-P	 Graphite	 Opx (enstatite)	 Calcite
 Ni-Co-Fe-P	 Native iron	 Cpx (hedenbergite)	 Calcite (+Mg)
 Ni-Fe-P (altered)	 Fe-ox (magnetite)	 Cpx (diopside)	 Dolomite
 Pentlandite	 Fe-ox (altered)	 Augite	 Ferroan dolomite
 Pyrrhotite	 Chromite	 Amphibole (Fe-hbl.)	 Ankerite
 Pyrrhotite (altered)	 Titanomagnetite	 Quartz	 Magnesian ankerite
 Chalcopyrite	 Rutile	 K-feldspar	 Ca-Mn-Fe-Mg-carbonate
 Cubanite	 Ilmenite	 Orthoclase	 Siderite
 Digenite	 Titanite	 Orthoclase (+Ba)	 Siderite (+Mg)
 Fe-Cu-Zn-sulphide	 Ulvospinel	 Hyalophane	 Rhodochrosite
 Cu-Fe-Ni-sulphide	 Armalcolite	 Plagioclase	 Siliceous matrix (glass)
 Fe-Cu-sulphide	 Zircon	 Anorthite	 Fe-siliceous matrix (glass)
 Cinnabar	 Monazite	 Albite	 Fe-siliceous matrix (glass) 2
 Pyrite	 Apatite	 Muscovite	 Hisingerite
 Pyrite (altered)	 Barite	 Biotite	 Rutile-clay mix
 Pyrite (+As+Ni+Co)	 Fluorite	 Fe-Mg-chlorite	 Fe-ox-silicate mix
 Arsenopyrite	 Forsterite	 Kaolinite	 Fe-ox-sulf-silicate mix
 Galena	 Fayalite	 Smectite+/-illite	 SiC (from polishing)
	 Unclassified, not classified, not analysed		

**Fig. 7.** Legend of detected minerals for the AQM-SEM mineral maps of this report.

Note: not all AQM mineral maps contain the complete set of minerals shown in this legend.

The bulk mineralogy shown in Figure 2 and the summary table Table 2 have certain individual minerals grouped, e.g., carbonates, orthopyroxenes, K-feldspars. The detailed bulk mineralogy *xlsx* file contains quantitative data for all individual minerals. The summary table shows the grouped minerals.

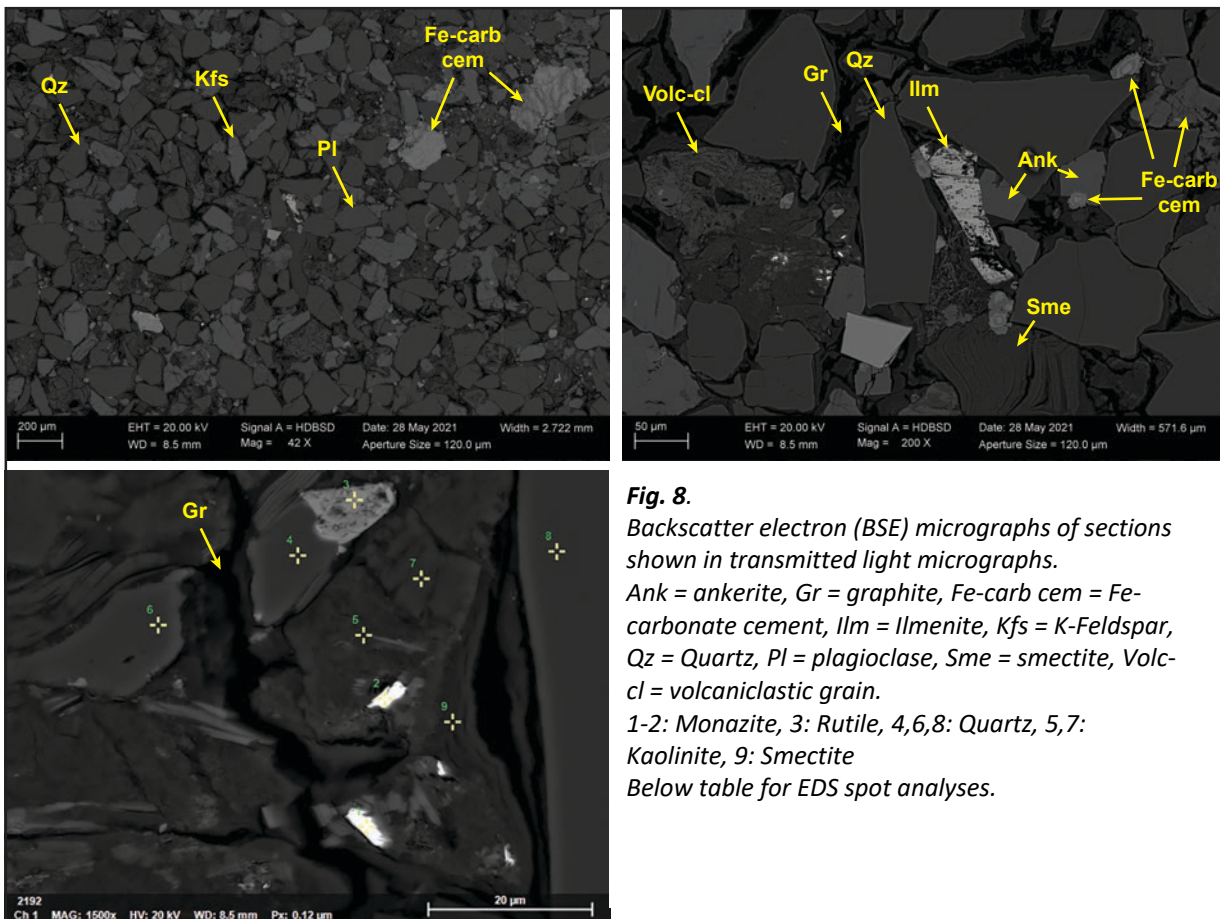
## 2) Results

### 2.1. FP94-4-5\_049.50 Summary

Grey coarse silt-sized, texturally moderately mature, compositionally immature, angular, arkosic and graphitic sandstone/wacke.

Framework minerals predominantly are quartz, variably clay-altered feldspar (K-feldspar and plagioclase), volcanoclastic grains, and minor detrital carbonate and heavy minerals. Graphite/graphitic carbon predominantly occurs in the matrix and to lesser amounts as aggregates. Matrix consists of clays (kaolinite, smectite-illite), Fe-Mg-chlorite and minor sulphides (predominantly pyrite). Accessory minerals are rutile, titanite, ilmenite, apatite, monazite, and others.

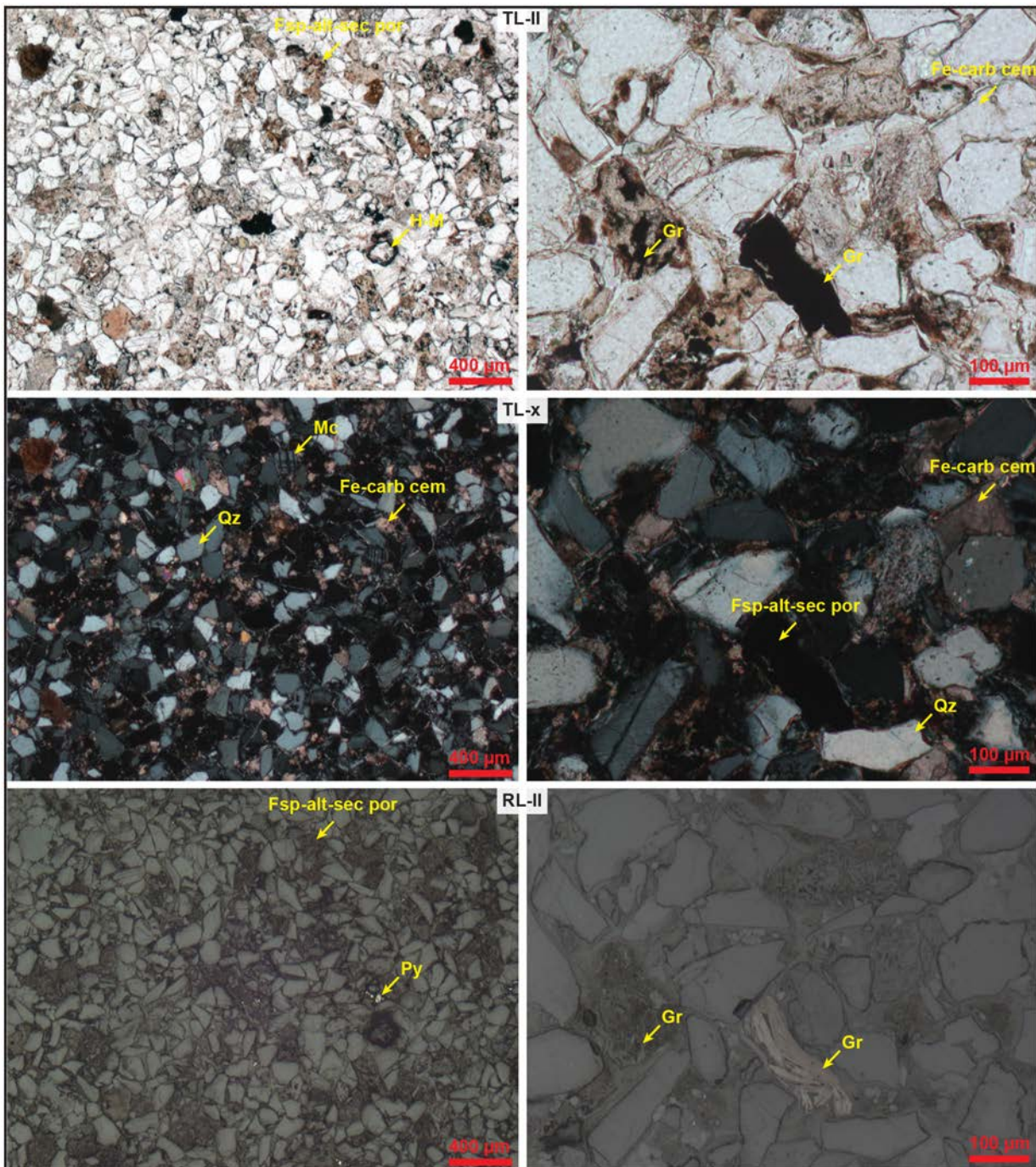
### 2.2. FP94-4-5\_049.50 SEM-BSE/EDS



**Fig. 8.** Backscatter electron (BSE) micrographs of sections shown in transmitted light micrographs. Ank = ankerite, Gr = graphite, Fe-carb cem = Fe-carbonate cement, Ilm = Ilmenite, Kfs = K-Feldspar, Qz = Quartz, Pl = plagioclase, Sme = smectite, Volc-cl = volcanoclastic grain. 1-2: Monazite, 3: Rutile, 4,6,8: Quartz, 5,7: Kaolinite, 9: Smectite  
Below table for EDS spot analyses.

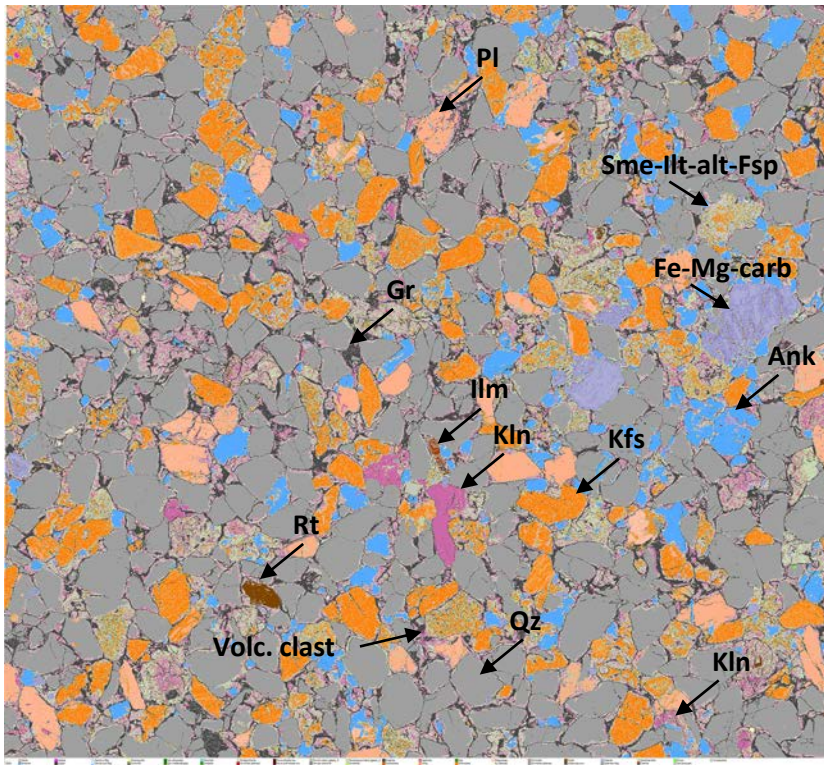
Spectrum	Mineral	O	Na	Mg	Al	Si	P	S	K	Ca	Ti	Fe	La	Ce	Nd	Th
1	Monazite	20.78			2.26	2.36	15.59			0.45			14.00	29.55	13.52	1.50
2	Monazite	21.55			2.99	3.22	14.40			0.35			13.24	28.93	11.64	3.68
3	Rutile	38.01		0.20	0.56	0.85		0.05		0.33	46.69	13.30				
4	Quartz	47.09				52.33					0.58					
5	Kaolinite	42.91		1.28	24.82	28.97						2.02				
6	Quartz	47.12				52.88										
7	Kaolinite	50.69			25.55	23.46						0.30				
8	Quartz	46.64			0.37	53.00										
9	Smectite	41.18	0.59	4.04	14.95	32.57			0.76	0.57	0.38	4.95				

2.3. FP94-4-5\_049.50 Microscopy



**Fig. 9.** Quartz (Qz) with slightly undulose extinction, K-feldspar (Kfs) include moderate amounts of microcline (Mc). Matrix consists of Fe-carbonate cements (Fe-carb-cem) and clays. Opaque minerals: graphite/graphitic carbon (Gr; as flaky aggregates and disseminated in matrix), metal oxides (Fe-Ti-oxides), and sulphides (predominantly pyrite (Py)) occurring as grains and replacement of secondary porosity in feldspars (Fsp-alt-sec-por). Minor heavy minerals (H-M) as accessory phase. TL-II: transmitted light micrograph with plane polarized light (ppl). TL-x: crossed polars. RL-II: reflected light micrograph with ppl.

2.4. FP94-4-5\_049.50 AQM-SEM

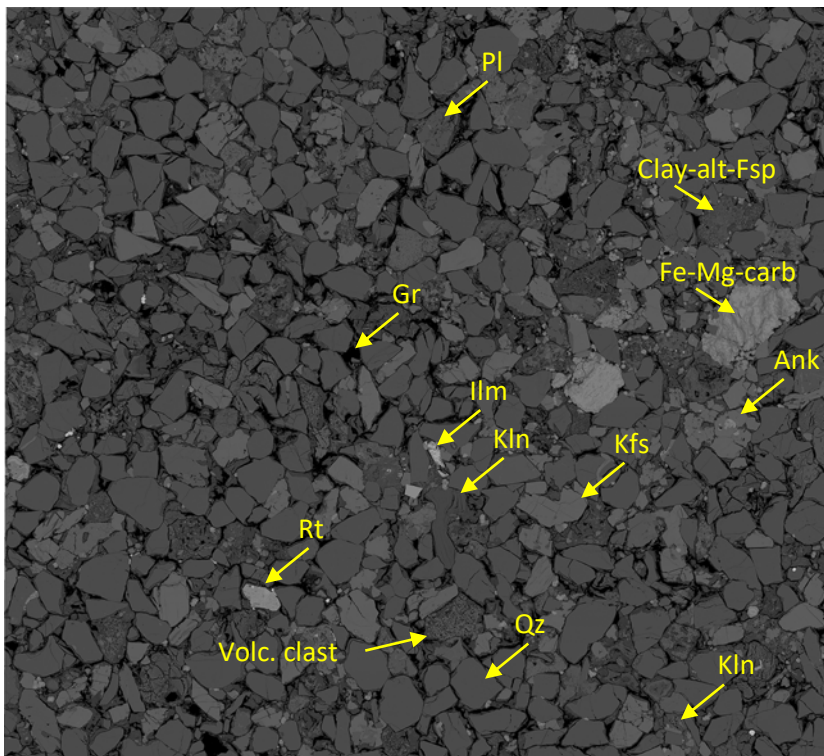


**Fig. 10.** Mineral map and corresponding BSE map of AQM-SEM analysis.

Detrital minerals are predominantly quartz [Qz], K-feldspar [Kfs], plagioclase [Pl], clay-altered (smectite-illite; Sme-illt) KFs, and feldspar-phyric volcaniclastic clast. Kaolinite [Kln] occurs in the matrix and as alteration product. Quartz grains show clay coating. Rutile [Rt] and ilmenite [Ilm] occur as accessory minerals. Ankerite [Ank] occurs as later-stage cements together with Fe-Mg carbonates. Graphite [Gr] occurs within the matrix and as aggregates of flaky graphite minerals.

200 μm

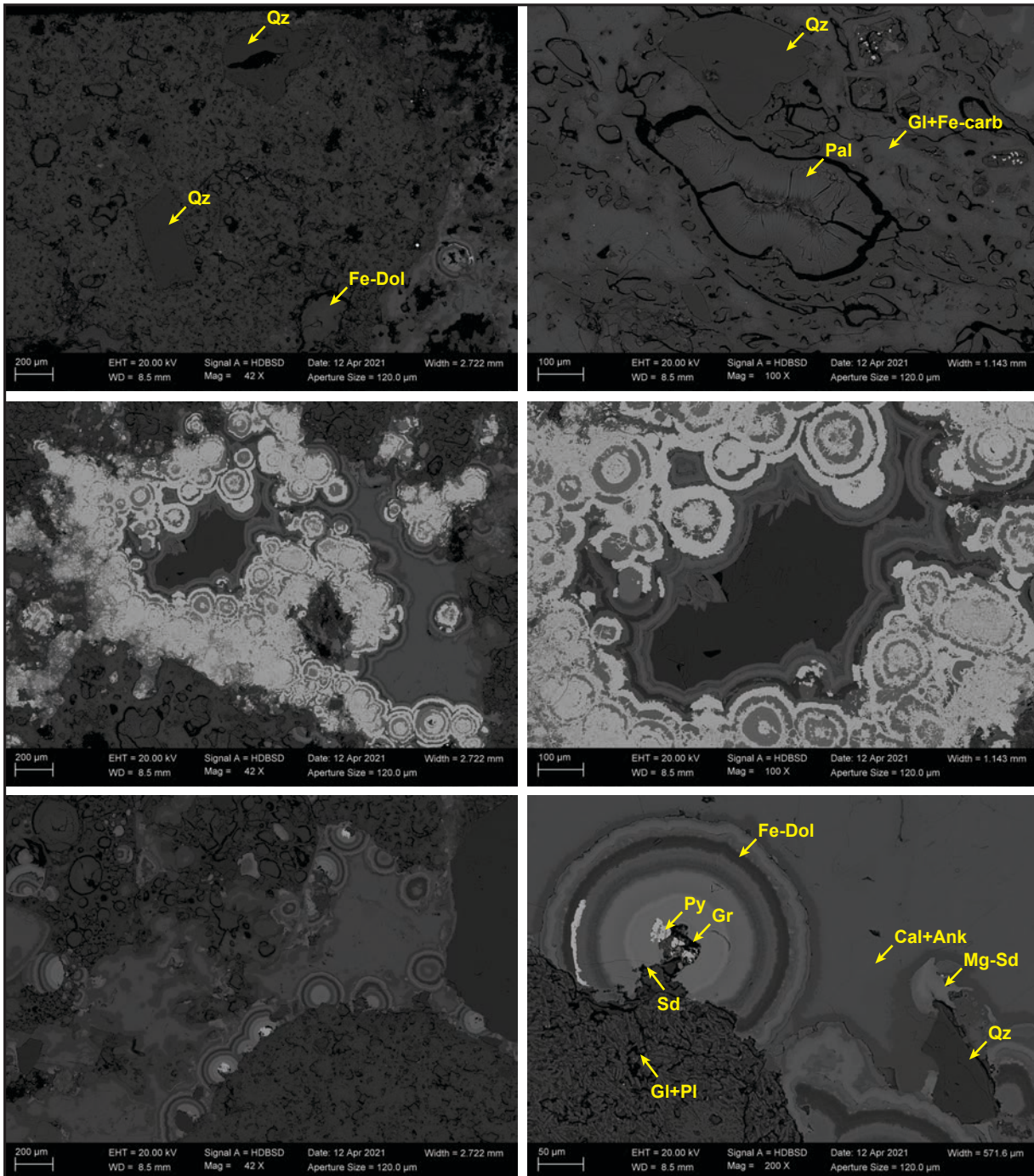
Image of thin-section, width 23 mm



2.5. FP94-4-5\_054.80 Summary

Reddish green-beige volcanoclastic lapillistone/ taxite with high amounts of palagonized glassy sections, glass-filled amygdules, Fe-Mg±Mn±Ca -carbonate- (locally bladed), pyrite-, and/or quartz-filled vug space. Detrital grains consist of shattered/fractured quartz, feldspar (K-feldspar), igneous lithic clasts, accessory monazite. Matrix/ vug space predominantly filled with spherules with concentric layering of Fe-Mg±Mn±Ca-carbonate and melnikovit-pyrite. Amorphous graphite occurs in areas of locally devitrified glass.

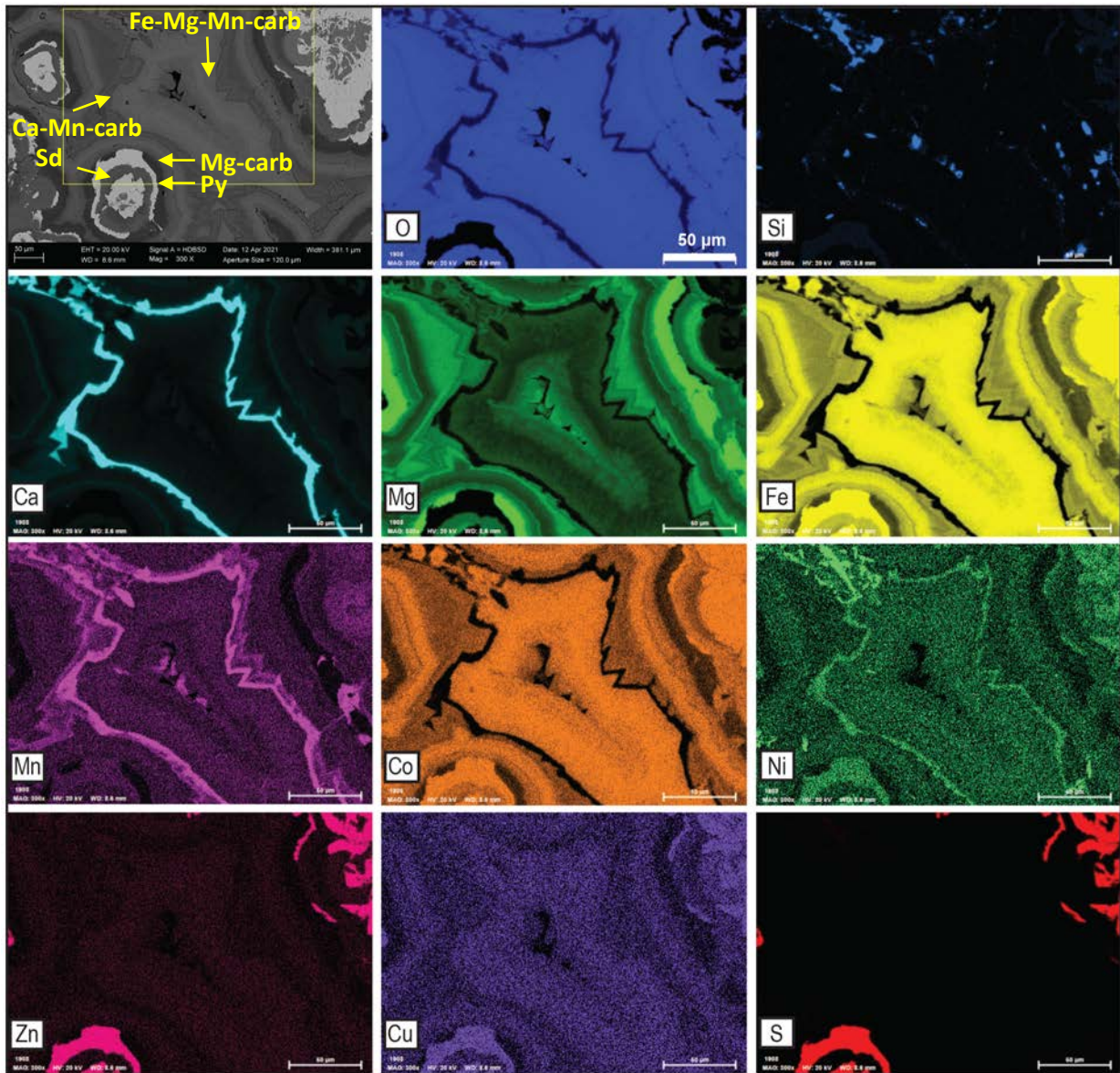
2.6. FP94-4-5\_054.80 SEM-BSE/EDS



**Fig. 11.** Backscatter electron (BSE) micrographs. Upper row: Detrital quartz [Qz] in a glassy, locally palagonized matrix, which is partially replaced by Fe-Mg±Ca-carbonates (ankerite [ank], calcite [cal], dolomite [dol], siderite [Sd]). Middle row: melnikovit-pyrite concentricly interlayered with carbonates shown in transmitted light micrographs. Bottom row: Fe-Mg±Mn±Ca carbonate spherules with minor pyrite replacement growing inwards into vug space.

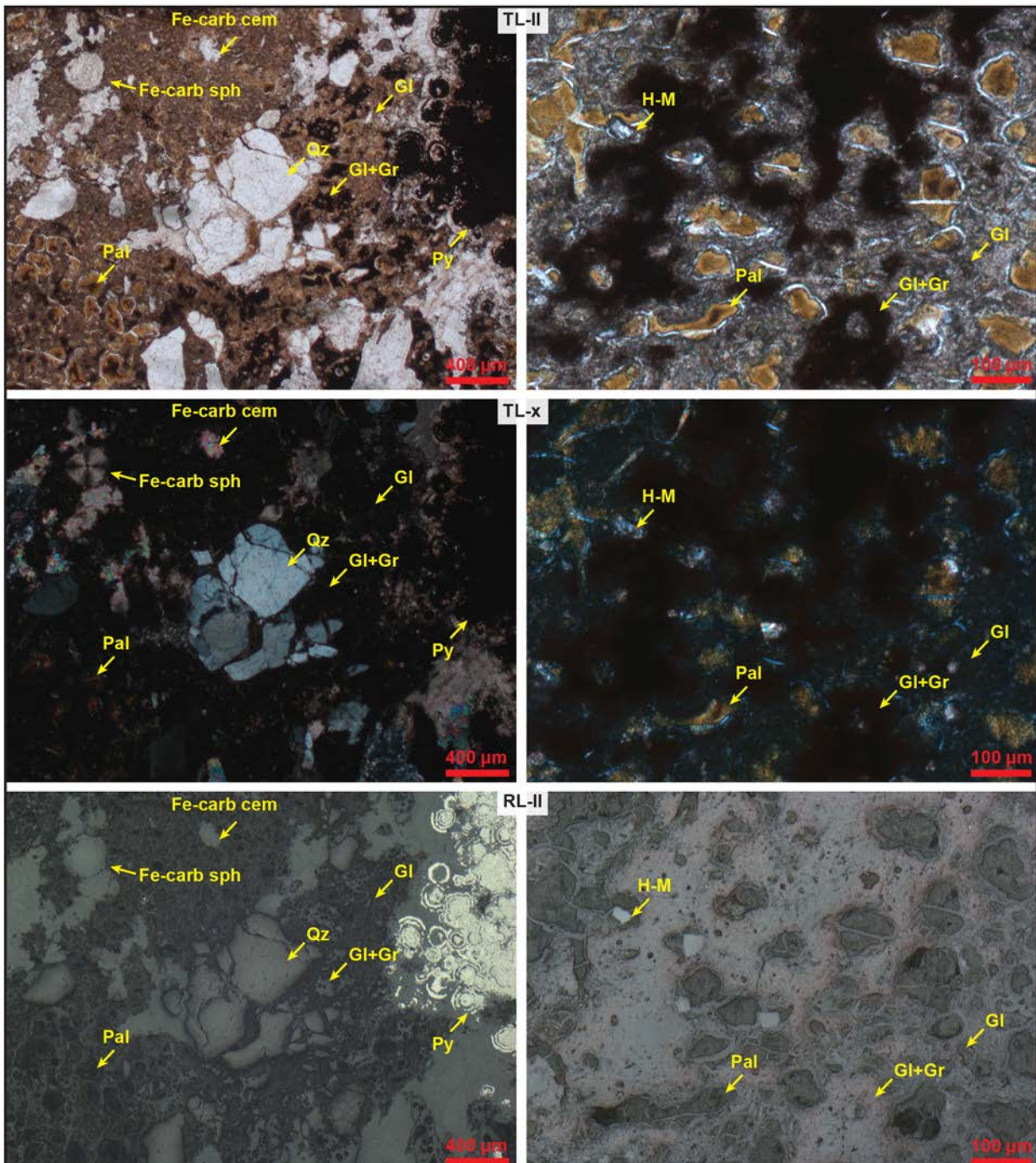
FP94-4-5\_054.80

SEM-EDS element map

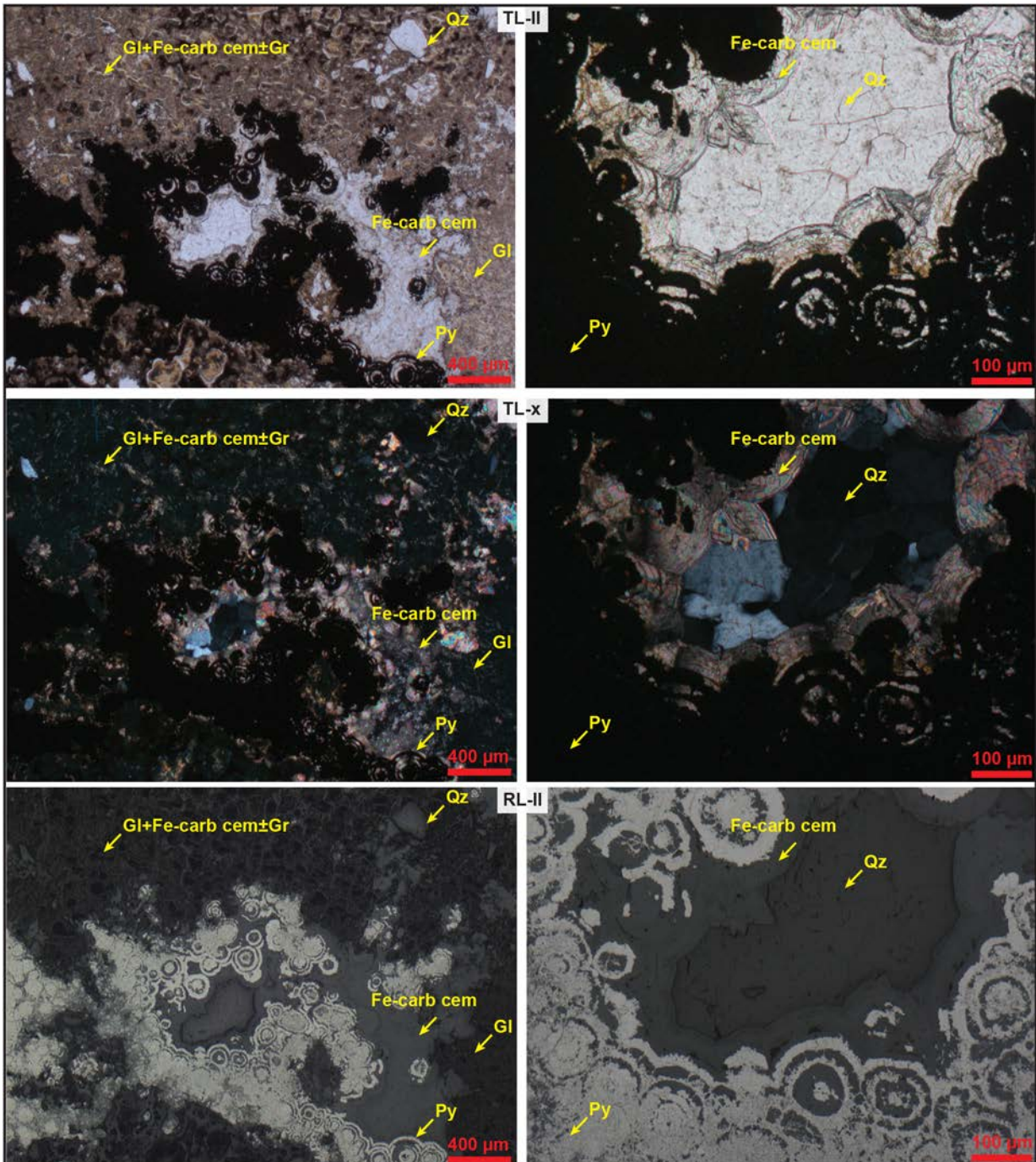


**Fig. 12.** Backscatter electron (BSE) and EDS element maps to show zonation and variable contents of Fe-Mg±Mn±Ca carbonates. Silica indicates presence of glassy matrix. Manganese predominantly associated with Ca-rich layer, Mg- and/or Fe-rich carbonates form the predominate vug fill. The latter appears to be associated with traces of Co, whereas traces of Ni are associated with the Ca±Mn layers. Concentric layers in upper right and lower left corner replaced by pyrite, which contains traces of Zn and Cu. Note: Cobalt intensities may also be derived from peak overlap with the Fe- K $\beta$ -peak and have to be considered with caution.

2.7. FP94-4-5\_054.80 Microscopy



**Fig. 13.** Angular to subangular shattered/fractured quartz [Qz] grains in a glassy matrix, locally clay altered and/or palagonized [Pal] with variable amounts of amorphous graphite [Gl+Gr]. Quartz is fractured/shattered with slightly undulose extinction. Fe-Mg-carbonates [Fe-carb-cem] occur replacing the glassy matrix and frequently form concentric spherules with typical spherule-cross [Fe-carb-sph]. Colloform melnikovit-pyrite locally replaces Fe-Mg-carbonate spherules forming concentric interlayered pyrite-carbonates spherule clusters. The red tint in the bottom right reflected light micrograph may be a result of finely-disseminated Mn-oxides in the altered glassy-carbonate matrix with Mn derived from carbonates. Angular heavy minerals (H-M: probably zircon) scattered in matrix. Other detrital minerals are K-feldspars and plagioclase, monazite as accessory mineral, galena as other sulphide. TL-II: transmitted light micrograph with plane polarized light (ppl). TL-x: crossed polars. RL-II: reflected light micrograph with ppl.

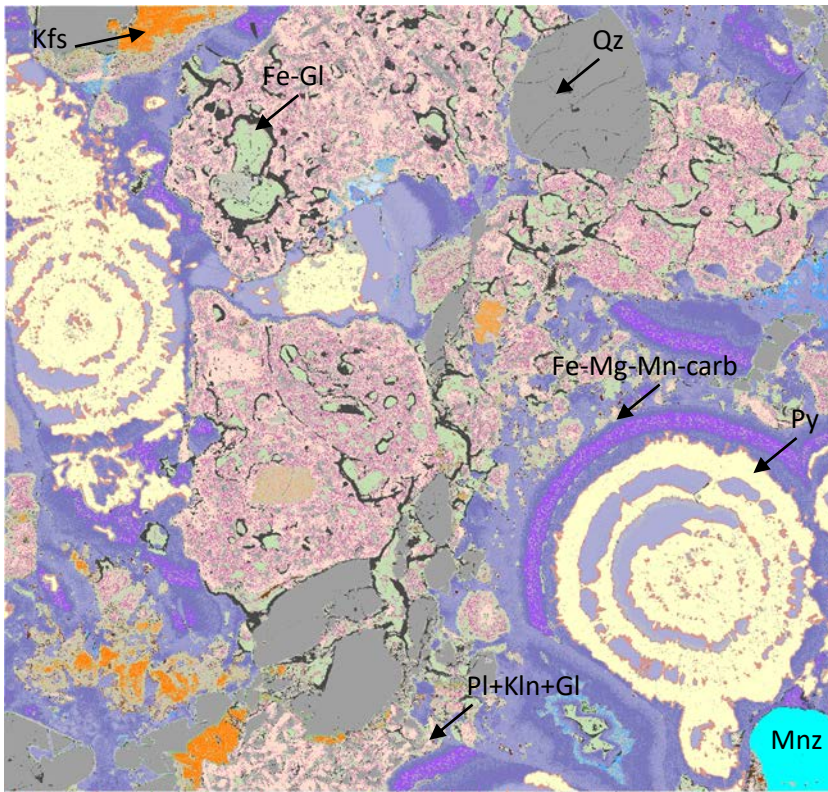


**Fig. 14.** Colloform melnikovit-pyrite concentricly interlayered with Fe-Mg-carbonates that locally are bladed and growing inwards into amygdule space. Center of amygdule filled with quartz. Matrix consists of variably clay-palagonite-altered glassy matrix, partially replaced by carbonates and with variable amounts of amorphous graphite/graphitic carbon.

TL-II: transmitted light micrograph with plane polarized light (ppl). TL-x: crossed polars. RL-II: reflected light micrograph with ppl.



2.8. FP94-4-5\_054.80 AQM-SEM



**Fig. 15.** Mineral map and corresponding BSE map of AQM-SEM analysis of 054.80a.

Detrital minerals are predominantly quartz [Qz], locally associated with K-feldspar [Kfs] and fractured/shattered in places. Volcaniclastic material consists of plagioclase [Pl] plus clay-altered [Kln+Sme-Ilt] aggregates that contain Fe-Mg-rich palagonitic glass [Fe-Gl] sections. Monazite occurs as accessory minerals.

Fe-Mg±Mn±Ca-carbonates (blueish-purple colours) with varying Fe-Mg±Mn±Ca-contents form concentric spherules interlayered with/replaced by pyrite.

Graphite [Gr] occurs within the matrix as amorphous grain coating.

50 µm

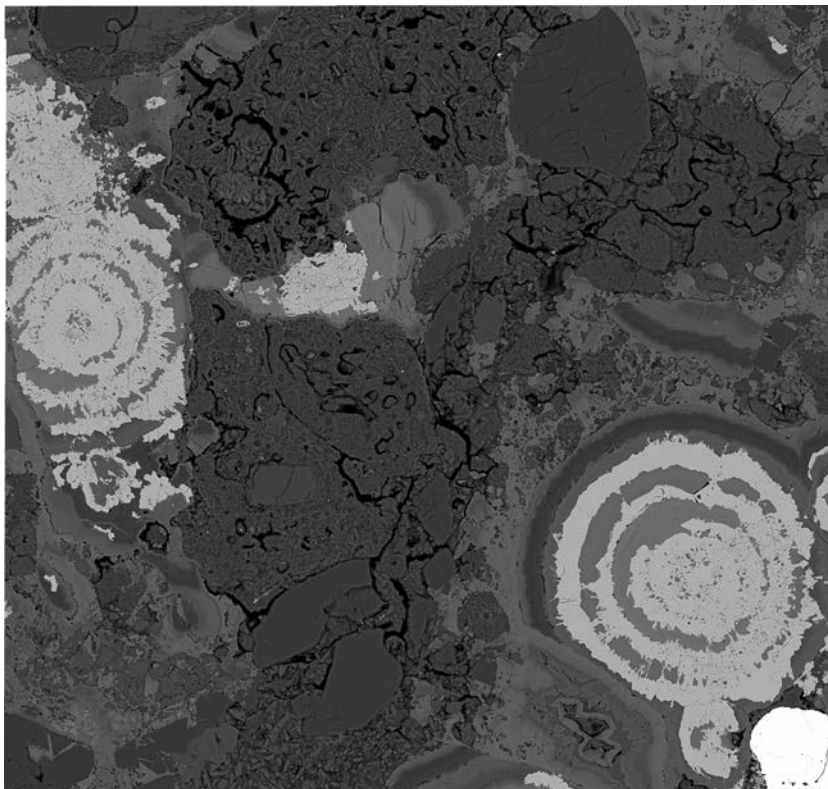
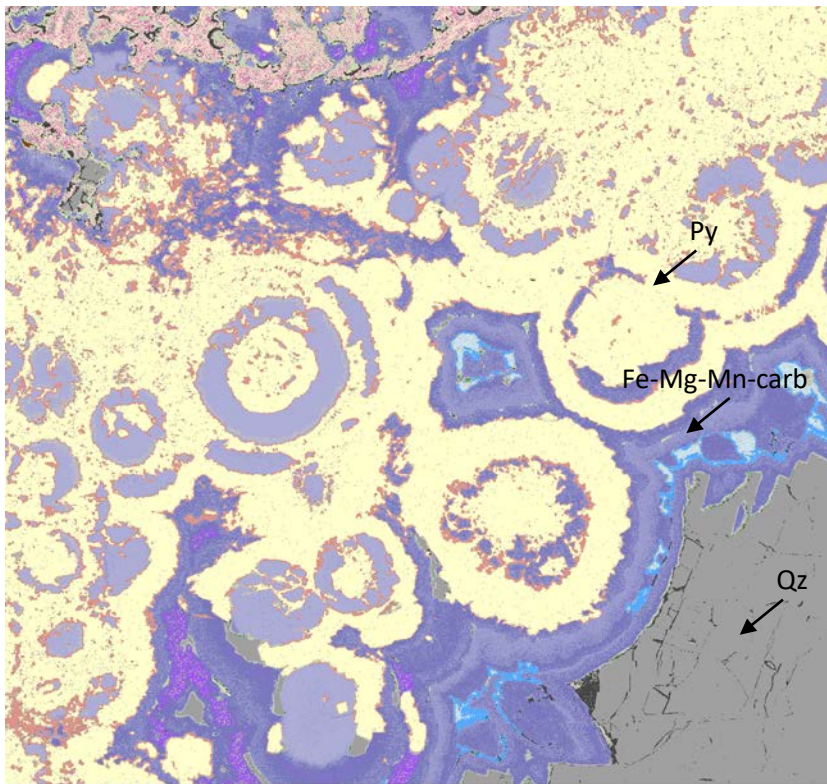


Image of thin-section, width 23 mm



FP94-4-5\_054.80b

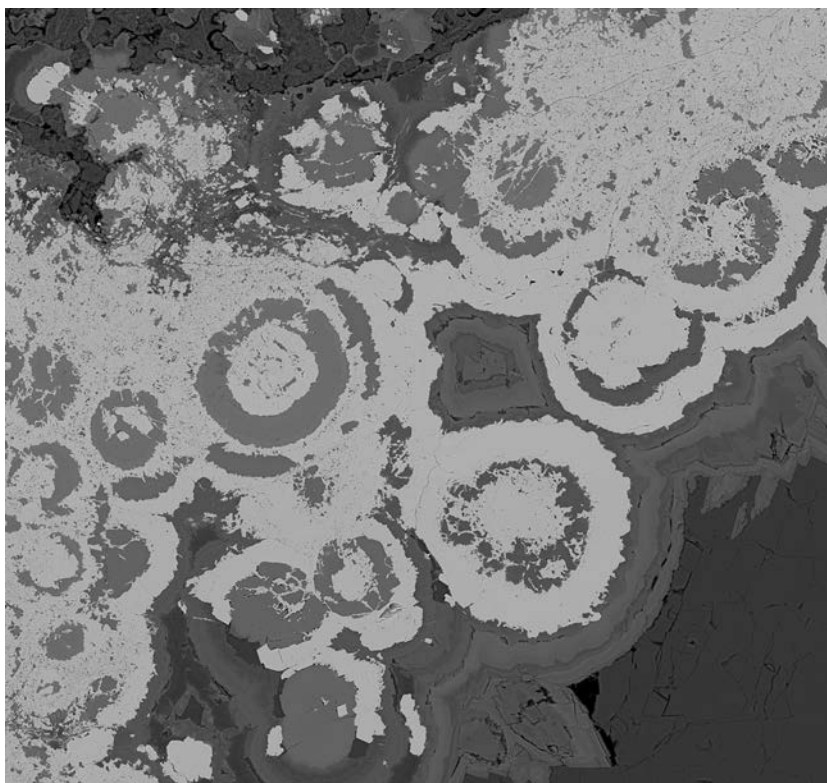
AQM-SEM



**Fig. 16.** Mineral map and corresponding BSE map of AQM-SEM analysis of 054.80b.

Mineralogy as described for 054.80a.

Image of thin-section, width 23 mm



2.9. FP94-4-5\_066.26 Summary

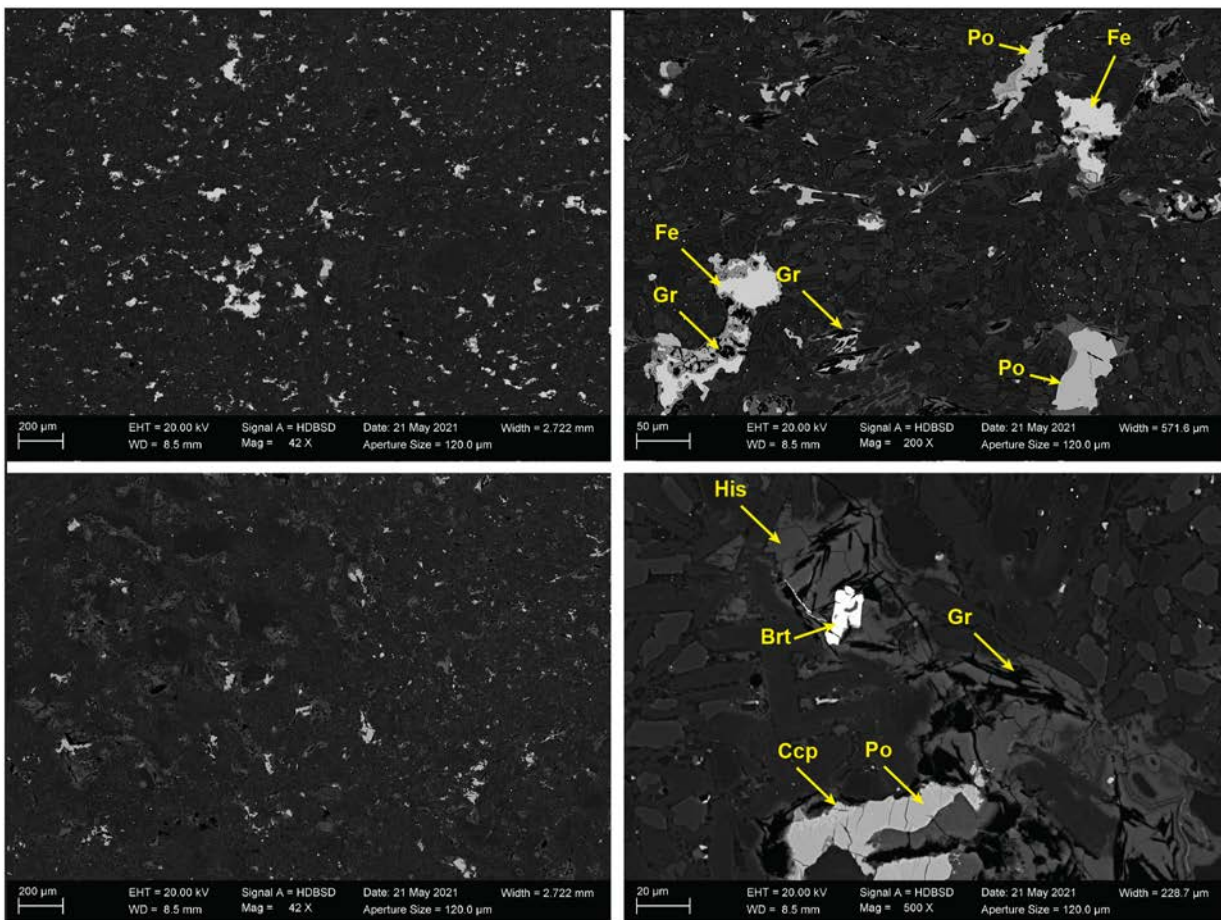
Fine-crystalline basalt with up to a mm-sized xenocrysts and phenocrysts and micron-sized Fe-droplets dispersed in matrix. Native iron occurs as up to few hundred  $\mu\text{m}$  in size and commonly has a coating of magnetite and is associated with pyrrhotite. Pyrrhotite occurs in similar size and often has pentlandite flames and inclusions of chalcopyrite. Native iron and pyrrhotite are associated with graphite and locally with Fe-Ni-phosphides, such as., e.g., schreibersite. On thin-section-scale an Fe-rich section seems to be intruded into/ intermingled with a more pyrrhotite-rich section.

The matrix consists of plagioclase microlite laths with intersertal siliceous glass. Graphite occurs with the sulphides/native Fe and as few hundred micron-sized aggregates. Graphite commonly is coated in/associated with a Fe-siliceous phase (hisingerite).

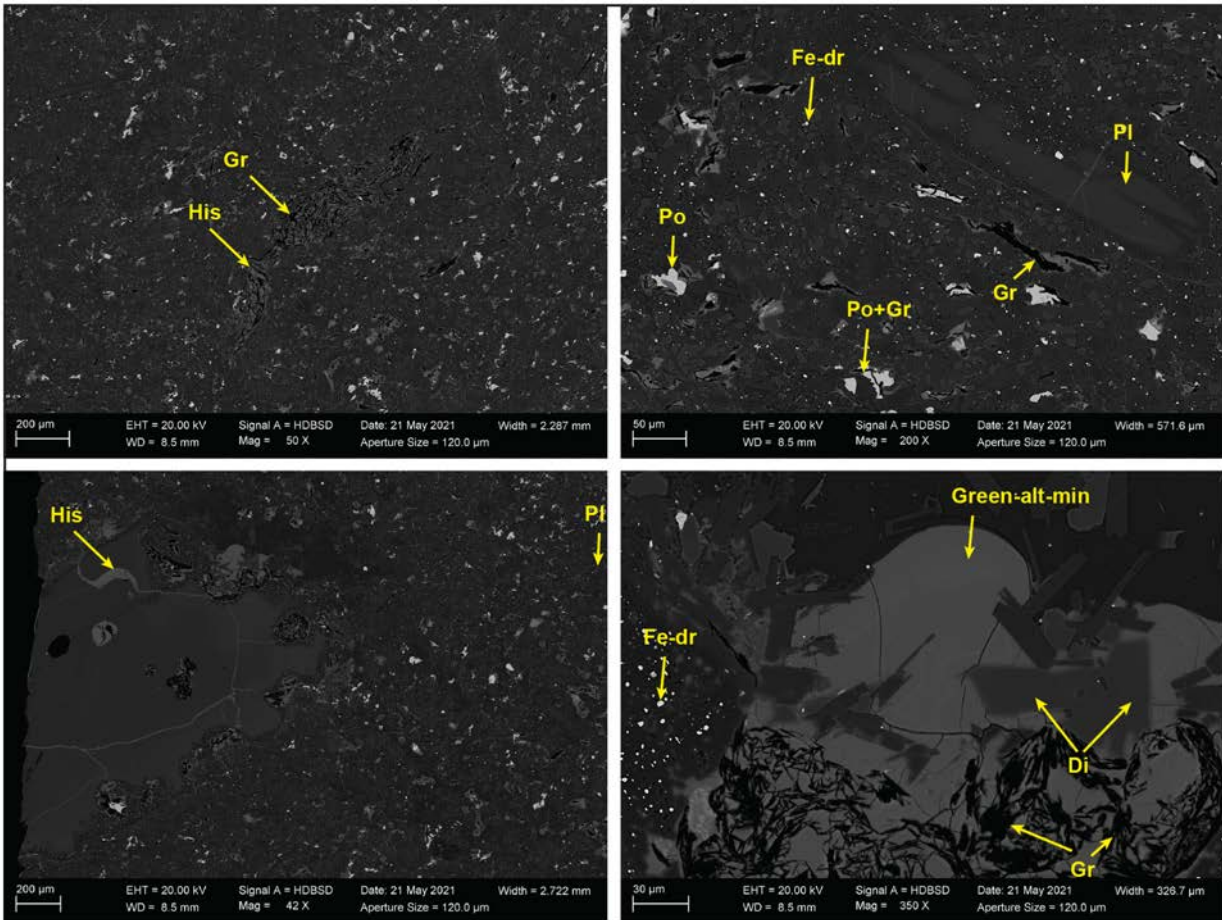
Plagioclase microlites appear to have a certain trachytic flow texture alignment.

Xenocrysts consist of orthopyroxene and minor relict olivine and commonly show oscillatory zoning and embayed rims. The outer zone of the xenocrysts are commonly rich in micron-sized Fe-droplets. Elongated lath-shaped plagioclase phenocrysts up to 200  $\mu\text{m}$  commonly show swallow tail habit.

2.10. FP94-4-5\_066.26 SEM-BSE/EDS

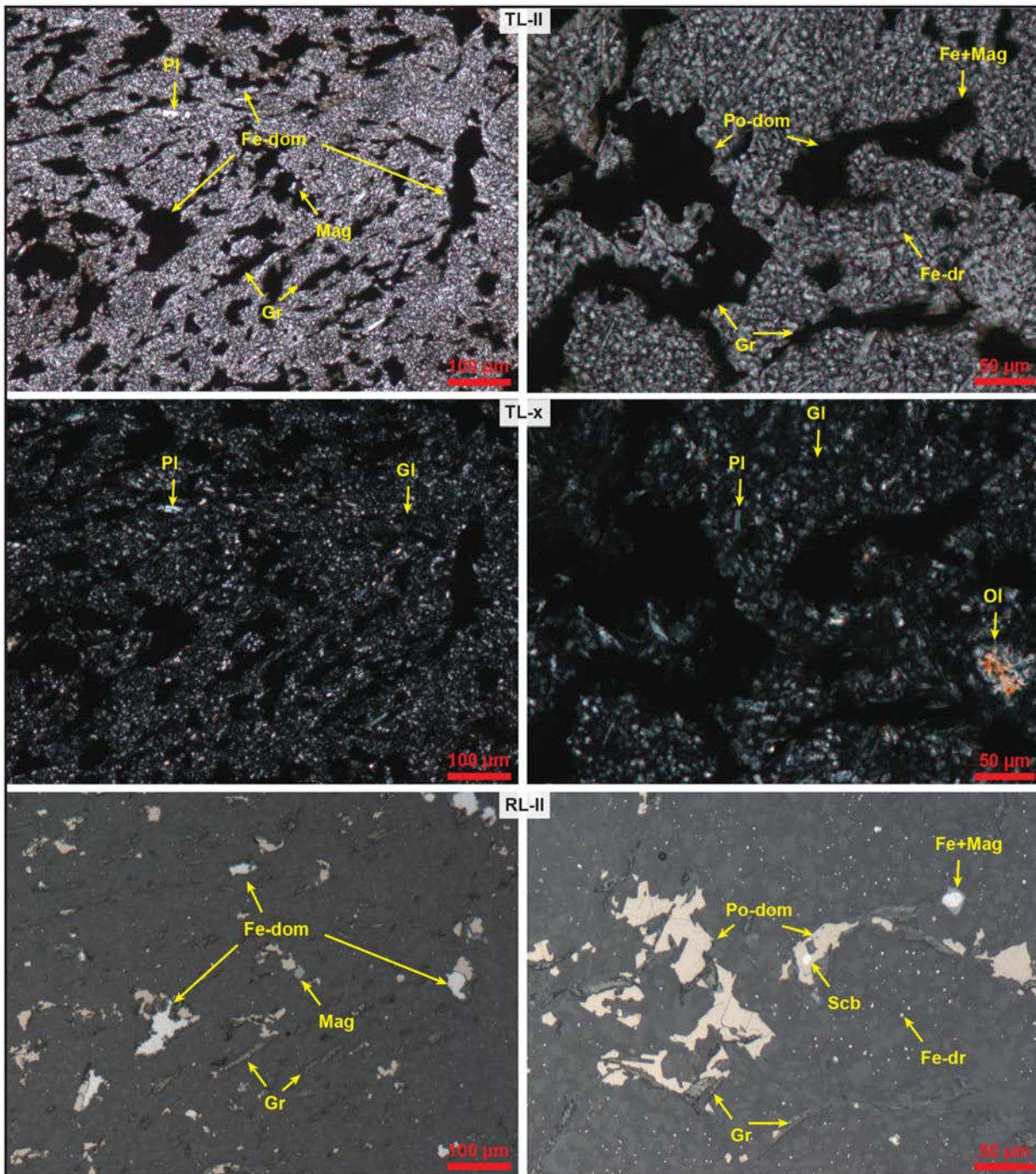


**Fig. 17.** Backscatter electron (BSE) micrographs. Upper row: Fe-dominated section. Lower left: Intermingled Fe- and pyrrhotite [Po] sections. Lower right: Detail of the pyrrhotite-rich section; hisingerite [His] coating graphite [Gr]. Chalcopyrite [Ccp] associated with pyrrhotite, barite [Brt] with graphite and hisingerite.

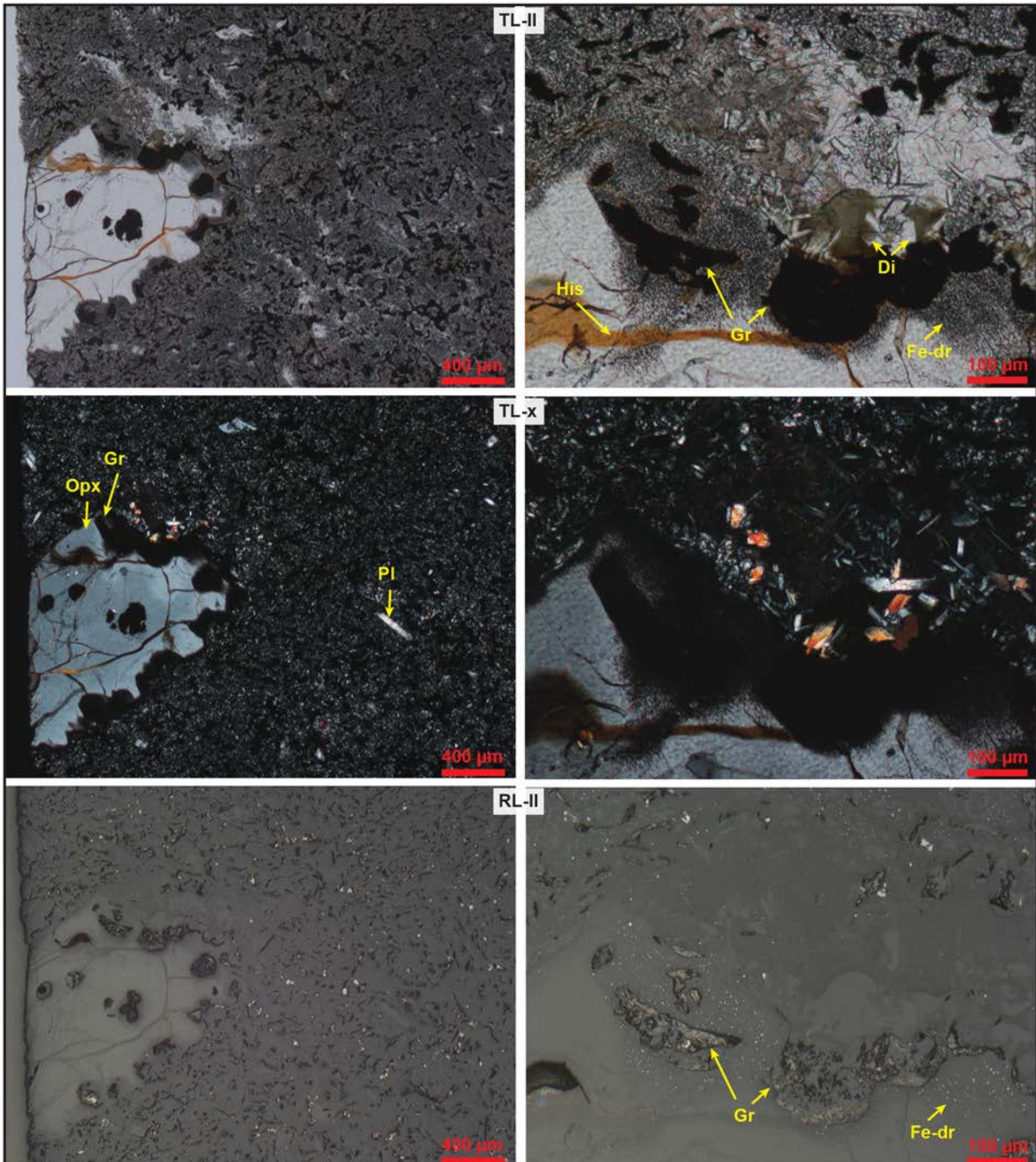


**Fig. 18.** Backscatter electron (BSE) micrographs. Upper left: Large aggregate of graphite [Gr] and hisingerite [His]. Upper right: Fe-rich section with large plagioclase [Pl] phenocryst with swallow tails. Lower row: Close-up of large orthopyroxene [Opx] xenocryst shown in Figure 20 with an outer zone rich in micron-sized Fe-droplets [Fe-dr], as well as diopside [Di] and a green alteration mineral (seen in Fig. 20).

2.11. FP94-4-5\_066.26 Microscopy

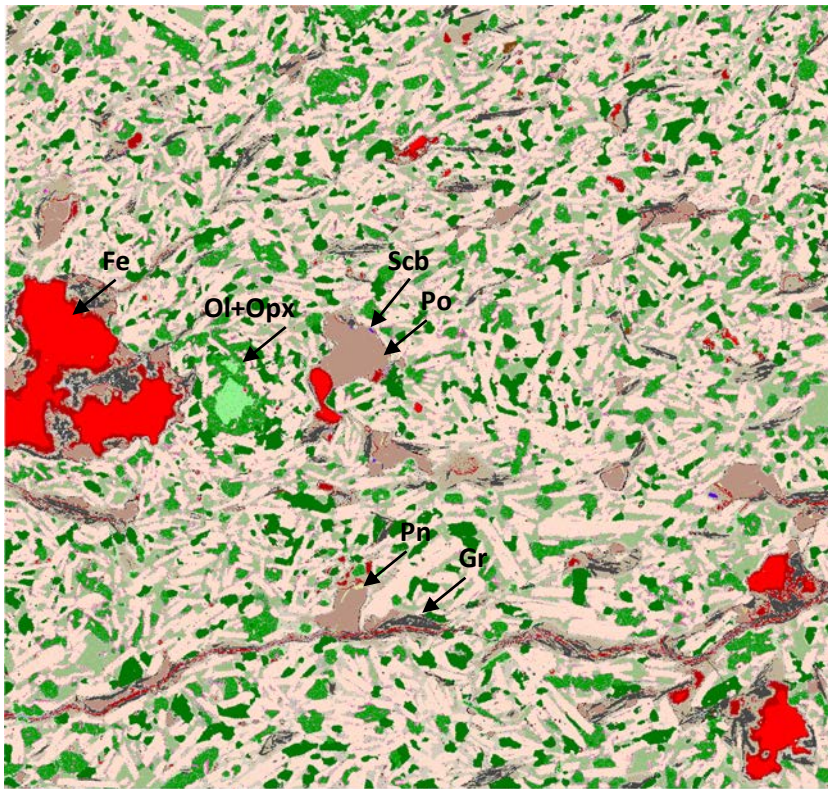


**Fig. 19.** Left column: section dominated by large irregular-shaped native iron [Fe] in association with pyrrhotite [Po], graphite [Gr], and magnetite [Mag]. Right column: Fe-dominated section intermingled with section that is dominated pyrrhotite, with lesser amounts of preserved native iron. Schreibersite {Scb} associated with pyrrhotite. Plagioclase [Pl] occurs as phenocrysts and as microlite laths in matrix with intersertal siliceous glass [Gl]. Relict olivine [Ol] phenocryst recognizable in TL-x. TL-II: transmitted light micrograph with plane polarized light (ppl). TL-x: crossed polars. RL-II: reflected light micrograph with ppl.



**Fig. 20.** Left column: Large orthopyroxene [Opx] (enstatite) xenocryst with solution embayments and green alteration mineral (poss. hornblende). Fractures of xenocryst filled with orange translucent hisingerite. Outer margin of orthopyroxene rich in Fe-droplets [Fe-dr] and graphite [Gr]. TL-II: transmitted light micrograph with plane polarized light (ppl). TL-x: crossed polars. RL-II: reflected light micrograph with ppl.

2.12. FP94-4-5\_066.26 AQM-SEM

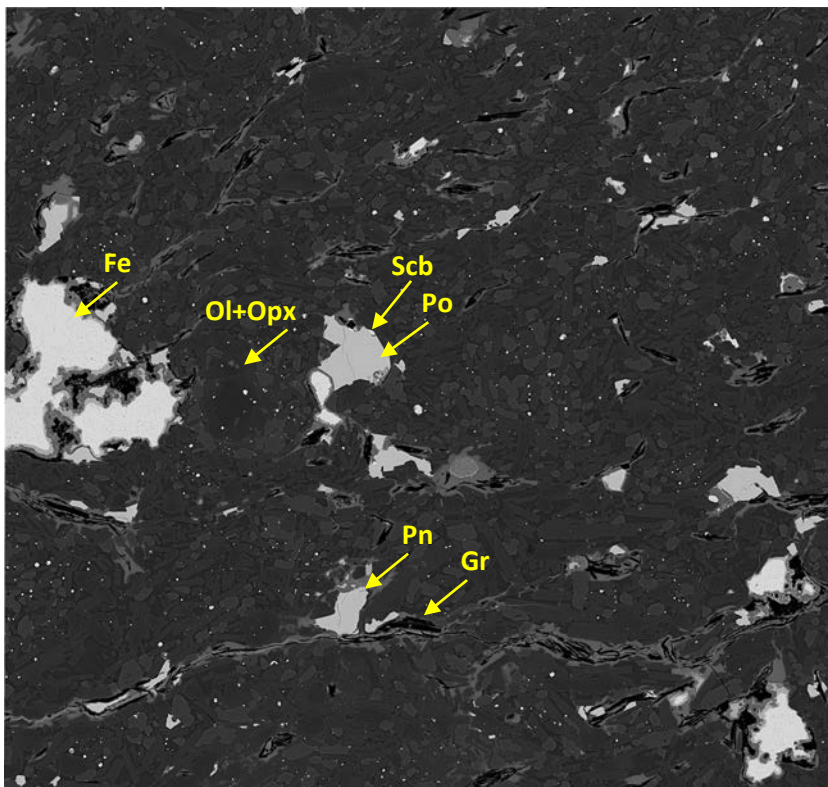


50 μm

**Fig. 21.** Mineral map and corresponding BSE map of AQM-SEM analysis of 066.26\_Fe-dominated.

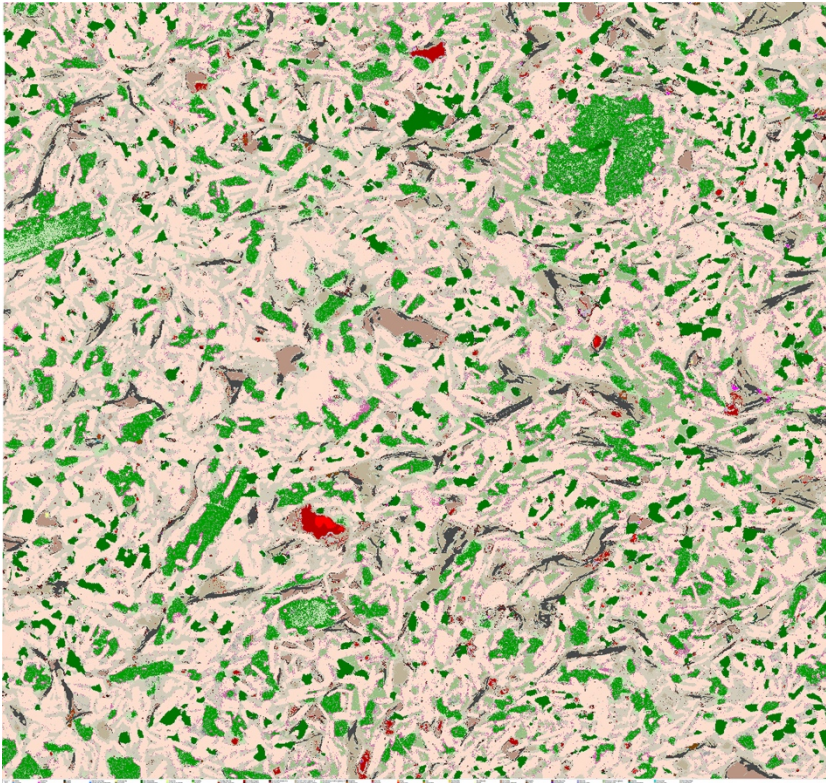
Native iron mantled by magnetite [Mag] in association with intergrown pyrrhotite [Po] and graphite [Gr]. Pentlandite [Pn] and chalcopyrite [Ccp] is intergrown with pyrrhotite, schreibersite [Scb] and other Ni-Fe-phosphides associated with native Fe and sulphides. Graphite and Fe-oxide also present in fractures. Matrix consists predominantly of euhedral to subhedral crystals of plagioclase, diopside, orthopyroxene [Opx], minor clinopyroxene with intersertal K-rich siliceous glass. Olivine [Ol] phenocryst with orthopyroxene corona with Fe droplets. Small Fe-droplets also disseminated in matrix. Due to small size possibly underrepresented in mineral map.

Image of thin-section, width 23 mm



FP94-4-5\_066.26

AQM-SEM



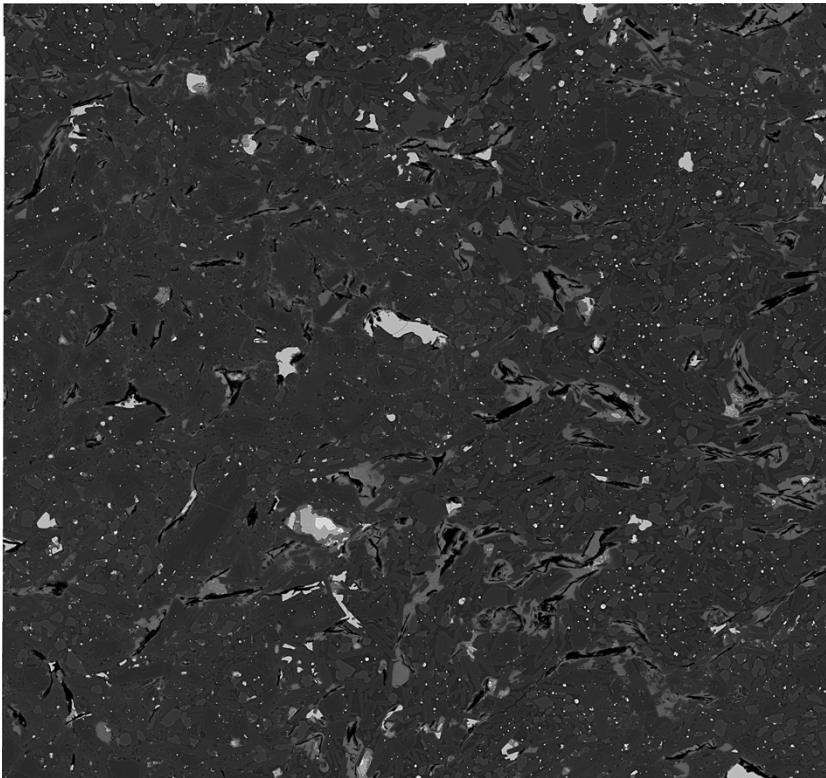
**Fig. 22.** Mineral map and corresponding BSE map of AQM-SEM analysis of 066.26\_Po-dominated.

Mineralogy as described for 066.26\_Fe-dom.

Image of thin-section, width 23 mm



50  $\mu$ m





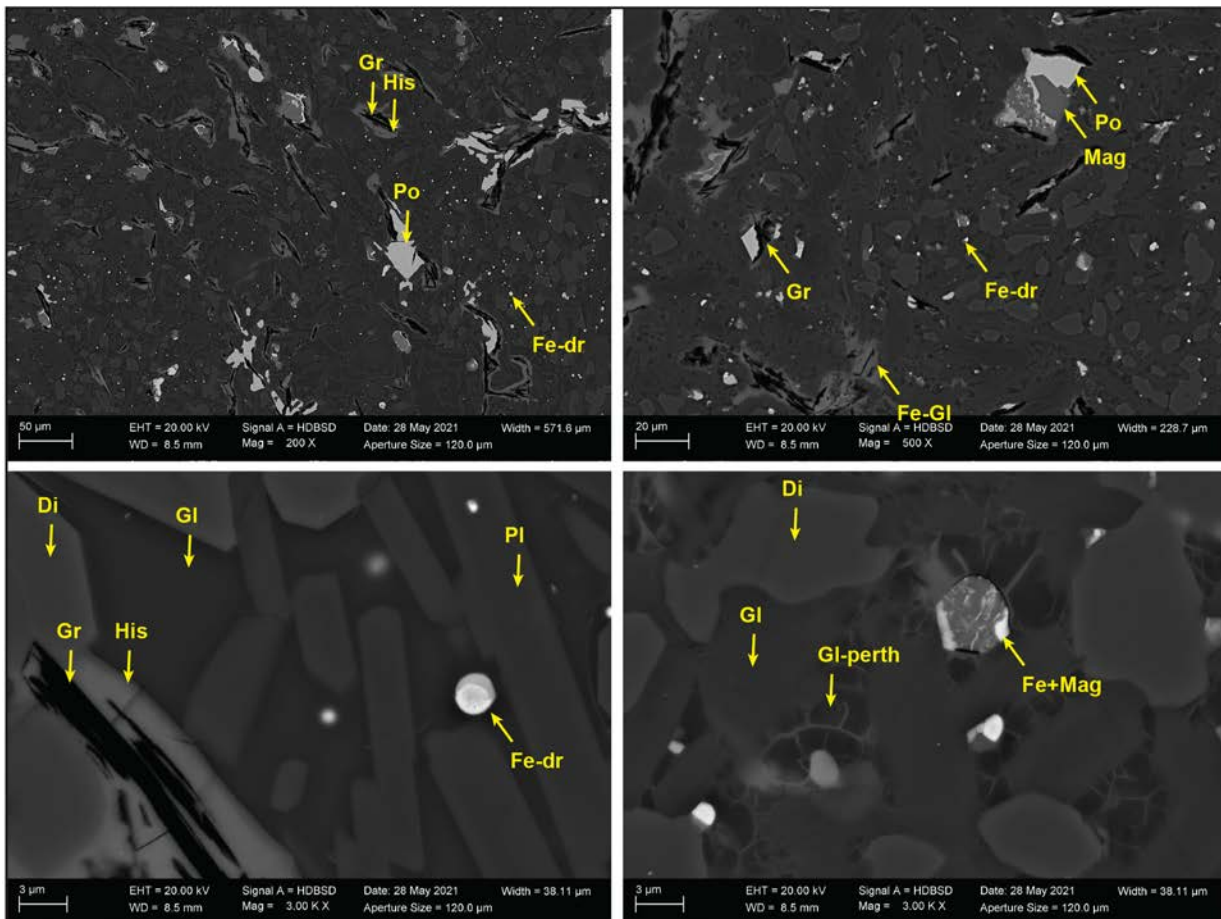
2.13. FP94-4-5\_075.90 Summary

Similar to previous. Fine-crystalline basalt with up to a mm-sized xenocrysts and phenocrysts and abundant micron-sized Fe-droplets dispersed in matrix. Native iron occurs as up to few hundred  $\mu\text{m}$  in size and commonly has a coating of magnetite and is associated with pyrrhotite. Pyrrhotite occurs as aggregates of similar size and commonly has pentlandite flames and an association with chalcopyrite. Native iron and pyrrhotite are frequently associated with graphite and locally with Fe-Ni-phosphides, such as., e.g., schreibersite. On thin-section-scale an Fe-rich section seems to be intruded into a more pyrrhotite-rich section.

The matrix consists of plagioclase microlite laths with intersertal siliceous glass. Glass in matrix often shows perthite-micro-fracturing. Graphite occurs with the sulphides/native Fe and as few hundred micron-sized aggregates. Graphite is commonly is coated in/associated with a Fe-siliceous phase (hisingerite).

Plagioclase microlites appear to have a certain trachytic texture alignment.

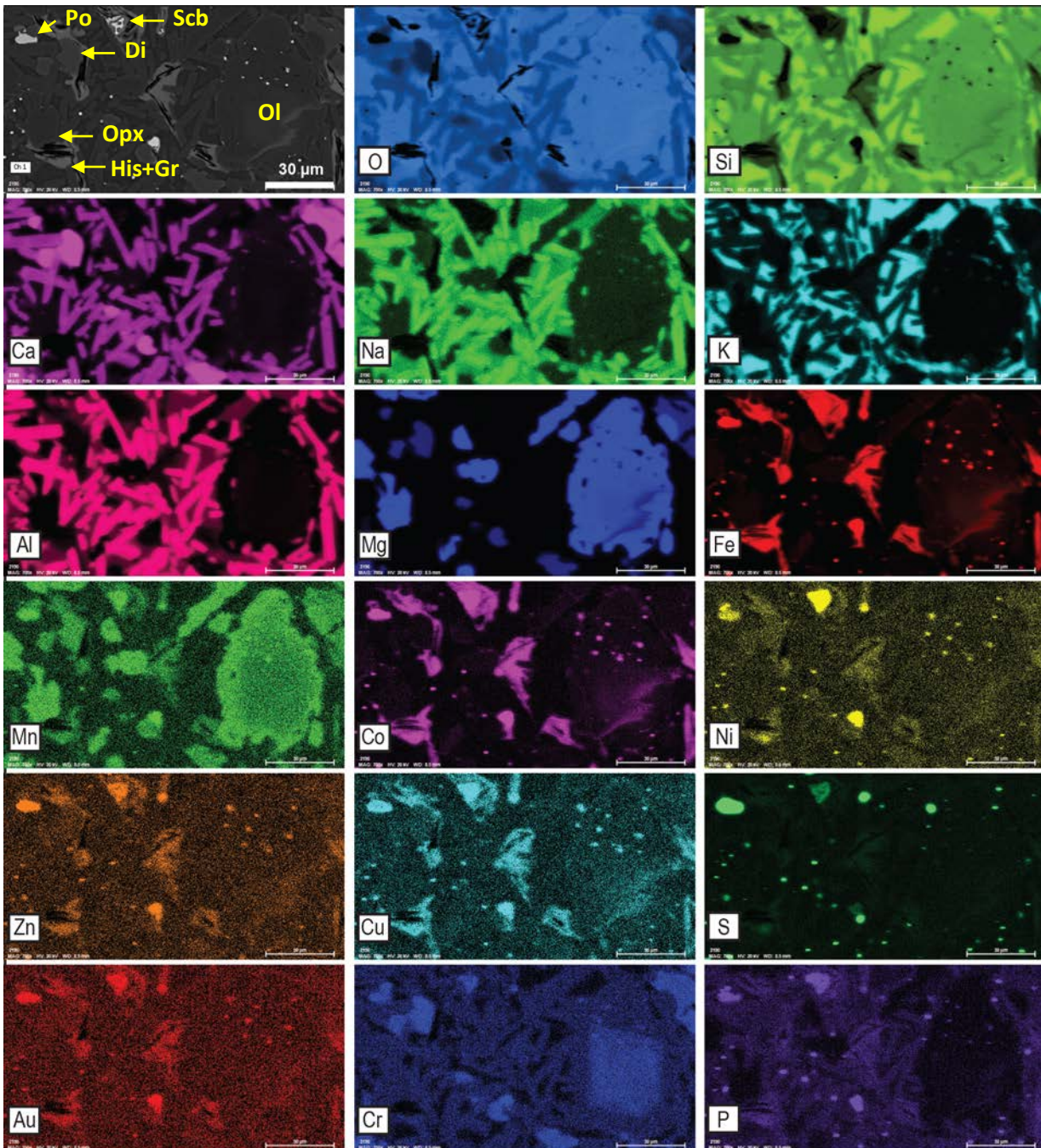
2.14. FP94-4-5\_075.90 SEM-BSE/EDS



**Fig. 23.** Backscatter electron (BSE) micrographs. Association of graphite [Gr] and hisingerite [His], pyrrhotite [Po] and magnetite [Mag] with abundant Fe-droplets [Fe-dr] dispersed in matrix. Plagioclase [Pl] microlites, diopside [Di] and orthopyroxene [Opx] with intersertal glass [GI]. Glassy matrix frequently with perthitic fractures.

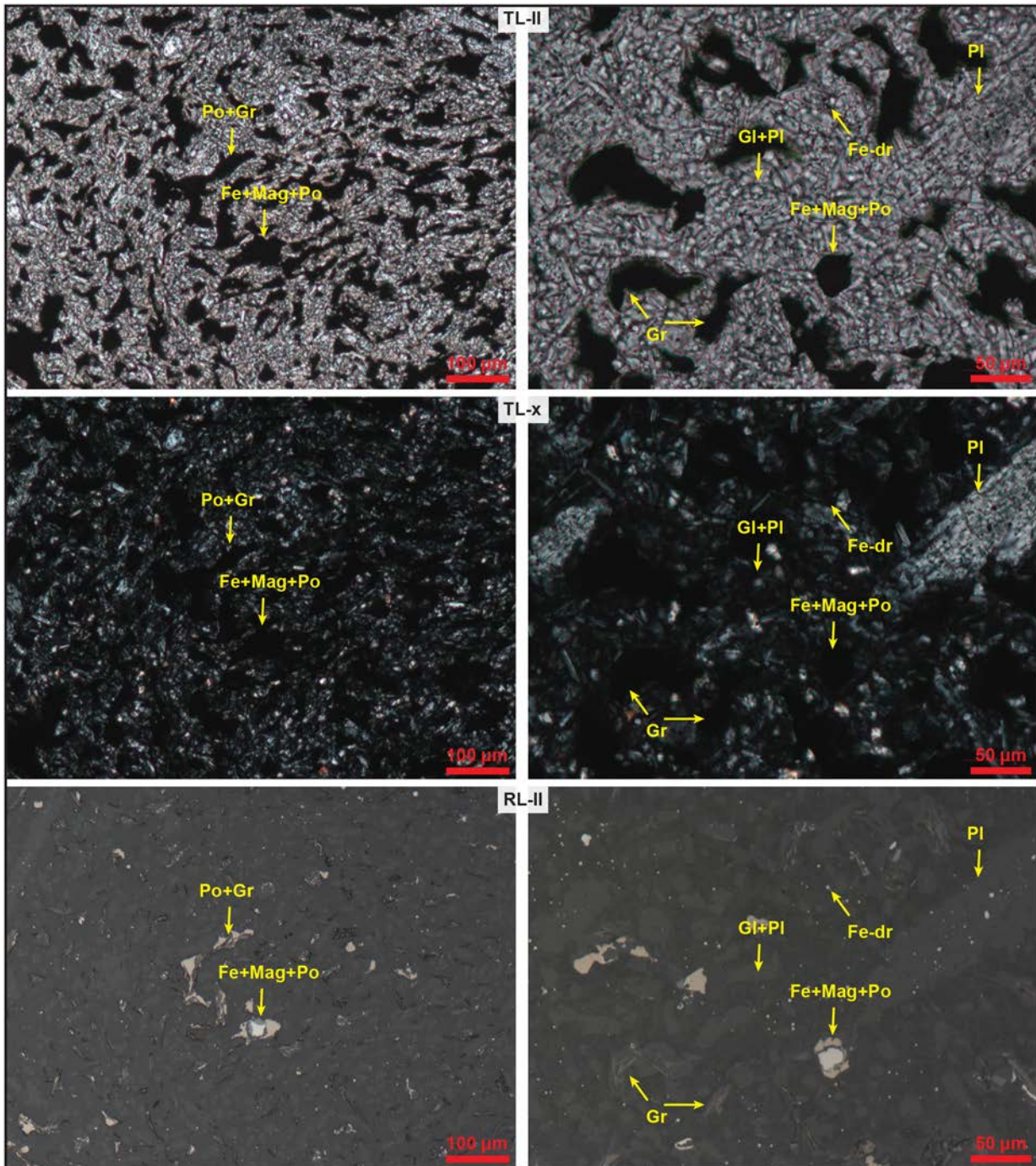
FP94-4-5\_075.90

SEM-EDS element maps

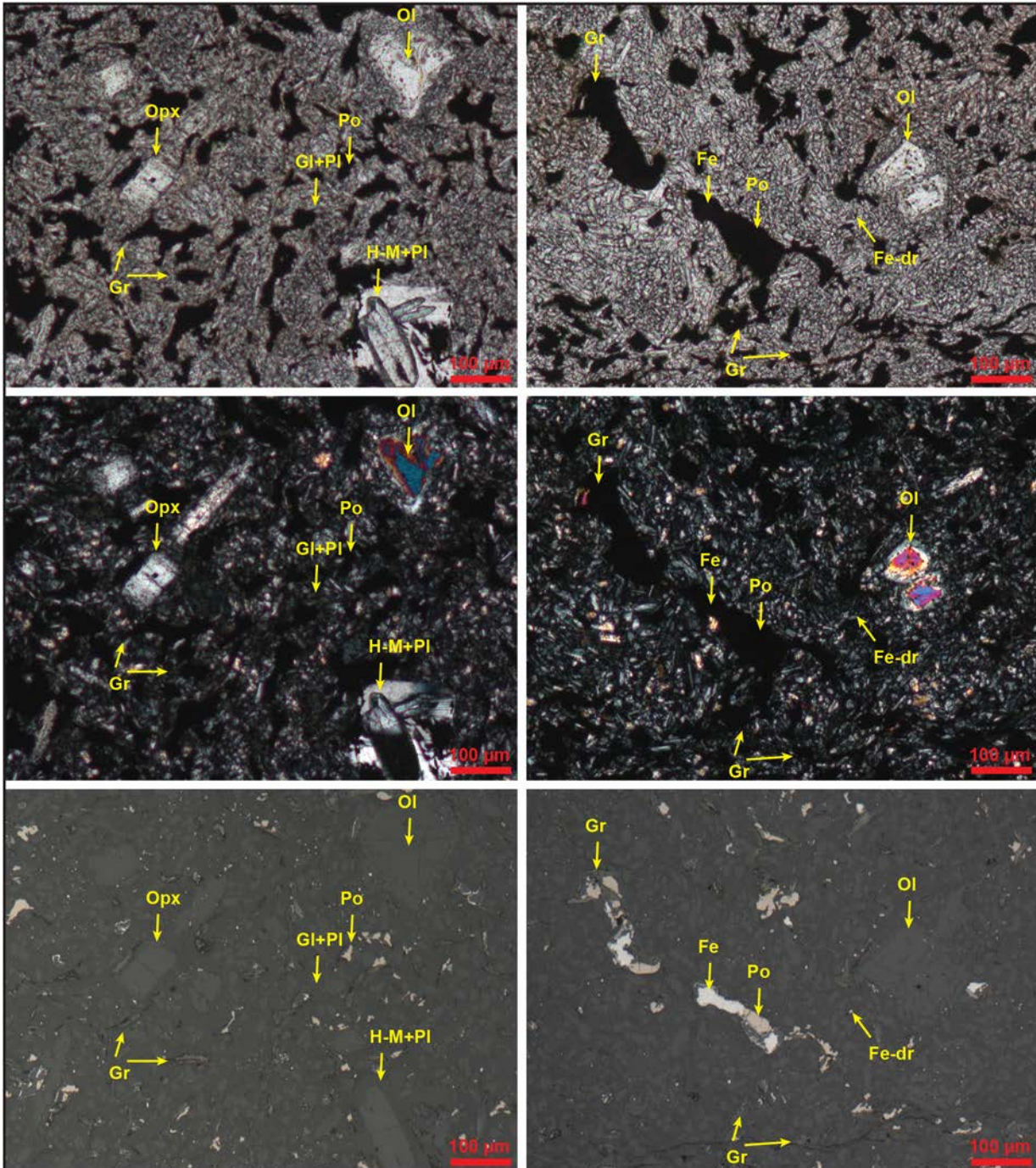


**Fig. 24.** Element maps to illustrate the K-bearing siliceous intersertal glassy matrix between plagioclase microlites and minor diopside (Di) and orthopyroxene (Opx). Olivine (forsterite) xenocryst with a Cr-bearing core. Dispersed in matrix and xenocryst are Fe-droplets (Fe-dr) with variable amounts of Ni, Co, P, and S. Schreibersite (Scb) associated with graphite and Fe-bearing glassy matrix (His = hisingerite). Au appears elevated in schreibersite and pyrrhotite (Po), as well as in the Fe-bearing glassy matrix. Cobalt intensities may also be derived from peak overlap with the Fe-K $\beta$ -peak and have to be considered with caution.

2.15. FP94-4-5\_075.90 Microscopy



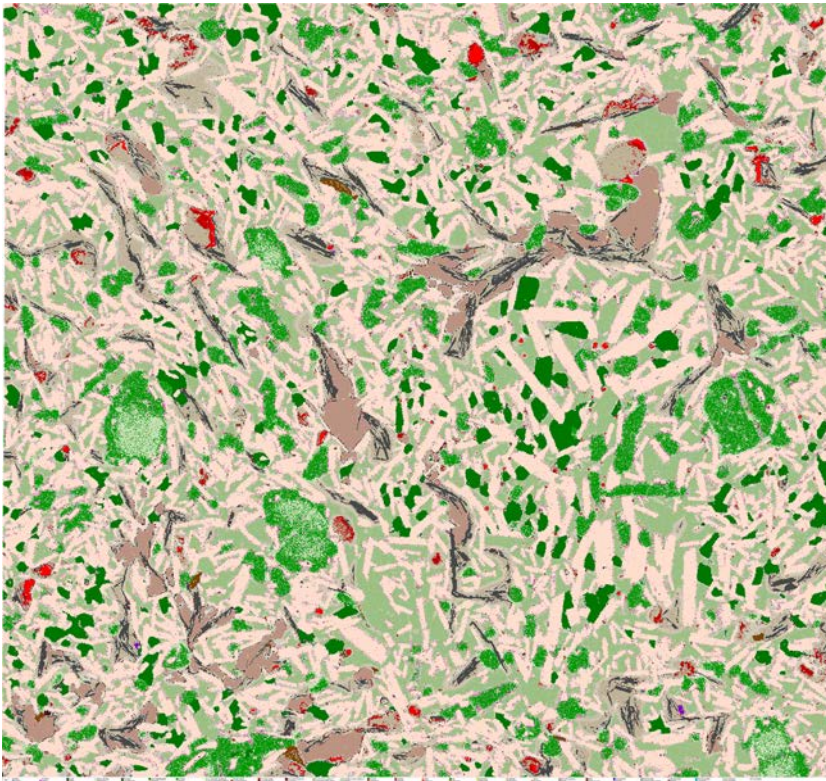
**Fig. 25.** Left column: Fine-crystalline basalt with abundant opaques (graphite [Gr], pyrrhotite [Po], native Fe, glass [Gl]). Micron-sized Fe-droplets[Fe-dr] disperse in matrix consisting of plagioclase [Pl] microlites and glass. Right column: same thin-section, different area showing the variation in grain size within one sample. TL-II: transmitted light micrograph with plane polarized light (ppl). TL-x: crossed polars. RL-II: reflected light micrograph with ppl.



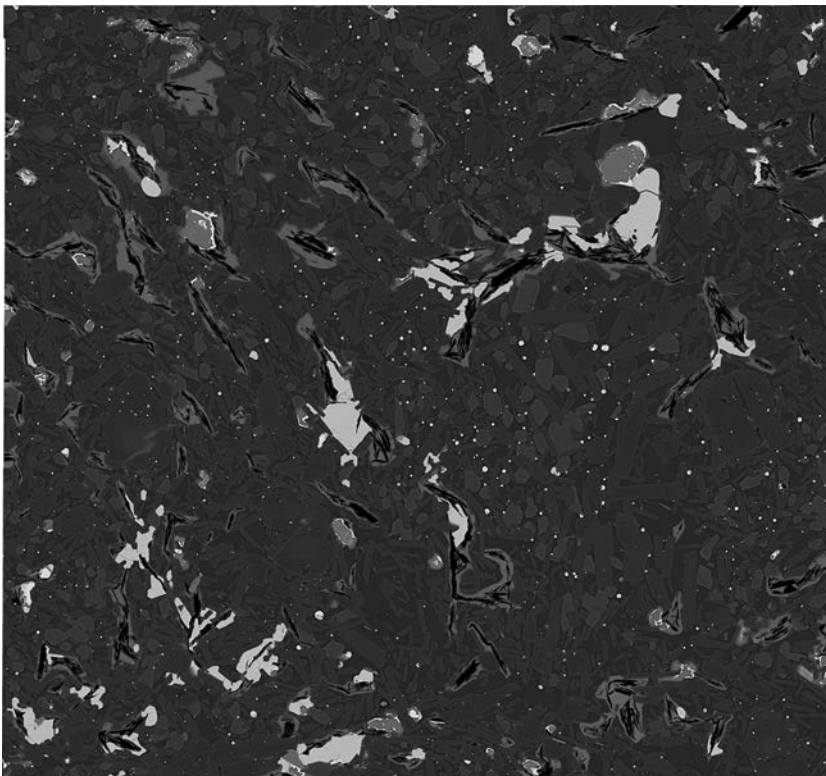
**Fig. 26.** Large phenocrysts (orthopyroxene [Opx] and plagioclase [Pl]) and xenocrysts (olivine [Ol], heavy mineral [H-M]) within the same thin section. Micron-sized Fe-droplets [Fe-dr] disperse in matrix consisting of plagioclase microlites and glass [Gl].

TL-II: transmitted light micrograph with plane polarized light (ppl). TL-x: crossed polars. RL-II: reflected light micrograph with ppl.

2.16. FP94-4-5\_075.90 AQM-SEM



50 µm



**Fig. 27.** Mineral map and corresponding BSE map of AQM-SEM analysis.

Smaller droplets of native iron mantled by magnetite in association with intergrown pyrrhotite and graphite. Pentlandite and chalcopyrite is intergrown with large pyrrhotite minerals, schreibersite and other Ni-Fe-phosphides associated with native Fe and sulphides. Graphite and Fe-oxide also present in fractures. Matrix consists predominantly of euhedral to subhedral crystals of plagioclase, diopside, orthopyroxene, minor clinopyroxene with intersertal K-rich siliceous glass. Fe-Mg-chlorite-altered olivine phenocryst with orthopyroxene corona with Fe droplets. Small Fe-droplets also disseminated in matrix. Due to small size possibly underrepresented in mineral map.

Image of thin-section, width 23 mm

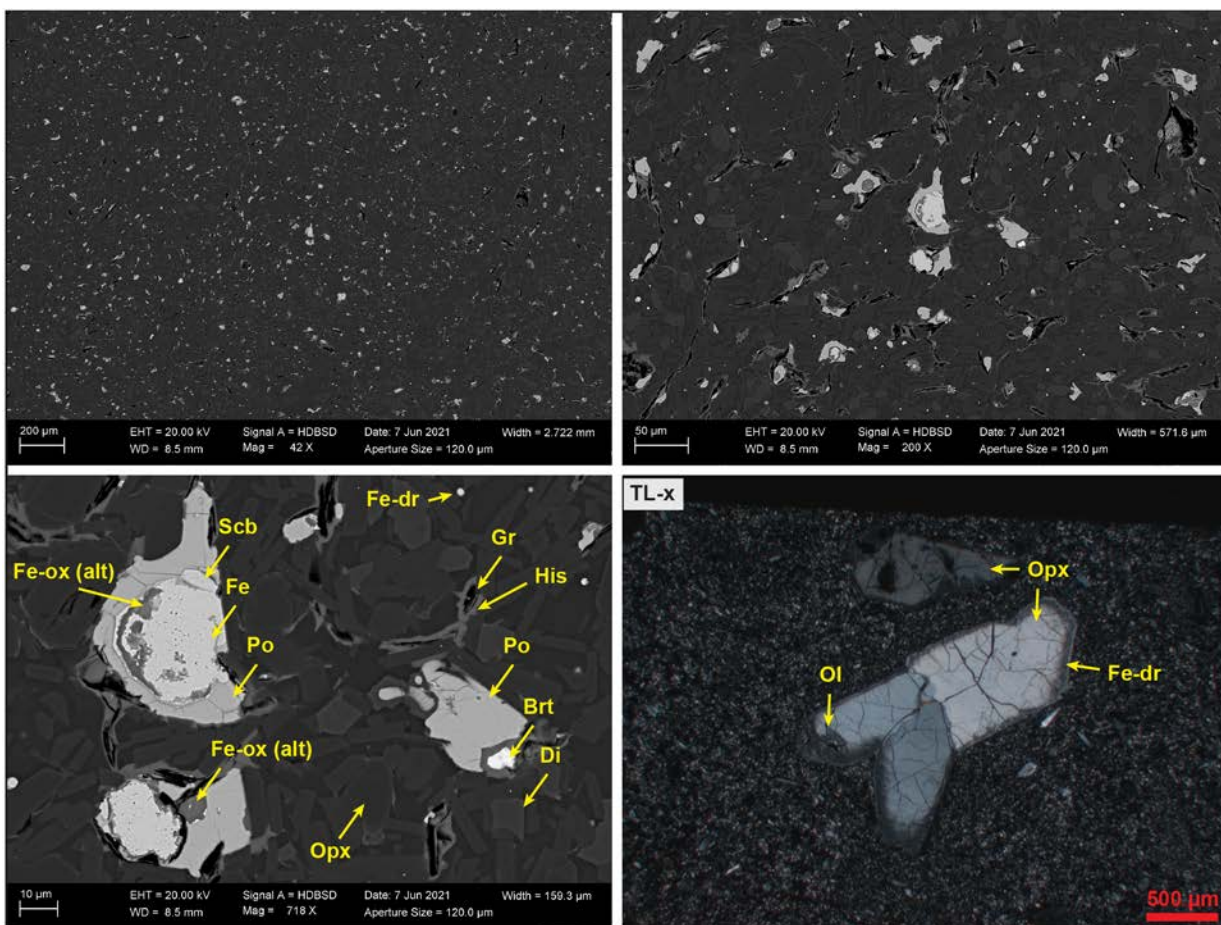


2.17. FP94-4-5\_087.13 Summary

Similar to previous. Fine-crystalline basalt with up to a mm-sized xenocrysts and phenocrysts and abundant micron-sized Fe-droplets dispersed in matrix. Native iron occurs up to few tens of  $\mu\text{m}$  in size and commonly has a coating of magnetite and is associated with pyrrhotite. Pyrrhotite occurs as aggregates of similar size and locally with pentlandite flames and an association with chalcopyrite. Native iron and pyrrhotite are frequently associated with graphite and locally with Fe-Ni-phosphides, such as., e.g., schreibersite.

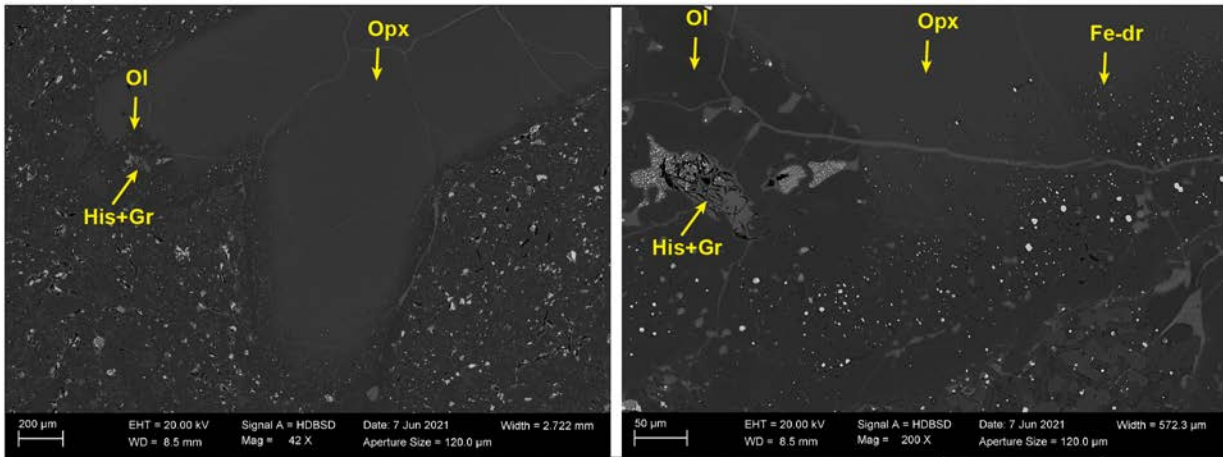
The matrix consists of plagioclase microlite laths, orthopyroxene, and diopside with intersertal siliceous glass. Graphite occurs with the sulphides/native Fe and as few hundred micron-sized aggregates. Graphite is commonly is coated in/associated with a Fe-siliceous phase (hisingerite).

2.18. FP94-4-5\_087.13 SEM-BSE/EDS

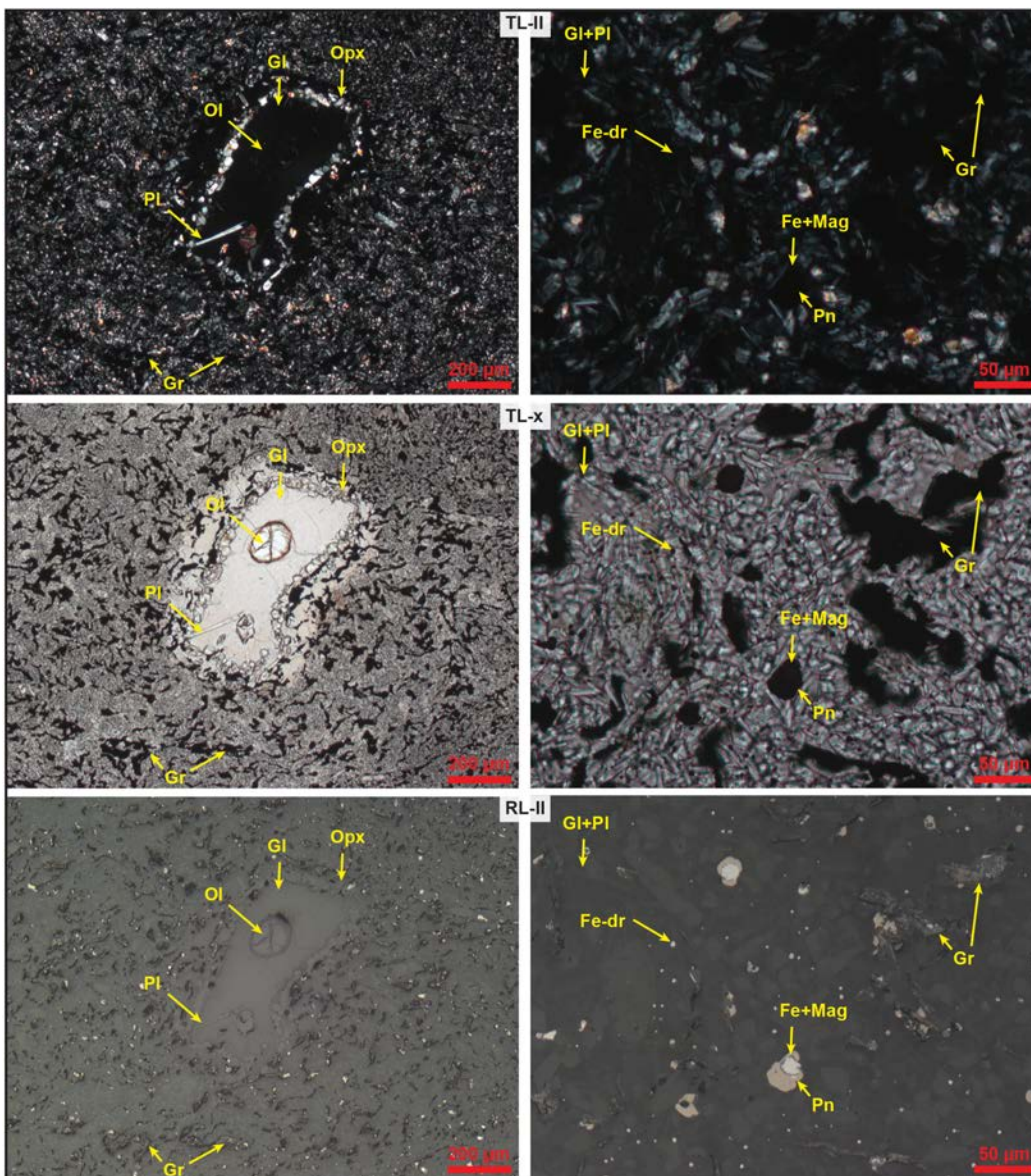


**Fig. 28.** Backscatter electron (BSE) micrographs. Disseminated aggregates of pyrrhotite [Po], graphite [Gr], native Fe, and a native Fe-droplet-rich matrix. Occurrences of mm-sized xenocrysts of orthopyroxene [Opx] and olivine [Ol] with an outer margin extremely rich in micron-sized Fe-droplets. Graphite associated with hisingerite [His].

Next page: close up of Opx+Ol xenocrysts with Fe-droplet-rich outer margin.

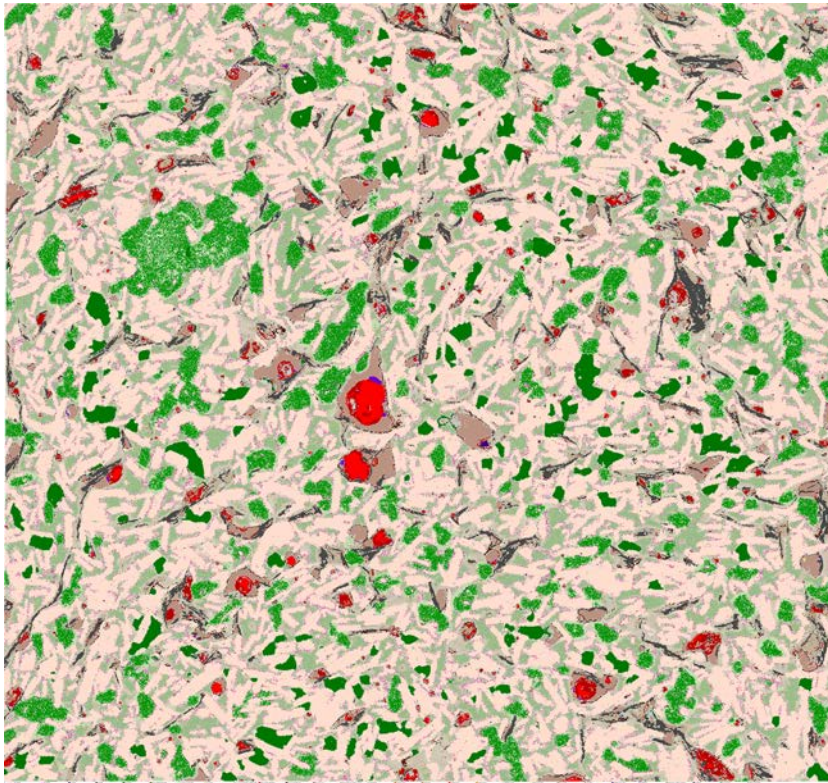


2.19. FP94-4-5\_087.13 Microscopy



**Fig. 29.** Left column: Fine-crystalline basalt with abundant opaques (graphite, pyrrhotite, native Fe) and a large glass [GI]-filled amygdale with a central relict olivine [OI] and an orthopyroxene [Opx] corona. Right column: Association of native Fe with magnetite [Mag] rim and Fe-droplets [Fe-dr] dispersed in matrix. Pyrrhotite associated with pentlandite [Pn]. TL-II: transmitted light micrograph with plane polarized light (ppl). TL-x: crossed polars. RL-II: reflected light micrograph with ppl.

2.20. FP94-4-5\_087.13 AQM-SEM

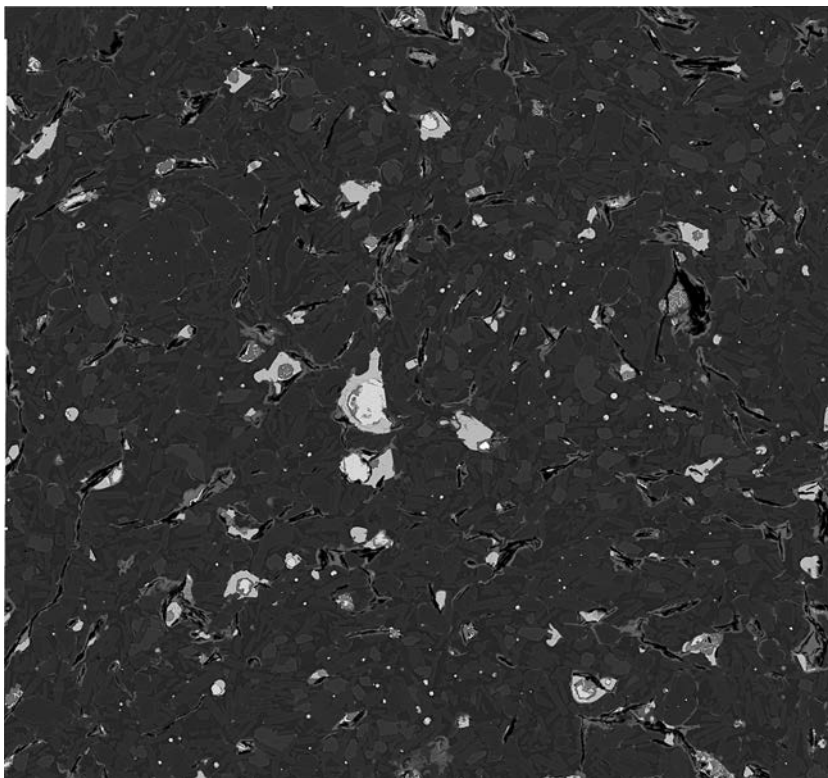


**Fig. 30.** Mineral map and corresponding BSE map of AQM-SEM analysis.

*Native iron mantled by magnetite in association with pyrrhotite and locally with schreibersite. Graphite and Fe-oxide also present in fractures. Matrix consists predominantly of euhedral to subhedral crystals of plagioclase, diopside, orthopyroxene, minor clinopyroxene with intersertal K-rich siliceous glass. Small Fe-droplets also disseminated in matrix. Due to small size possibly underrepresented in mineral map.*

*Image of thin-section, width 23 mm*

— 50 μm



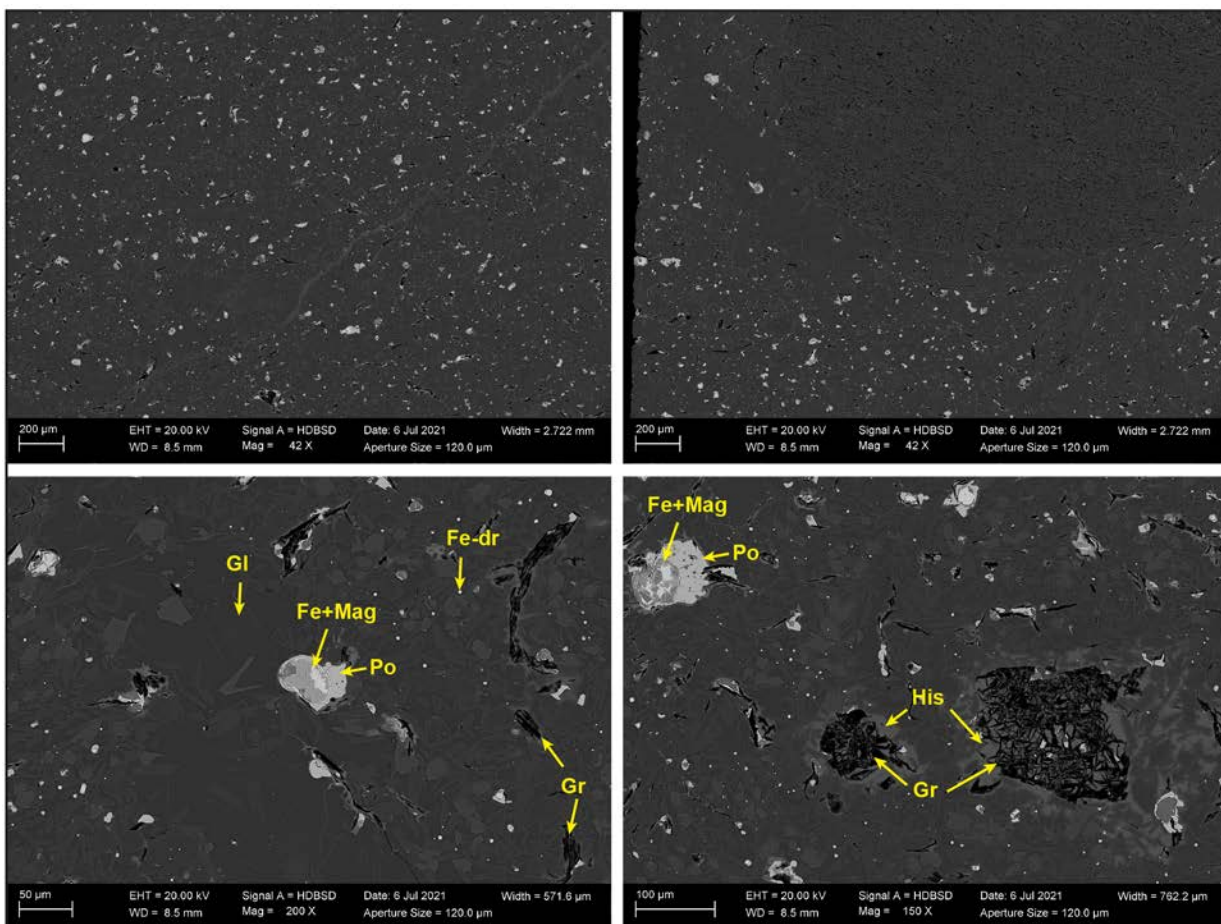


2.21. FP94-4-5\_095.40 Summary

Fine-crystalline basalt with up to a mm-sized devitrified glass xenocrysts and glassy pressure shadow mineralisation. Abundant micron-sized Fe-droplets dispersed in matrix. Native iron occurs variably oxidized up to few tens of  $\mu\text{m}$  in size and commonly has a coating of magnetite and is associated with pyrrhotite. Native iron and pyrrhotite are frequently associated with graphite and locally with Fe-Ni-phosphides, such as., e.g., schreibersite. 50 – 200  $\mu\text{m}$  large aggregates of graphite surrounded by halo of hisingerite.

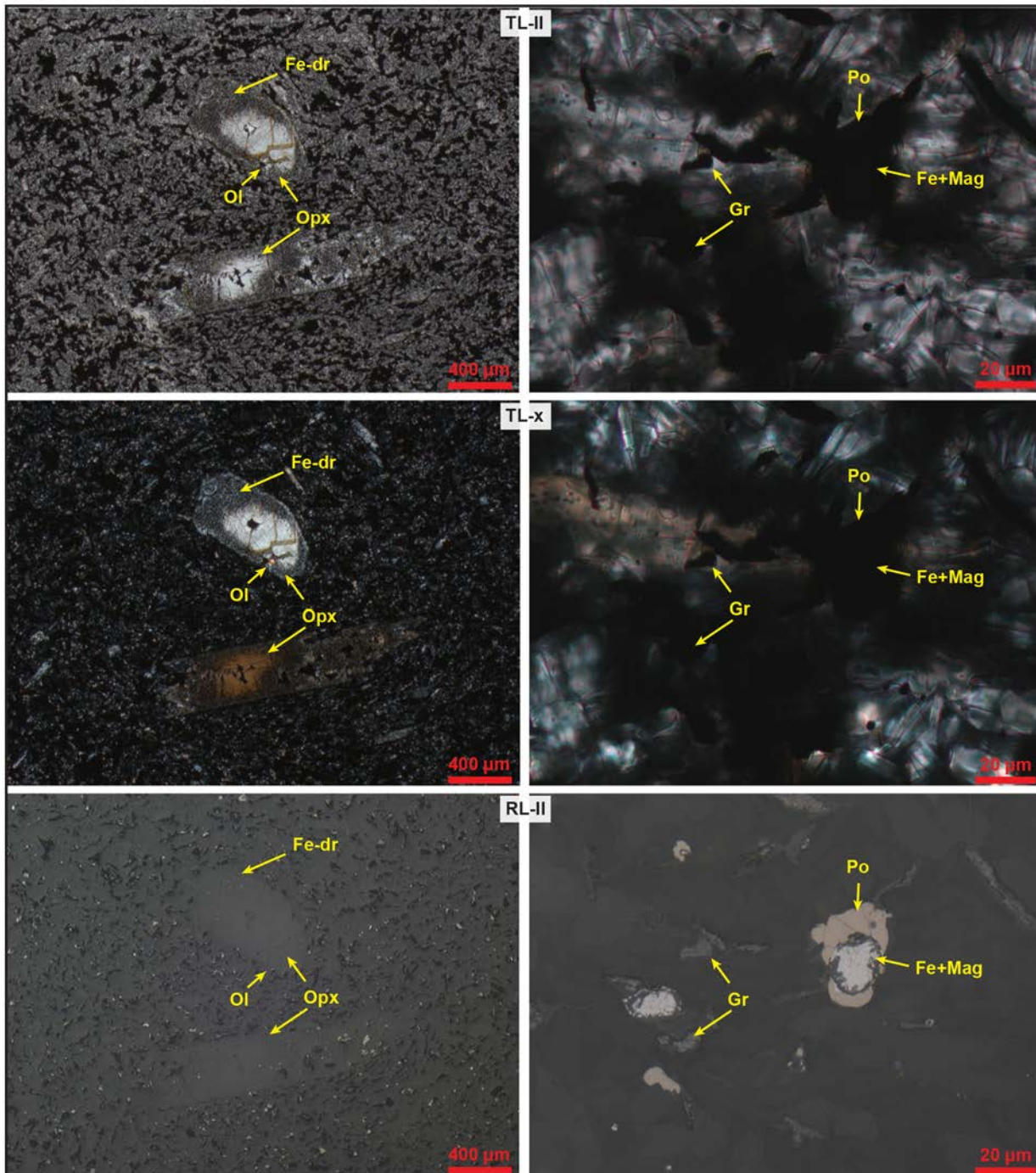
The matrix consists of plagioclase microlite laths, orthopyroxene, and diopside with intersertal siliceous glass. Graphite occurs with the sulphides/native Fe and as few hundred micron-sized aggregates. Graphite is commonly is coated in/associated with a Fe-siliceous phase (hisingerite). Hisingerite also as vein/fracture fill. Higher amounts of glassy matrix and vein fills than previous samples.

2.22. FP94-4-5\_095.40 SEM-BSE/EDS

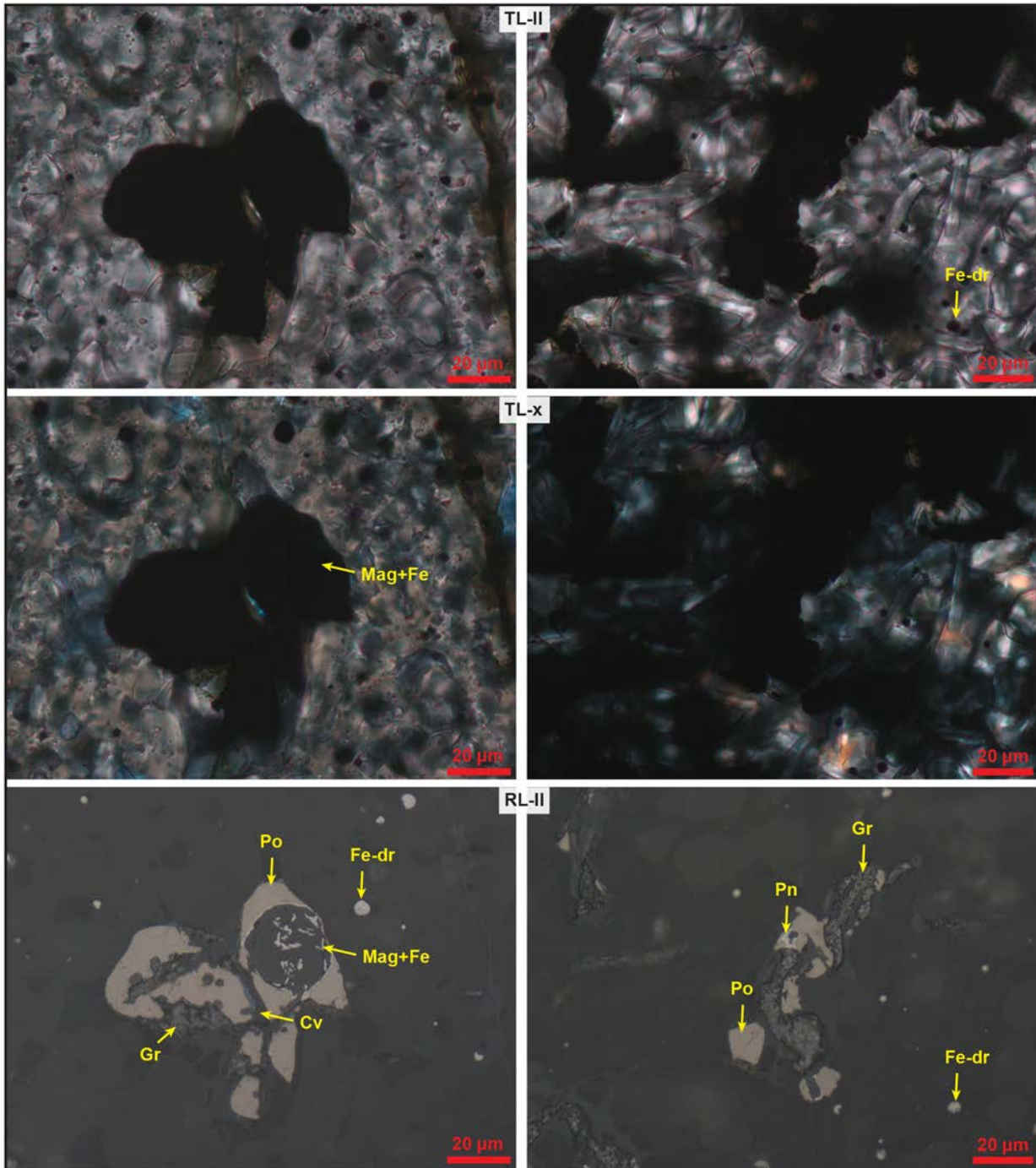


**Fig. 31.** Backscatter electron (BSE) micrographs. Disseminated droplets of pyrrhotite [Po], magnetite [Mag], graphite [Gr], native Fe, and a native Fe-droplet-rich matrix. Occurrences of mm-sized devitrified glass [Gl]-filled vugs. Graphite associated with hisingerite [His].

2.23. FP94-4-5\_095.40 Microscopy



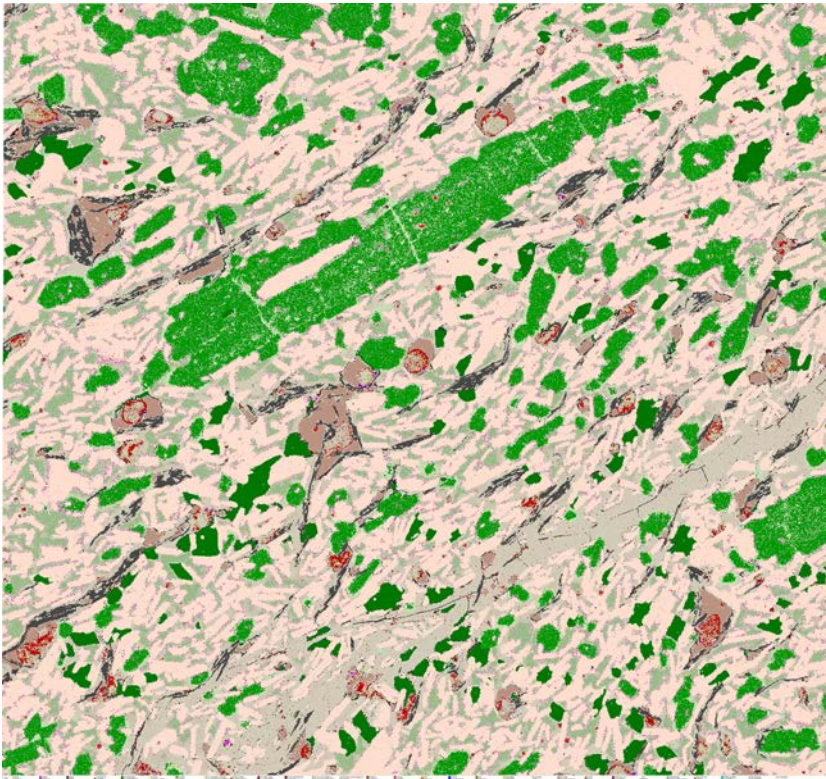
**Fig. 32.** Left column: Fine-crystalline basalt with large orthopyroxene [Opx] xenocrysts and relict olivine [Ol]. Micron-sized Fe-droplets [Fe-dr] in outer zone of orthopyroxene. Right column: Native iron with magnetite[Mag] rim and association with pyrrhotite [Po]. TL-II: transmitted light micrograph with plane polarized light (ppl). TL-x: crossed polars. RL-II: reflected light micrograph with ppl.



**Fig. 33.** Strongly oxidized native Fe and association with pyrrhotite [Po], pentlandite [Pn], covellite Cv], and graphite [Gr]. Fe-droplets [Fe-dr] in matrix.

TL-II: transmitted light micrograph with plane polarized light (ppl). TL-x: crossed polars. RL-II: reflected light micrograph with ppl.

2.24. FP94-4-5\_095.40 AQM-SEM

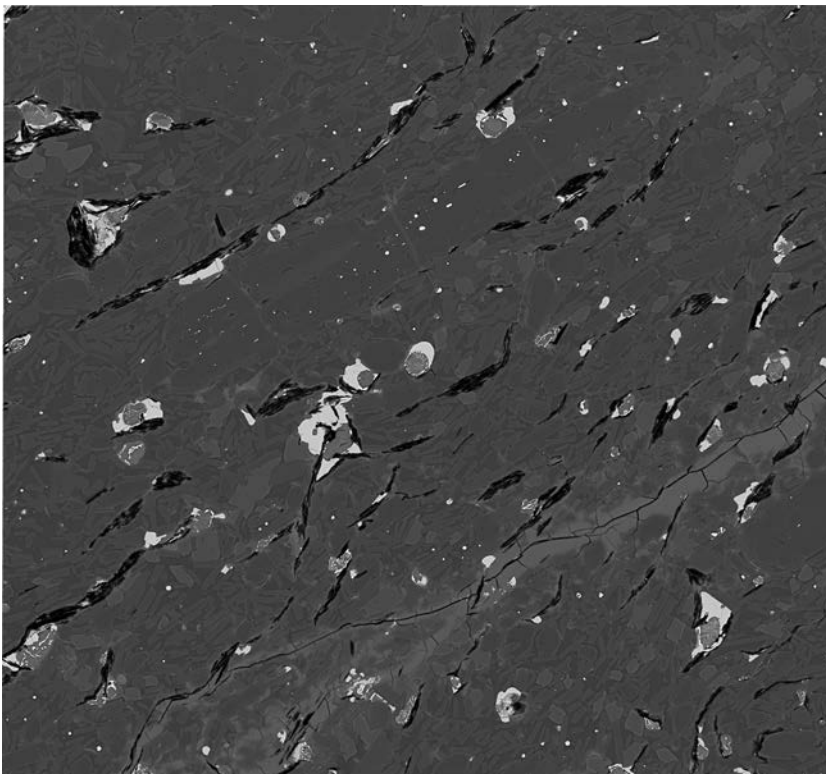


**Fig. 34.** Mineral map and corresponding BSE map of AQM-SEM analysis.

Strongly oxidized native iron associated with intergrown pyrrhotite and graphite. Large orthopyroxene phenocryst with Fe-Mg-chlorite altered block boudinage fractures. Fe droplets in opx. Small Fe-droplets also disseminated in matrix. Fracture filled by hisingerite. Phenocrysts, graphite, and sulphides tectonically aligned (shadow pressure mineralization, sigma clasts)

Image of thin-section, width 23 mm

50 µm

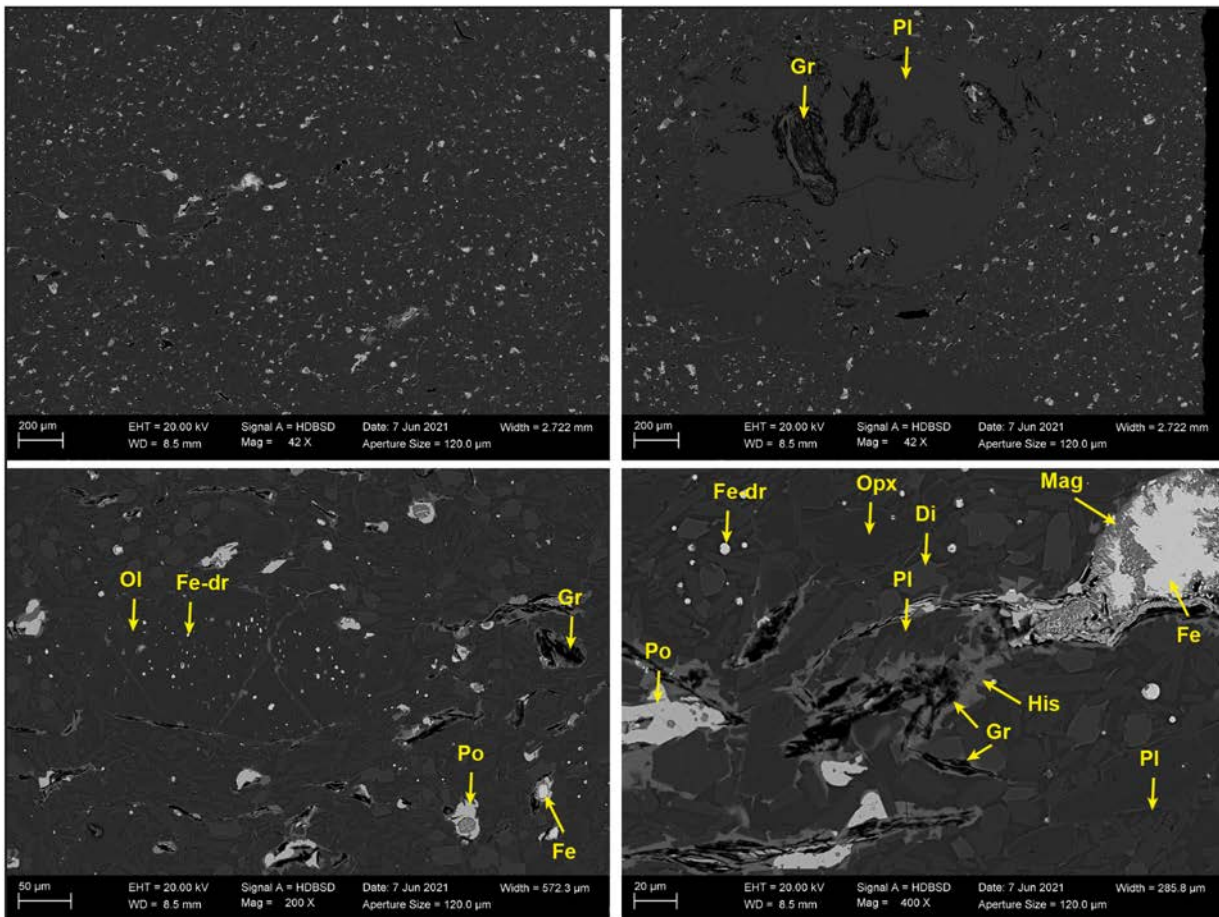


2.25. FP94-4-5\_103.68 Summary

Fine-crystalline basalt with up to few mm-sized albite and orthopyroxene phenocrysts, as well as olivine xenocrysts. Large pheno- and xenocrysts appear aligned. Native iron occurs variably oxidized up to few hundreds of  $\mu\text{m}$  in size and commonly has a coating of magnetite and is associated with pyrrhotite. Native iron and pyrrhotite are frequently associated with graphite and locally with Fe-Ni-phosphides, such as., e.g., schreibersite. Graphite aggregates surrounded by halo of hisingerite. Abundant micron-sized Fe-droplets dispersed in matrix.

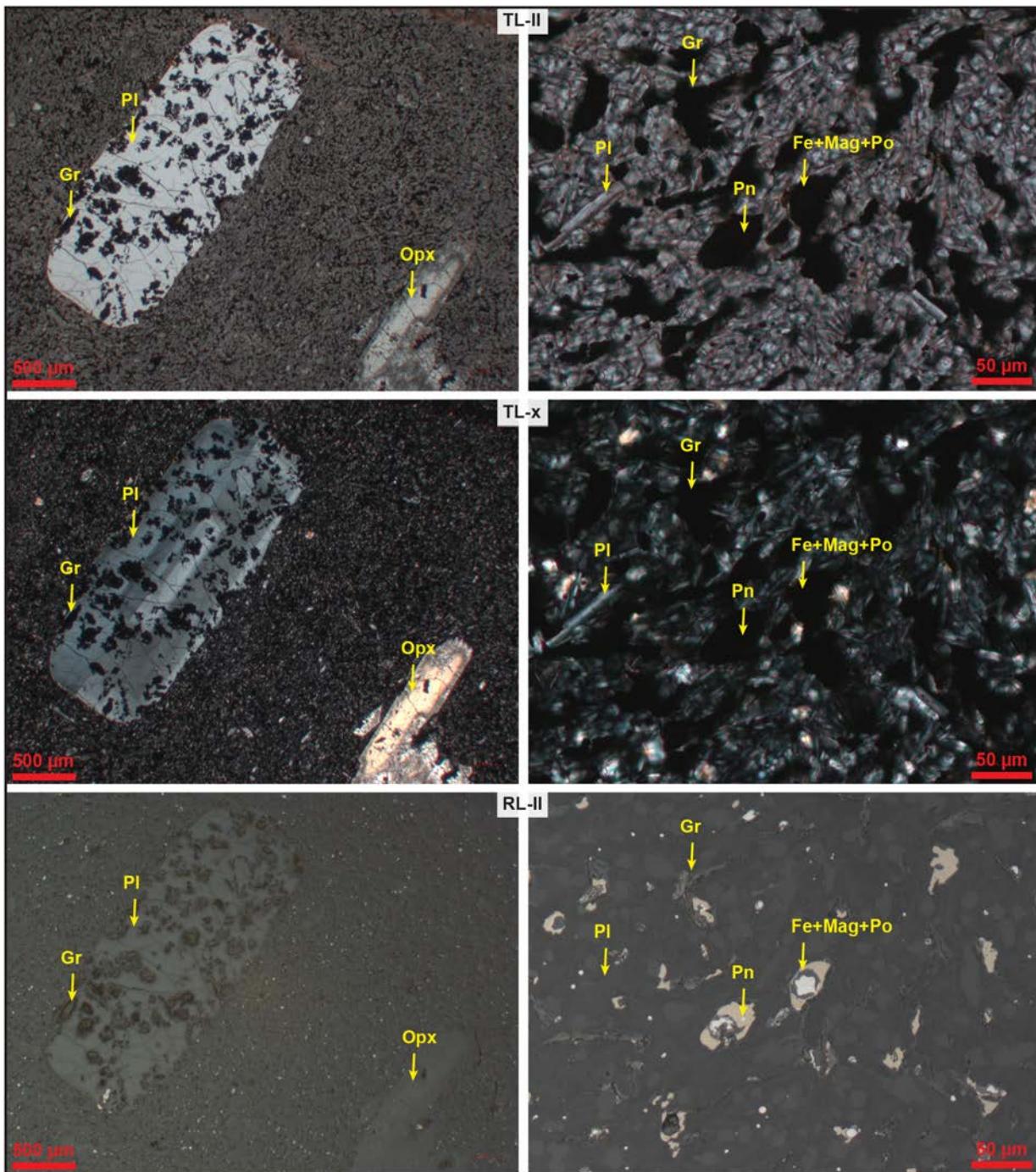
The matrix consists of plagioclase microlite laths, orthopyroxene, and diopside with intersertal siliceous glass. Graphite occurs with the sulphides/native Fe and as few hundred micron-sized aggregates. Graphite is commonly is coated in/associated with a Fe-siliceous phase (hisingerite). Hisingerite also as vein/fracture fill. Moderate to strong alignment of plagioclase microlites, native iron-pyrrhotite-graphite aggregates, and phenocrysts.

2.26. FP94-4-5\_103.68 SEM-BSE/EDS

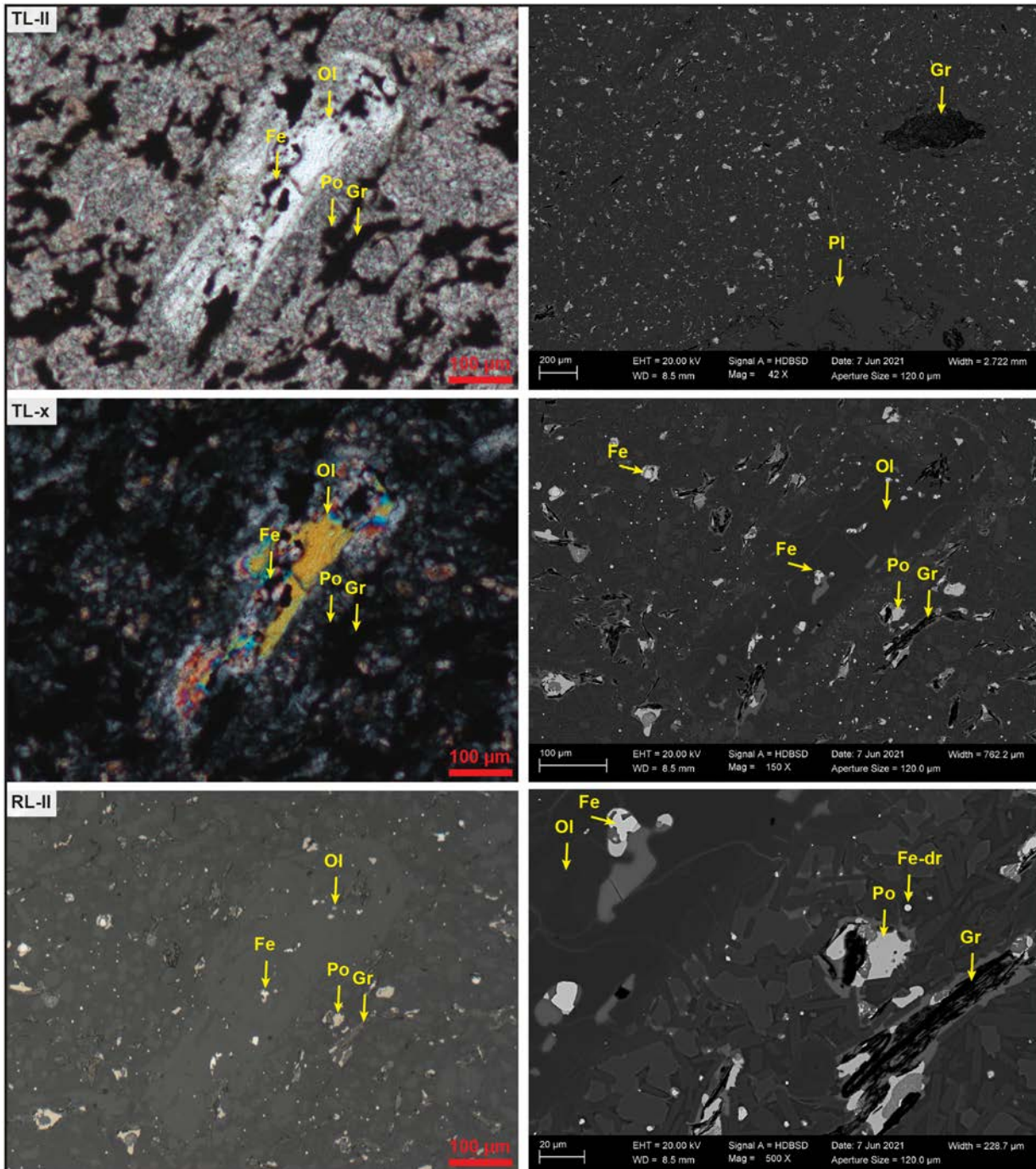


**Fig. 35.** Backscatter electron (BSE) micrographs. Disseminated aggregates of pyrrhotite [Po], magnetite [Mag], graphite [Gr], native Fe, and a native Fe-droplet-rich matrix. Occurrences of mm-sized albite [Pl] phenocrysts and olivine [Ol] xenocrysts. Olivine with Fe-droplet-rich core. Native iron variably altered, associated with pyrrhotite and graphite. Graphite associated with hisingerite [His]. Plagioclase microlites in pressure shadow of native Fe occur as stacked crystals.

2.27. FP94-4-5\_103.68 Microscopy

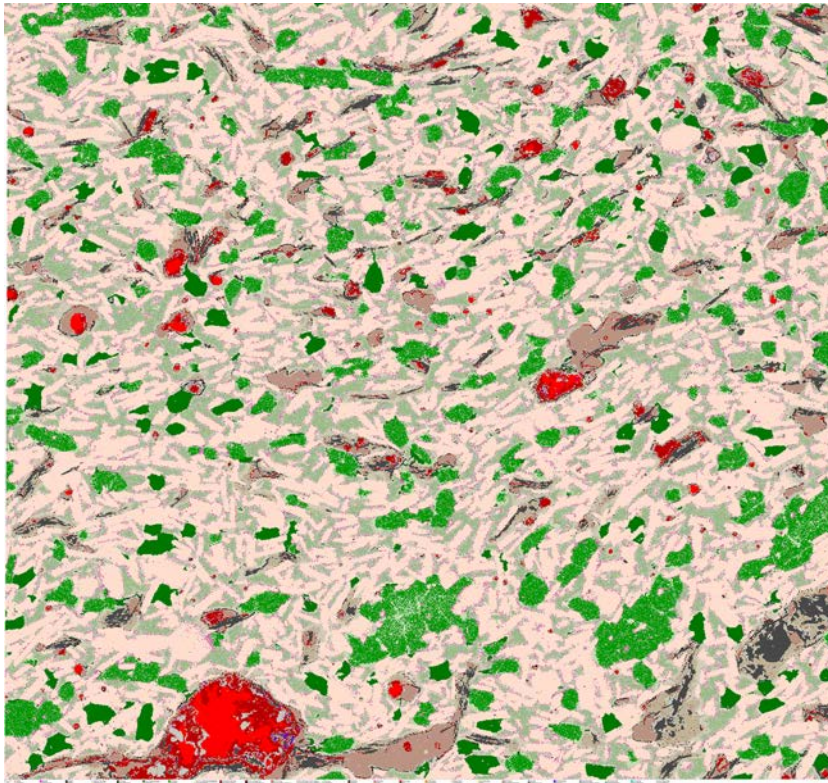


**Fig. 36.** Left column: Large aligned oscillatory zoned plagioclase [Pl] and orthopyroxene [Opx] phenocrysts. Right column: Native iron with magnetite [Mag] rim and association with pyrrhotite [Po]. Fe-droplets in matrix. Pentlandite [Pn] flames in pyrrhotite. TL-II: transmitted light micrograph with plane polarized light (ppl). TL-x: crossed polars. RL-II: reflected light micrograph with ppl.



**Fig. 37.** Left column: Large aligned olivine [Ol] (forsterite) xenocrysts with solution embayments. Native Fe within olivine. Pyrrhotite [Po] associated with graphite [Gr]. TL-II: transmitted light micrograph with plane polarized light (ppl). TL-x: crossed polars. RL-II: reflected light micrograph with ppl. Right column: Backscatter electron (BSE) micrographs of olivine [Ol] xenocryst, large graphite [Gr] aggregate, and plagioclase [Pl] phenocryst. Native Fe with magnetite [Mag] rim and association with pyrrhotite. Fe-droplets in matrix and in olivine.

2.28. FP94-4-5\_103.68 AQM-SEM



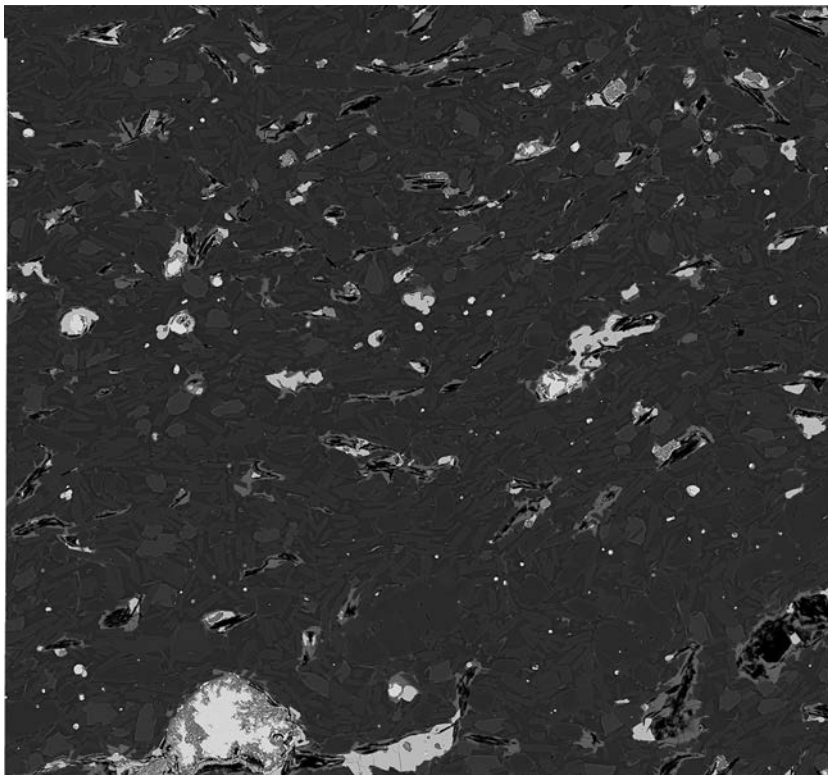
50 µm

**Fig. 38.** Mineral map and corresponding BSE map of AQM-SEM analysis.

Variably oxidized native iron associated with intergrown pyrrhotite, graphite, and minor schreibersite, up to ca. 50 µm native Fe.

Native Fe+Mag+Po, graphite, phenocrysts, and plagioclase aligned.

Image of thin-section, width 23 mm



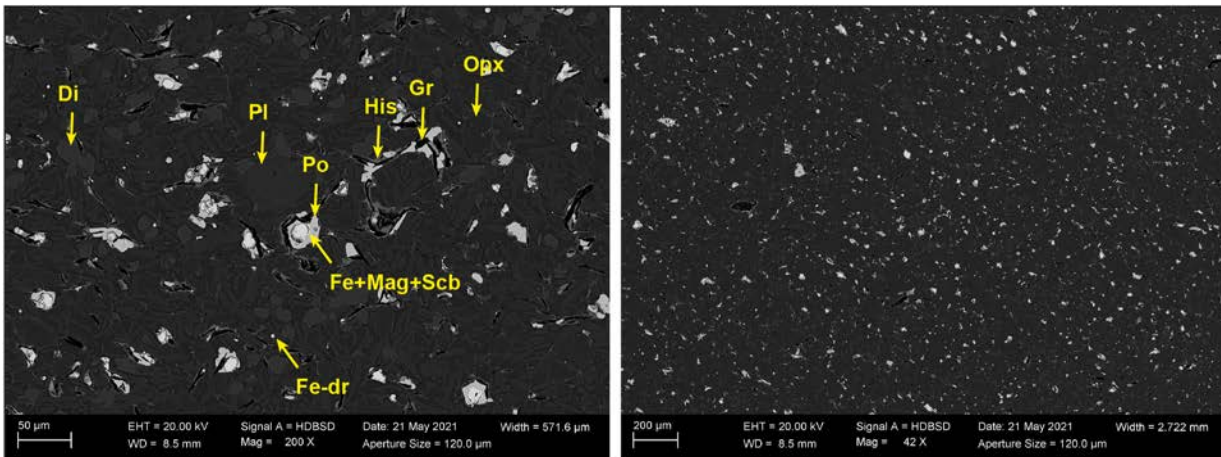


2.29. FP94-4-5\_110.90 Summary

Fine-crystalline basalt with up to few hundreds  $\mu\text{m}$ -sized albite and orthopyroxene phenocrysts, as well as olivine xenocrysts. Native iron with variably but minor oxidized rims, often with minor associated pyrrhotite. Native iron commonly is rimmed by magnetite and a second rim of 'cleaner'-appearing Fe and Fe-Ni-phosphides, such as., e.g., schreibersite. When present, pyrrhotite and graphite and minor covellite form the outer phases. Native Fe-droplets in the matrix are present, but less frequent than in samples stratigraphically above.

The matrix consists of plagioclase microlite laths, orthopyroxene, and diopside with intersertal siliceous glass and ?palagonitic glass. The latter having a rusty brown-orangy appearance in plane polarized light and also fills amygdaloidal vug space. Plagioclase phenocrysts commonly with swallow-tails. Graphite occurs with the sulphides/native Fe and as larger aggregates. Graphite is commonly is coated in/associated with a Fe-siliceous phase (hisingerite).

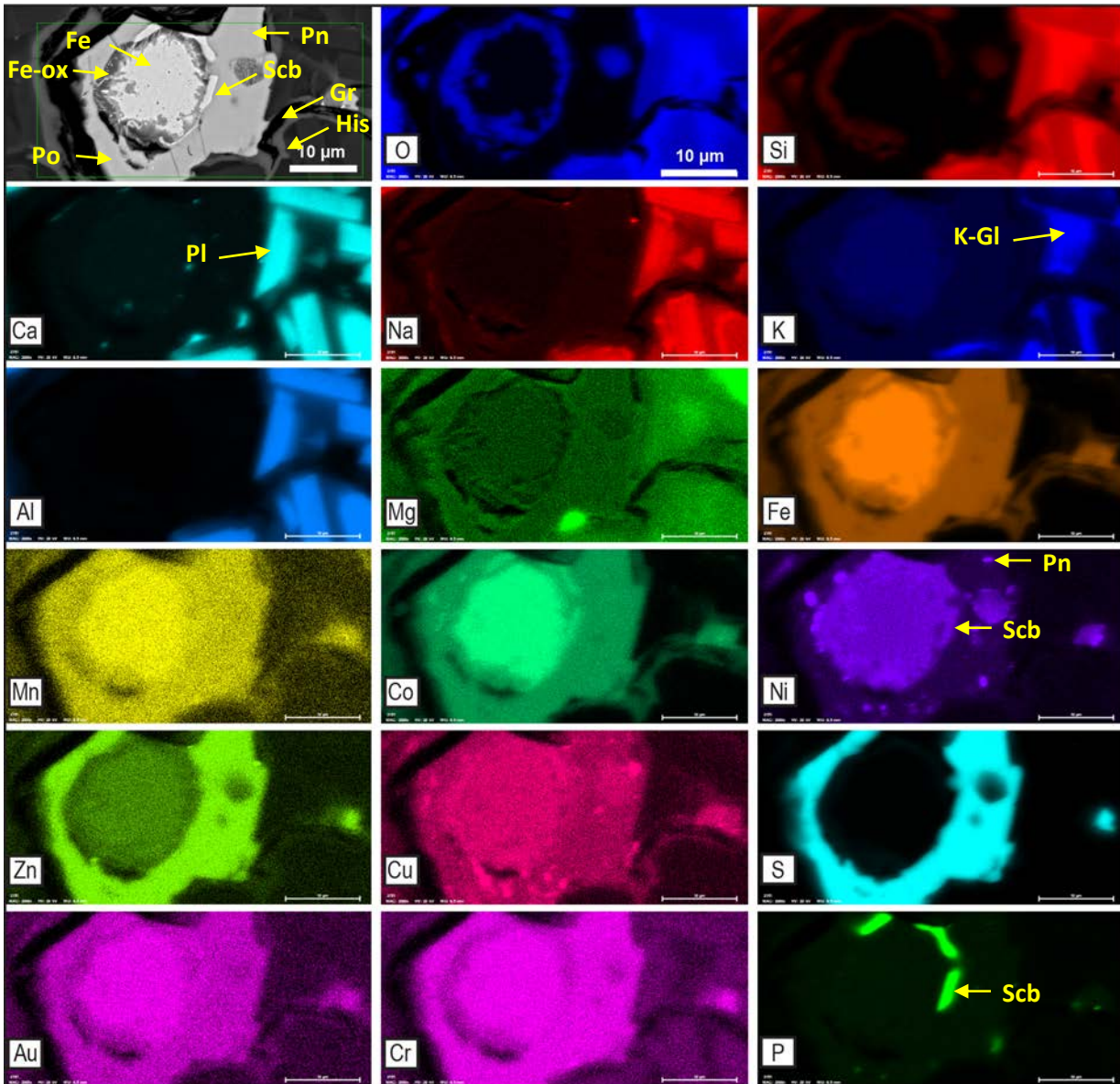
2.30. FP94-4-5\_110.90 SEM-BSE/EDS



**Fig. 39.** Backscatter electron (BSE) micrographs. Abundant disseminated aggregates of native Fe, pyrrhotite [Po], graphite [Gr], and moderate amounts of native Fe-droplet matrix. Native iron with magnetite [Mag] rim and second rim of Fe+schreibersite [Scb] and associated with pyrrhotite and graphite. Graphite associated with hisingerite. Plagioclase [Pl] microlites, diopside [Di], orthopyroxene [Opx], and glass [Gl] forming the matrix.

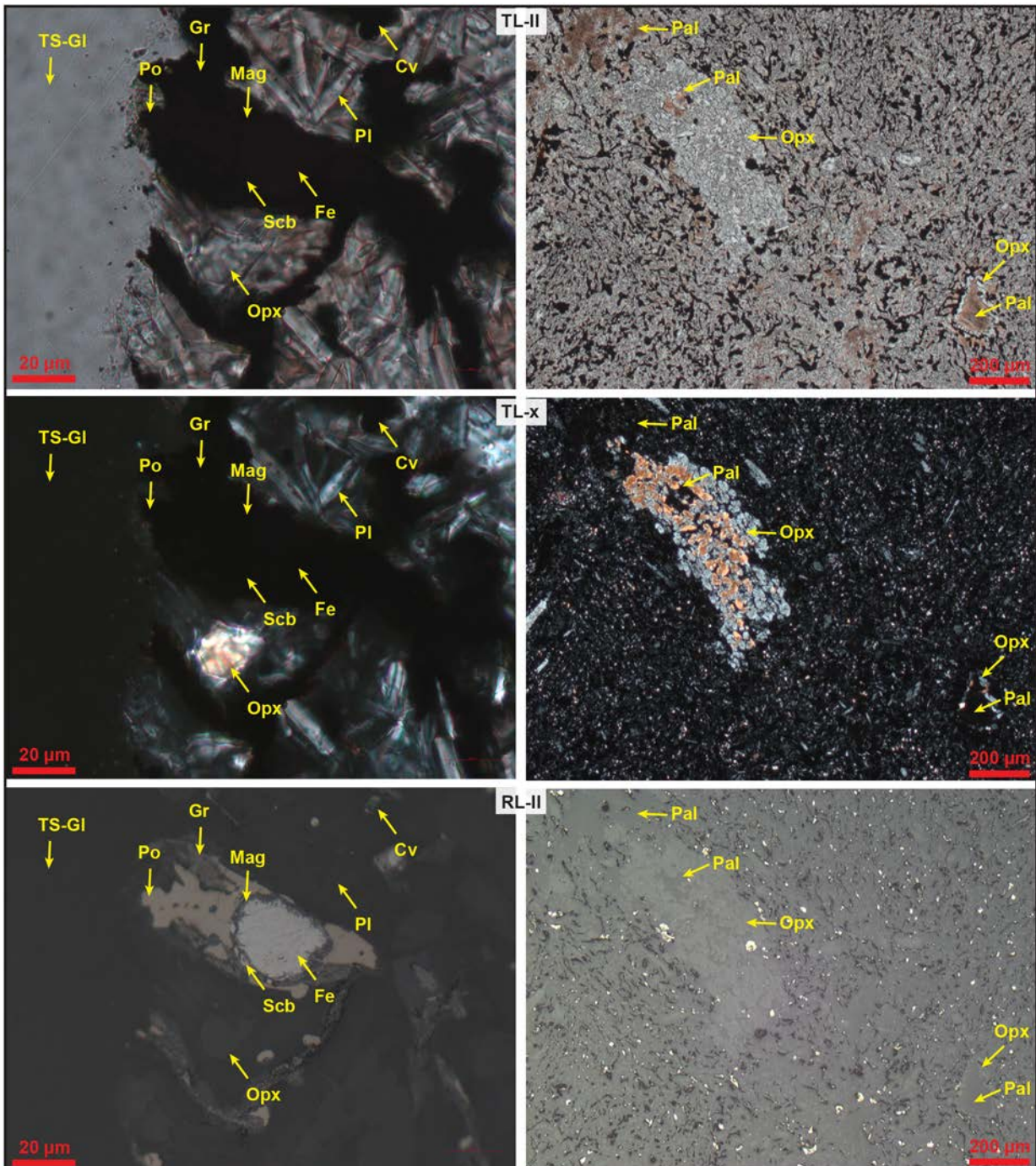
FP94-4-5\_110.90

SEM-EDS element map



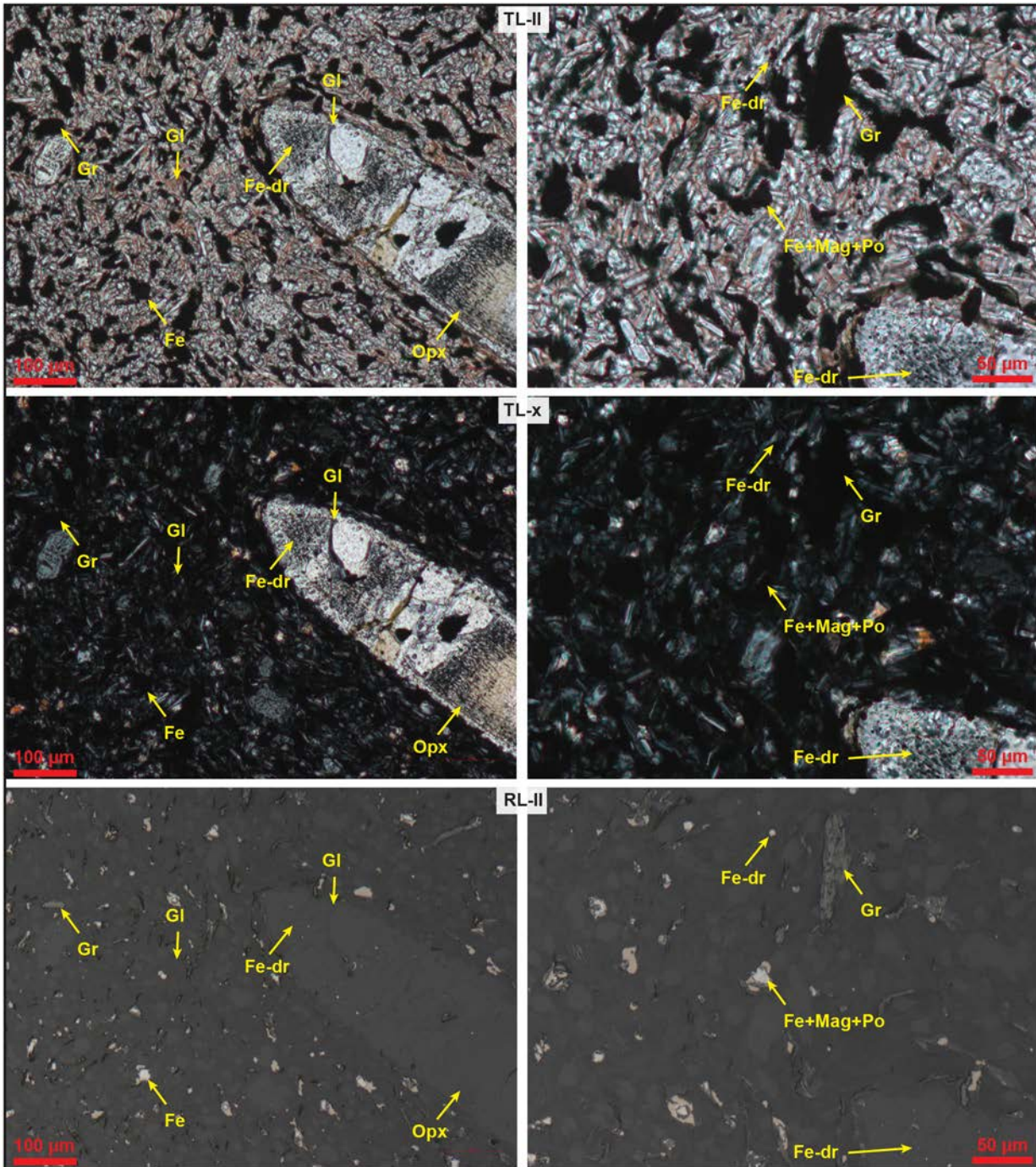
**Fig. 40.** Element maps to illustrate the native Fe with Fe-oxide rim and a secondary rim of Fe and schreibersite [Scb] and the association with pyrrhotite [Po] and graphite [Gr]. Pyrrhotite with pentlandite [Pn] inclusion. Graphite is coated by hisingerite [His]. Matrix consists of plagioclase [Pl], pyroxene, and siliceous K-bearing glass [K-Gl].

2.31. FP94-4-5\_110.90 Microscopy



**Fig. 41.** Left column: Native Fe with magnetite [Mag] rim and secondary rim of schreibersite [Scb] in association with pyrrhotite [Po] and graphite [Gr]. Minor occurrences of covellite [Cv]. Thin-section glass [TS-Gl] illustrates the opaque nature of glass (natural or anthropogenic). Right column: Cumulate of orthopyroxene [Opx] with intersertal palagonitic [Pal] glassy matrix. Palagonitic vug fill with orthopyroxene corona to right hand side.

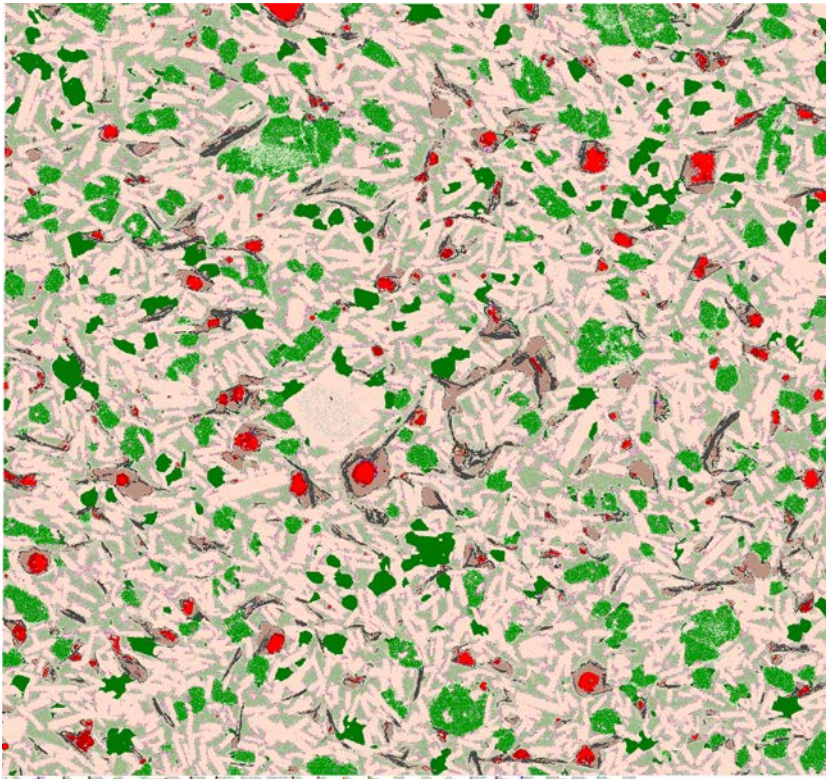
TL-II: transmitted light micrograph with plane polarized light (ppl). TL-x: crossed polars. RL-II: reflected light micrograph with ppl.



**Fig. 42.** Left column: Large altered orthopyroxene [Opx] phenocryst with Fe-droplet-rich outer zone. Native Fe, pyrrhotite [Po], and graphite [Gr] disseminated with glassy [Gl] and palagonitic matrix. Right column: Native Fe with magnetite [Mag] rim and secondary rim in association with pyrrhotite and graphite. Minor occurrences of Fe-droplets in matrix.

TL-II: transmitted light micrograph with plane polarized light (ppl). TL-x: crossed polars. RL-II: reflected light micrograph with ppl.

2.32. FP94-4-5\_110.90 AQM-SEM



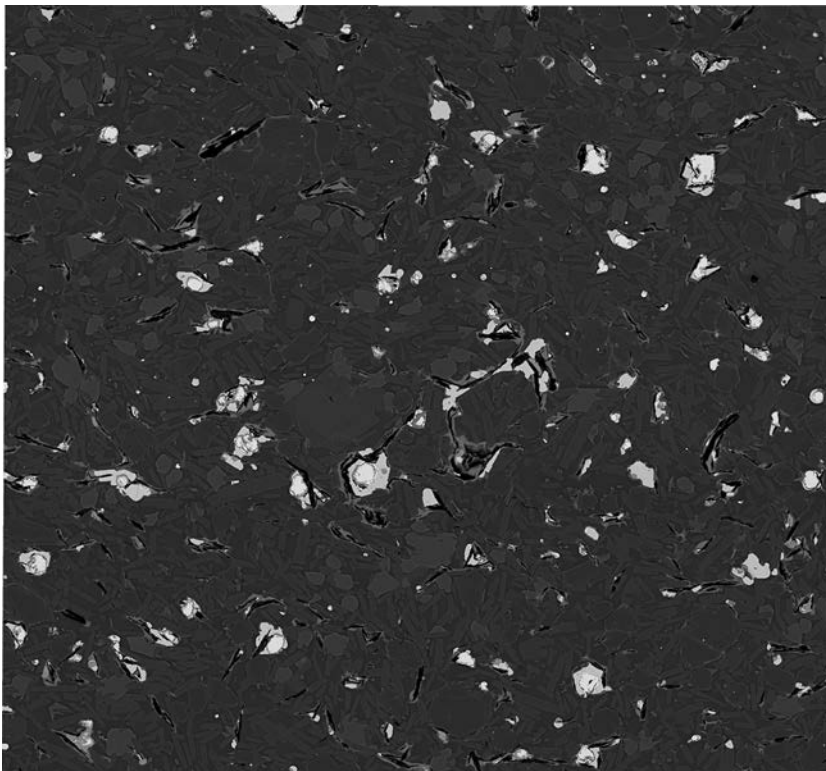
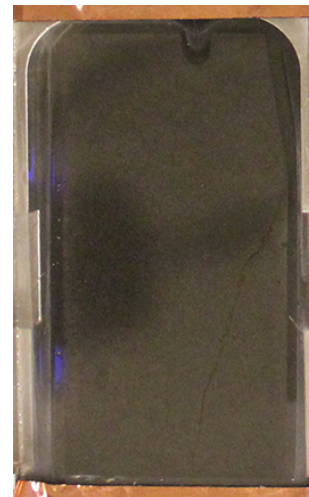
**Fig. 43.** Mineral map and corresponding BSE map of AQM-SEM analysis.

*Native iron with magnetite rim associated with pyrrhotite, graphite, and minor schreibersite.*

*Larger orthopyroxene and plagioclase phenocrysts in plagioclase microlite-rich matrix with intersertal glass.*

*Image of thin-section, width 23 mm*

50 µm

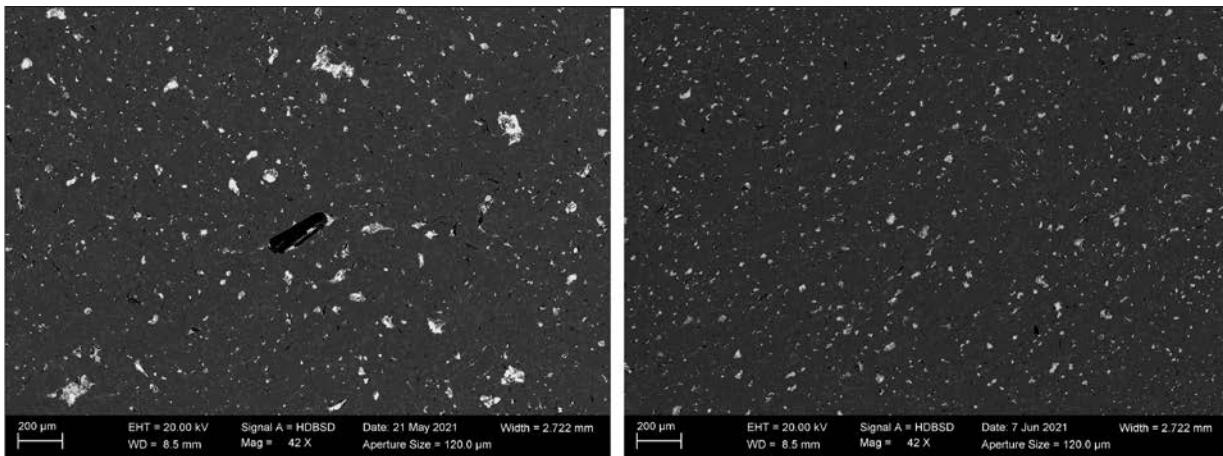


### 2.33. FP94-4-5\_121.80 Summary

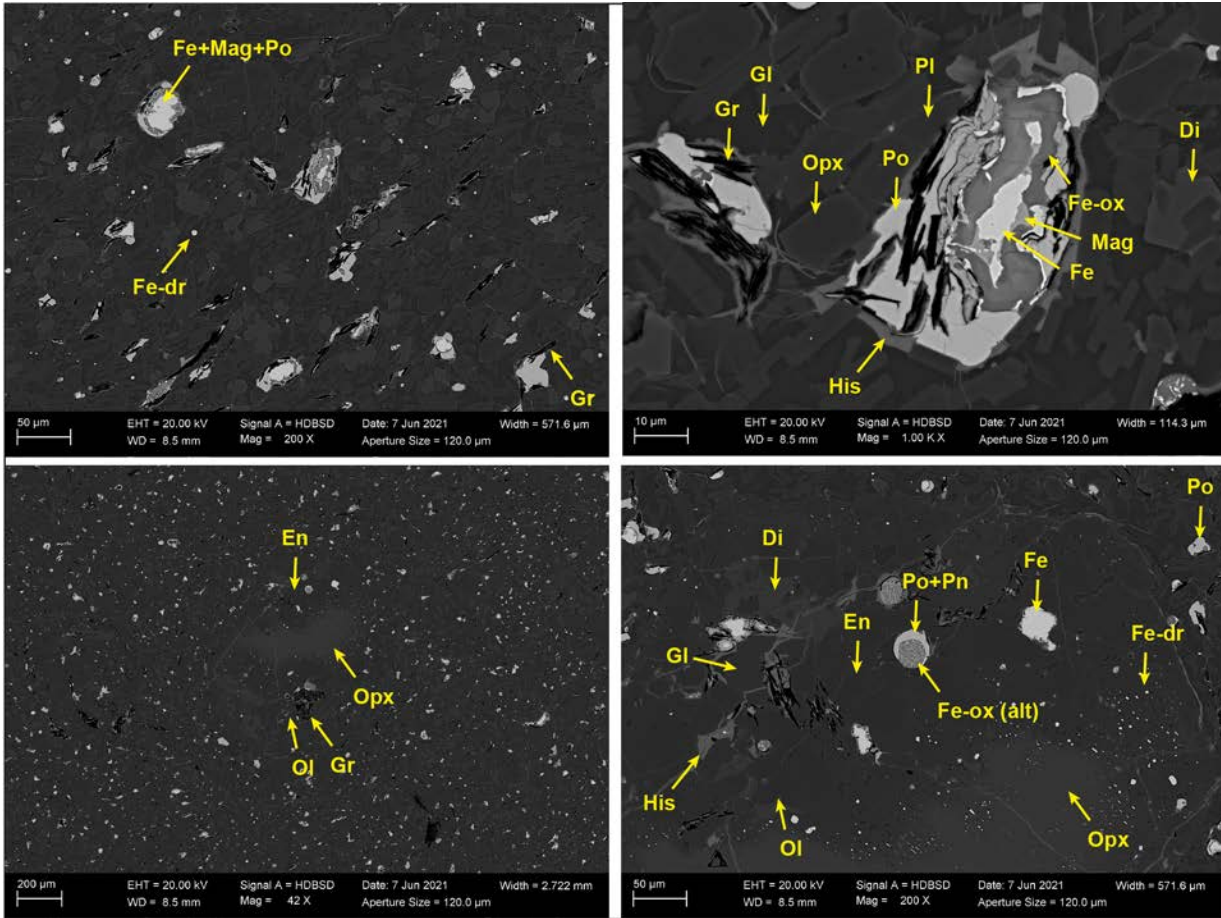
Fine-crystalline basalt with up to few hundreds  $\mu\text{m}$ -sized orthopyroxene-altered olivine xenocrysts, as well as plagioclase and orthopyroxene phenocrysts. Native iron with variably but minor oxidized rims, often with associated pyrrhotite. Native iron commonly is rimmed by magnetite and locally with a second rim of 'cleaner'-appearing Fe and Fe-Ni-phosphides, such as., e.g., schreibersite. When present, pyrrhotite and graphite and minor covellite form the outer phases. Native Fe-droplets in the matrix are present, but less frequent than in samples stratigraphically above. Graphite occurs with the sulphides/native Fe and as larger aggregates.

The matrix consists of plagioclase microlite laths, orthopyroxene, and diopside with intersertal siliceous glass. Palagonite occurs with a rusty brown-orangy appearance in plane polarized light filling amygdaloidal vug space. Graphite is commonly is coated in/associated with a Fe-siliceous phase (hisingerite). Plagioclase microlites are aligned and native Fe+sulphide aggregates show signs of light shearing.

### 2.34. FP94-4-5\_121.80 SEM-BSE/EDS

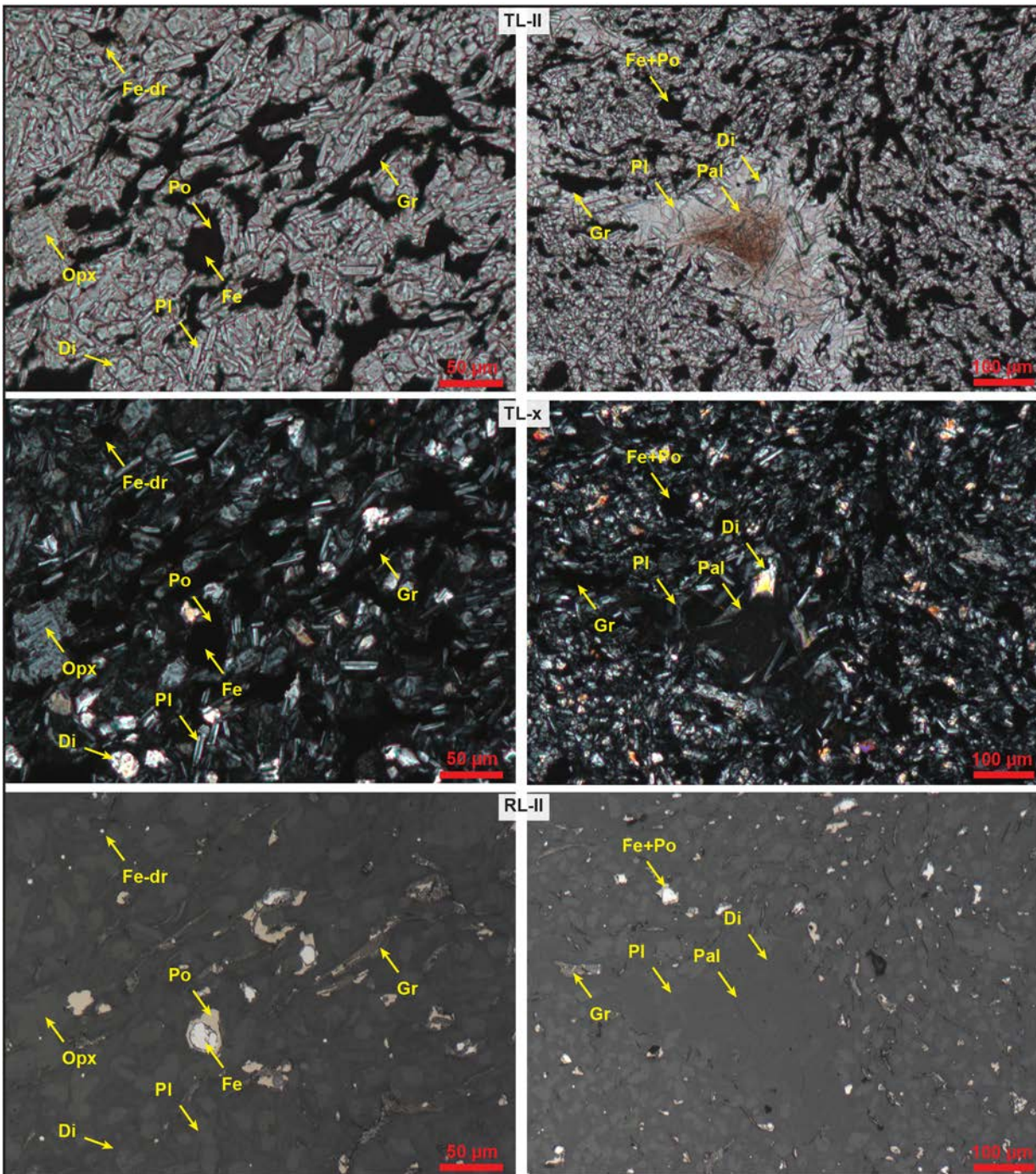


**Fig. 44.** Backscatter electron (BSE) micrographs. Abundant disseminated aggregates of native Fe, graphite, pyrrhotite, and minor amounts of native Fe-droplet matrix. Note: different grain size within in one sample.



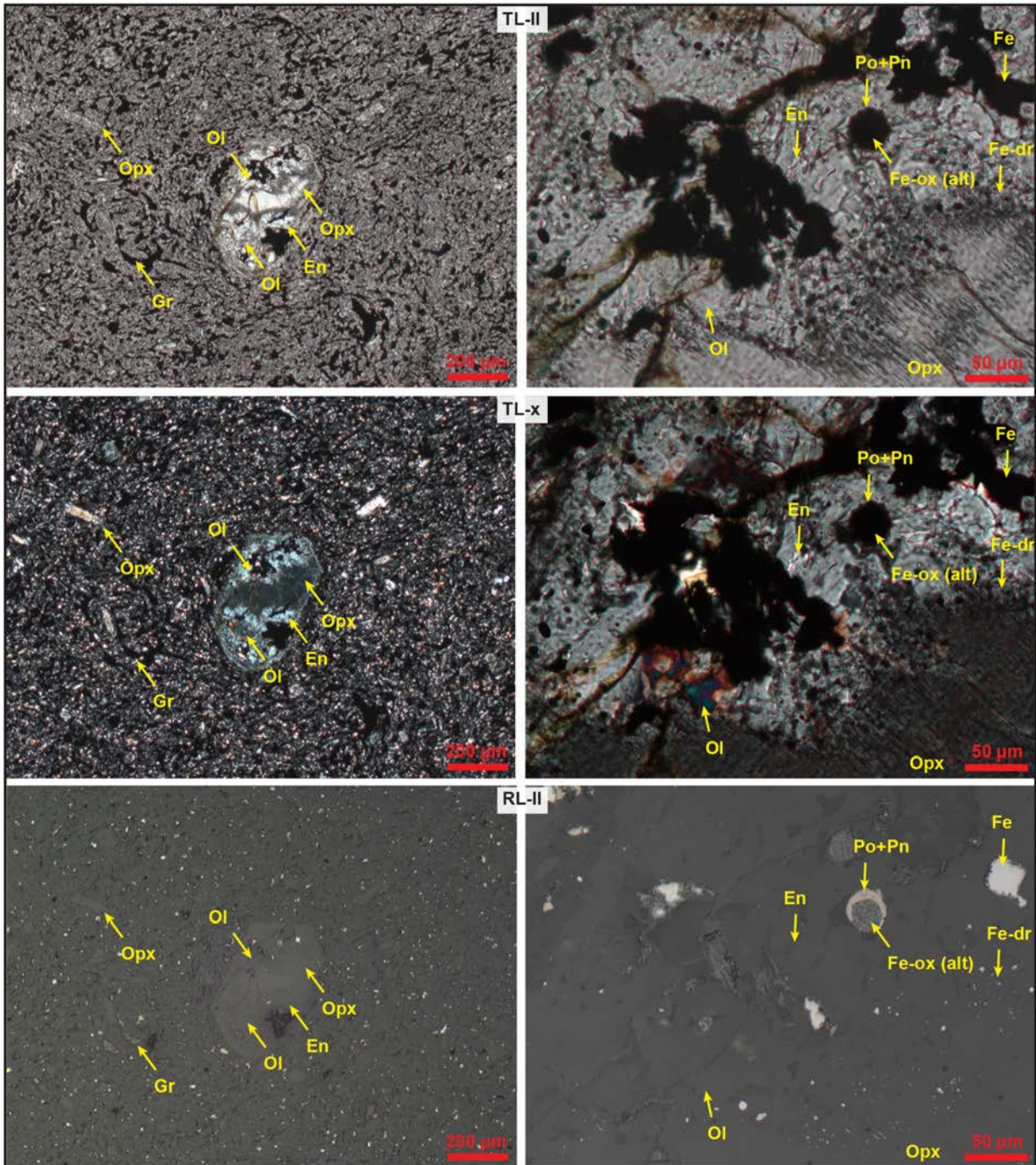
**Fig. 45.** Backscatter electron (BSE) micrographs. Abundant disseminated aggregates of native Fe, pyrrhotite [Po], graphite [Gr], and moderate amounts of native Fe-droplets in matrix. Micron-sized Fe-droplets in zones cross-cutting orthopyroxene [Opx]-altered olivine [Ol]. Native iron with oxidized rim and second rim of Fe, schreibersite [Scb] and associated with pyrrhotite [Po] and graphite [gr]. Graphite associated with hisingerite [His]. Plagioclase [Pl] microlites, diopside [Di], orthopyroxene [Opx], and glass [Gl] forming the matrix. Slight foliation recognizable on aligned graphite+sulphide+native Fe aggregate (upper left image).

2.35. FP94-4-5\_121.80 Microscopy



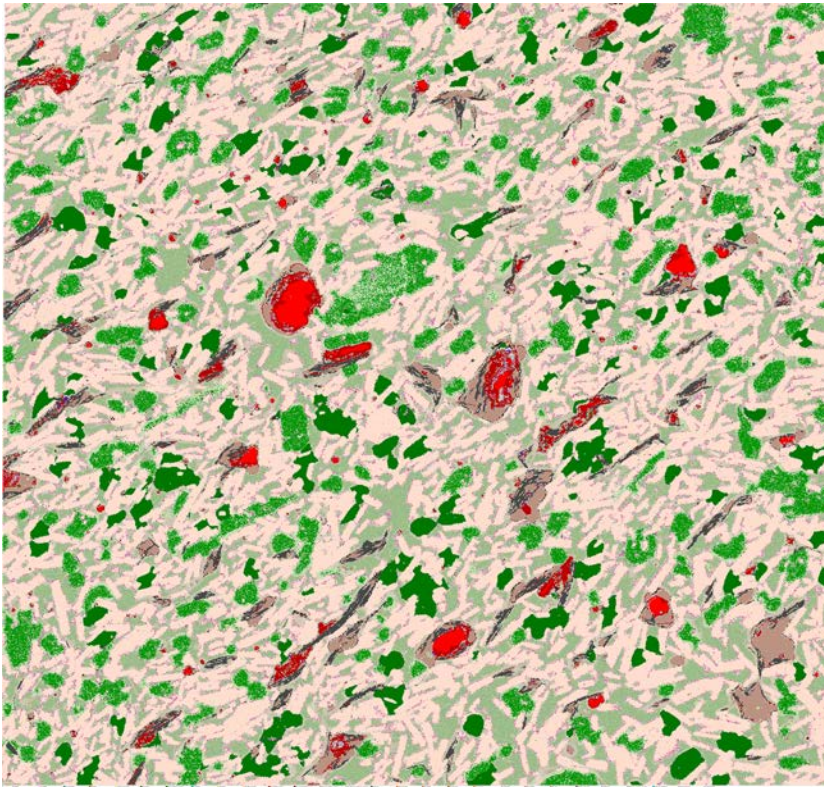
**Fig. 46.** Left column: Native Fe with magnetite rim and secondary rim in association with pyrrhotite [Po]. Graphite [Gr] and plagioclase [Pl] microlites show alignment/foliation. Minor occurrences of Fe-droplets in matrix. Right column: Glass [Gl] and palagonite [Pal]-filled vug space with acicular plagioclase laths and diopside [Di].  
 TL-II: transmitted light micrograph with plane polarized light (ppl). TL-x: crossed polars. RL-II: reflected light micrograph with ppl.





**Fig. 47.** Left column: Large orthopyroxene [Opx], partially enstatite [En]-altered olivine [Ol] xenocryst with cross-cutting Fe-droplet-rich zone. Right column: close-up of relict olivine in orthopyroxene, pyrrhotite [Po] plus altered Fe and preserved Fe, and Fe-droplet-rich zone. TL-II: transmitted light micrograph with plane polarized light (ppl). TL-x: crossed polars. RL-II: reflected light micrograph with ppl.

2.36. FP94-4-5\_121.80 AQM-SEM



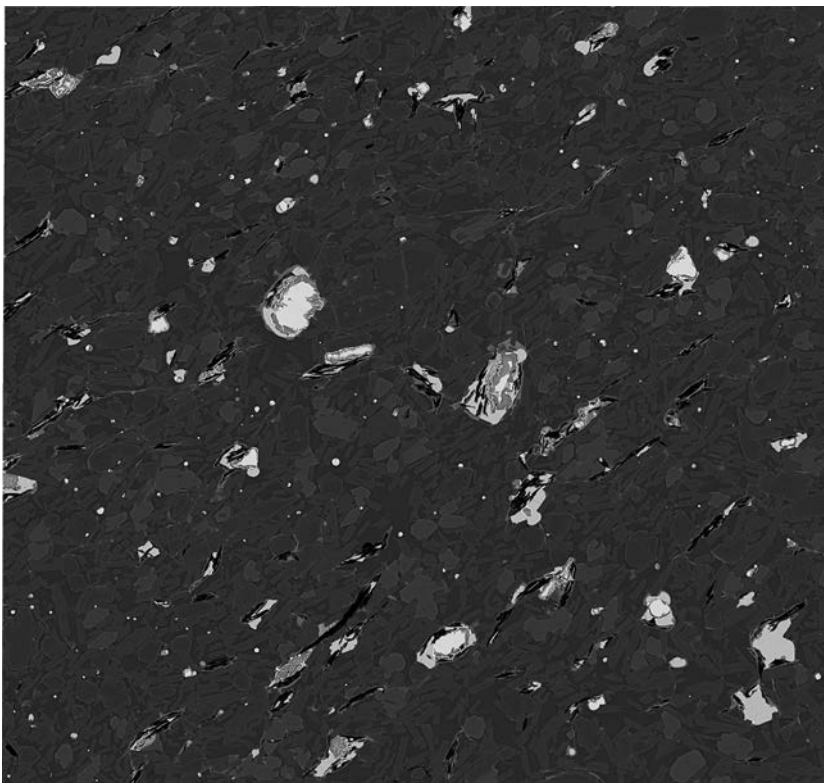
**Fig. 48.** Mineral map and corresponding BSE map of AQM-SEM analysis.

*Native iron with magnetite rim associated with pyrrhotite, graphite, and minor schreibersite.*

*Foliation/alignment indicated by larger orthopyroxene phenocrysts, plagioclase microlites, and graphite. Matrix with intersertal glass.*

*Image of thin-section, width 23 mm*

— 50  $\mu$ m

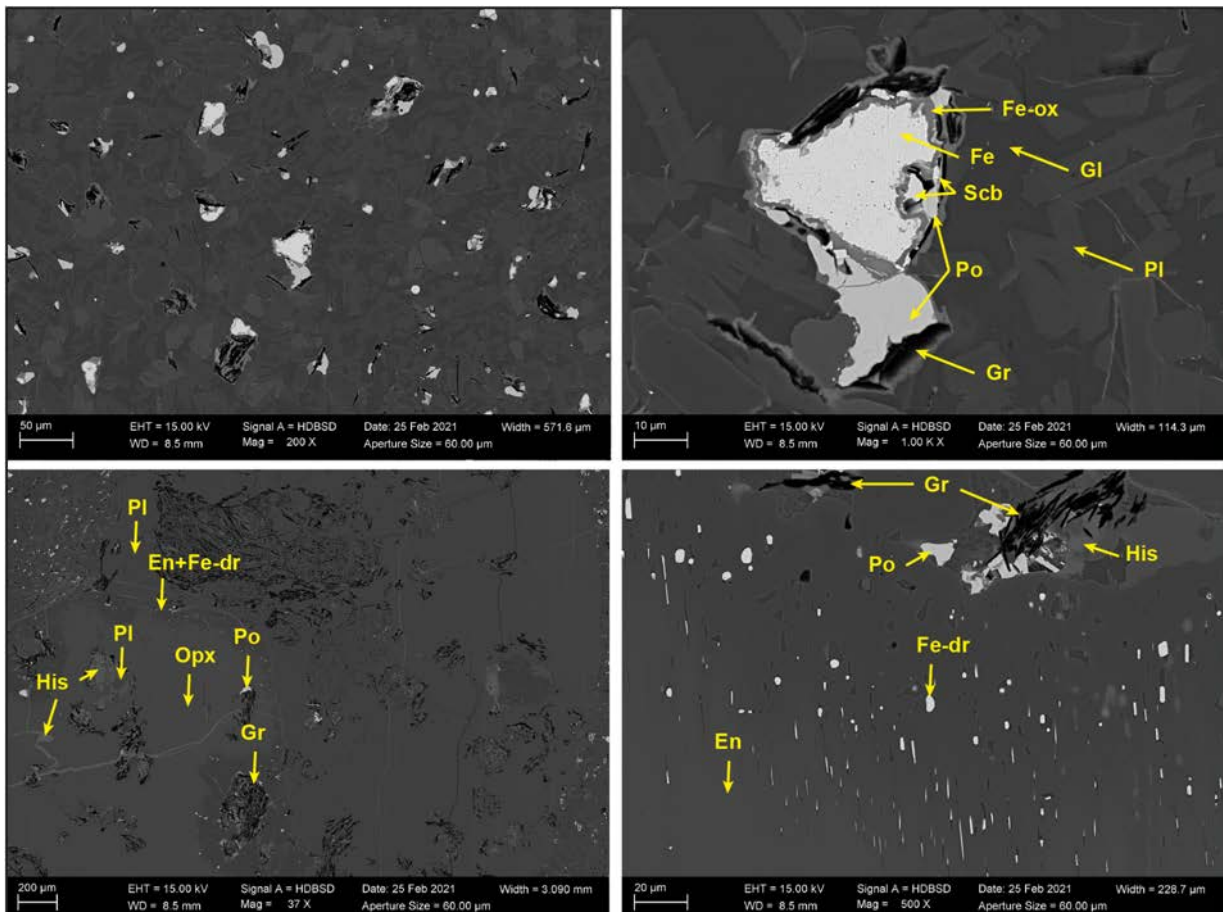


2.37. FP94-4-5\_126.30 Summary

Fine-crystalline basalt with up to few mm-sized orthopyroxene-plagioclase glomerocrysts, as well as ?plagioclase-filled amygdules and locally devitrified glass. Native iron with variably but minor oxidized rims, commonly with associated schreibersite, pyrrhotite, and graphite. Native Fe-droplets in the matrix are present, but less frequent than in samples stratigraphically above. Graphite occurs with the sulphides/native Fe and as larger aggregates. Plagioclase phenocrysts are oscillatory zoned and twinned. Orthopyroxene have an outer zone rich in Fe-droplets.

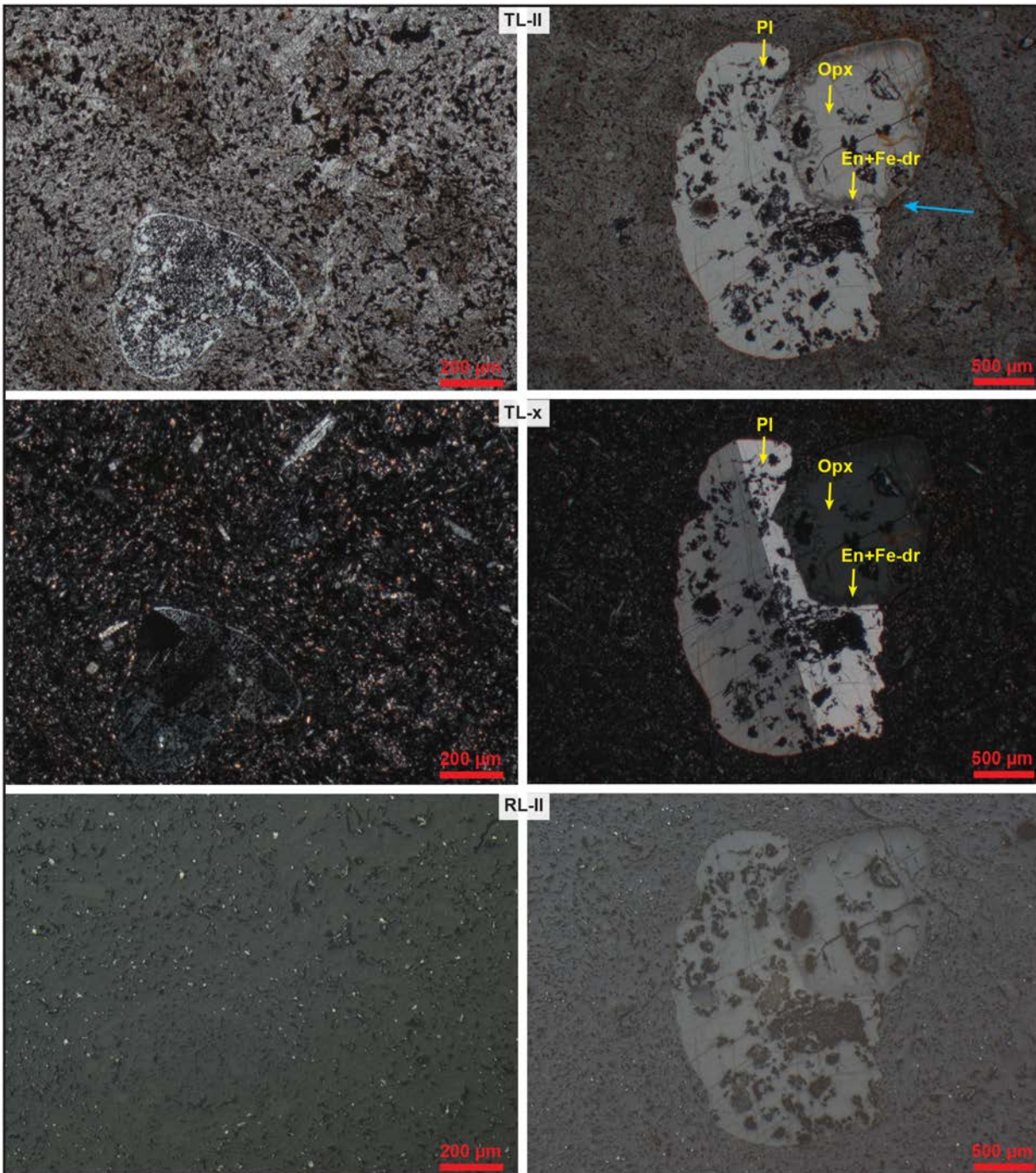
The matrix consists of plagioclase microlite laths, orthopyroxene, and diopside with intersertal siliceous K-bearing glass. Possible palagonite occurs as rusty brown-orangy patches and alteration haloes around phenocrysts extending into groundmass. Graphite commonly is coating the native Fe and pyrrhotite, with minor hisingerite.

2.38. FP94-4-5\_126.30 SEM-BSE/EDS

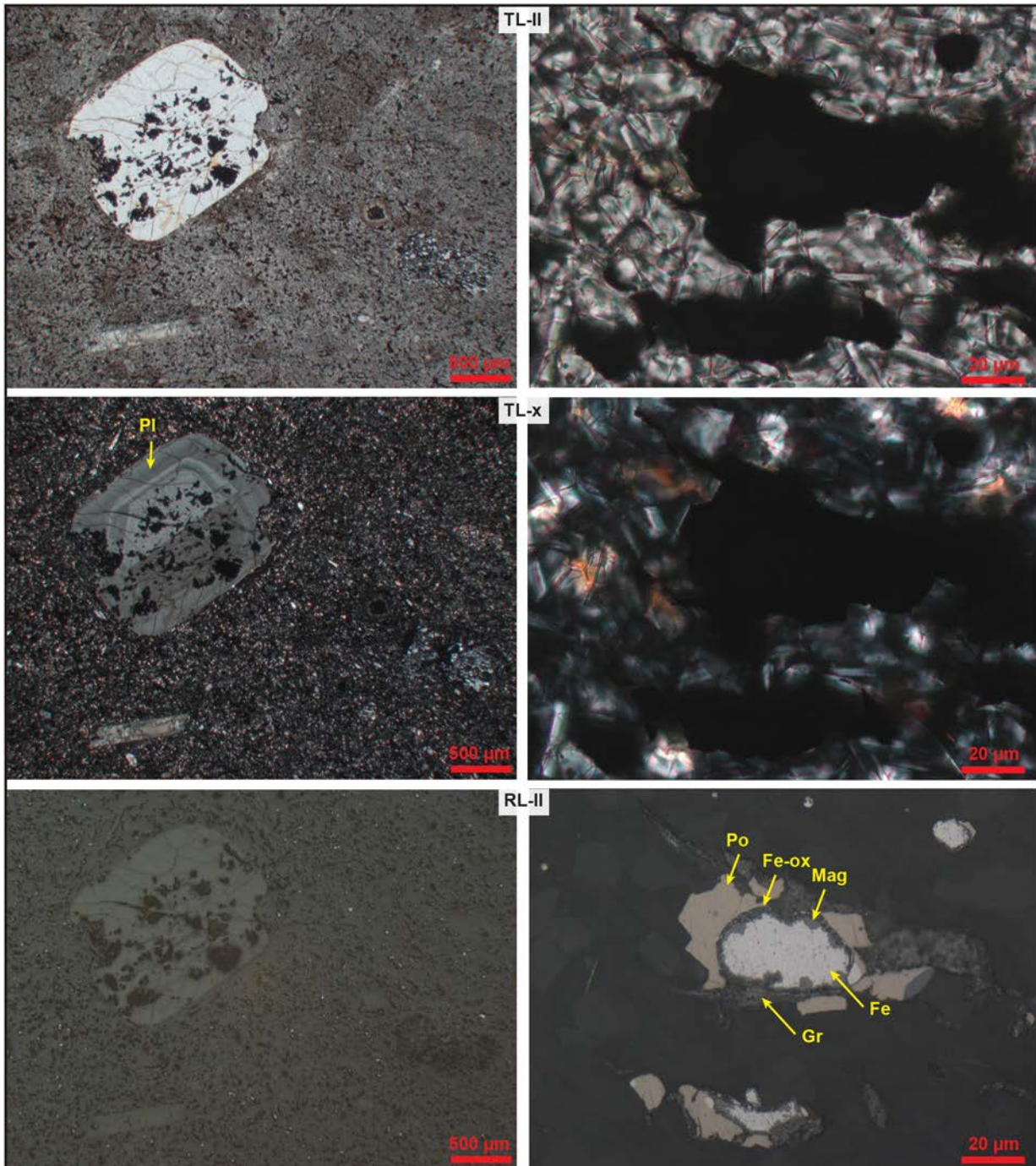


**Fig. 49.** Backscatter electron (BSE) micrographs. Upper row: Abundant disseminated aggregates of native Fe, graphite [Gr], pyrrhotite [Po], and very minor amounts of micron/sized native Fe-droplet in matrix. Native iron with oxidized rim and second rim of Fe+schreibersite [Scb] and associated with pyrrhotite and graphite. Graphite associated with minor hisingerite [His]. Bottom row: Glomerocryst of plagioclase [PI] and orthopyroxene [Opx] (shown in following optical microscope micrograph) with abundant graphite enclaves. Orthopyroxene with an enstatite [En]-composition rim rich in Fe-droplets.

2.39. FP94-4-5\_126.30 Microscopy

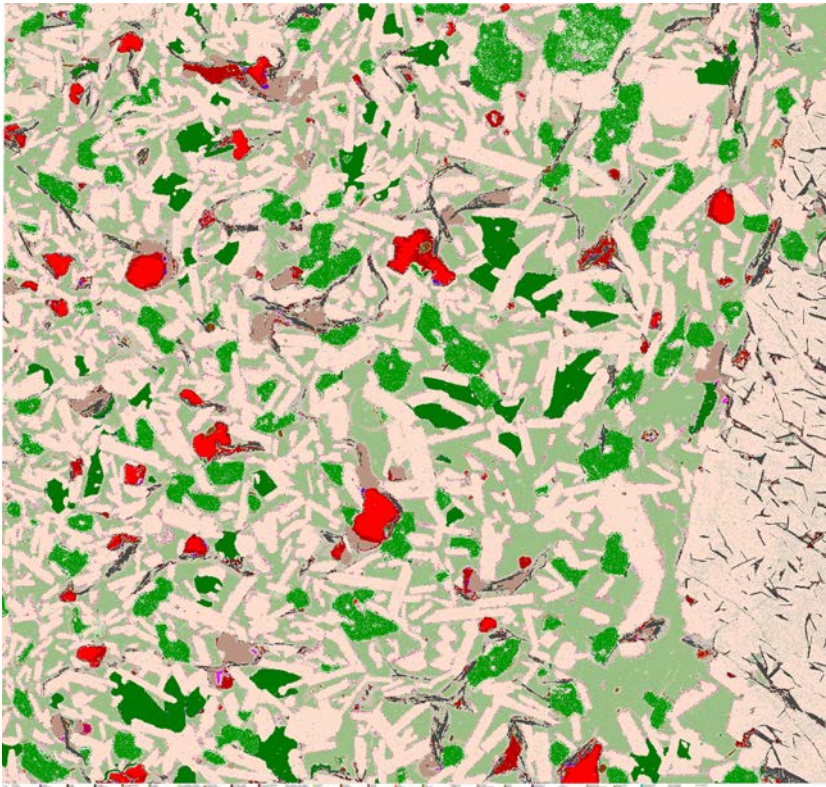


**Fig. 50.** Left column: Large ?plagioclase-filled amygdale. Right column: Large orthopyroxene [Opx] and plagioclase [Pl] glomerocryst with solution embayments. Blue arrow indicates section shown in previous BSE micrograph. Orthopyroxene with enstatite [En] rim rich in Fe-droplets. TL-II: transmitted light micrograph with plane polarized light (ppl). TL-x: crossed polars. RL-II: reflected light micrograph with ppl.



**Fig. 51.** Left column: Large plagioclase [Pl] phenocryst with oscillatory zoning and twinning and solution embayments. Right column: Native iron with magnetite [Mag] rim and association with schreibersite [Scb], pyrrhotite [Po], and graphite [Gr].  
 TL-II: transmitted light micrograph with plane polarized light (ppl). TL-x: crossed polars. RL-II: reflected light micrograph with ppl.

2.40. FP94-4-5\_126.30 AQM-SEM

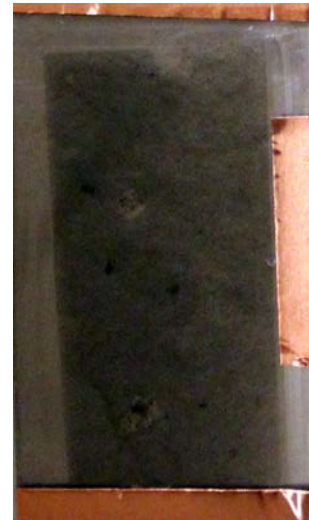


**Fig. 52.** Mineral map and corresponding BSE map of AQM-SEM analysis.

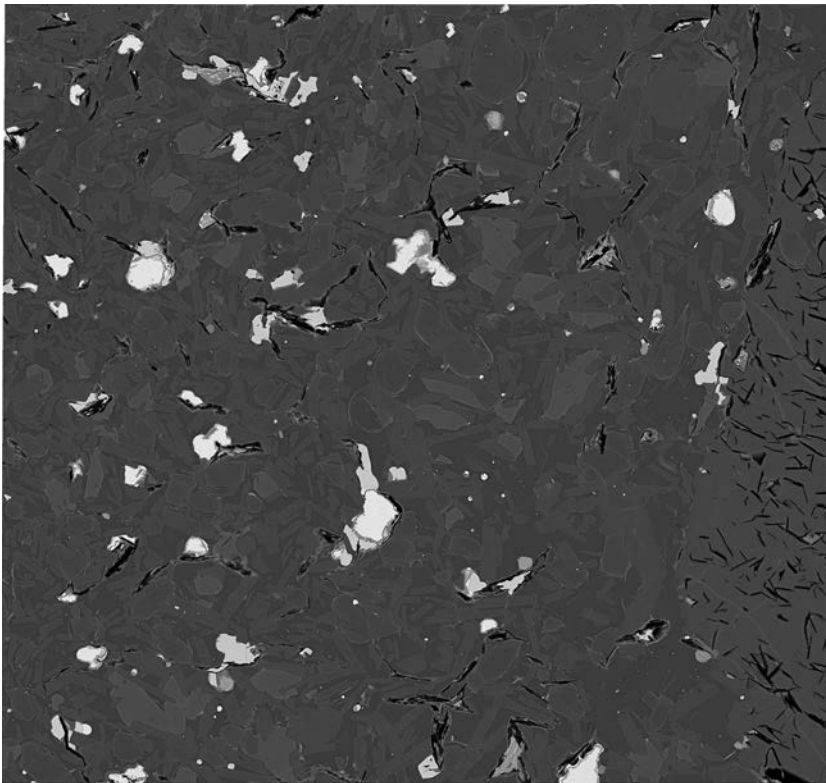
*Native iron with oxidized rim associated with pyrrhotite, graphite, and minor schreibersite.*

*Right hand side: graphite-rich devitrified glass. Matrix with plagioclase microlites, diopside, and intersertal glass.*

*Image of thin-section, width 23 mm*



— 50 µm

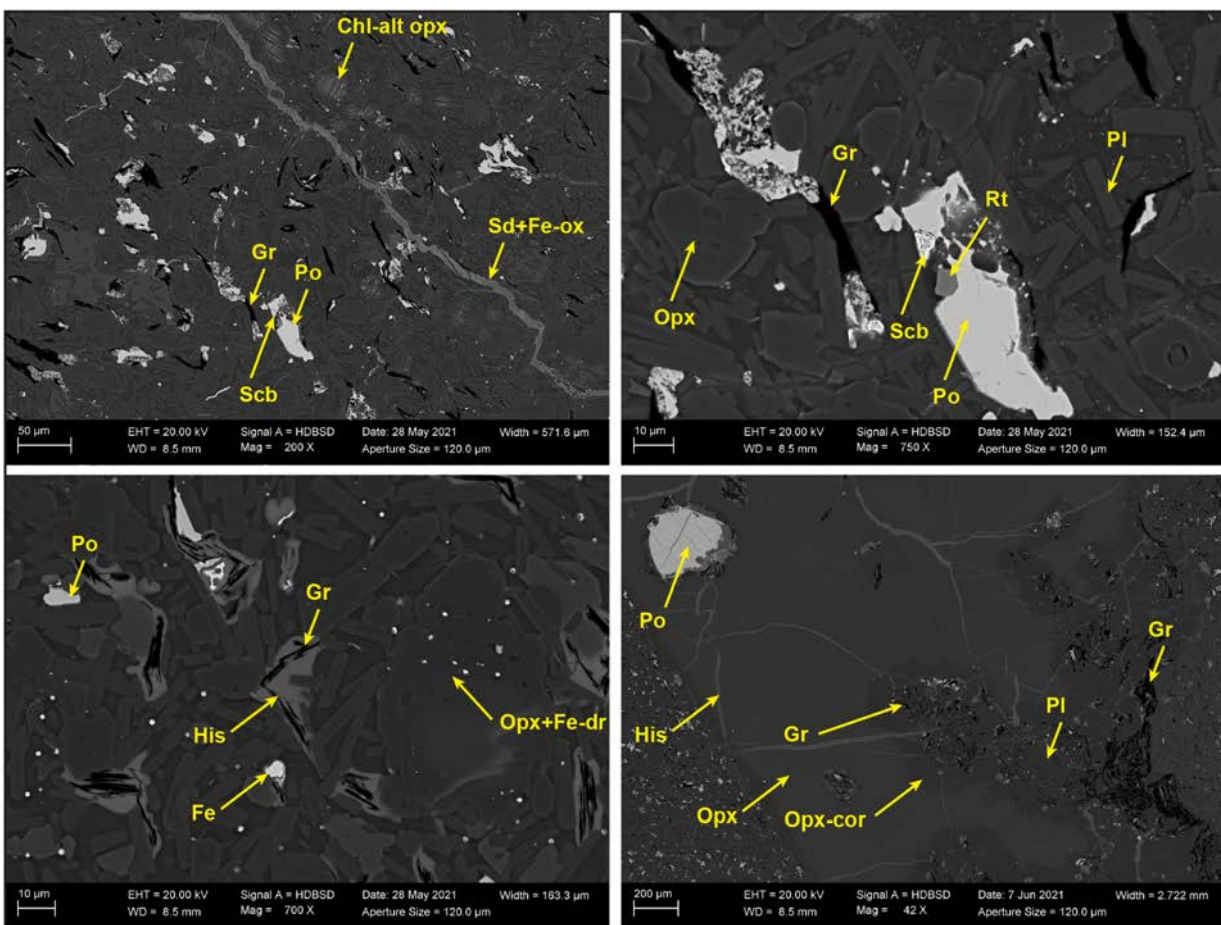


2.41. FP94-4-5\_127.45 Summary

Strongly fractured fine-crystalline basalt with tens of  $\mu\text{m}$ -sized pyrrhotite+graphite aggregates and up to several mm-sized orthopyroxene phenocrysts and glomerocrysts. Very minor preserved native iron. Pyrrhotite locally with pentlandite flames and Fe-Ni-phosphides, such as., e.g., schreibersite.

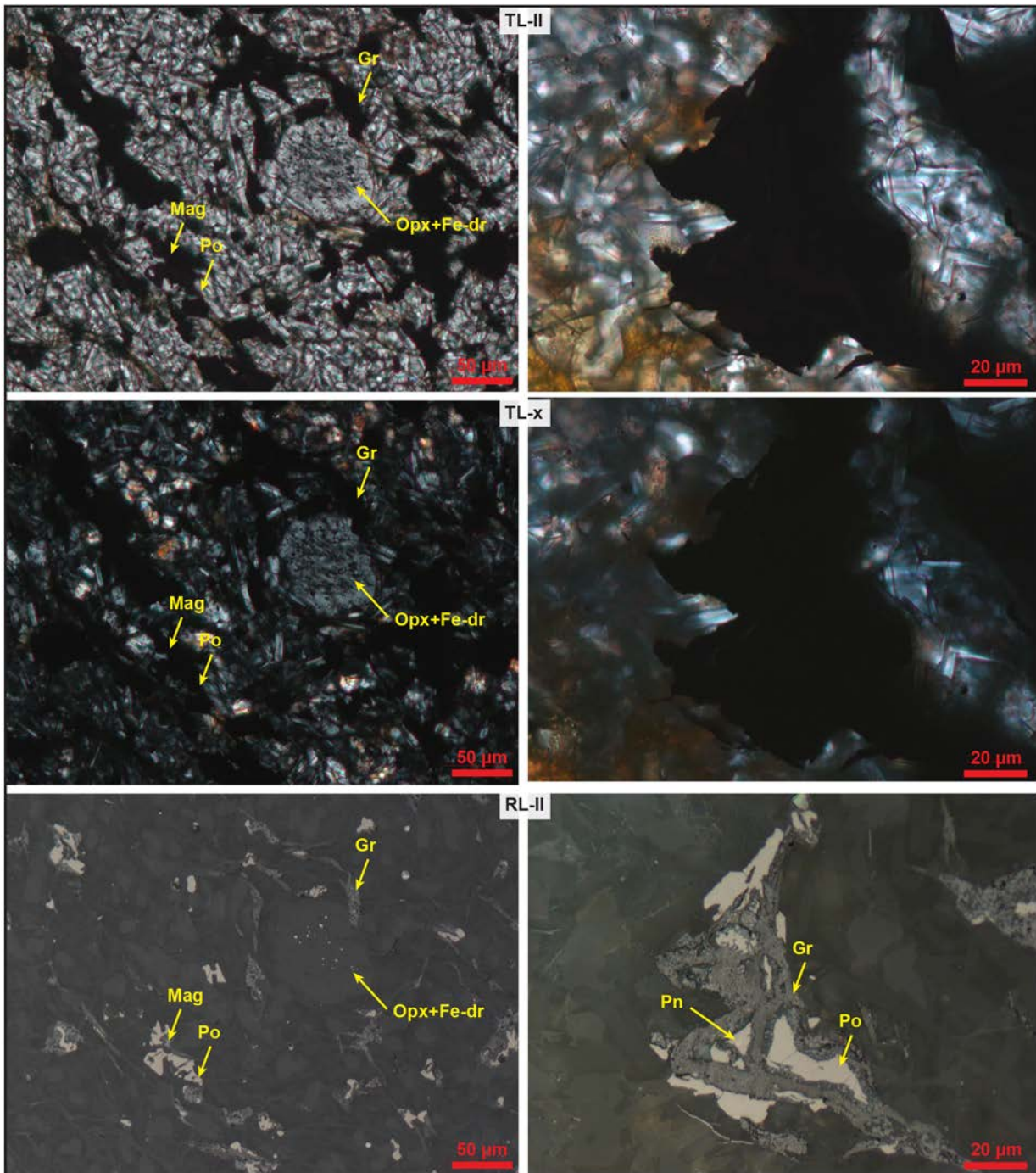
The matrix consists of plagioclase microlite laths, Fe-Mg-chlorite-altered orthopyroxene, and diopside with intersertal siliceous glass. Graphite occurs with the sulphides. Graphite is commonly is coated in/associated with a Fe-siliceous phase (hisingerite). Large orthopyroxene phenocrysts with secondary orthopyroxene coronas around graphite-rich clusters and cross-cut by hisingerite veinlets. Conjugate sets of joints cross-cutting rock and filled with siderite and locally Fe-oxide. Fe-phases also extend into groundmass.

2.42. FP94-4-5\_127.45 SEM-BSE/EDS



**Fig. 53.** Backscatter electron (BSE) micrographs. Disseminated aggregates of pyrrhotite [Po], graphite [Gr], and minor schreibersite [Scb] in a matrix of plagioclase [Pl] microlites, orthopyroxene [Opx], and diopside [Di]. Fracture filled with siderite [Sd] and Fe-oxide. Orthopyroxene locally with Fe-droplets. Graphite associated with hisingerite [His]. Hisingerite also in veinlets in large orthopyroxene phenocryst. Bottom right also shown on next page.

2.43. FP94-4-5\_127.45 Microscopy

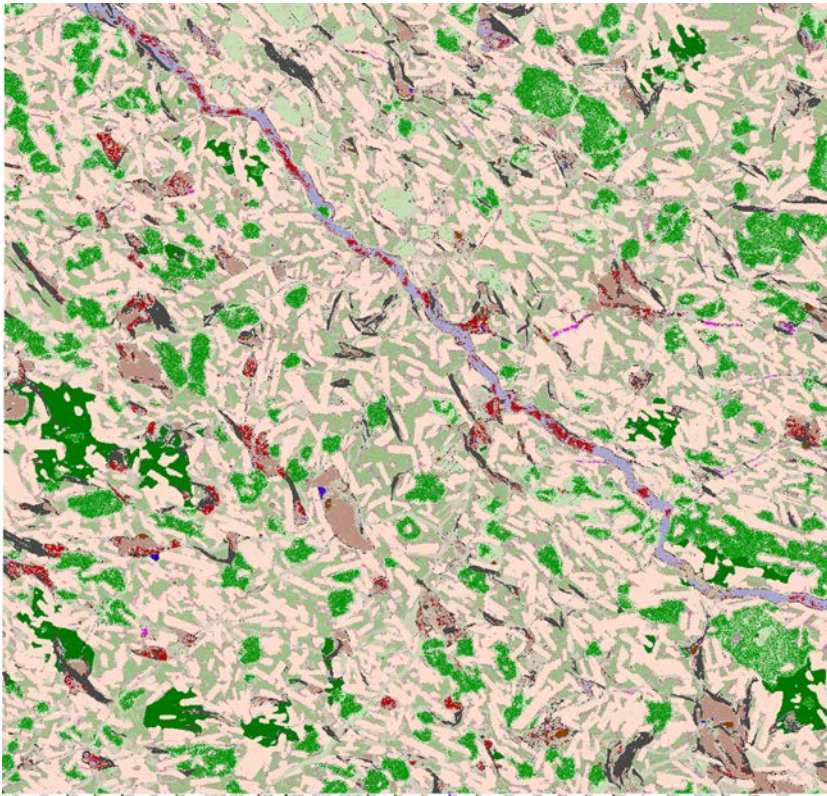


**Fig. 54.** Left column: Pyrrhotite [Po] associated with Fe-oxide and graphite [Gr] and orthopyroxene [Opx] phenocryst with Fe-droplets. Right column: Close-up of pyrrhotite-graphite aggregate in association with pentlandite [Pn]. Matrix with rusty-brown orange altered orthopyroxene, plagioclase [P], and insertal glassy matrix [G].

TL-II: transmitted light micrograph with plane polarized light (ppl). TL-x: crossed polars. RL-II: reflected light micrograph with ppl.



2.44. FP94-4-5\_127.45 AQM-SEM

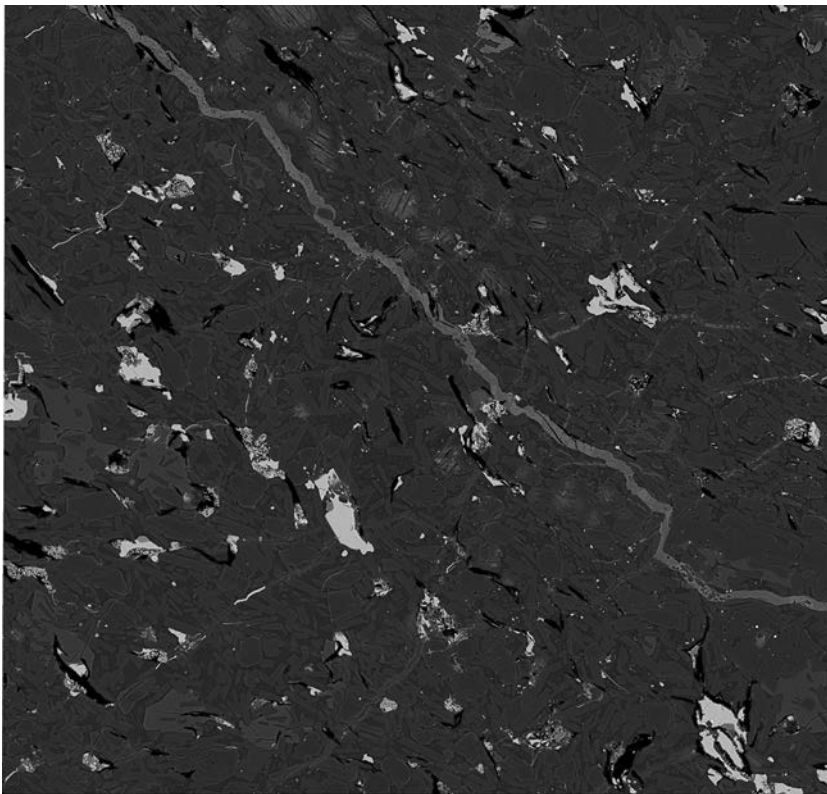


**Fig. 55.** Mineral map and corresponding BSE map of AQM-SEM analysis.

*Iron oxide in association with pyrrhotite and locally with schreibersite. Siderite, Fe-oxide, and minor graphite fill fractures. Matrix consists predominantly of euhedral to subhedral crystals of plagioclase, orthopyroxene, minor anhedral clinopyroxene with intersertal K-rich siliceous glass. Moderate to minor amounts of small Fe-droplets disseminated in matrix. Orthopyroxene chlorite-altered near fracture. Fracture is part of a set of conjugate joints.*

*Image of thin-section, width 23 mm*

50 μm

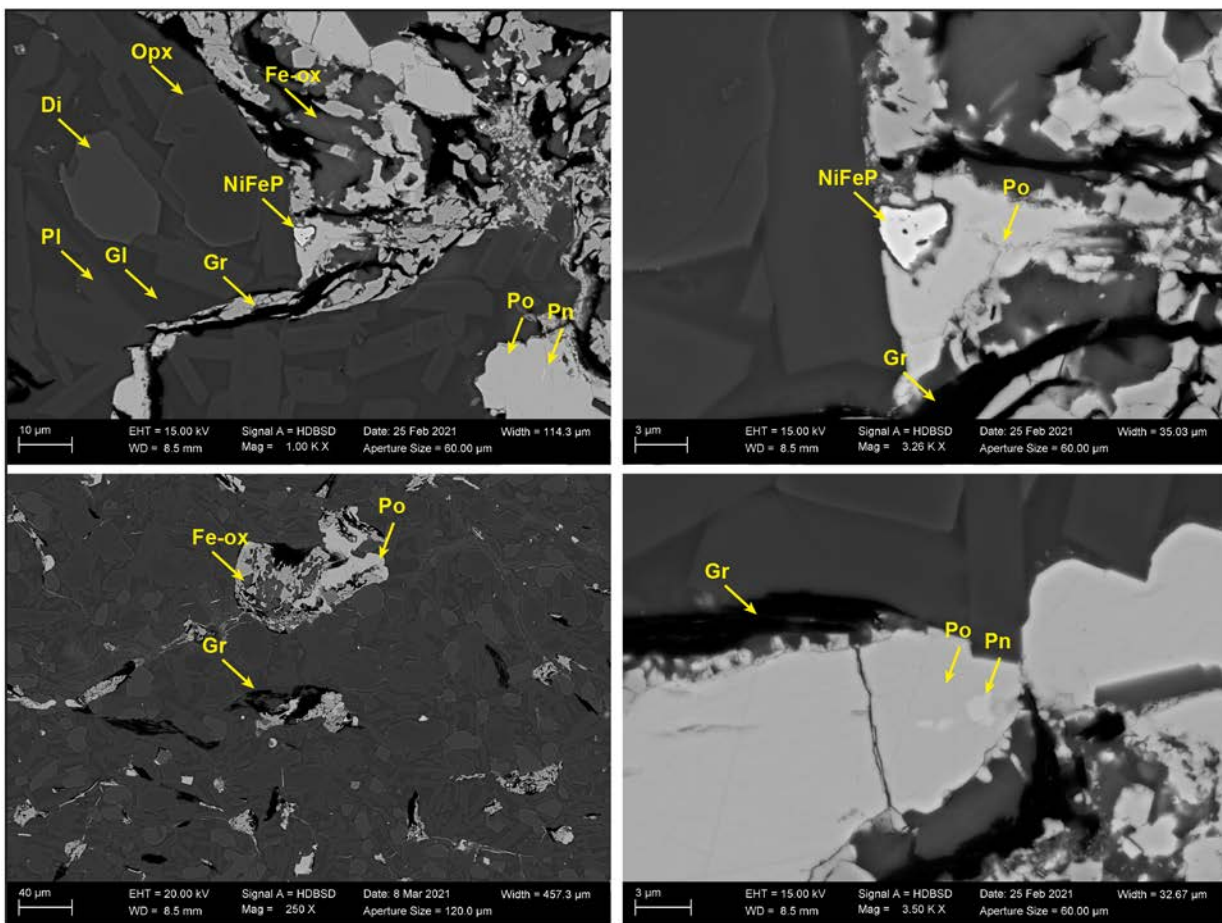


2.45. FP94-4-5\_127.98 Summary

Foliated/sheared fine-crystalline basalt with tens of  $\mu\text{m}$ -sized pyrrhotite-graphite aggregates and up to several mm-sized glass-filled amygdules and orthopyroxene phenocrysts and glomerocrysts. No or very minor preserved native iron. Pyrrhotite locally with Cu-sulphides (chalcopyrite, cubanite) and pentlandite flames and Ni-rich Ni-Fe-phosphides, minor schreibersite.

The matrix consists of plagioclase microlite laths, Fe-Mg-chlorite-altered orthopyroxene, and diopside with intersertal K-rich siliceous glass. Graphite occurs with the sulphides. Graphite is commonly is not associated with hisingerite. Large orthopyroxene phenocrysts with undulose extinction. Plagioclase microlites and sulphides+graphite are aligned with the foliation.

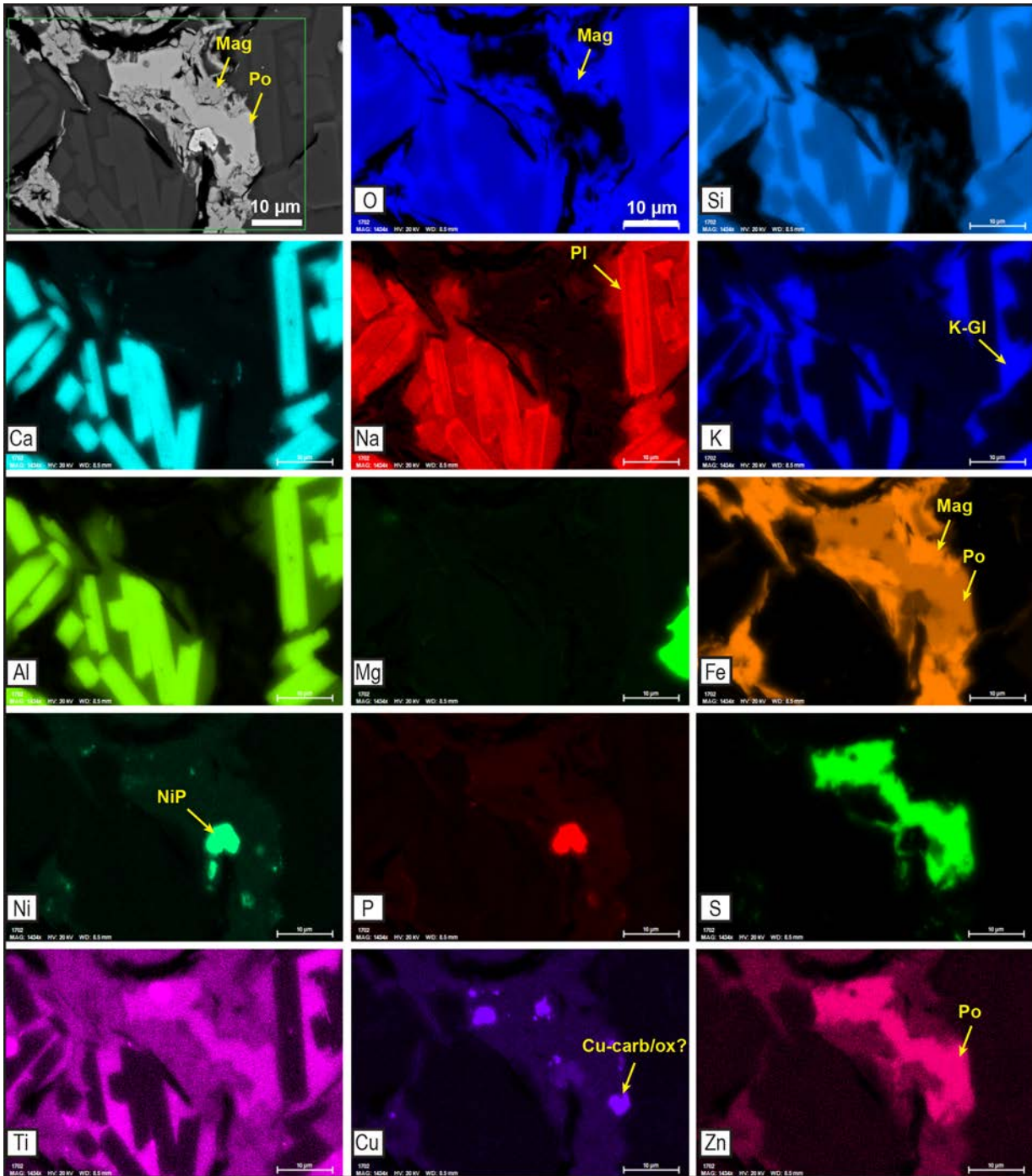
2.46. FP94-4-5\_127.98 SEM-BSE/EDS



**Fig. 56.** Backscatter electron (BSE) micrographs. Foliated and bent aggregates of pyrrhotite [Po], graphite [Gr], Fe-oxide and an Ni-rich Ni-Fe-phosphide [NiFeP] in a matrix of plagioclase [Pl] microlites, orthopyroxene [Opx], and diopside [Di] and intersertal K-rich siliceous glass [Gl]. Pyrrhotite commonly contains pentlandite [Pn] flames.

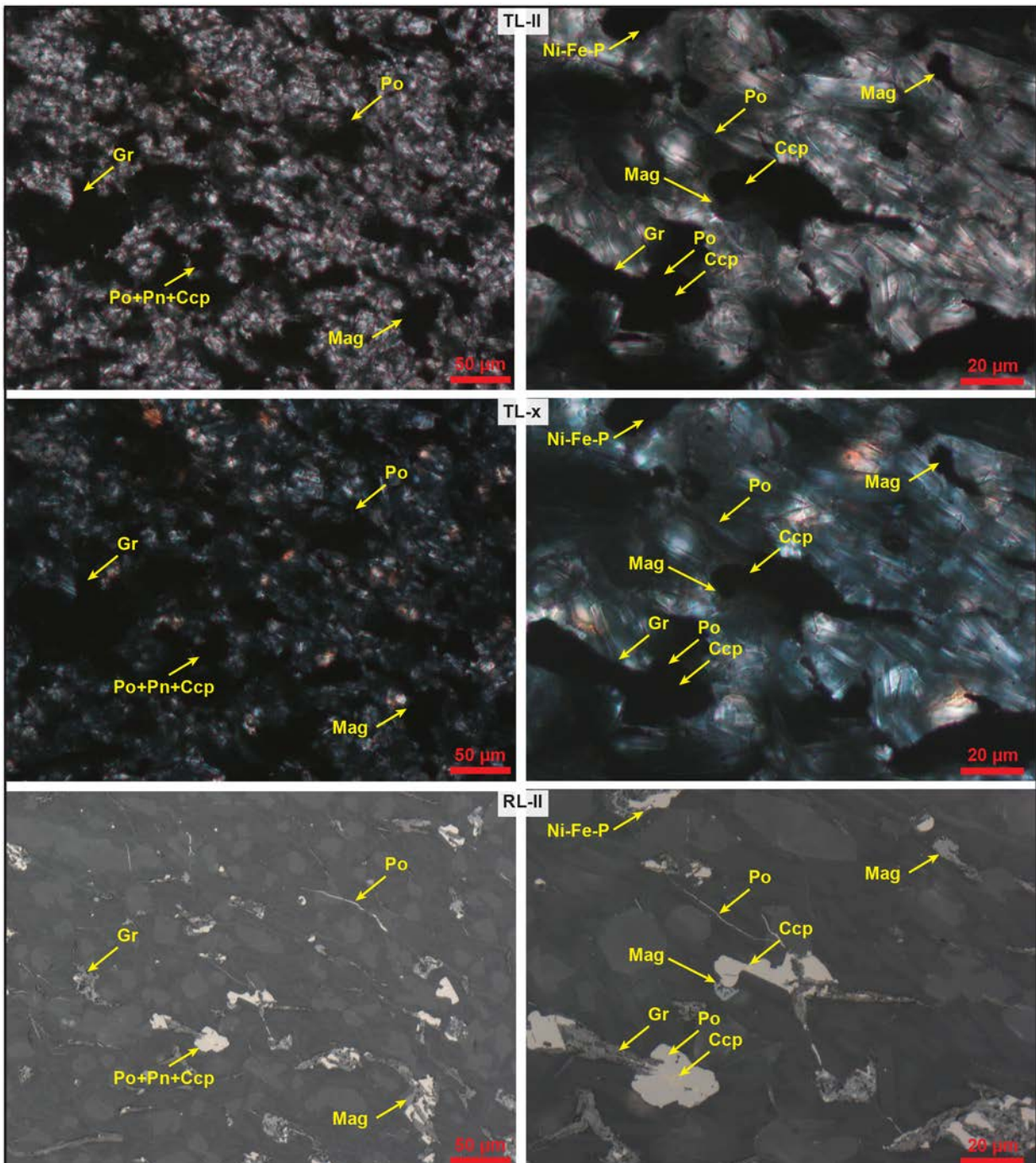
FP94-4-5\_127.98

SEM-EDS element map

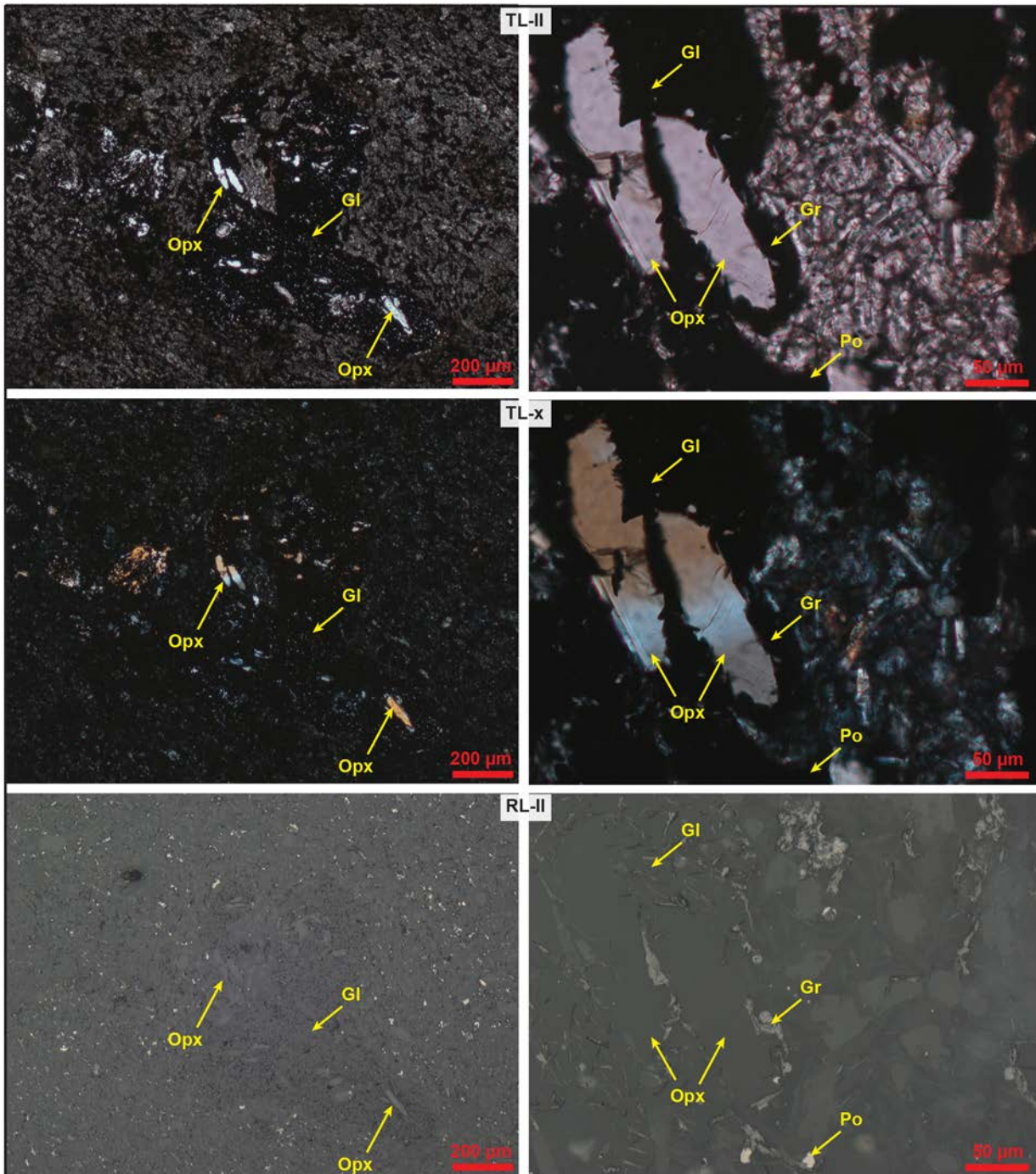


**Fig. 57.** Element maps to illustrate the association of pyrrhotite [Po], magnetite [Mag], Ni-rich Ni-Fe-phosphide [NiP] and pentlandite [Pn]. Associated with pyrrhotite+magnetite is a Cu-phase (carbonate or oxide). Plagioclase [Pl] microlites show an oscillatory zonation in the Na-content. Insertal glass is K-rich and siliceous [K-Gl].

2.47. FP94-4-5\_127.98 Microscopy

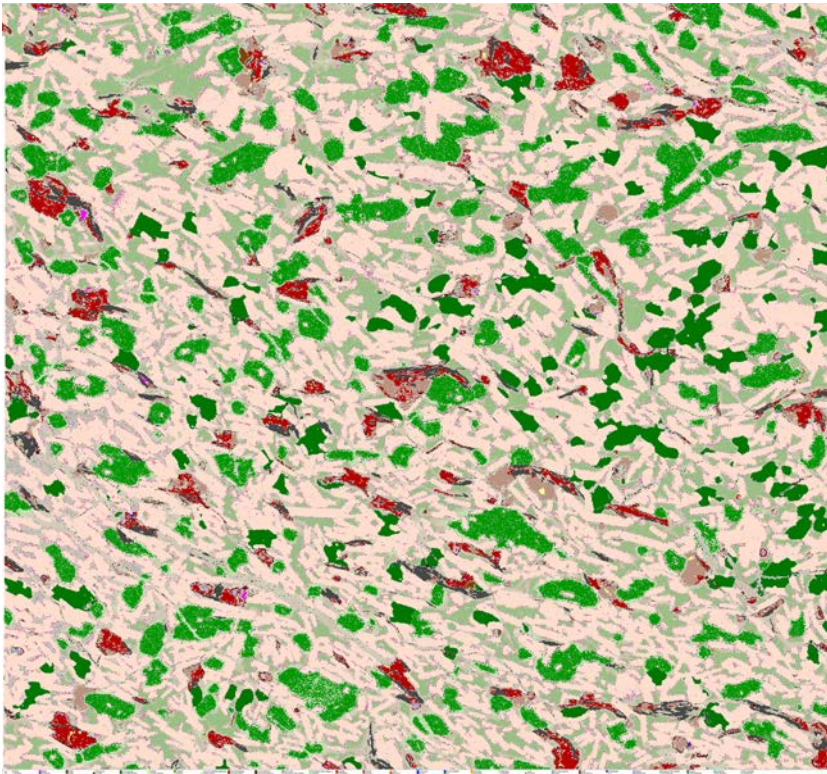


**Fig. 58.** Pyrrhotite [Po] associated with magnetite [Mag] and graphite [Gr]. Pyrrhotite commonly with pentlandite [Pn] flames, chalcopyrite [Ccp] inclusions, and locally associated with Ni-Fe-phosphide [NiFeP]. TL-II: transmitted light micrograph with plane polarized light (ppl). TL-x: crossed polars. RL-II: reflected light micrograph with ppl.



**Fig. 59.** Left column: Glass [Gl]-filled amygdule with orthopyroxene [Opx] and plagioclase [Pl] phenocrysts. Right column: Close-up of orthopyroxene phenocrysts with undulose extinction. Matrix consisting of intersertal glass [Gl].  
 TL-II: transmitted light micrograph with plane polarized light (ppl). TL-x: crossed polars. RL-II: reflected light micrograph with ppl.

2.48. FP94-4-5\_127.98 AQM-SEM

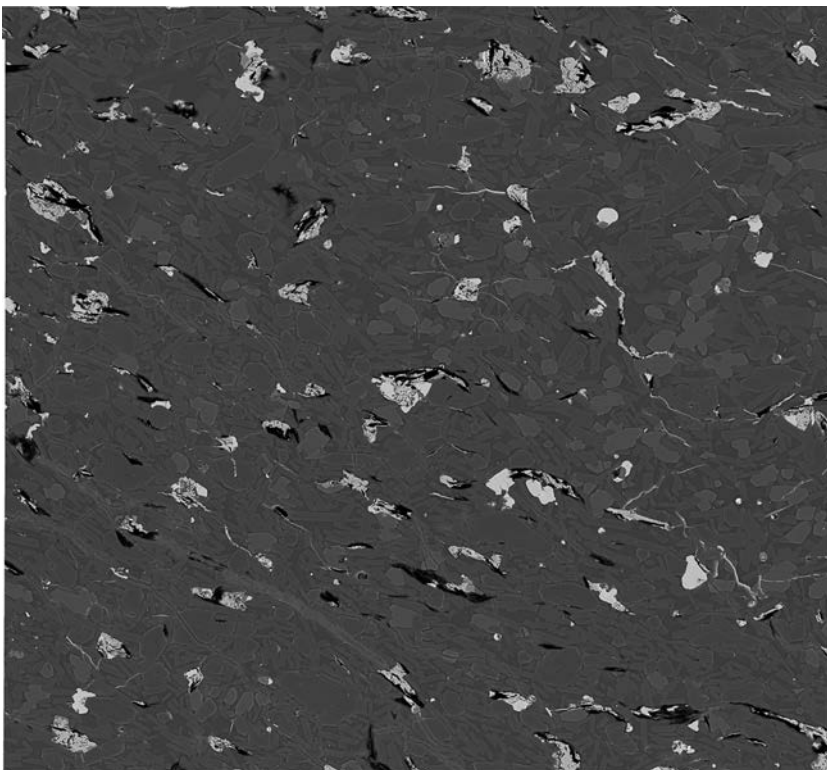


**Fig. 60.** Mineral map and corresponding BSE map of AQM-SEM analysis.

*Iron oxide in association with pyrrhotite and locally with Cu-sulphides and Ni-Fe-phosphides. Matrix consists predominantly of euhedral to subhedral crystals of plagioclase, orthopyroxene, minor anhedral clinopyroxene with intersertal K-rich siliceous glass. Plagioclase, sulphides, and graphite aligned to foliation.*

*Image of thin-section, width 23 mm*

50  $\mu$ m

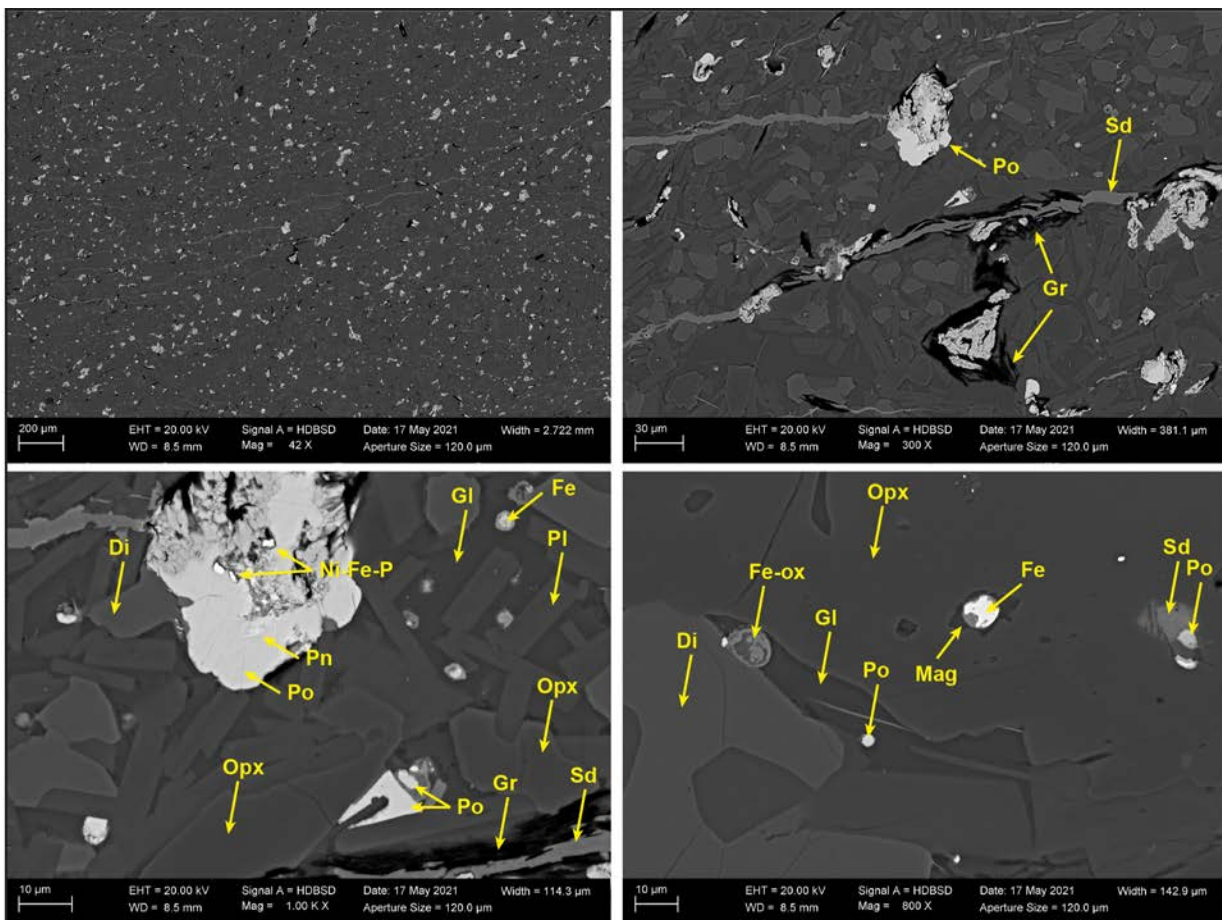


2.49. FP94-4-5\_131.60 Summary

Foliated/sheared fine-crystalline basalt with hundreds of  $\mu\text{m}$ - up to mm-sized orthopyroxene phenocrysts which commonly have an outer zone rich in Fe-droplets. Very minor preserved native iron, primarily as droplets in phenocrysts. Pyrrhotite locally with Ni-rich Ni-Fe-phosphides and Cu-sulphides (chalcopyrite, cubanite) and associated with magnetite and graphite.

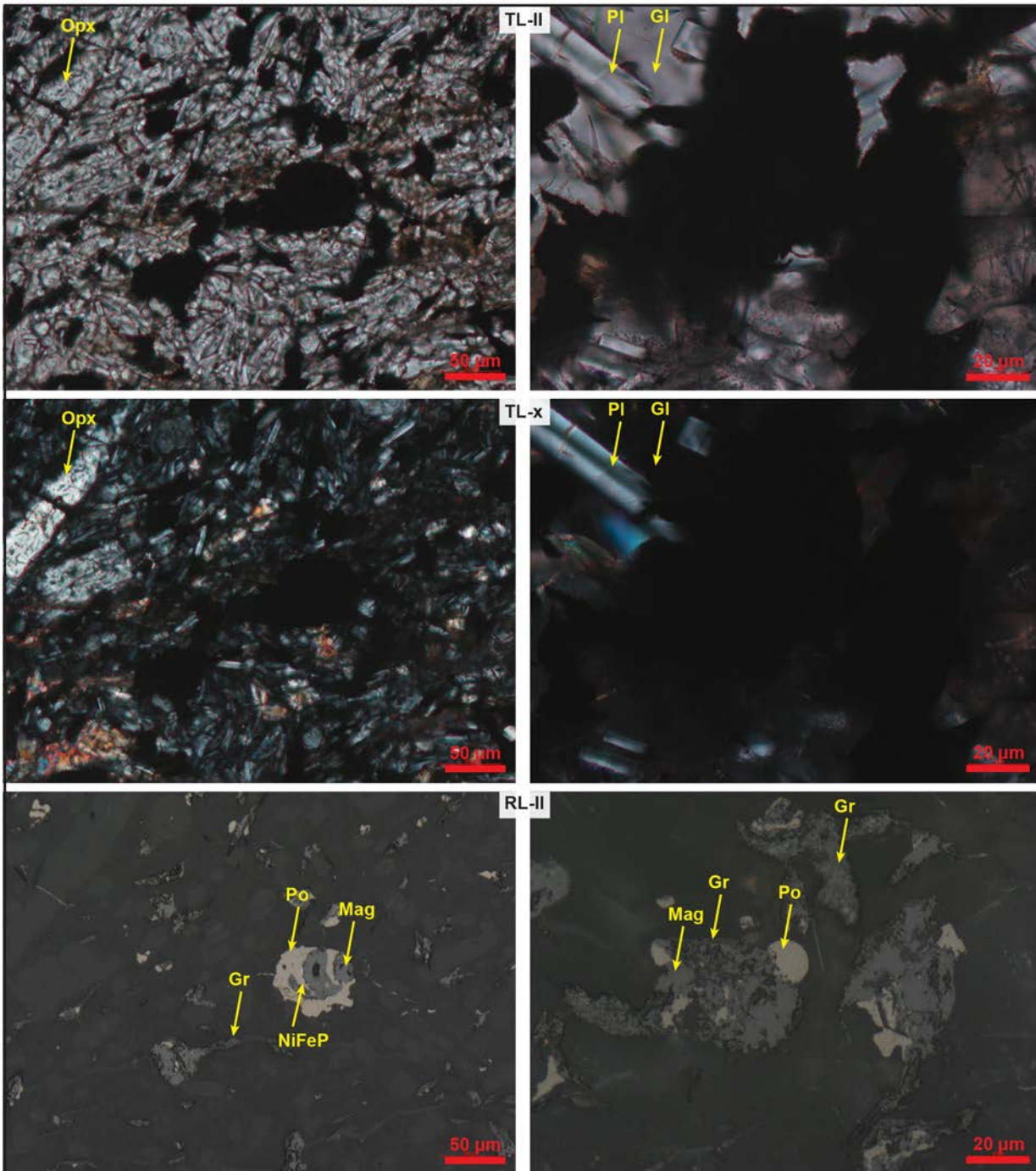
The matrix consists of plagioclase microlite laths, Fe-Mg-chlorite-altered orthopyroxene, and diopside with intersertal K-rich siliceous glass. Graphite occurs with the sulphides. As previous, graphite is not associated with hisingerite. Plagioclase microlites and sulphides-graphite aggregates are aligned with the foliation, shearing-related fractures locally with S-C-fabrics. Fractures filled with siderite and Fe-oxide.

2.50. FP94-4-5\_131.60 SEM-BSE/EDS



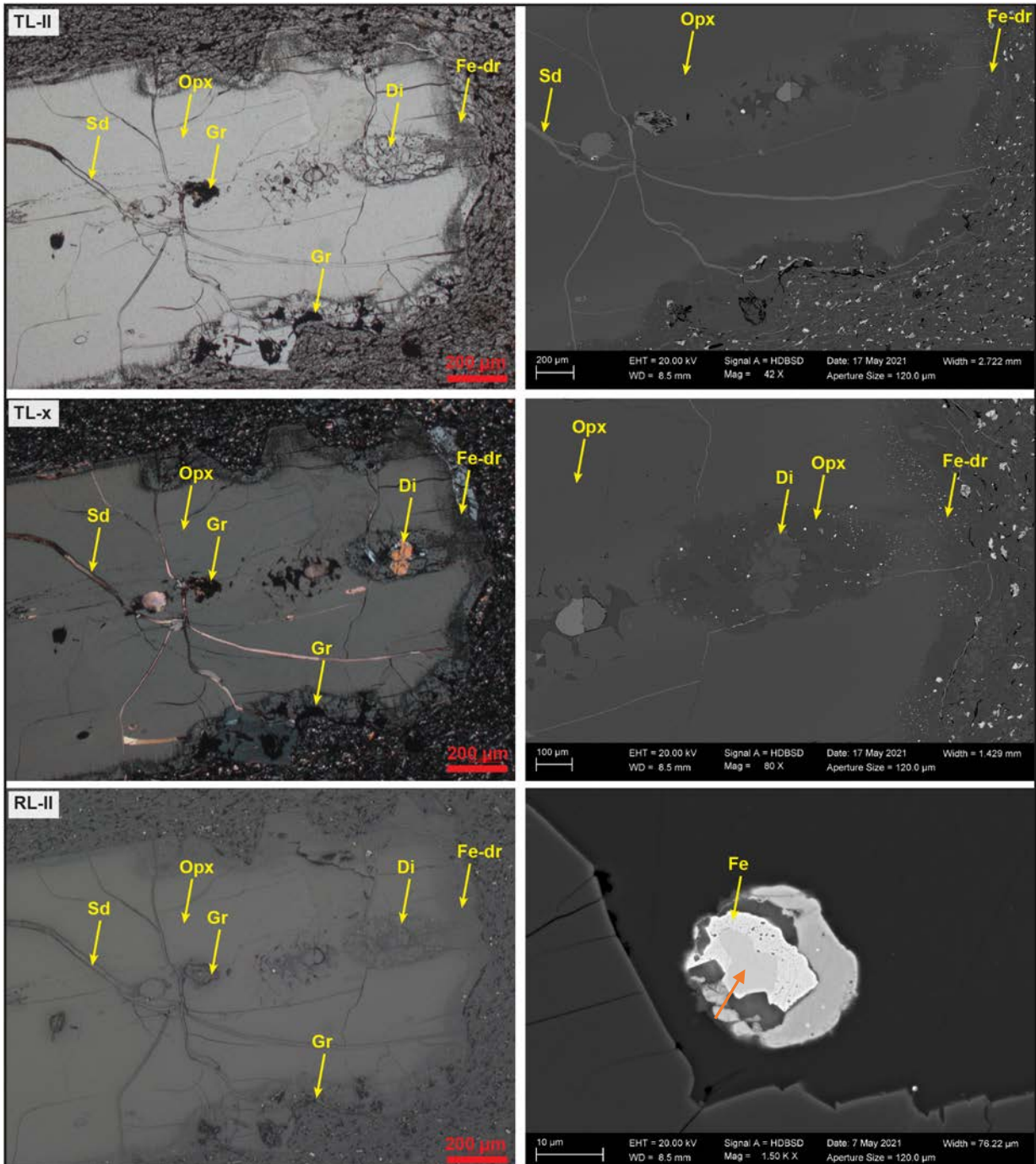
**Fig. 61.** Backscatter electron (BSE) micrographs. Siderite [Sd]-filled fractures in fine-crystalline basalt with pyrrhotite [Po], graphite [Gr], Fe-oxide aggregates that are associated with Ni-rich Ni-Fe-phosphide [NiFeP] in a matrix of plagioclase [Pl] microlites, orthopyroxene [Opx], and diopside [Di] and intersertal K-rich siliceous glass [Gl]. Pyrrhotite commonly contains pentlandite [Pn] flames. Graphite draping pyrrhotite and siderite. Bottom right: Fe-droplet in large orthopyroxene phenocryst.

2.51. FP94-4-5\_131.60 Microscopy



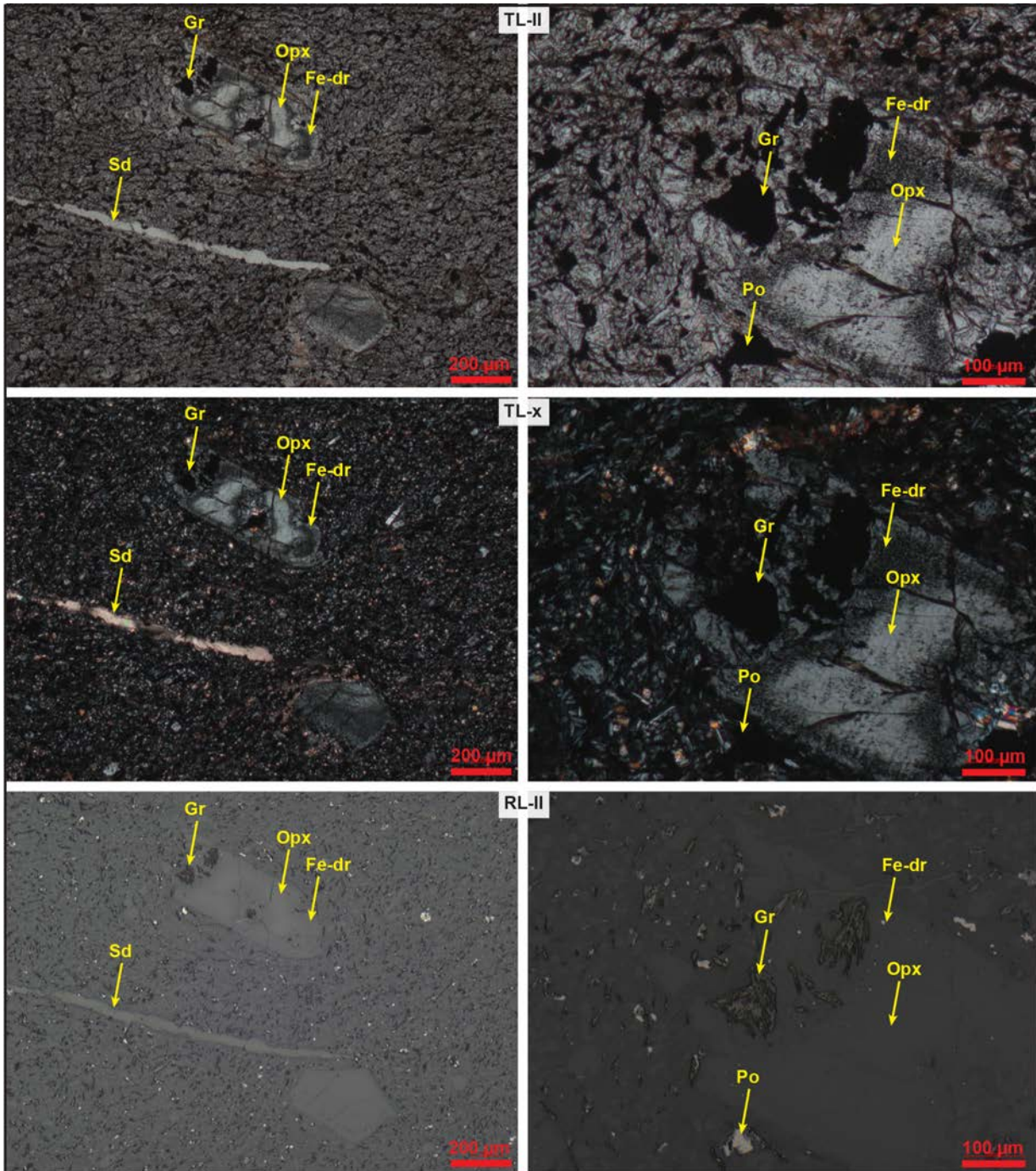
**Fig. 62.** Pyrrhotite [Po] associated with magnetite [Mag] and graphite [Gr]. Pyrrhotite with chalcopyrite [Ccp] inclusions and locally associated with Ni-Fe-phosphide [NiFeP]. Orthopyroxene [Opx] and plagioclase [Pl] in a K-rich siliceous glass [Gl] matrix.  
 TL-II: transmitted light micrograph with plane polarized light (ppl). TL-x: crossed polars. RL-II: reflected light micrograph with ppl.





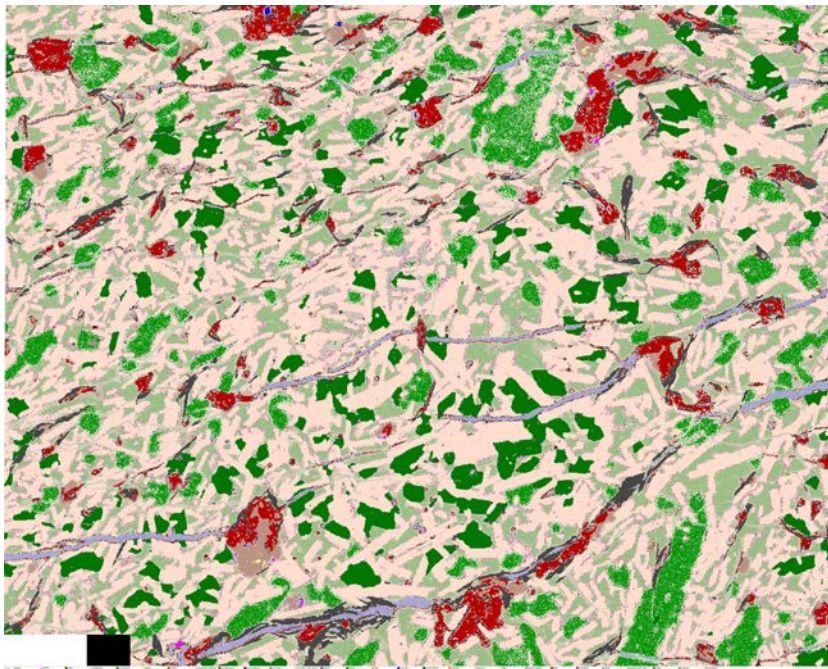
**Fig. 63.** Large orthopyroxene [Opx] phenocryst with solution embayments and with an Fe-droplet-rich outer zone and graphite [Gr] aggregates and Fe-droplets in central area. Phenocryst cross-cut by siderite [Sd]-filled fractures. Bottom right: Native Fe with second 'cleaner' Fe phase, possibly representing cohenite (orange arrow).

TL-II: transmitted light micrograph with plane polarized light (ppl). TL-x: crossed polars. RL-II: reflected light micrograph with ppl. Right column: BSE micrographs.



**Fig. 64.** Large orthopyroxene [Opx] phenocryst with solution embayments and with an Fe-droplet-rich outer zone and graphite [Gr] aggregates and Fe-droplets in central area. Siderite [Sd]-filled fractures. TL-II: transmitted light micrograph with plane polarized light (ppl). TL-x: crossed polars. RL-II: reflected light micrograph with ppl.

2.52. FP94-4-5\_131.60 AQM-SEM

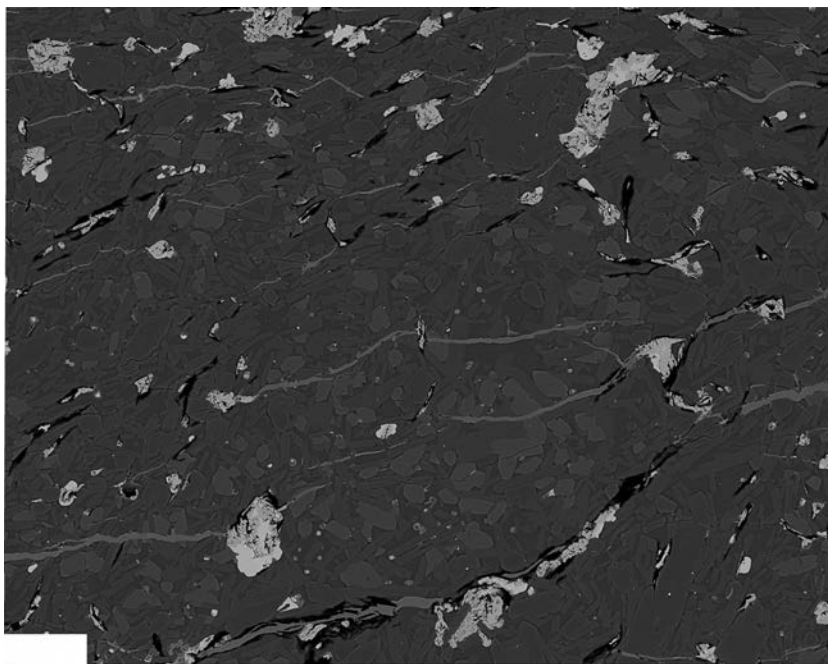


**Fig. 65.** Mineral map and corresponding BSE map of AQM-SEM analysis.

*Iron oxide in association with pyrrhotite and locally with Cu-sulphides and Ni-Fe-phosphides. Matrix consists predominantly of euhedral to subhedral crystals of plagioclase, orthopyroxene, minor anhedral clinopyroxene with intersertal K-rich siliceous glass. Plagioclase, sulphides, and graphite aligned to foliation. Siderite-filled fractures.*

*Image of thin-section, width 23 mm*

50 µm



### 2.53. FP94-4-5\_142.42 Summary

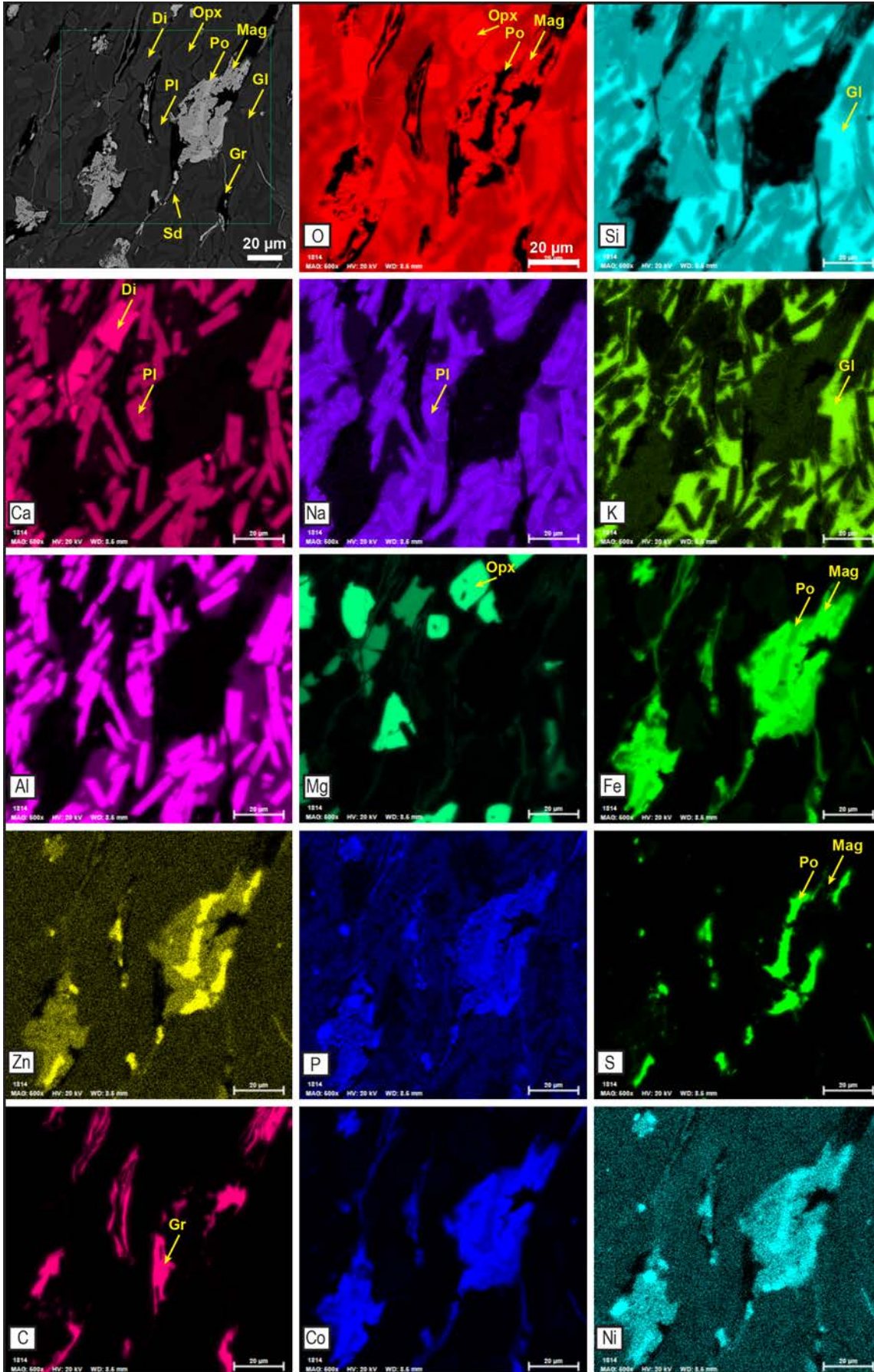
Foliated/sheared fine-crystalline basalt with hundreds of  $\mu\text{m}$ - up to mm-sized orthopyroxene and siderite-Fe-Mg-chlorite-altered olivine xenocryst. No or very minor preserved native iron. Pyrrhotite locally with Ni-rich Ni-Fe-phosphides and Cu-sulphides (chalcopyrite, cubanite) and associated with magnetite and graphite.

The matrix consists of plagioclase microlite laths, Fe-Mg-chlorite+siderite-altered orthopyroxene, and diopside with intersertal K-rich siliceous glass. Graphite occurs with the sulphides. As previous, graphite is not associated with hisingerite. Plagioclase microlites and sulphides+graphite are aligned with the foliation. Fractures filled with siderite and minor Fe-oxide.

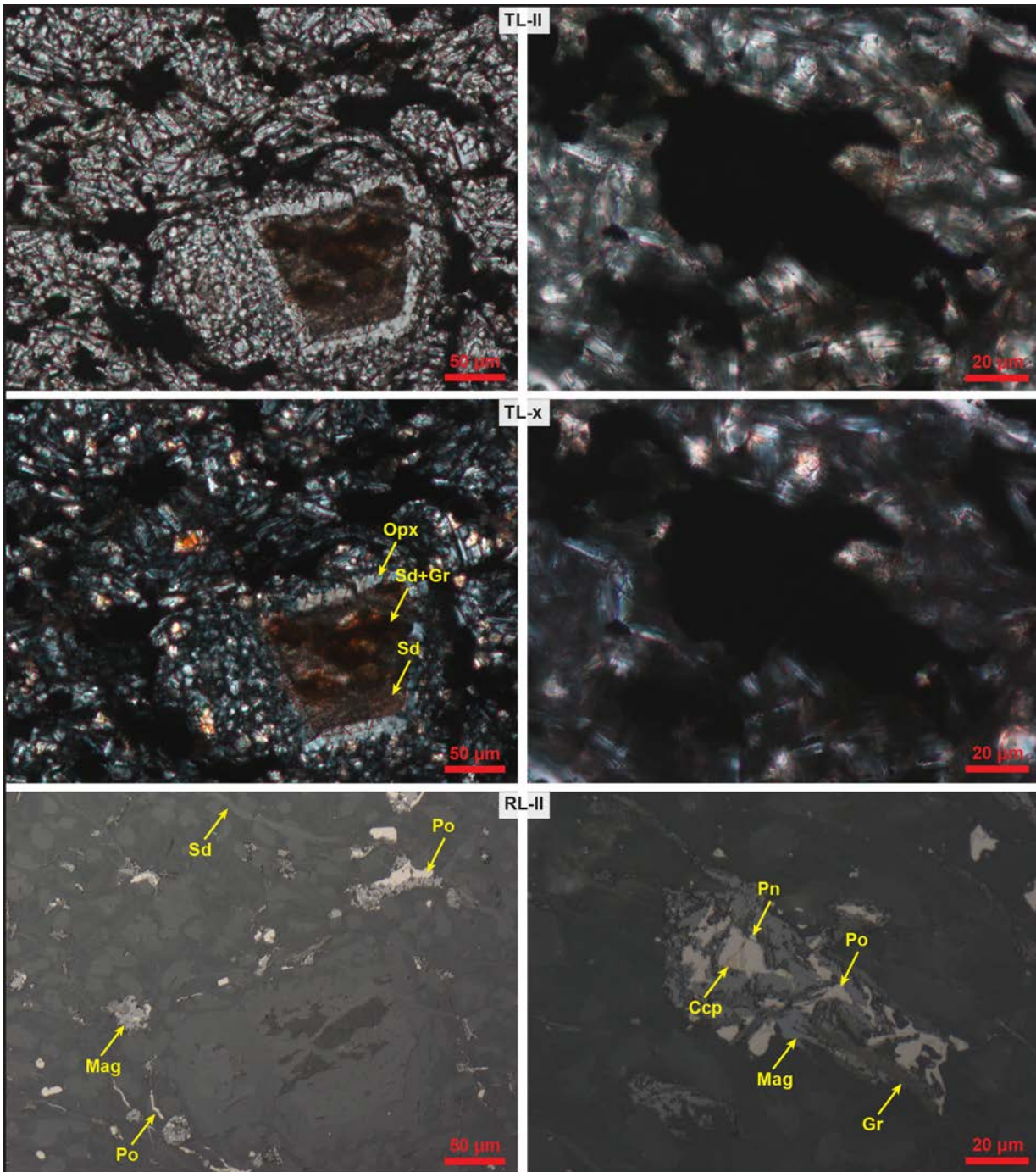
### 2.54. FP94-4-5\_142.42 SEM-BSE/EDS element map

See next page.

**Fig. 66.** Element maps to illustrate the association of pyrrhotite [Po], magnetite [Mag], and graphite [Gr], which are aligned to the foliation, as are diopside [Di] and orthopyroxene [Opx]. Plagioclase [Pl] microlites are also aligned and show a zonation in the Na-content. Intersertal glass is K-rich and siliceous [K-Gl]. Pyrrhotite contains traces of Ni and Zn, magnetite traces of Co. Siderite [Sd] associated with graphite.

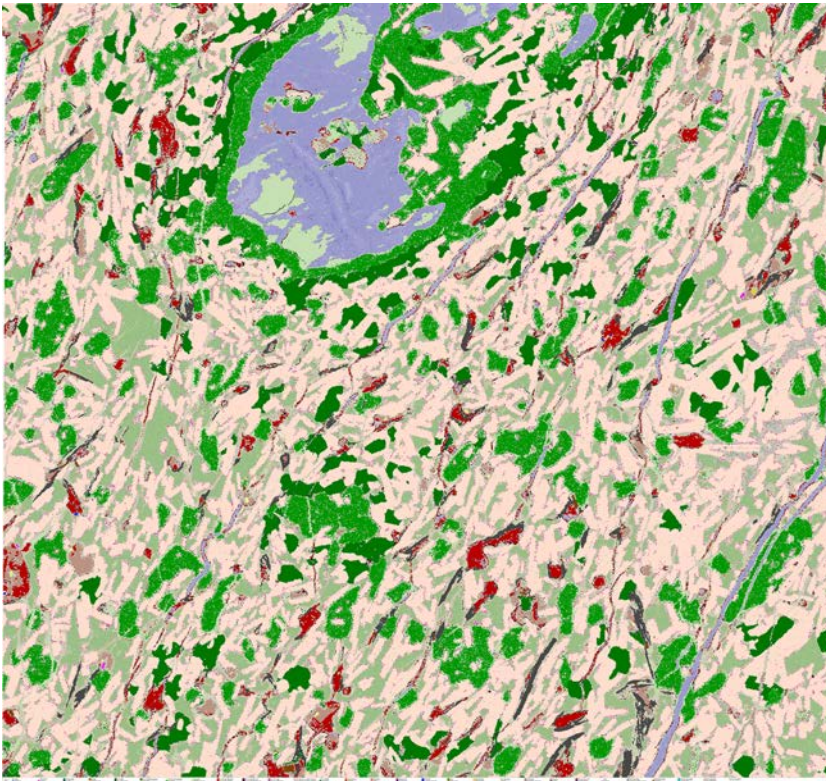


2.55. FP94-4-5\_142.42 Microscopy



**Fig. 67.** Left column: Siderite [Sd]+graphite [Gr]-altered olivine [Ol] phenocryst with orthopyroxene [Opx] corona. Magnetite [Mag] associated with pyrrhotite [Po] and graphite disseminated in matrix. Fracture filled with siderite and locally pyrrhotite. Right column: Pyrrhotite associated with magnetite and graphite. Pyrrhotite with chalcopyrite [Ccp] inclusions and locally associated with pentlandite [Pn]. TL-II: transmitted light micrograph with plane polarized light (ppl). TL-x: crossed polars. RL-II: reflected light micrograph with ppl.

2.56. FP94-4-5\_142.42 AQM-SEM

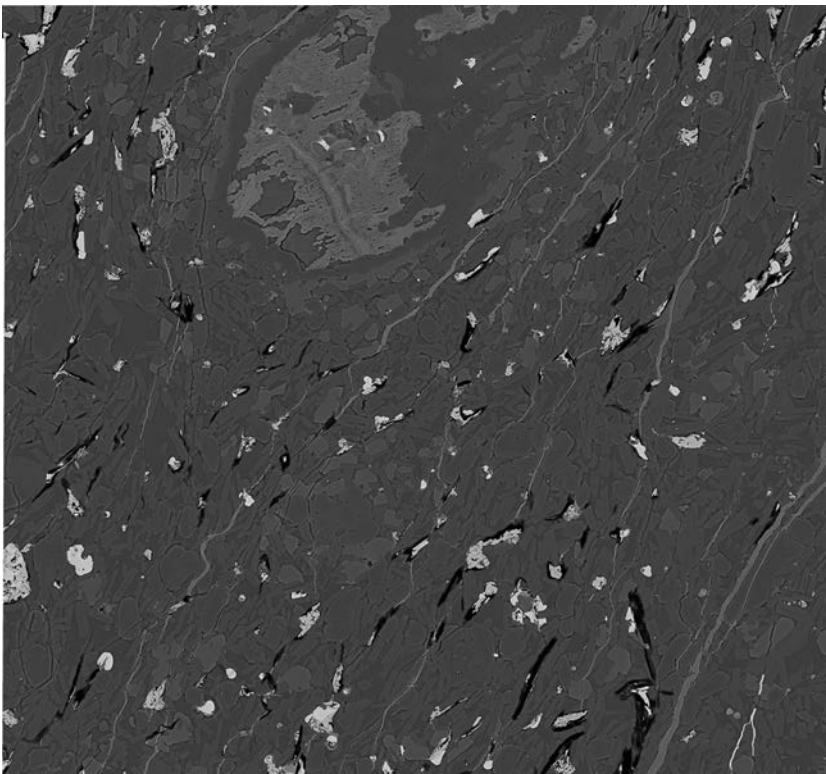


**Fig. 68.** Mineral map and corresponding BSE map of AQM-SEM analysis.

*Siderite+Fe-Mg-chlorite-altered olivine xenocryst with orthopyroxene corona and solution embayments. Matrix consists predominantly of euhedral to subhedral crystals of plagioclase, orthopyroxene, minor anhedral clinopyroxene with intersertal K-rich siliceous glass. Plagioclase, sulphides, and graphite aligned to foliation. Siderite-filled fractures.*

*Image of thin-section, width 23 mm*

50 µm

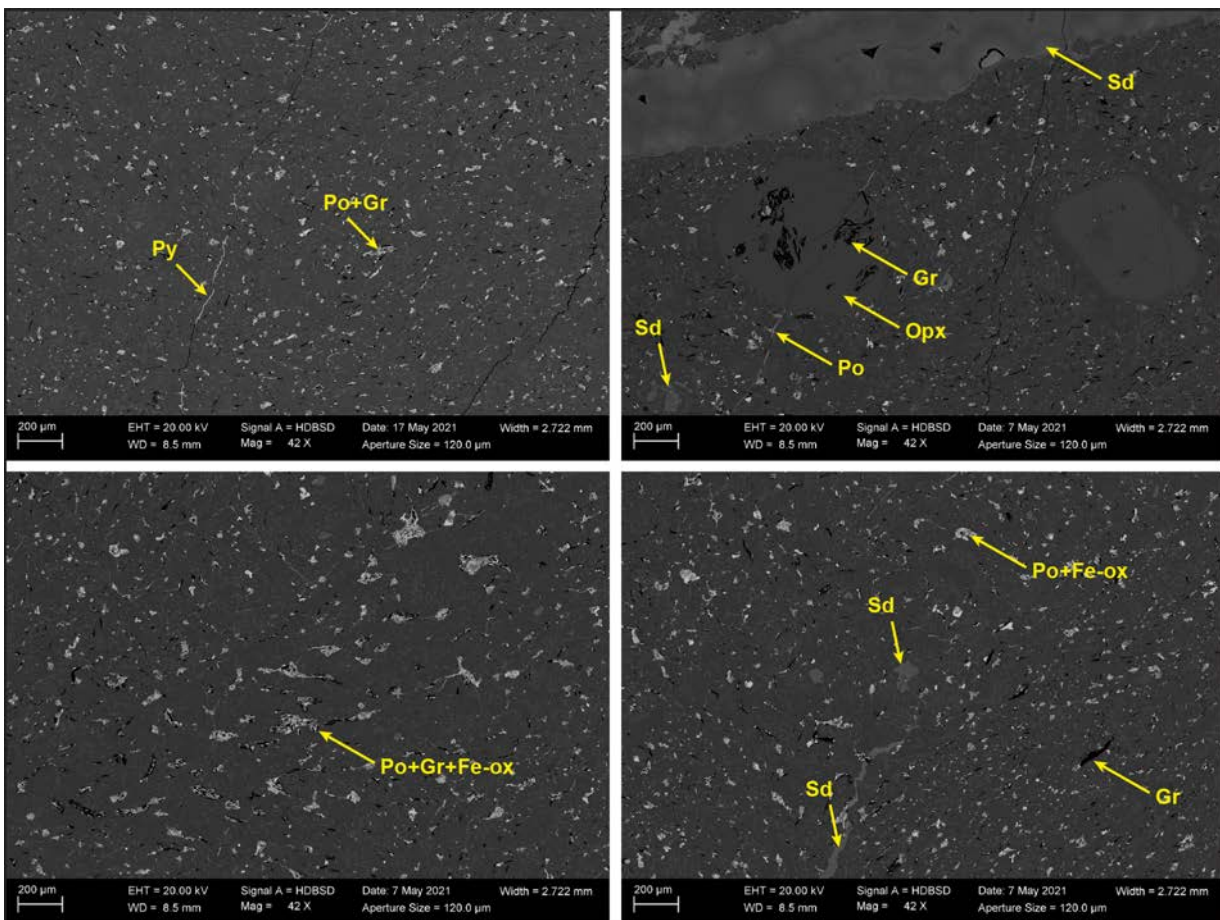


2.57. FP94-4-5\_153.20 Summary

Slightly foliated fine-medium-crystalline basalt with Fe-carbonate-filled blocky fractures with spherule crosses. Fractures locally filled with late-stage pyrite and/or graphite. No apparent preserved native iron. Pyrrhotite commonly with Cu-sulphides (chalcopyrite) and associated with magnetite and graphite, locally with rutile.

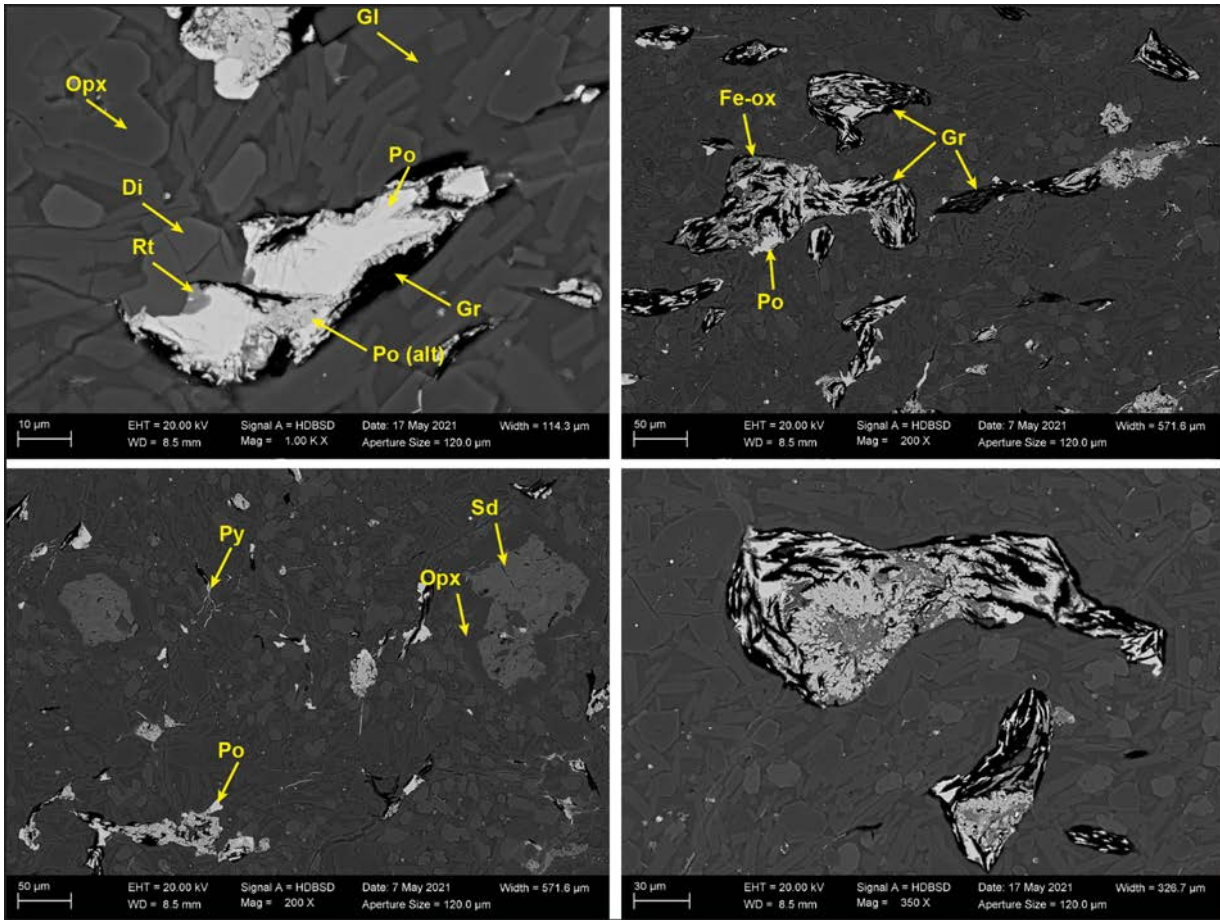
The matrix consists of plagioclase microlite laths, Fe-Mg-chlorite-altered orthopyroxene, and diopside with intersertal K-rich siliceous glass. Phenocrysts consist of orthopyroxene and siderite-altered olivine with orthopyroxene coronas. Graphite occurs with the sulphides and in fractures. As previous, graphite is not associated with hisingerite.

2.58. FP94-4-5\_153.20 SEM-BSE/EDS element maps



**Fig. 69.** Backscatter electron (BSE) micrographs. Upper row: Abundant disseminated aggregates of pyrrhotite [Po], magnetite [Mag], and graphite [Gr]. All four micrographs at same magnification, illustrating the variability in grain size within the sample at thin section scale. Smaller fractures are locally filled with late-stage pyrite [Py] and/or siderite [Sd]. Large blocky fractures filled with siderite, commonly with spherulitic texture. Orthopyroxene [Opx] phenocrysts rich in graphite [Gr].

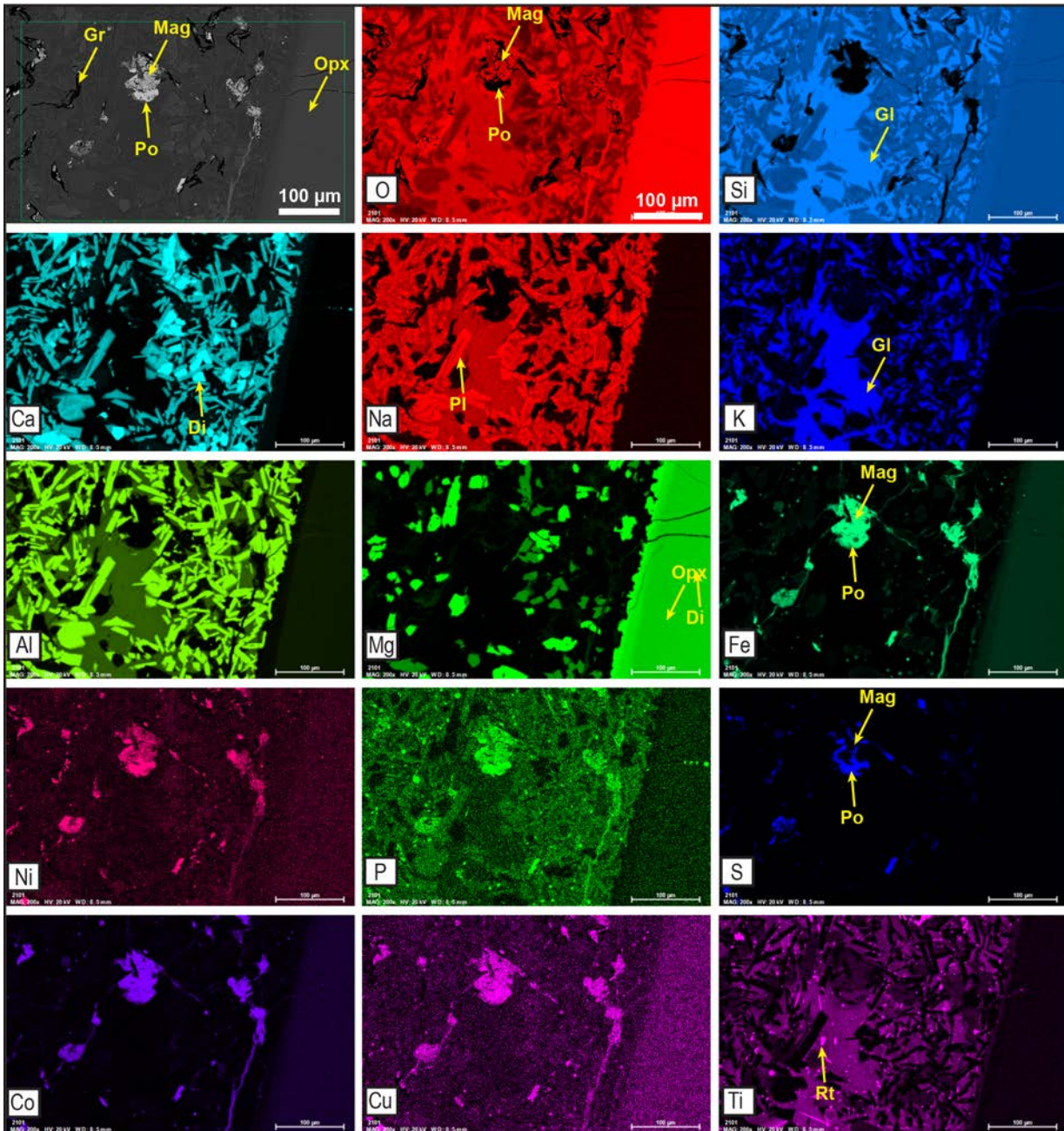




**Fig. 70.** Backscatter electron (BSE) micrographs. Close-up of the pyrrhotite [Po], Fe-oxide, graphite [Gr] aggregates. Pyrite [Py] as late-stage fill in small fractures. Note: graphite not associated with hisingerite, as in sections of the upper flow. Phenocrysts of ?olivine replaced by siderite [Sd] and with orthopyroxene [Opx] corona. Matrix consists of K-rich siliceous glass [Gl]. Rutile [Rt] locally associated with pyrrhotite-magnetite-graphite aggregates.

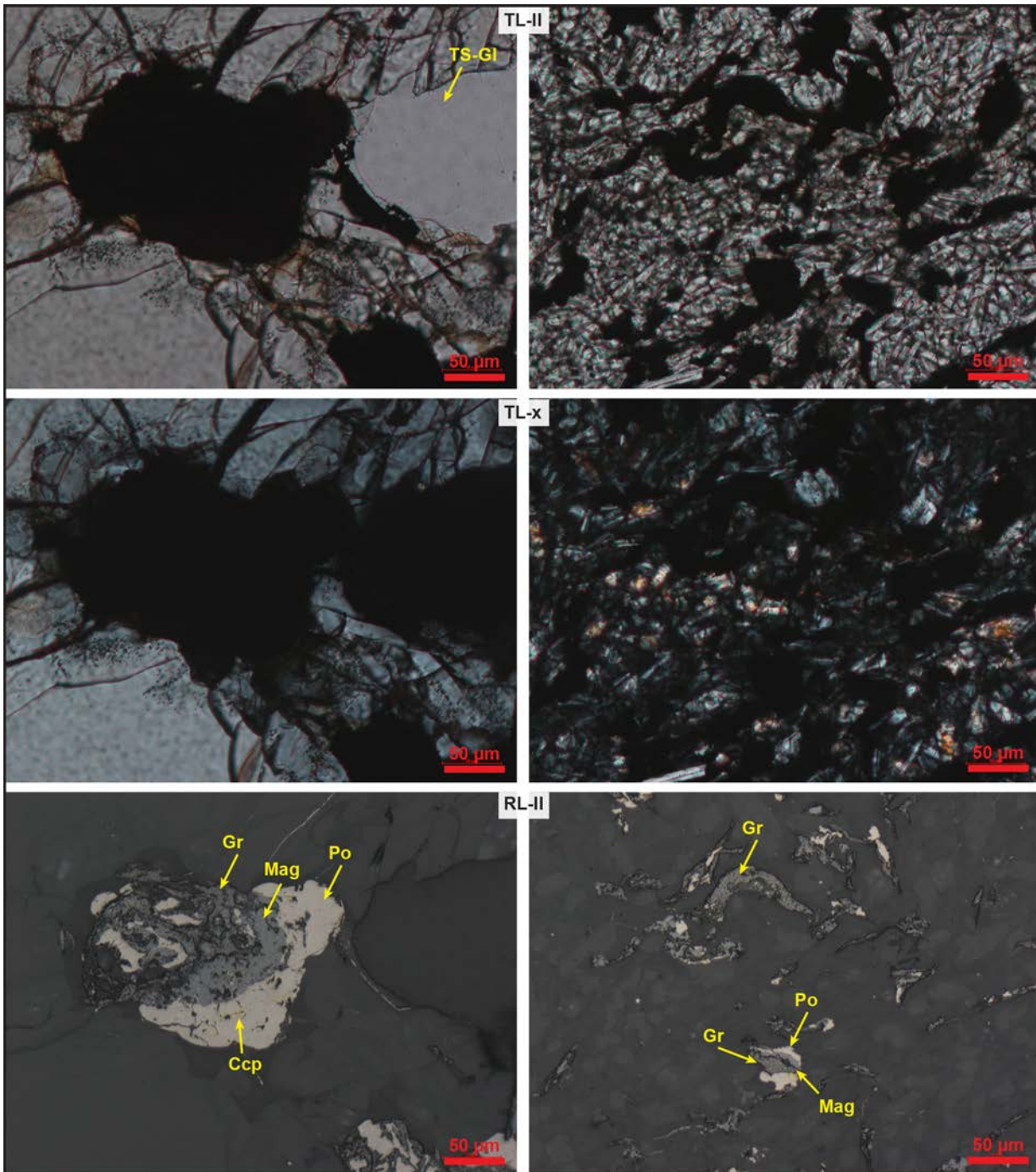
FP94-4-5\_153.20

SEM-EDS element map

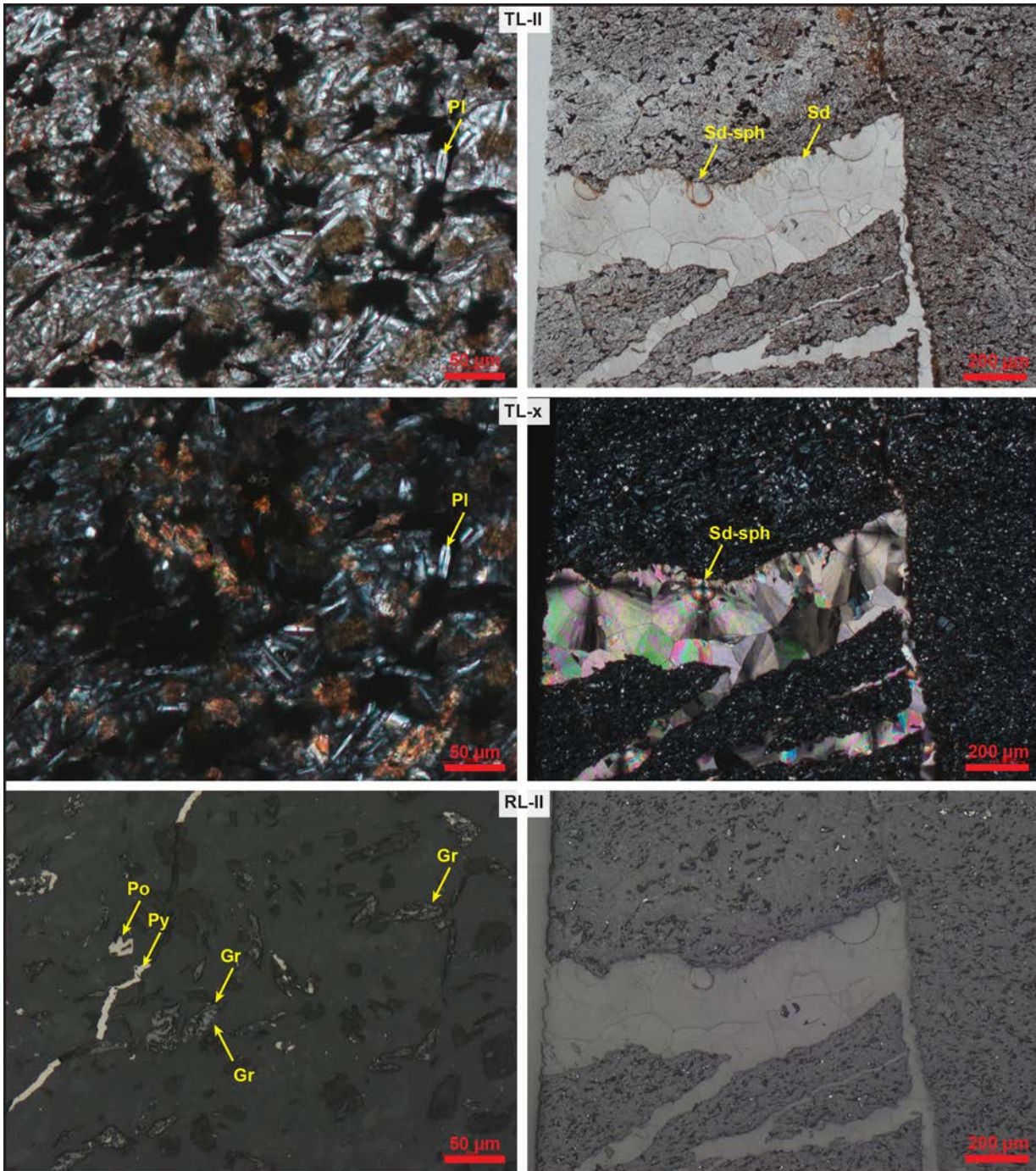


**Fig. 71.** Element maps to illustrate the association of pyrrhotite [Po], magnetite [Mag], and graphite [Gr], which are aligned to the foliation, as are diopside [Di] and orthopyroxene [Opx]. Plagioclase [Pl] microlites are also aligned and show a zonation in the Na-content. Insertal glass is K-rich and siliceous [Gl]. Pyrrhotite contains traces of Ni and Zn, magnetite traces of Co. Ti-oxide phases, e.g., rutile [Rt], associated with pyrrhotite aggregates and dispersed in matrix.

2.59. FP94-4-5\_153.20 Microscopy



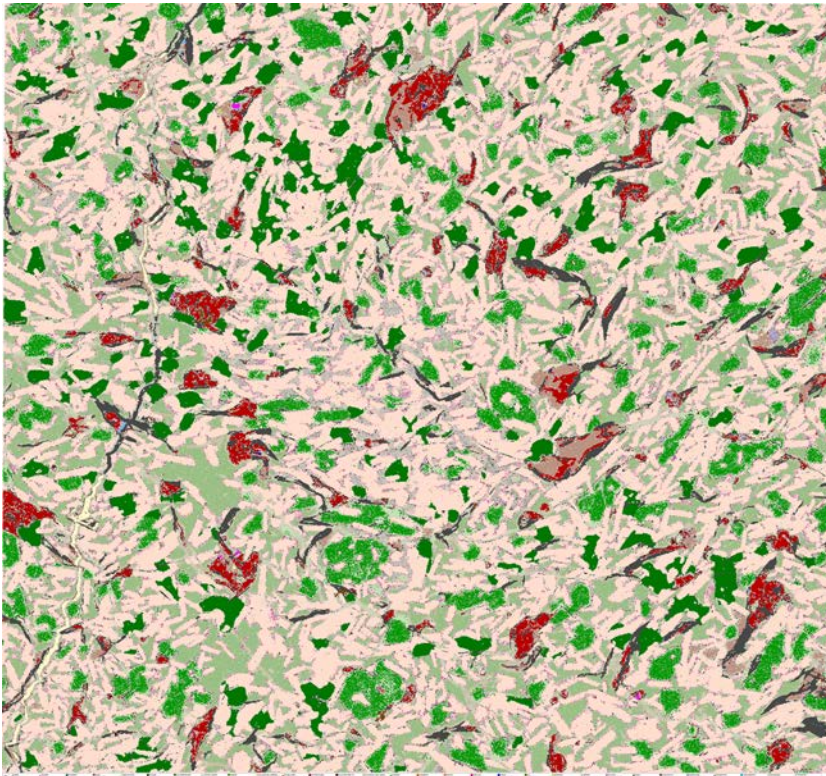
**Fig. 72.** Left column: Pyrrhotite [Po], magnetite [Mag], and graphite [Gr] in association with chalcopyrite [Ccp]. Note: Large plucked grain/ thin-section glass on right hand side of micrograph. Right column: Association of pyrrhotite, magnetite, and graphite. TL-II: transmitted light micrograph with plane polarized light (ppl). TL-x: crossed polars. RL-II: reflected light micrograph with ppl.



**Fig. 73.** Left column: Pyrrhotite [Po] and graphite [Gr] disseminated in matrix, pyrite [Py] also as later-stage fracture fill. Right column: Large blocky fracture filled with spherulitic siderite [Sd] displaying spherulite [Sph] crosses.

TL-II: transmitted light micrograph with plane polarized light (ppl). TL-x: crossed polars. RL-II: reflected light micrograph with ppl.

2.60. FP94-4-5\_153.20 AQM-SEM

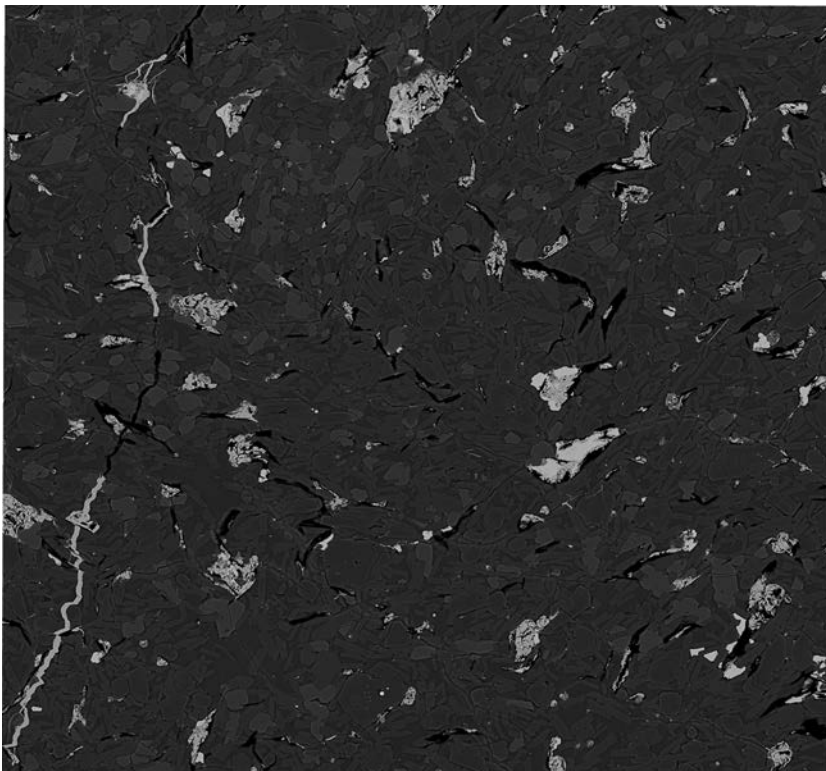


**Fig. 74.** Mineral map and corresponding BSE map of AQM-SEM analysis.

*Pyrrhotite and magnetite in association with graphite and chalcopyrite. Matrix consists predominantly of euhedral to subhedral crystals of plagioclase, orthopyroxene, minor anhedral clinopyroxene with intersertal K-rich siliceous glass. Fractures filled with pyrite and locally graphite.*

*Image of thin-section, width 23 mm*

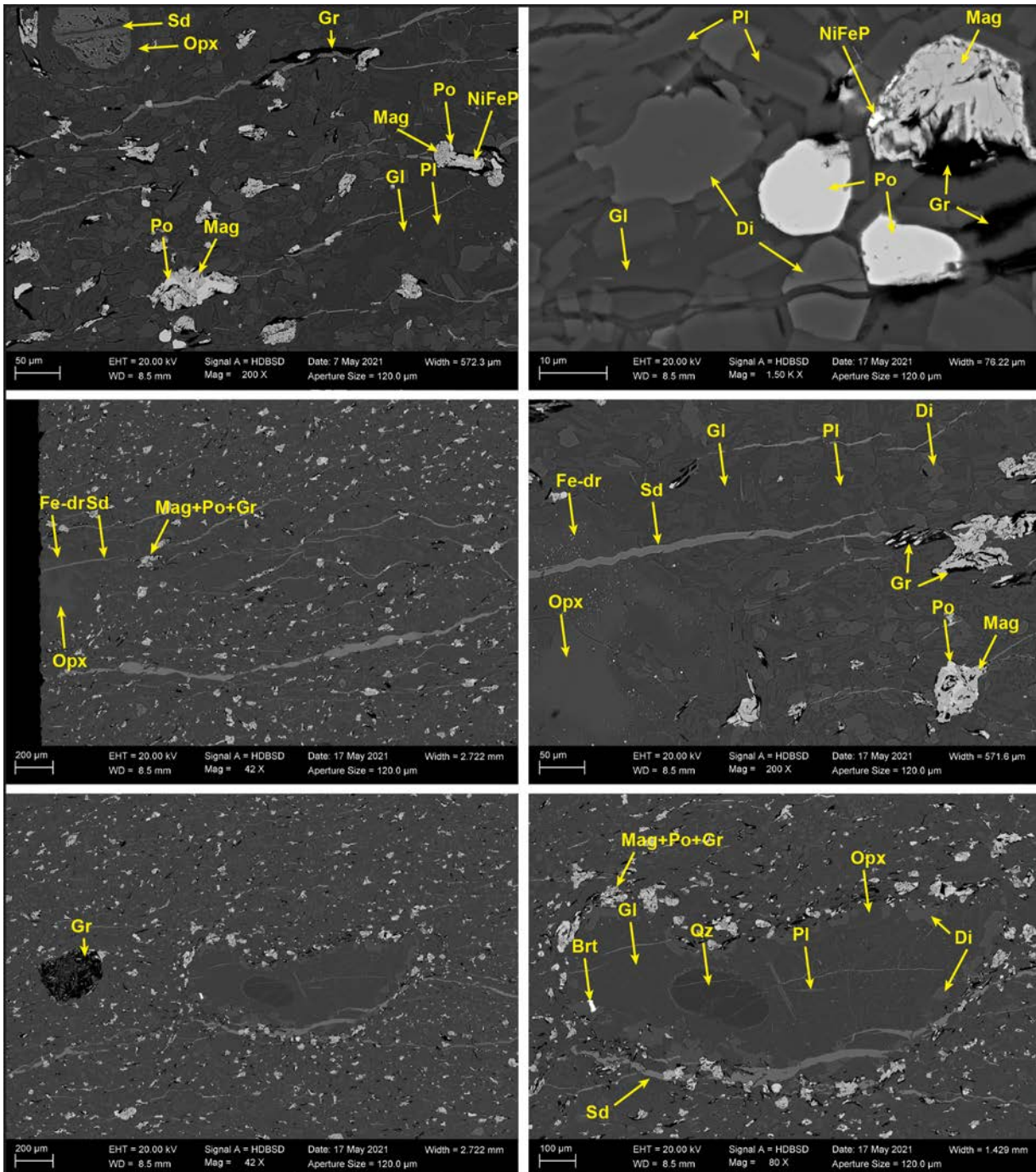
50 µm



2.61. FP94-4-5\_159.70 Summary

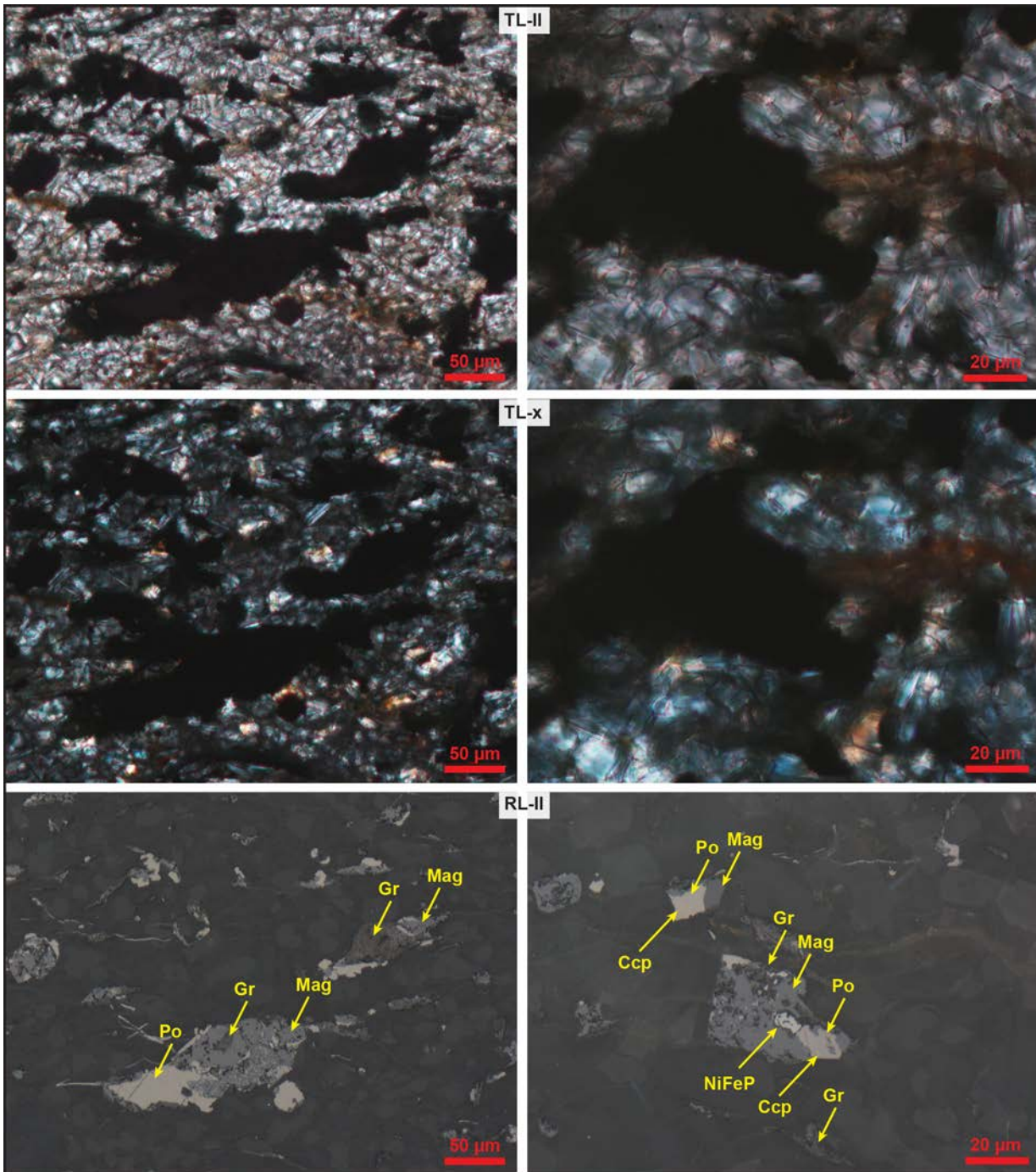
Fine-crystalline basalt with abundant siderite-filled fractures. No apparent preserved native iron. Pyrrhotite commonly associated with pentlandite and Cu-sulphides (chalcopyrite), magnetite and graphite, locally with NiFe-phosphide. The matrix consists of plagioclase microlite laths, Fe-Mg-chlorite-altered orthopyroxene, and diopside with sections rich in intersertal K-rich siliceous glass. Phenocrysts consist of orthopyroxene and siderite-altered olivine and K-rich siliceous glass-filled amygdules.

2.62. FP94-4-5\_159.70 SEM-BSE/EDS

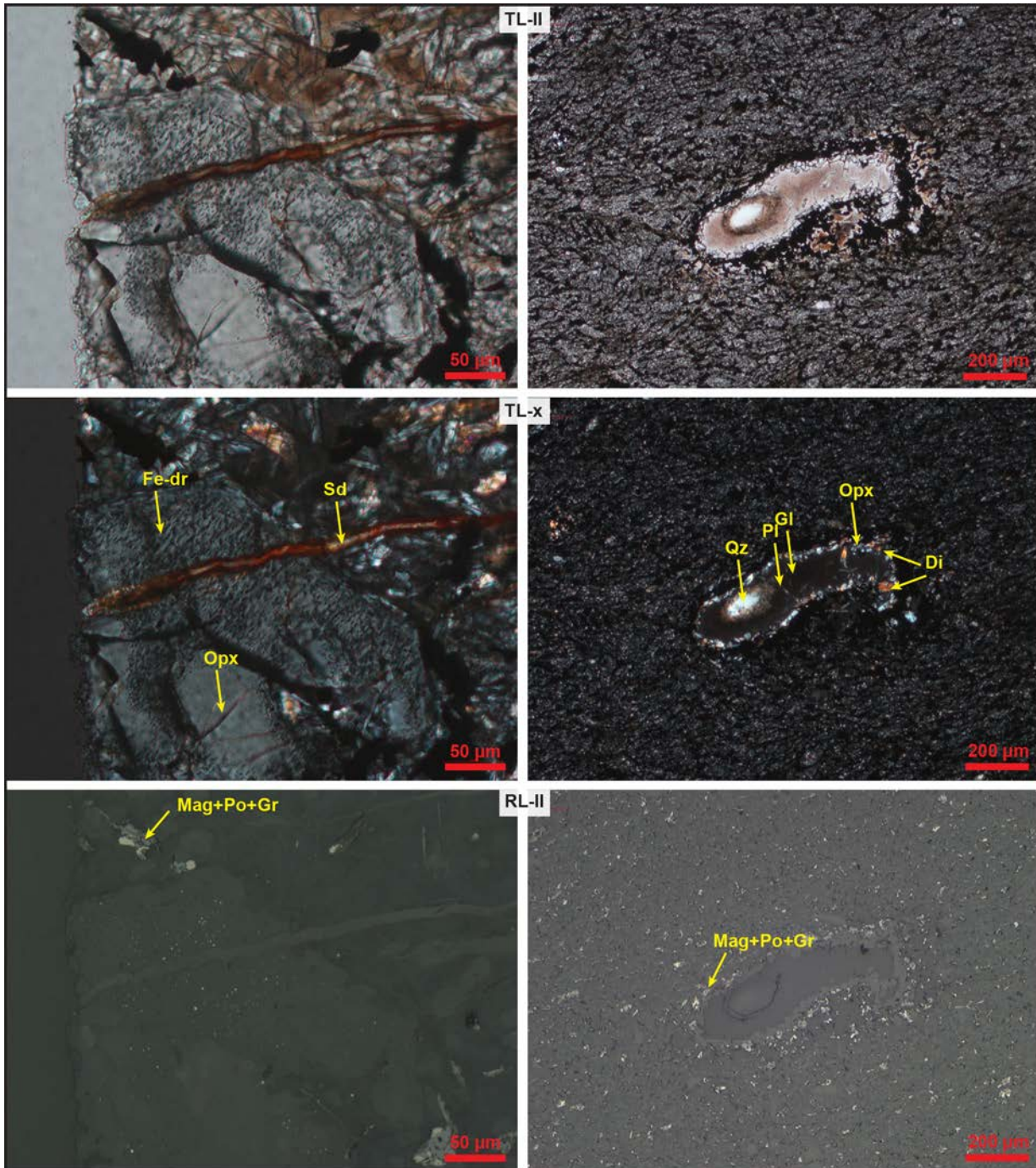


**Fig. 75.** Backscatter electron (BSE) micrographs. Aggregates of pyrrhotite-magnetite-graphite. Siderite as late-stage fill in small fractures. Phenocrysts of olivine replaced by siderite and with orthopyroxene corona. Matrix consists of K-rich siliceous glass. Bottom row: K-rich siliceous glass-filled amygdule with orthopyroxene-diopside rime and acicular plagioclase. Oval center in amygdule filled with quartz [Qz]. Barite [Brt] at edge of amygdule.

2.63. FP94-4-5\_159.70 Microscopy



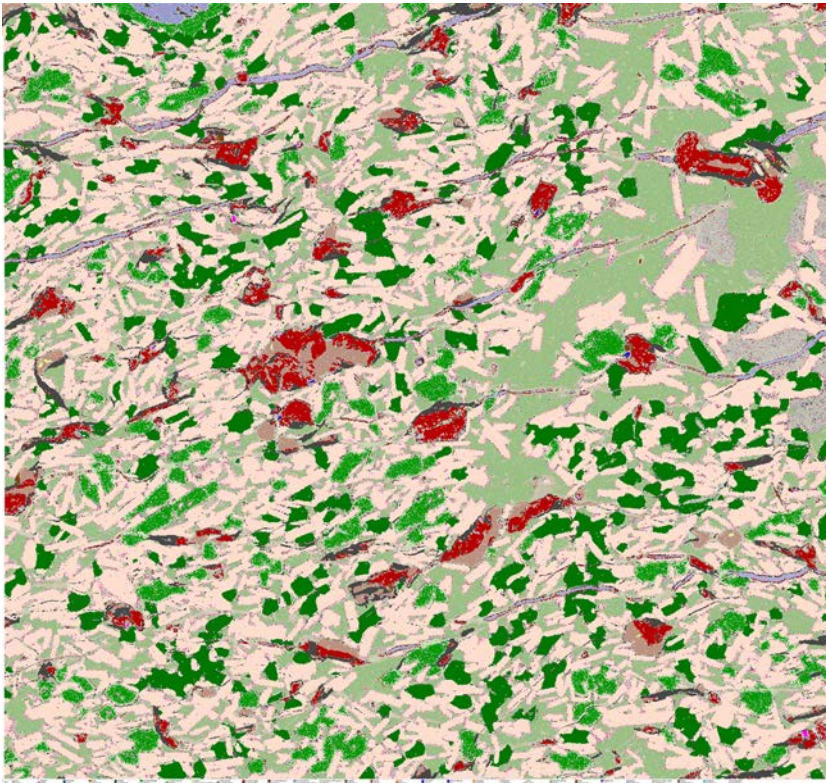
**Fig. 76.** Pyrrhotite [Po], magnetite [Mag], and graphite [Gr] disseminated in matrix, locally association with NiFeP and chalcopyrite [Ccp]. TL-II: transmitted light micrograph with plane polarized light (ppl). TL-x: crossed polars. RL-II: reflected light micrograph with ppl.



**Fig. 77.** Left column: Large orthopyroxene [Opx] phenocryst with a Fe-droplet-rich zone. Cross-cut by siderite [Sd]-filled fractures. Right column: K-rich siliceous glass [Gl]-filled amygdale shown in SEM-BSE micrograph. TL-II: transmitted light micrograph with plane polarized light (ppl). TL-x: crossed polars. RL-II: reflected light micrograph with ppl.



2.64. FP94-4-5\_159.70 AQM-SEM

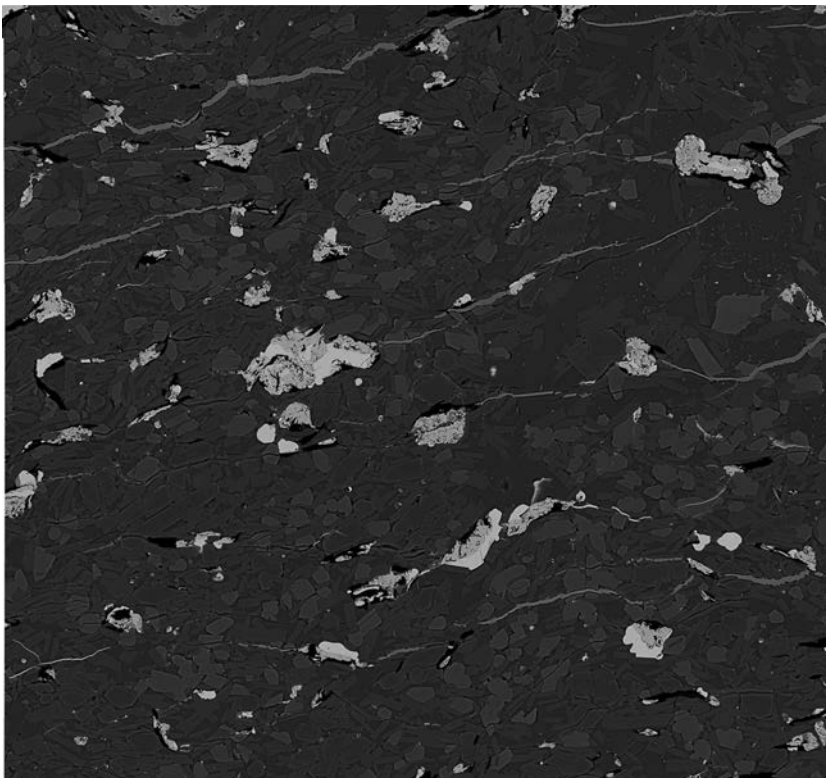


**Fig. 78.** Mineral map and corresponding BSE map of AQM-SEM analysis.

*Pyrrhotite and magnetite in association with graphite and chalcopyrite. Matrix consists predominantly of euhedral to subhedral crystals of plagioclase, orthopyroxene, minor anhedral clinopyroxene with large sections of intersertal K-rich siliceous glass. Fractures filled with siderite.*

*Image of thin-section, width 23 mm*

50  $\mu$ m

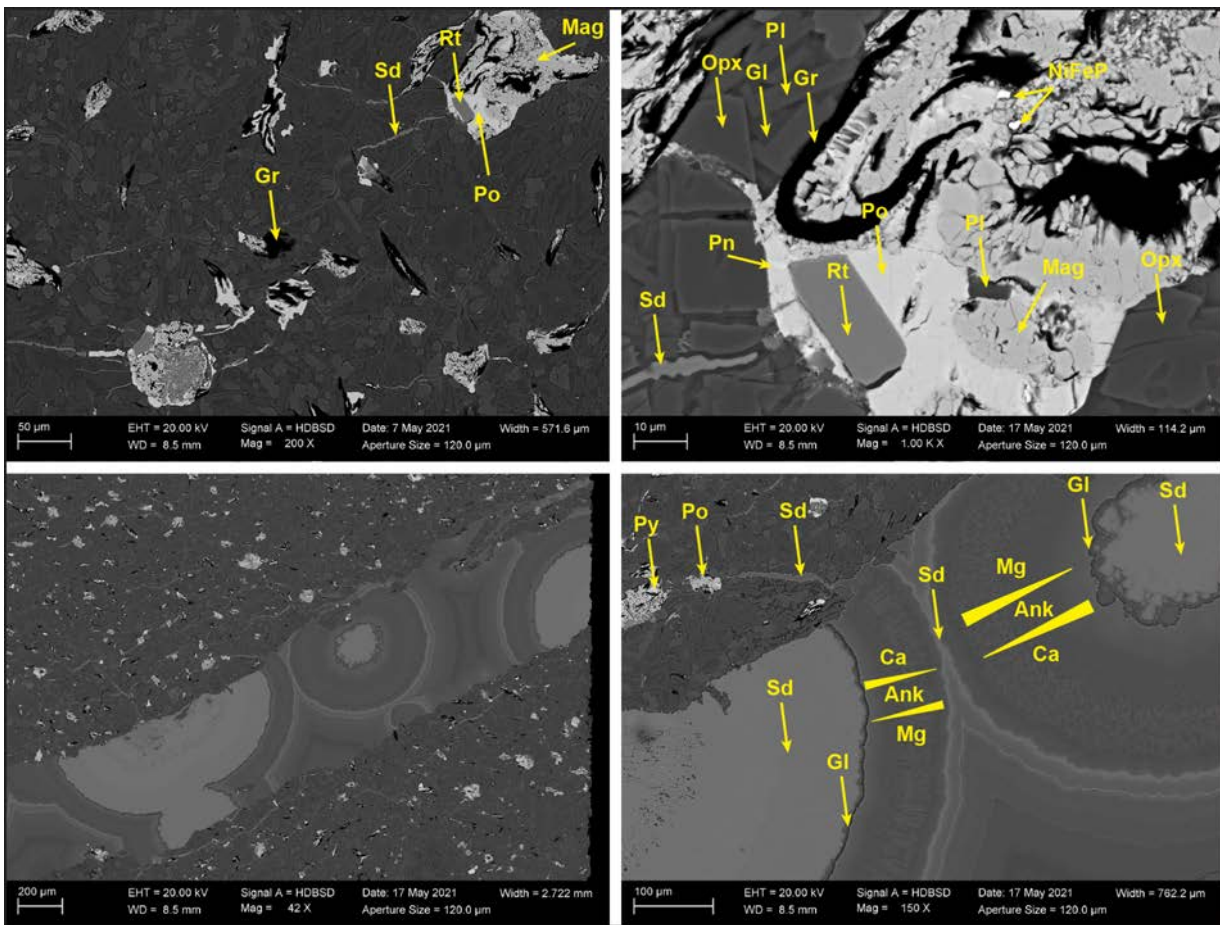


2.65. FP94-4-5\_170.47 Summary

Fractured fine-crystalline basalt with tens of  $\mu\text{m}$ -sized aggregates of pyrrhotite, graphite, and magnetite and up to several mm-sized orthopyroxene phenocrysts. No preserved native iron observed. Pyrrhotite commonly associated with pentlandite, chalcopyrite, and Ni-Fe-phosphides.

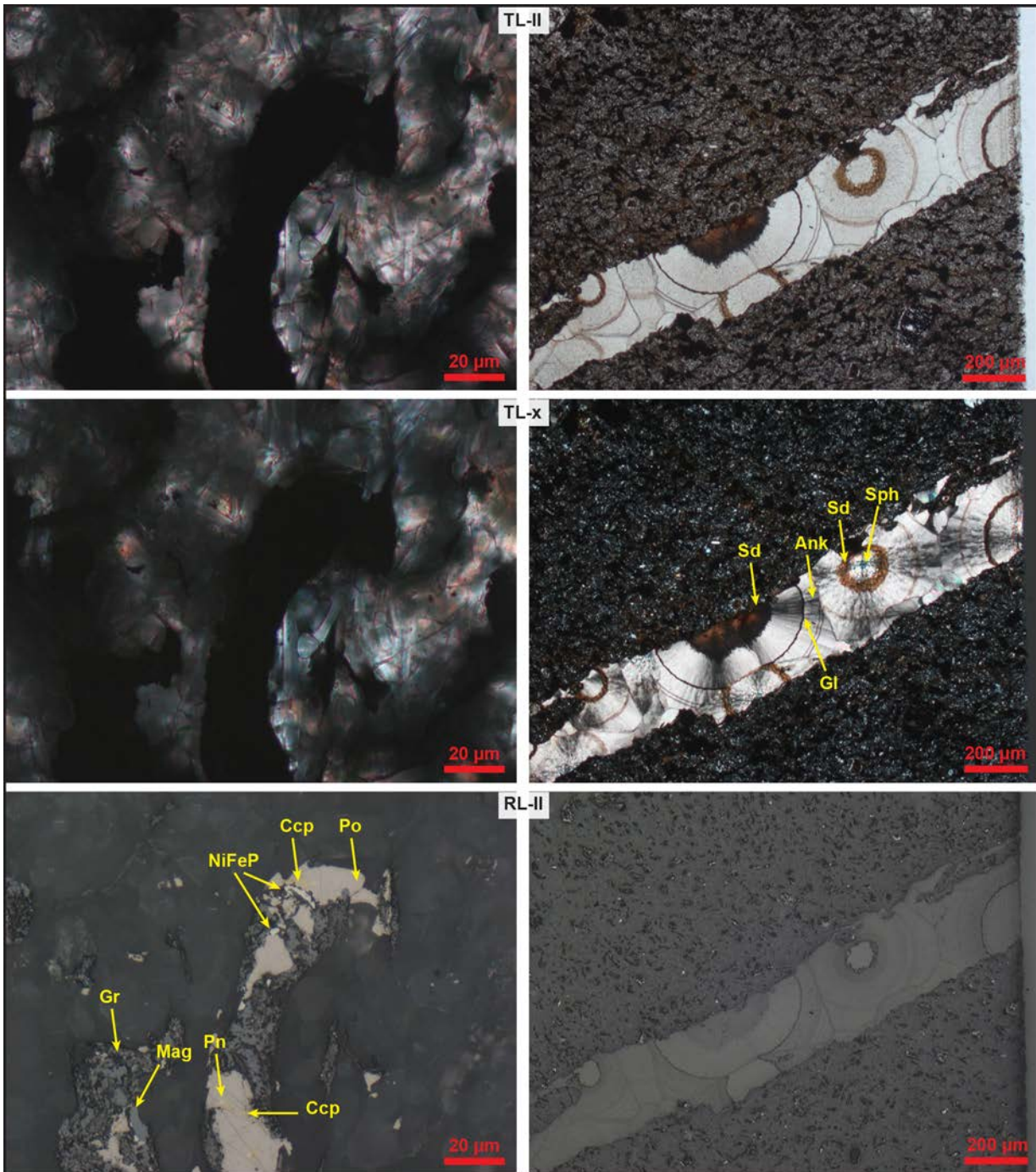
The matrix consists of plagioclase microlite laths, Fe-Mg-chlorite-altered orthopyroxene, and diopside with intersertal K-rich siliceous glass. Graphite occurs with the sulphides, locally strongly bent. Large blocky fractures filled by concentric siderite-ankerite spherulites with characteristic spherulite crosses in cross-polarized light.

2.66. FP94-4-5\_170.47 SEM-BSE/EDS

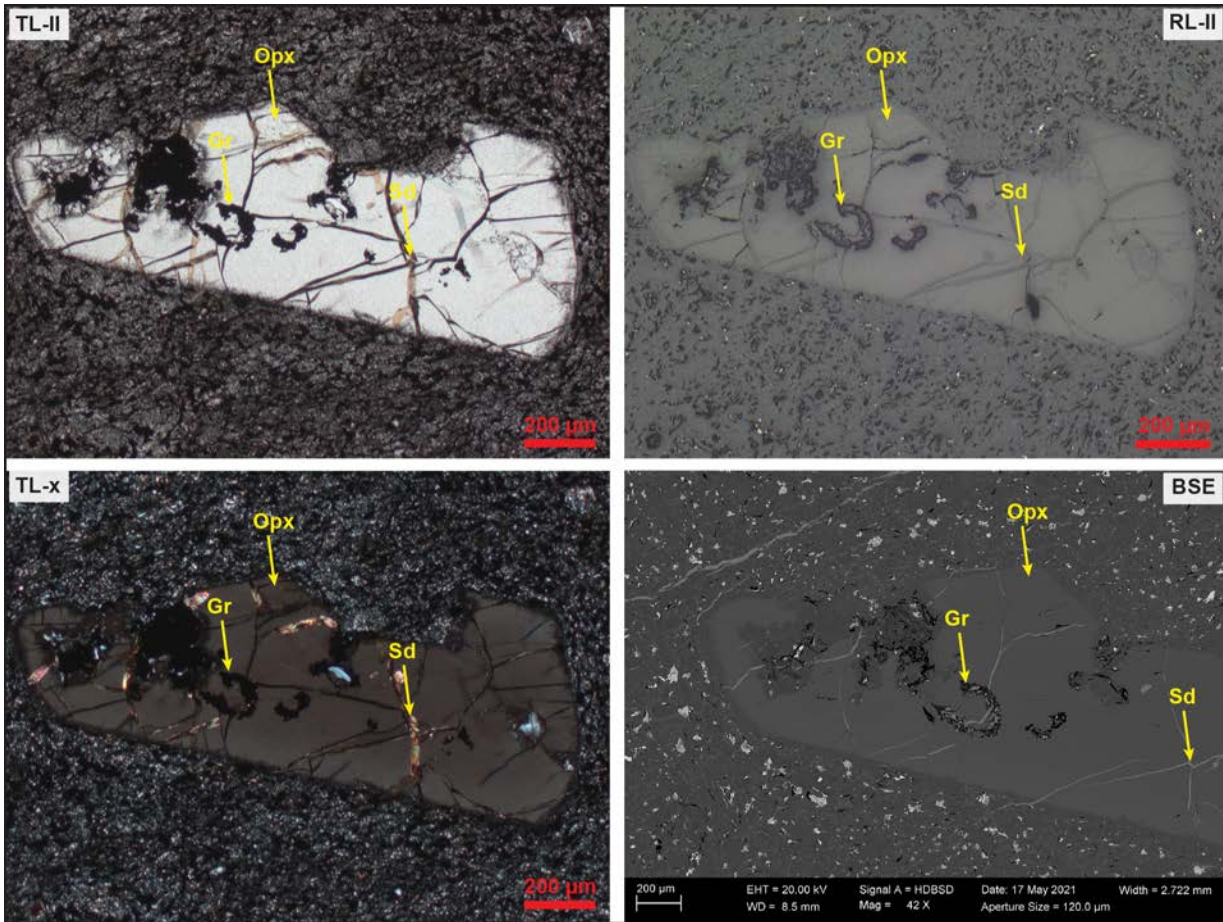


**Fig. 79.** Backscatter electron (BSE) micrographs. Aggregates of pyrrhotite [Po], magnetite [Mag], and graphite [Gr], locally NiFe-phosphide and rutile [Rt]. Orthopyroxene [Opx] block fractured with pyrrhotite remobilized into fracture. Graphite flakes strongly bent within pyrrhotite+magnetite aggregates. Siderite [Sd] as late-stage fill in small fractures. Siderite-fill in fractures with characteristic concentric spherulite texture. Cores consist of siderite rimmed by a thin layer of siliceous glass [Gl], followed by an ferroan ankerite [Ank] with decreasing Ca- and increasing Mg content. Matrix consists of K-rich siliceous glass.

2.67. FP94-4-5\_170.47 Microscopy



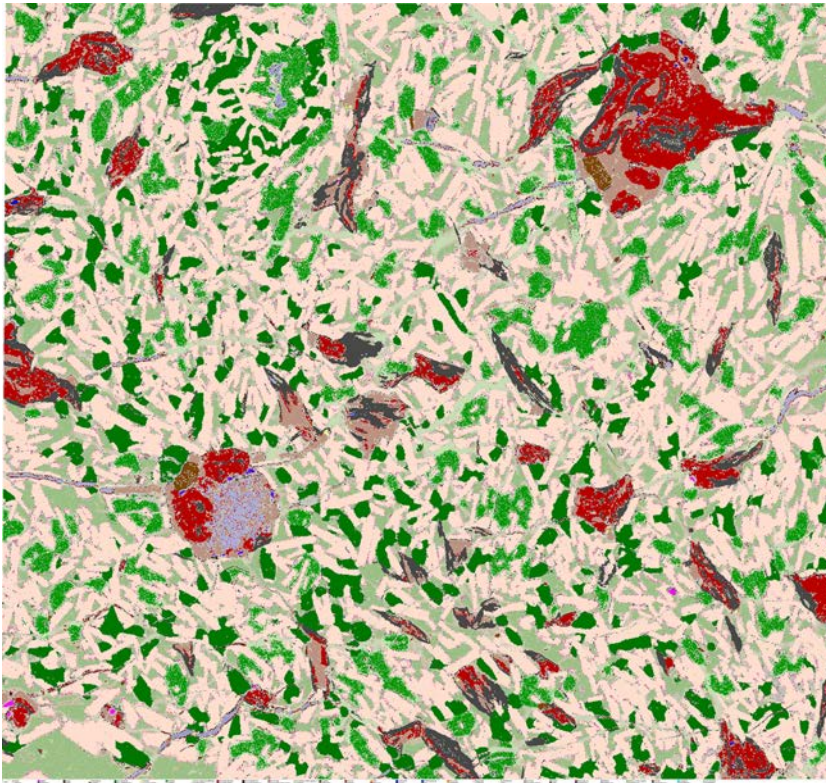
**Fig. 80.** Left column: Pyrrhotite [Po], magnetite [Mag], and graphite [Gr] associated with pentlandite [Pn], NiFeP, and chalcopyrite [Ccp]. Right column: Siderite [Sd]-ankerite [Ank] vein with spherulitic texture and characteristic spherulite crosses [Sph]. TL-II: transmitted light micrograph with plane polarized light (ppl). TL-x: crossed polars. RL-II: reflected light micrograph with ppl.



**Fig. 81.** Orthopyroxene [Opx] phenocryst with solution embayments, graphite [Gr], and crosscut by siderite [Sd]-filled fractures.

TL-II: transmitted light micrograph with plane polarized light (ppl). TL-x: crossed polars. RL-II: reflected light micrograph with ppl. BSE: Backscatter electron micrograph.

2.68. FP94-4-5\_170.47 AQM-SEM



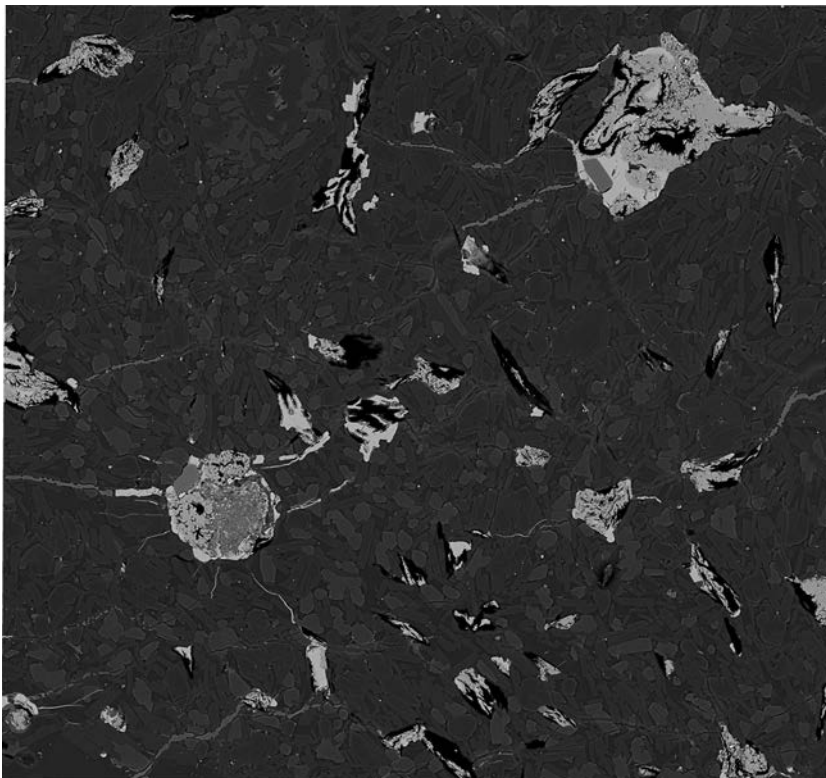
**Fig. 82.** Mineral map and corresponding BSE map of AQM-SEM analysis.

*Pyrrhotite and magnetite in association with graphite, chalcopyrite, pentlandite, and NiFeP.*

*Matrix consists predominantly of euhedral to subhedral crystals of plagioclase, orthopyroxene, minor anhedral clinopyroxene with large sections of intersertal K-rich siliceous glass. Fractures filled with siderite and pyrrhotite.*

*Image of thin-section, width 23 mm*

— 50 µm

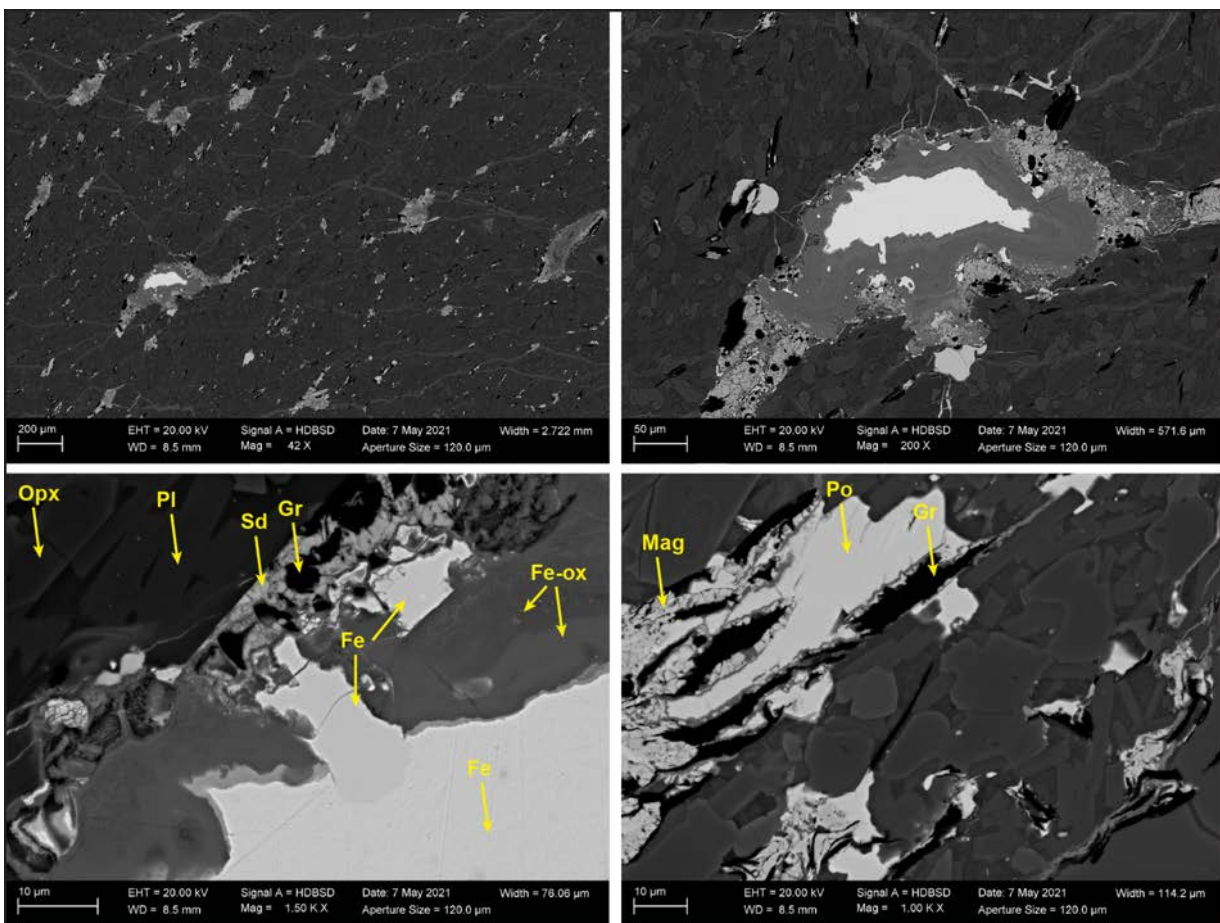


2.69. FP94-4-5\_177.40 Summary

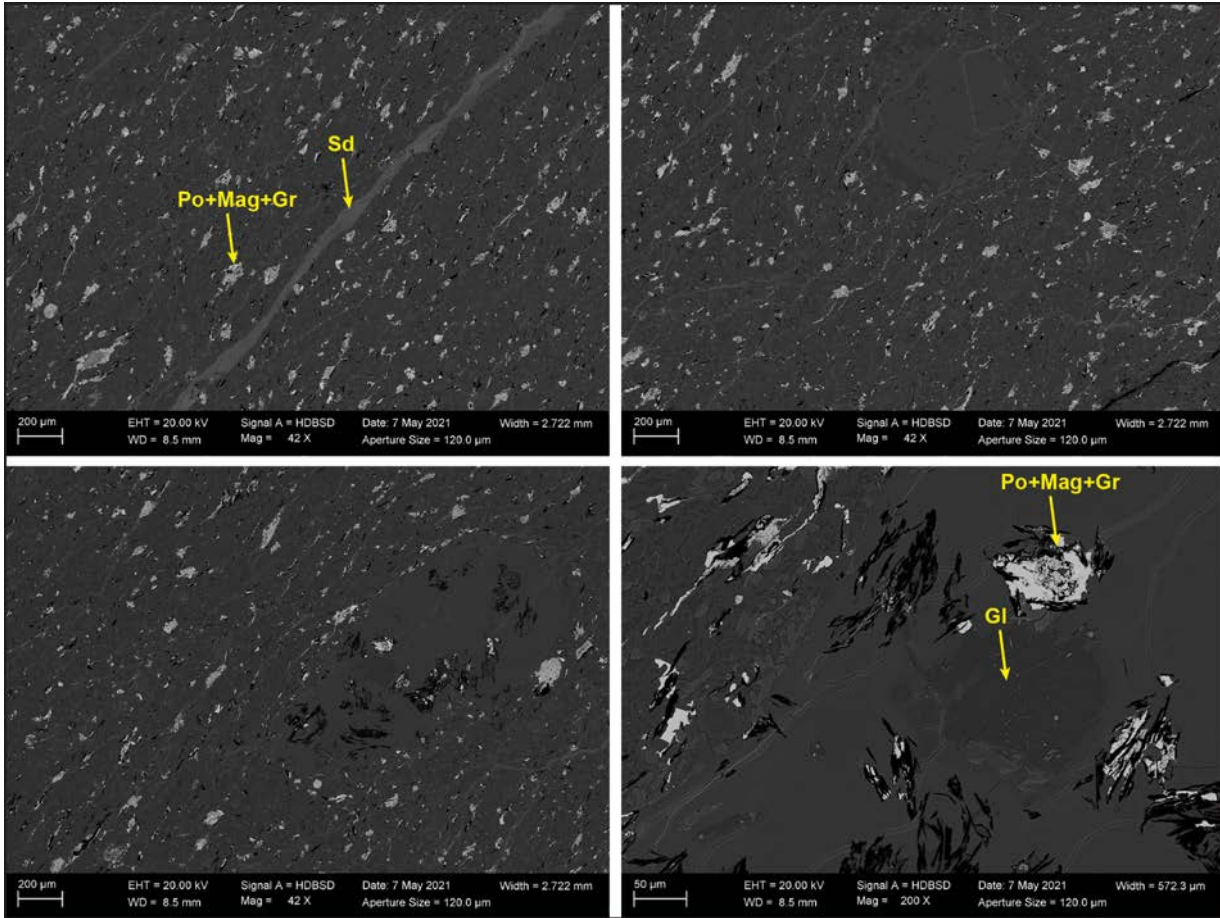
Foliated/sheared and fractured fine-crystalline basalt with hundreds of  $\mu\text{m}$ -sized pyrrhotite+graphite+magnetite aggregates. Native iron is locally, but minor, preserved and rimmed by a layered oxidation halo (Fe-oxides/hydroxides). Orthopyroxene phenocrysts and olivine xenocrysts occur Fe-Mg-chlorite±siderite altered. Pyrrhotite commonly associated with pentlandite, chalcopyrite, and Ni-Fe-phosphides..

The matrix consists of plagioclase microlite laths, Fe-Mg-chlorite-altered orthopyroxene, and diopside with intersertal K-rich siliceous glass. Graphite occurs with the sulphides, locally strongly bent. Abundant small conjugate sets of fractures cross-cut matrix and are filled with siderite and locally remobilized pyrrhotite. Amygdules are filled with glass and rimmed by orthopyroxene and diopside.

2.70. FP94-4-5\_177.40 SEM-BSE/EDS

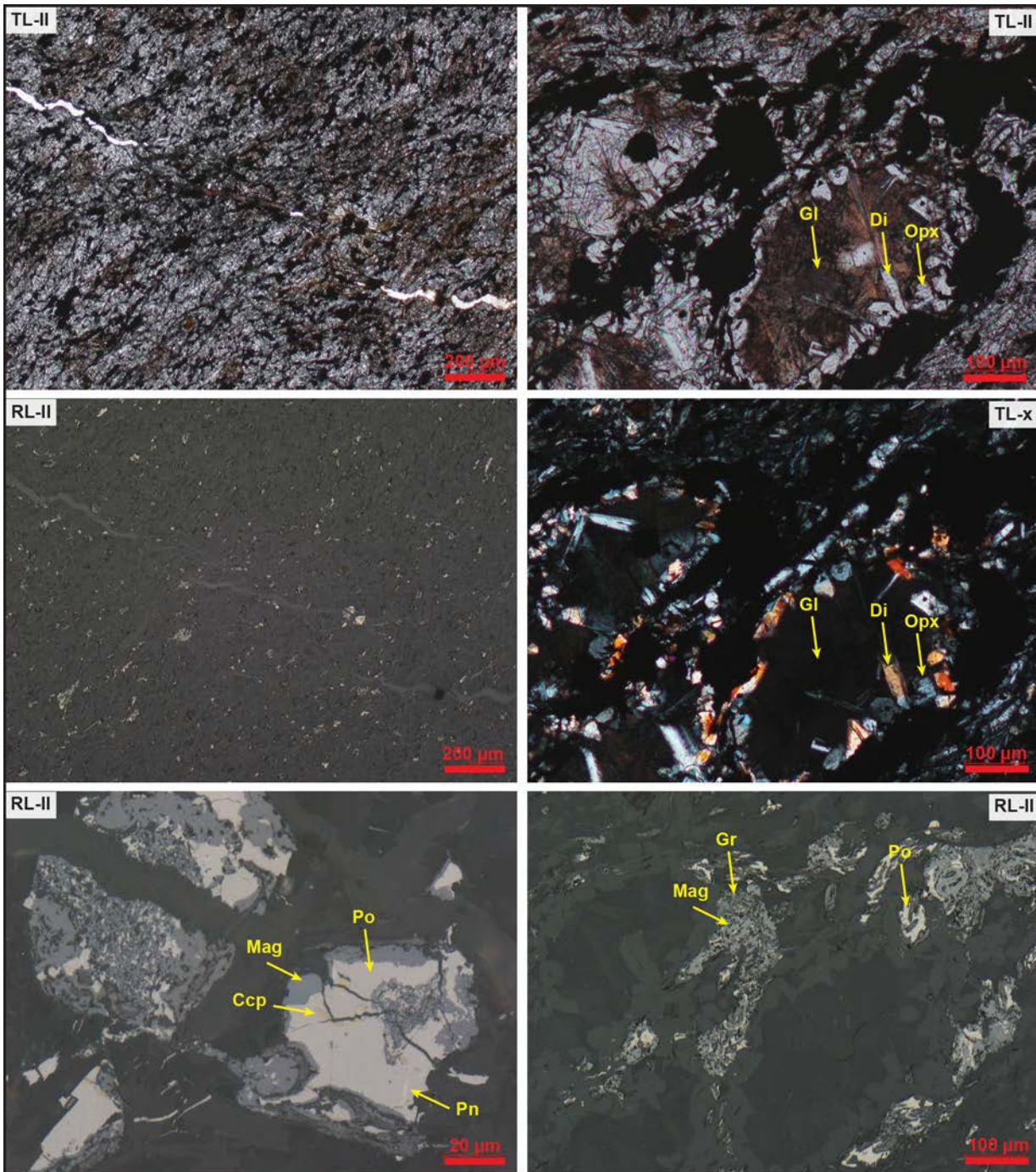


**Fig. 83.** Backscatter electron (BSE) micrographs. Disseminated aggregates of pyrrhotite [Po], magnetite [Mag], and graphite [Gr]. Native iron preserved in core of aggregate, surrounded by layered halo of Fe-oxide/hydroxide. Bottom left shows second 'cleaner' Fe phase, possibly representing cohenite, in association with the more 'spongy' looking native Fe. The latter contains traces of P (<1wt%). Plagioclase [Pl] microlites and orthopyroxene [Opx] in matrix.



**Fig. 84.** Backscatter electron (BSE) micrographs. Disseminated aggregates of pyrrhotite [Po], magnetite [Mag], and graphite [Gr] in foliated basalt. Pyrrhotite+magnetite+graphite aggregates draping around locally glass [GI] and graphite-filled altered phenocryst. Siderite [Sd]-filled fractures occur parallel to foliation and as small stepping connecting veinlets.

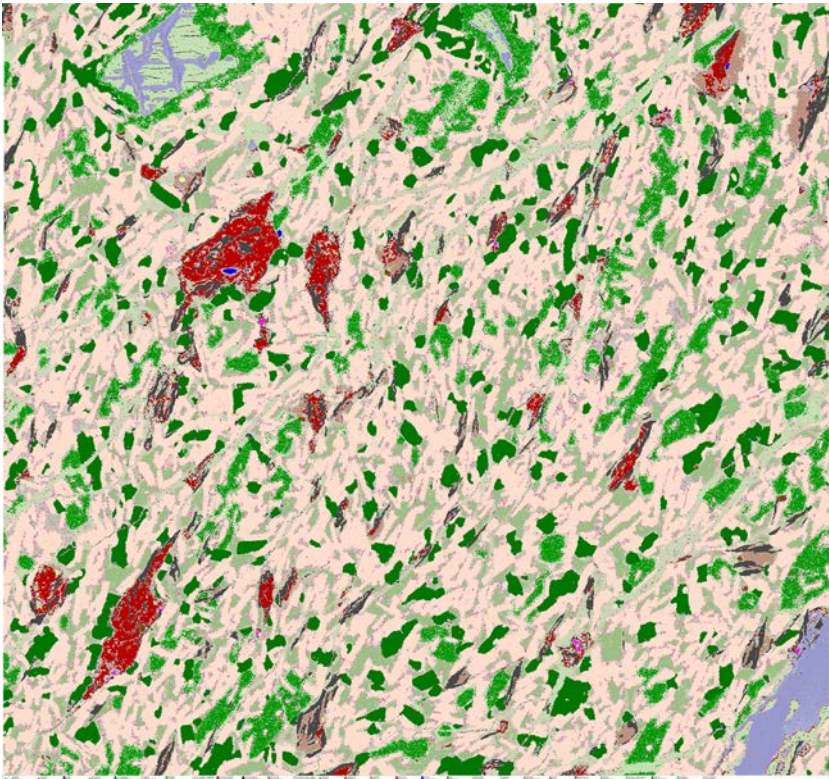
2.71. FP94-4-5\_177.40 Microscopy



**Fig. 85.** Mid-upper left: Stepping siderite [Sd]-filled fractures cross-cutting pyrrhotite [Po], magnetite [Mag], and graphite [Gr]-rich basalt. Bottom left: Pyrrhotite associated with pentlandite [Pn] and chalcopyrite [Ccp] in association with magnetite and graphite. Right column: Glass [Gl]-filled amygdule with diopside [Di]-orthopyroxene [Opx] corona and abundant magnetite-graphite and minor pyrrhotite. TL-II: transmitted light micrograph with plane polarized light (ppl). TL-x: crossed polars. RL-II: reflected light micrograph with ppl.



2.72. FP94-4-5\_177.40 AQM-SEM

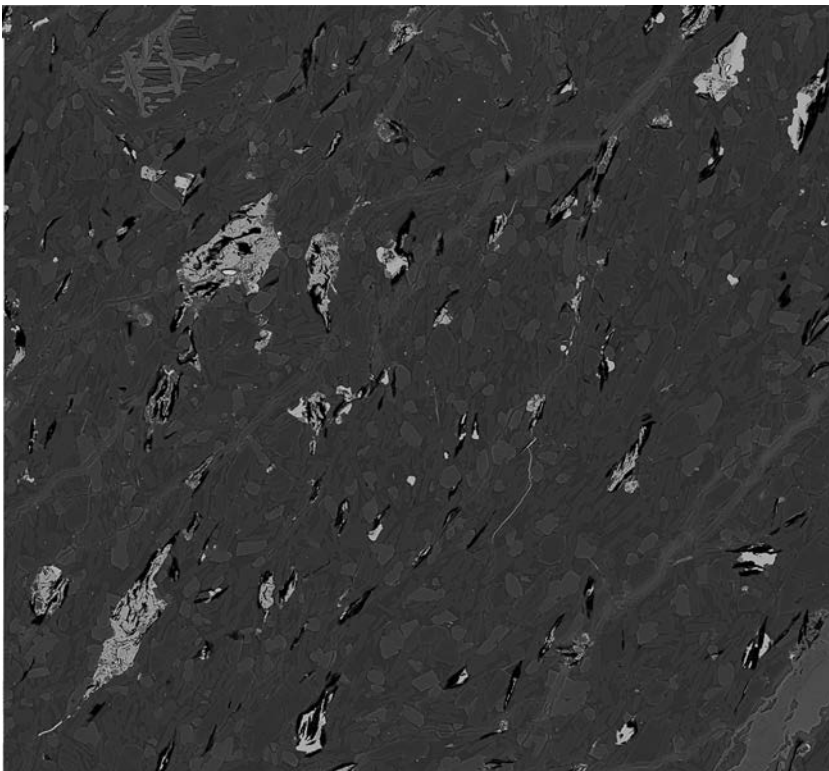


50 μm

**Fig. 86.** Mineral map and corresponding BSE map of AQM-SEM analysis.

*Pyrrhotite and magnetite in association with graphite, chalcopyrite, pentlandite, and NiFeP. Very minor preserved native iron. Fe-Mg-chlorite-altered olivine xenocryst with orthopyroxene corona and cross-cut by siderite-filled fractures. Matrix consists predominantly of euhedral to subhedral crystals of plagioclase, orthopyroxene, minor anhedral clinopyroxene with intersertal K-rich siliceous glass. Fractures filled with siderite.*

*Note: Observed native Fe was not included in mineral map, as this one grain it is not representative for the sample and would create a nugget effect in the data.*



*Image of thin-section, width 23 mm*

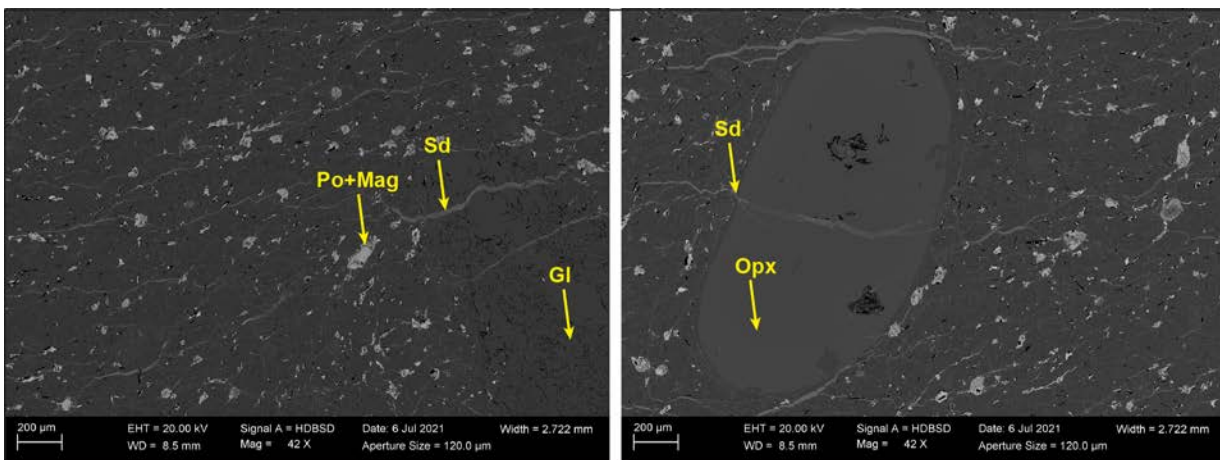


2.73. FP94-4-5\_183.87 Summary

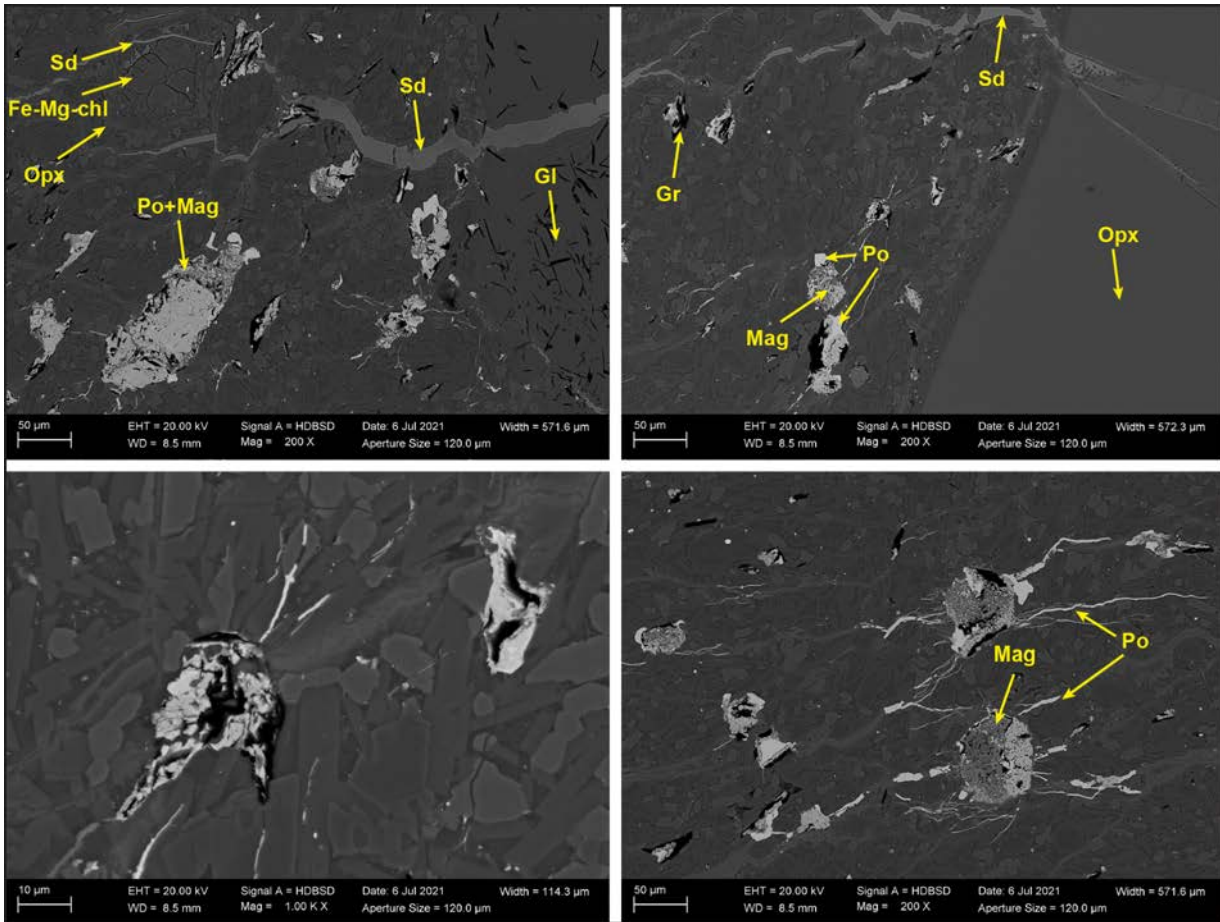
Foliated/sheared and fractured fine-crystalline basalt with tens of  $\mu\text{m}$ -sized pyrrhotite+graphite+magnetite aggregates. Large (mm-sized) rounded orthopyroxene phenocrysts and devitrified glass grains crosscut by siderite-filled fractures, as groundmass and sulphide-oxide aggregates. Minor olivine xenocrysts occur Fe-Mg-chlorite±siderite altered. Pyrrhotite commonly associated with pentlandite, chalcopyrite, and Ni-Fe-phosphides.

The matrix consists of plagioclase microlite laths, Fe-Mg-chlorite-altered orthopyroxene, and diopside with intersertal K-rich siliceous glass. Graphite occurs with the sulphides, but is less abundant than in stratigraphically upper samples. Abundant small fractures cross-cut matrix and are filled with siderite and locally remobilized pyrrhotite.

2.74. FP94-4-5\_183.87 SEM-BSE/EDS

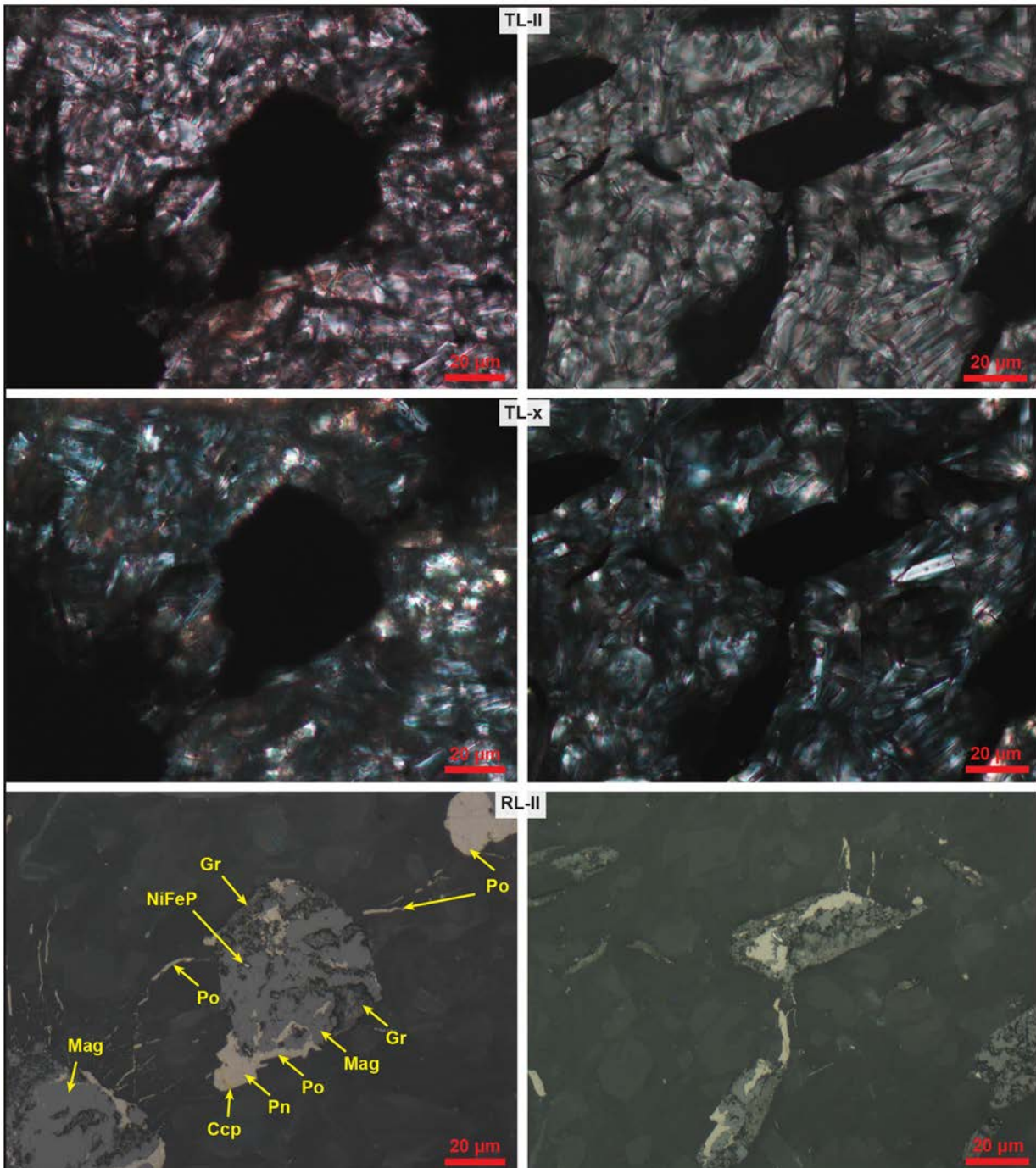


**Fig. 89.** Backscatter electron (BSE) micrographs. Disseminated aggregates of pyrrhotite [Po], magnetite [Mag], and graphite [Gr] in foliated basalt. Pyrrhotite+magnetite+graphite aggregates draping around locally glass [Gl]-filled vug and orthopyroxene [Opx] phenocryst. Siderite [Sd]-filled fractures occur parallel to foliation and as small stepping connecting veinlets and cross-cut glass and orthopyroxene.



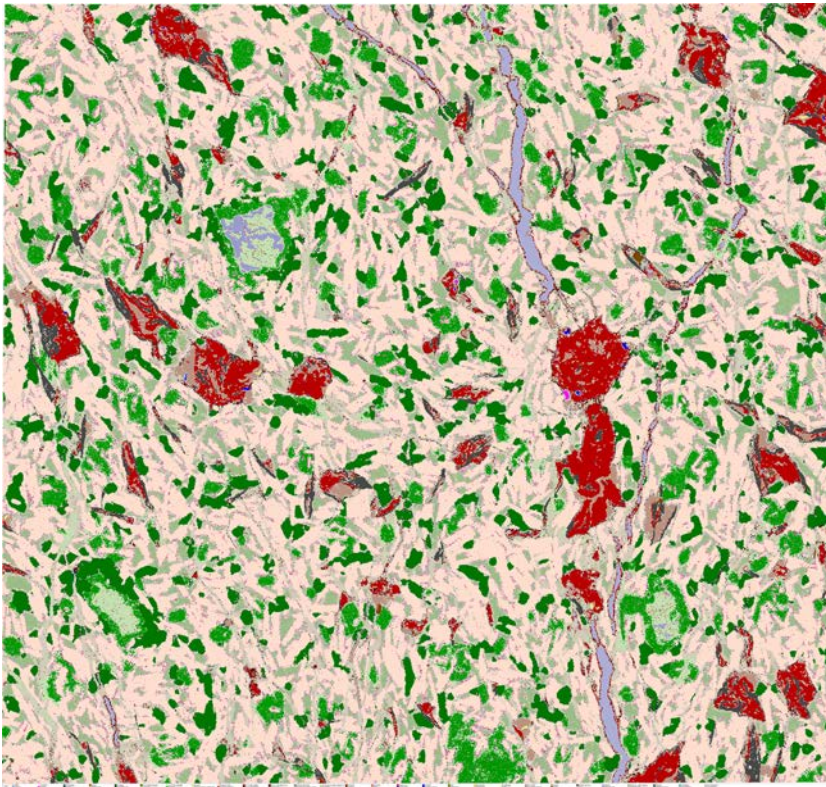
**Fig. 90.** Backscatter electron (BSE) micrographs. Aggregates of pyrrhotite [Po], magnetite [Mag], and graphite [Gr] with pyrrhotite being remobilized into surrounding fractures parallel to foliation. Siderite [Sd]-filled fractures occur parallel to foliation and as small stepping connecting veinlets and cross-cut glass and orthopyroxene [Opx].

2.75. FP94-4-5\_183.87 Microscopy



**Fig. 91.** Magnetite [Mag] associated with very minor NiFeP and graphite [Gr] and with pyrrhotite [Po] with chalcopyrite [Ccp] and pentlandite [Pn]. Pyrrhotite is remobilized and extends into small fractures. TL-II: transmitted light micrograph with plane polarized light (ppl). TL-x: crossed polars. RL-II: reflected light micrograph with ppl.

2.76. FP94-4-5\_183.87 AQM-SEM



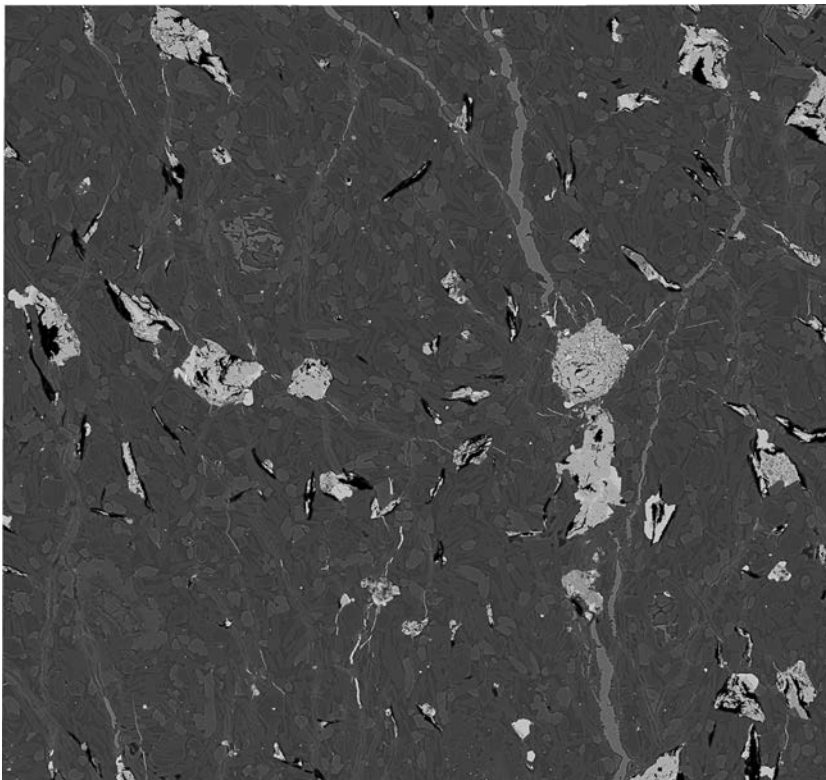
**Fig. 92.** Mineral map and corresponding BSE map of AQM-SEM analysis.

*Magnetite in association with pyrrhotite, graphite, chalcopyrite, pentlandite, and NiFeP. Very minor preserved native iron. Fe-Mg-chlorite - altered olivine xenocryst with orthopyroxene corona and cross-cut by siderite-filled fractures.*

*Matrix consists predominantly of euhedral to subhedral crystals of plagioclase, orthopyroxene, minor anhedral clinopyroxene with intersertal K-rich siliceous glass. Fractures filled with siderite.*

*Image of thin-section, width 23 mm*

50 µm

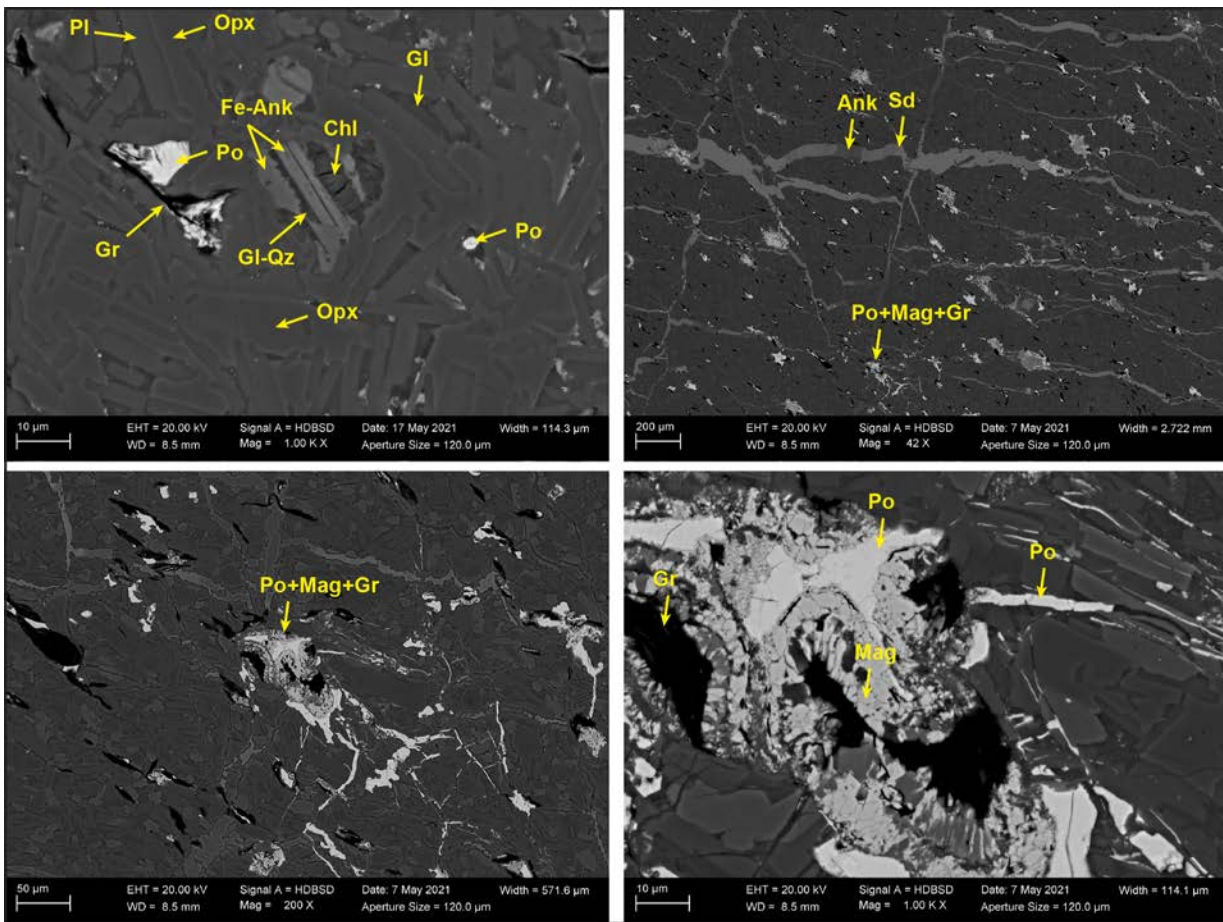


2.77. FP94-4-5\_187.55 Summary

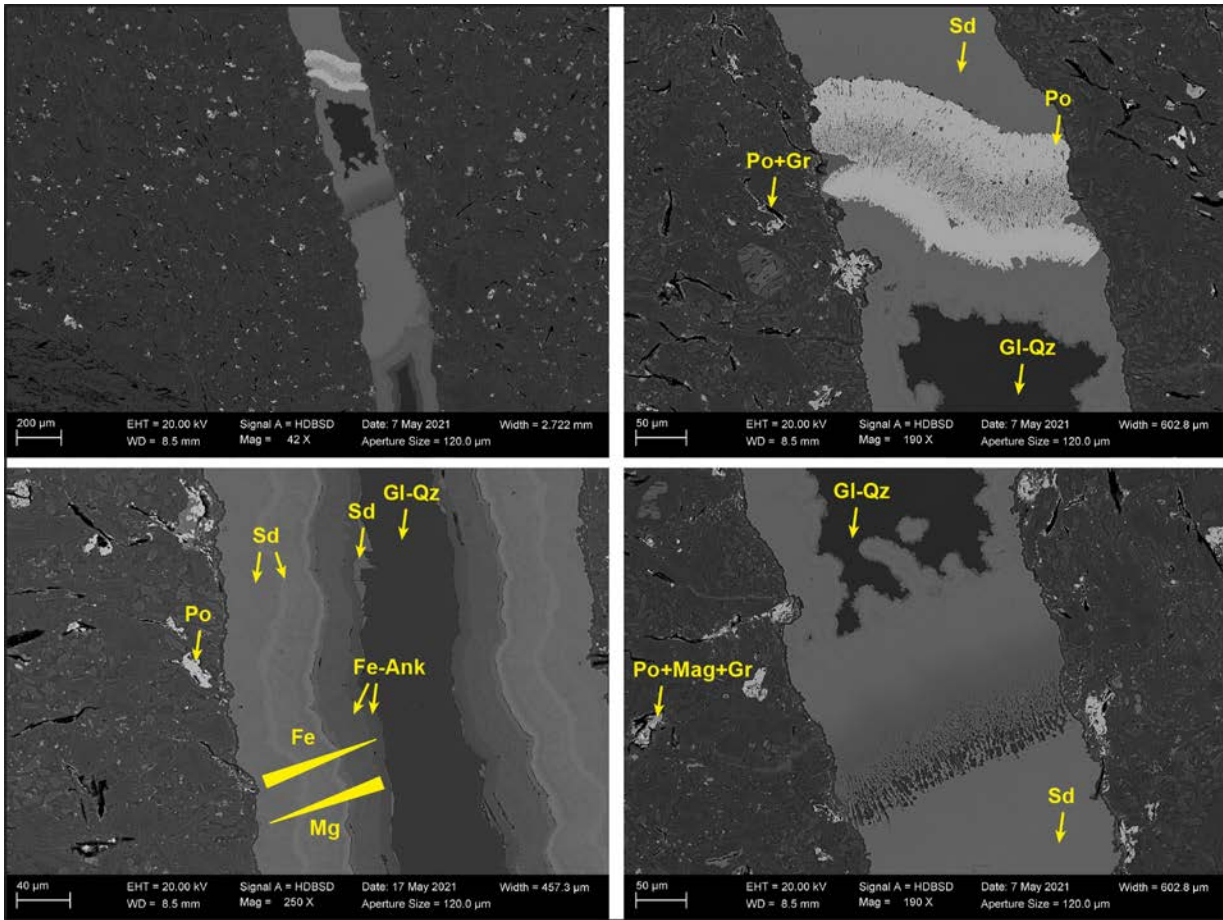
Strongly sheared and fractured fine-crystalline basalt with moderate aggregates of pyrrhotite, graphite, and magnetite aggregates. Pyrrhotite commonly associated with pentlandite and chalcopyrite, locally covellite.

The matrix consists of plagioclase microlite laths, Fe-Mg-chlorite-altered orthopyroxene, and diopside with intersertal K-rich siliceous glass. Graphite occurs with the sulphides, but is less abundant than in stratigraphically upper samples. Abundant small and large fractures cross-cut matrix and are filled with siderite-ankerite and locally remobilized pyrrhotite.

2.78. FP94-4-5\_187.55 SEM-BSE/EDS

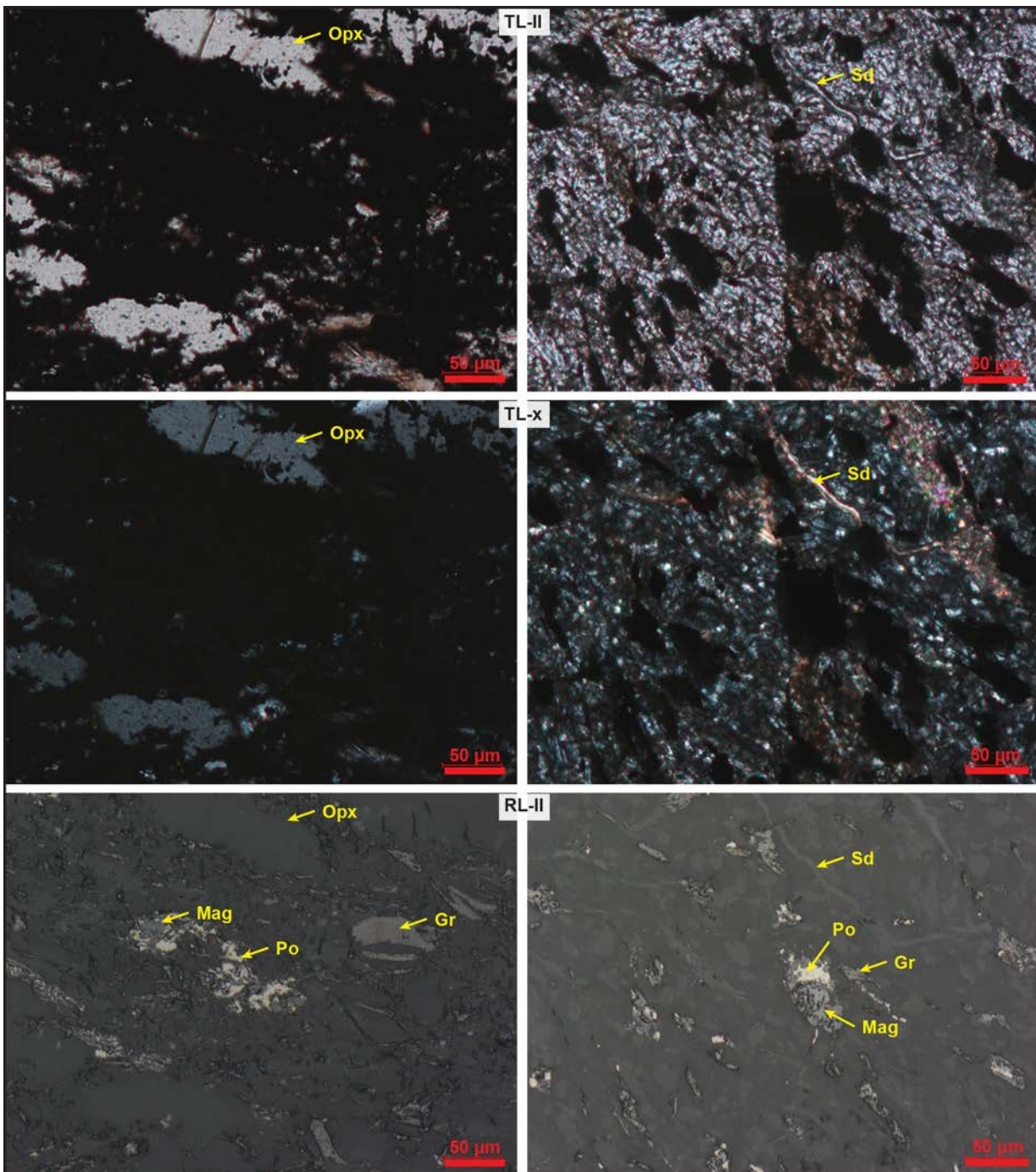


**Fig. 93.** Backscatter electron (BSE) micrographs. Aggregates of pyrrhotite [Po], magnetite [Mag], and graphite [Gr] with pyrrhotite being remobilized into surrounding fractures. Siderite [Sd]+ankerite [Ank]-filled fractures cross-cutting groundmass.



**Fig. 94.** Backscatter electron (BSE) micrographs. Groundmass with disseminated aggregates of pyrrhotite [Po], magnetite [Mag], and graphite [Gr]. Large fracture filled by different pulses of Fe-Mg-carbonates of siderite [Sd]-ankerite [Ank] composition. Central areas of fracture space filled by glass with quartz [GI-Qz] composition. Fluids apparently filling in fracture space parallel to fracture but also along the fracture where locally different fluid compositions meet and create intermingled/intergrown textures between Fe-Mg-carbonates, pyrrhotite, and siliceous glass.

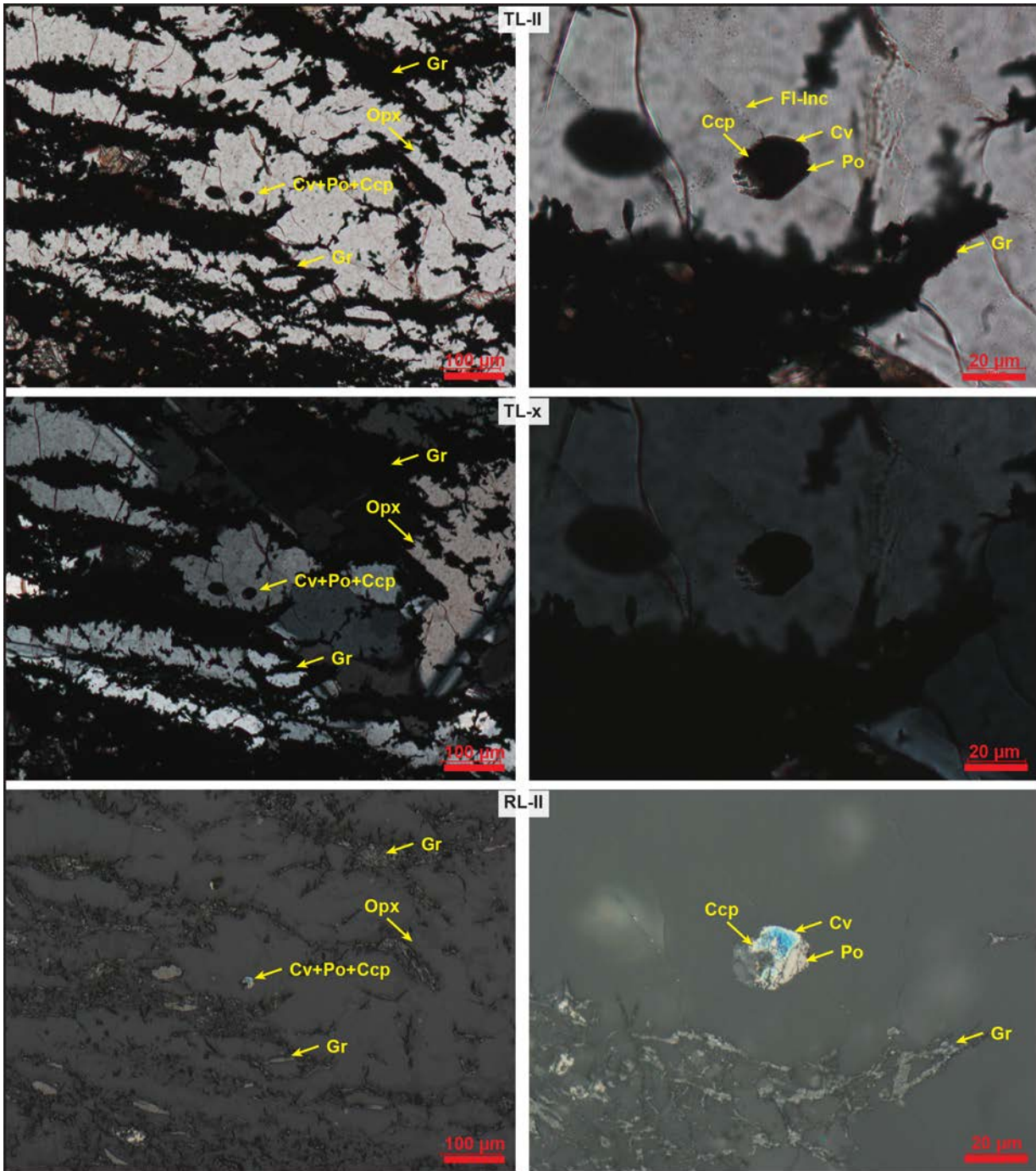
2.79. FP94-4-5\_187.55 Microscopy



**Fig. 95.** Left column: Graphite [Gr]-orthopyroxene [Opx]-rich thick shear fracture with aggregates of pyrrhotite [Po] and magnetite [Mag]. Right column: disseminated graphite+magnetite+pyrrhotite aggregates and smaller siderite [Sd]-filled fractures.

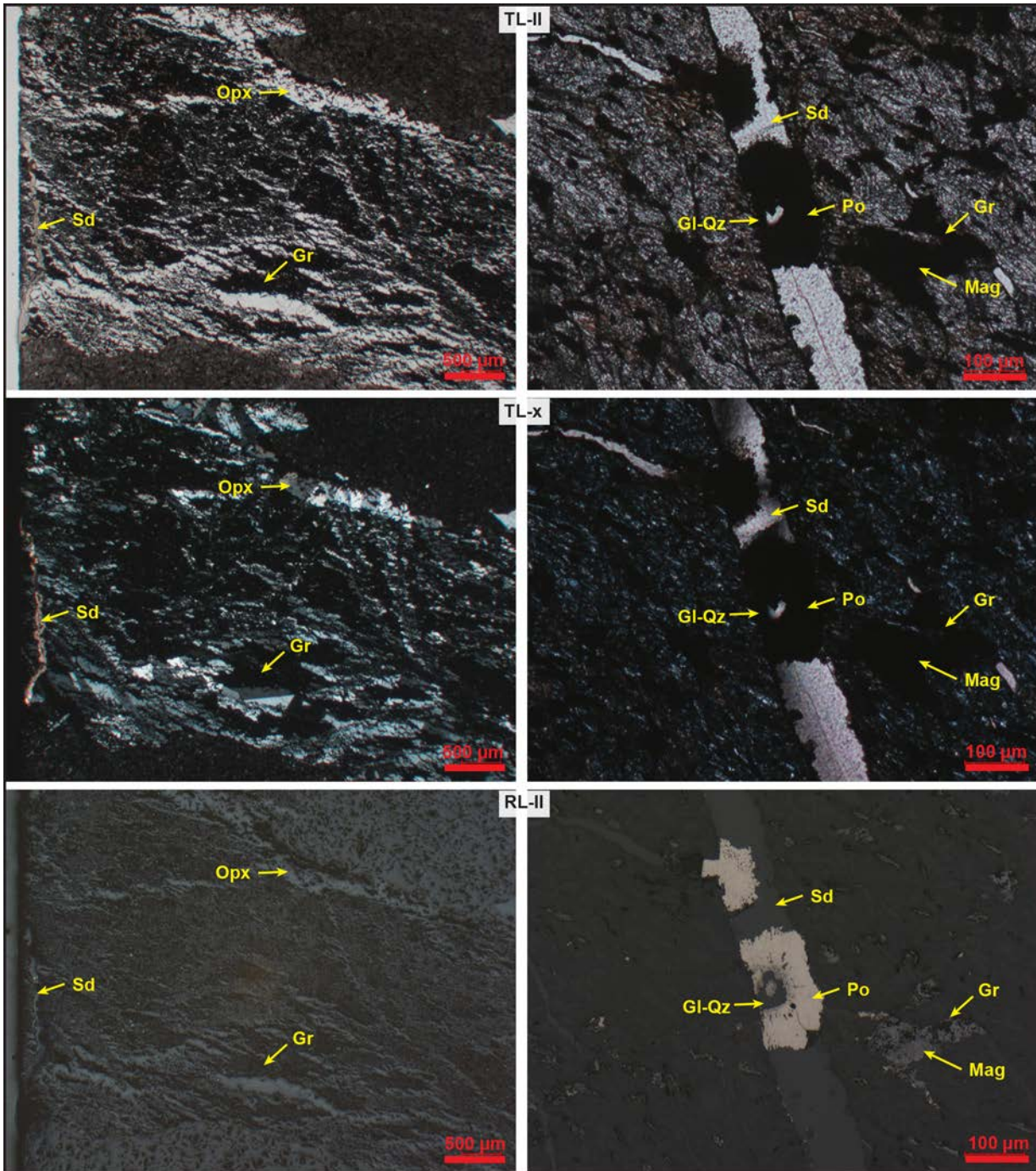
TL-II: transmitted light micrograph with plane polarized light (ppl). TL-x: crossed polars. RL-II: reflected light micrograph with ppl.





**Fig. 96.** Left column: Close-up of graphite [Gr]-orthopyroxene [Opx]-rich thick shear fracture with aggregate of pyrrhotite [Po], covellite [Cv], and relict chalcopyrite [Ccp]. Right column: Close-up of covellite associated with pyrrhotite and relict chalcopyrite.

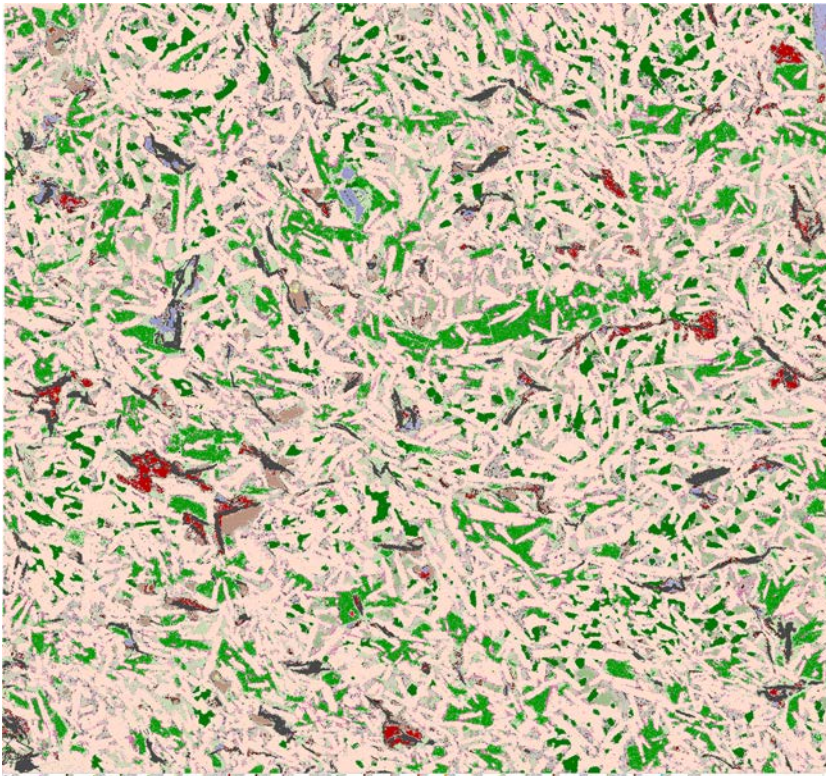
TL-II: transmitted light micrograph with plane polarized light (ppl). TL-x: crossed polars. RL-II: reflected light micrograph with ppl.



**Fig. 97.** Left column: Graphite [Gr]-orthopyroxene [Opx]-rich thick shear fracture cross-cut by later-stage siderite [Sd]-filled fracture. Right column: Close-up of siderite-filled fracture, locally filled with pyrrhotite [Po] and glass with quartz composition [GI-Qz]. Surrounding groundmass with magnetite [Mag] and graphite, minor pyrrhotite.

TL-II: transmitted light micrograph with plane polarized light (ppl). TL-x: crossed polars. RL-II: reflected light micrograph with ppl.

2.80. FP94-4-5\_187.55 AQM-SEM



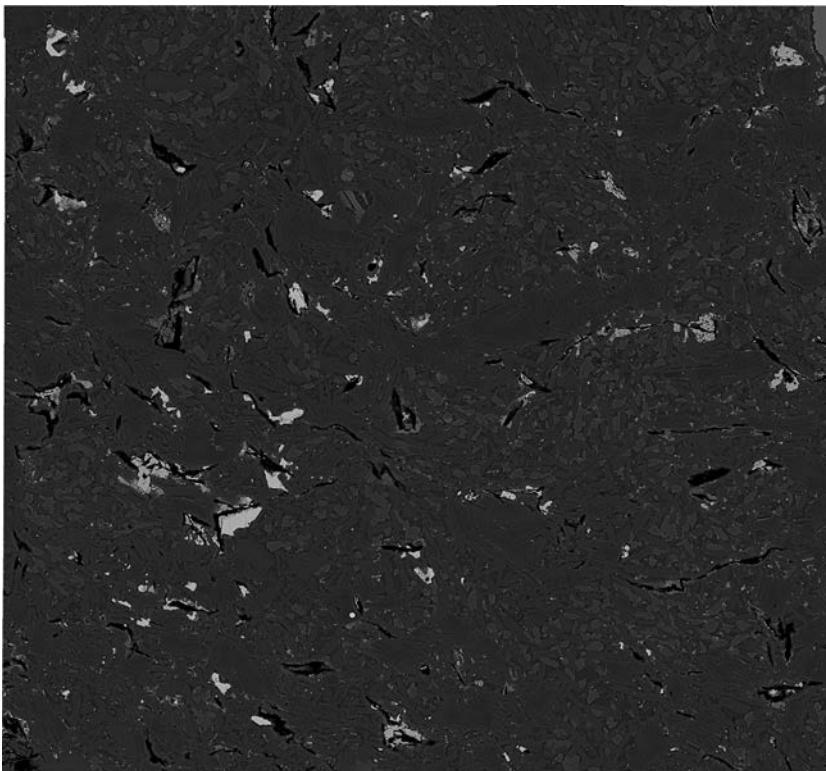
50 µm

**Fig. 98.** Mineral map and corresponding BSE map of AQM-SEM analysis.

*Magnetite in association with pyrrhotite and graphite, chalcopyrite. Fe-Mg-chlorite - altered phenocrysts with orthopyroxene corona and cross-cut by siderite-filled fractures.*

*Matrix consists predominantly of euhedral to subhedral crystals of plagioclase, orthopyroxene, minor anhedral clinopyroxene with intersertal K-rich siliceous glass. Upper right: Fracture filled with siderite.*

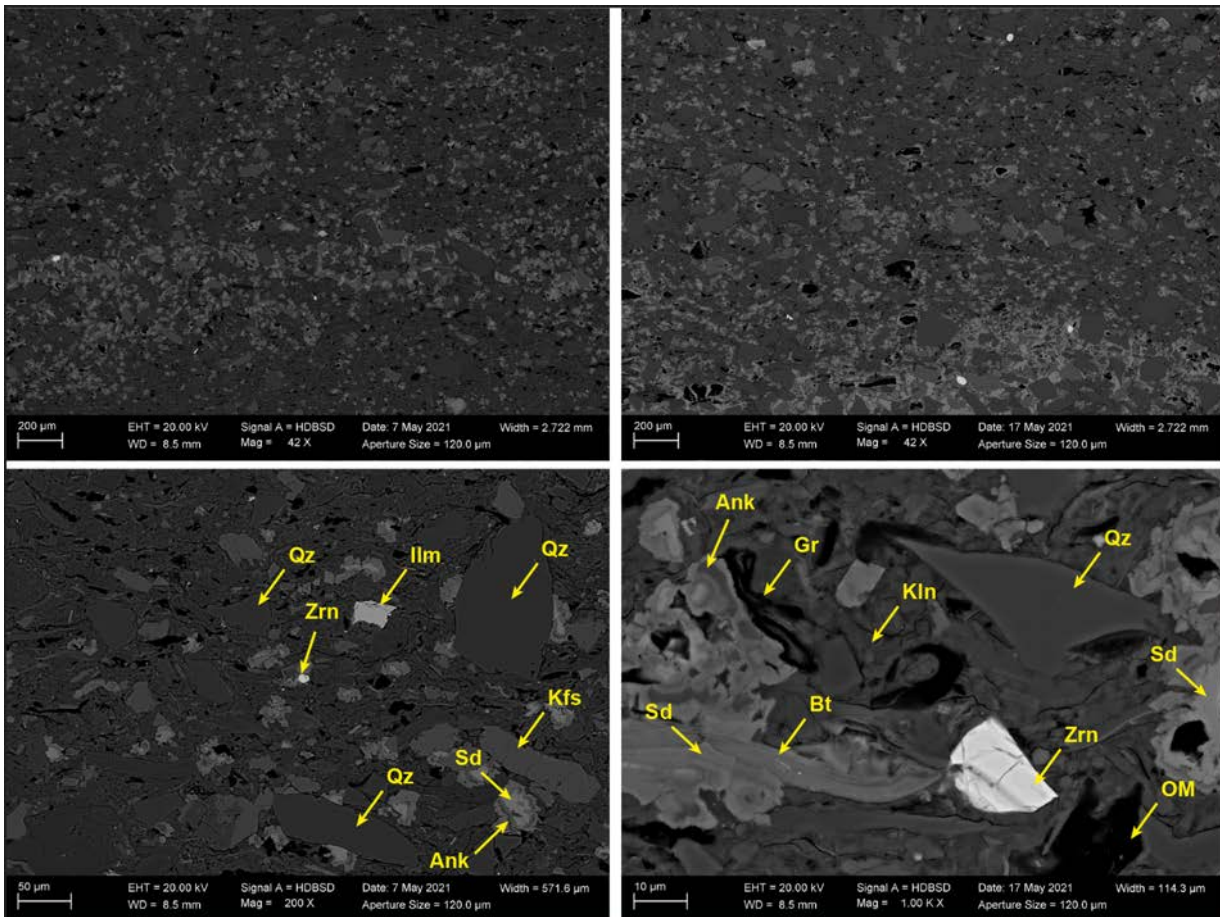
*Image of thin-section, width 23 mm. Note: Thick graphite-rich shear fracture at lower section of thin section.*



2.81. FP94-4-5\_190.54 Summary

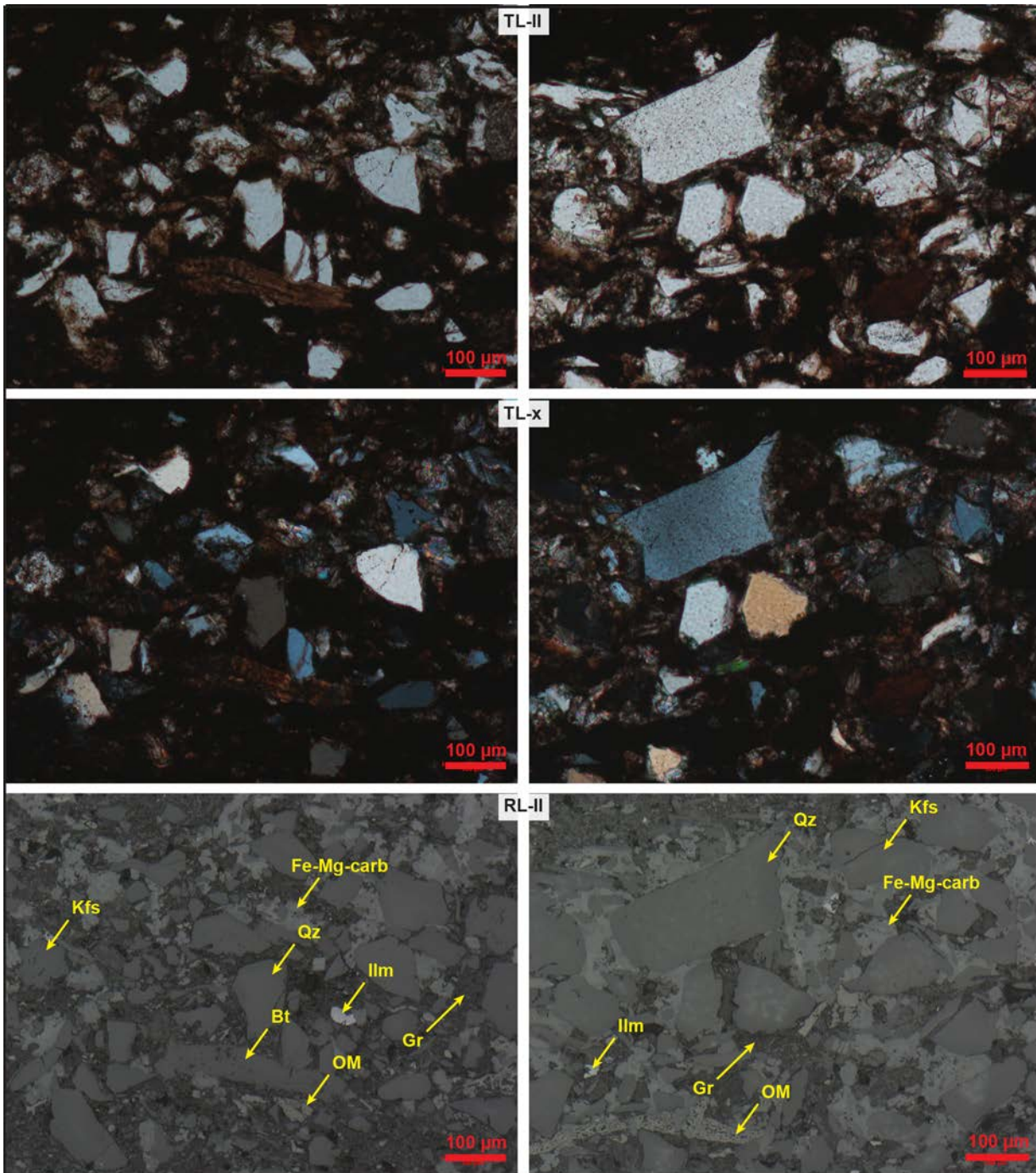
Laminated silty-sandy carbonaceous shale with angular quartz, subangular feldspars, and matrix consisting predominantly of kaolinite. Other minor and accessory minerals are kaolinite altered muscovite, Fe-Mg-chlorite altered biotite, rutile, ilmenite, apatite, zircon, as well as organic matter (wood) fragments. Graphite/graphitic carbon is dispersed in matrix. Carbonates of sideritic-ankeritic composition replace matrix subparallel to lamination and in patches. Sulphides are a very minor component and predominantly pyrite.

2.82. FP94-4-5\_190.54 SEM-BSE/EDS



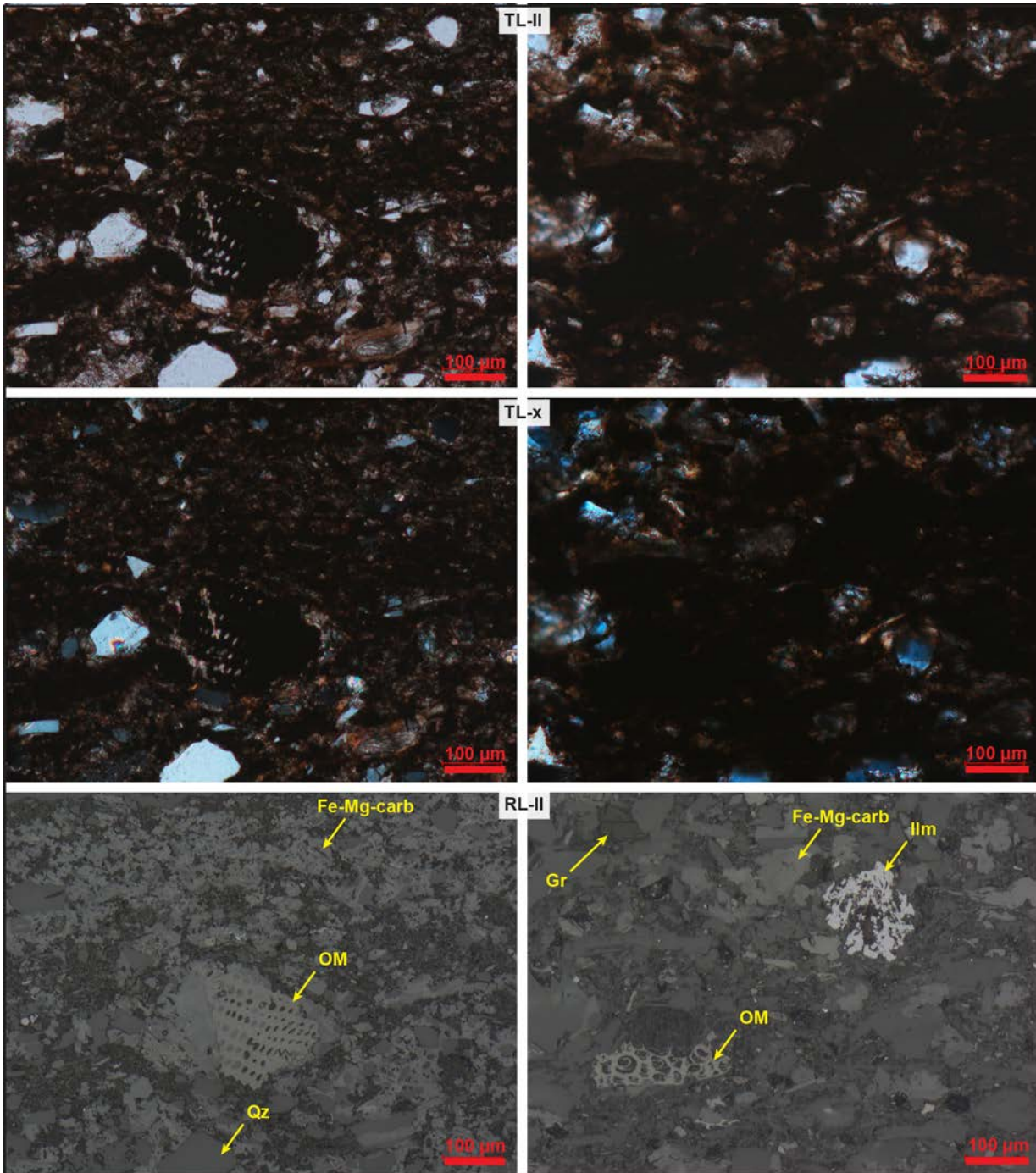
**Fig. 99.** Backscatter electron (BSE) micrographs. Silt to locally fine-sand sized angular quartz [Qz] grains and subangular K-feldspar [Kfs] and accessory ilmenite, biotite [Bt], [Ilm] and zircon [Zrc] in kaolinite [Kln]-rich matrix. Locally matrix replaced by Fe-Mg-carbonates (siderite [Sd]-ankerite [Ank]). Graphite/graphitic carbon [Gr] and organic matter [OM] fragments dispersed in matrix.

2.83. FP94-4-5\_190.54 Microscopy



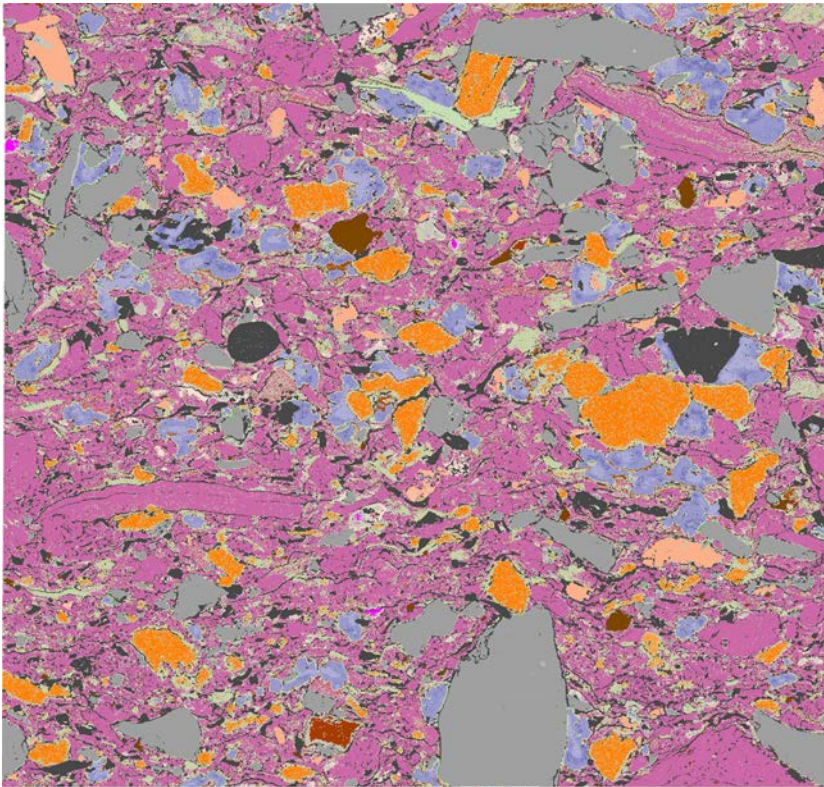
**Fig. 100.** Laminated compositionally immature carbonaceous silty shale with angular quartz [Qz], subangular feldspars (predominantly K-feldspar [Kfs], minor albite), Fe-Mg-chlorite altered biotite [Bt], kaolinite [Kln]-altered muscovite, and organic matter [OM] (wood/plant) fragments, as well as accessory rutile [Rt], ilmenite [Ilm], zircon [Zrc], and apatite [Ap]. Matrix predominantly consists of kaolinite plus aggregates of graphitic carbon [Gr] and commonly is replaced by Fe-Mg carbonates (siderite, ankerite, commonly rhythmically layered).

TL-II: transmitted light micrograph with plane polarized light (ppl). TL-x: crossed polars. RL-II: reflected light micrograph with ppl.



**Fig. 101.** Fe-Mg-carbonate replacing matrix clays. Note: difference in reflectance of organic matter [OM] (wood/plant fragments) and graphitic carbon [Gr] in matrix. Accessory ilmenite [Ilm]. TL-II: transmitted light micrograph with plane polarized light (ppl). TL-x: crossed polars. RL-II: reflected light micrograph with ppl.

2.84. FP94-4-5\_190.54 AQM-SEM

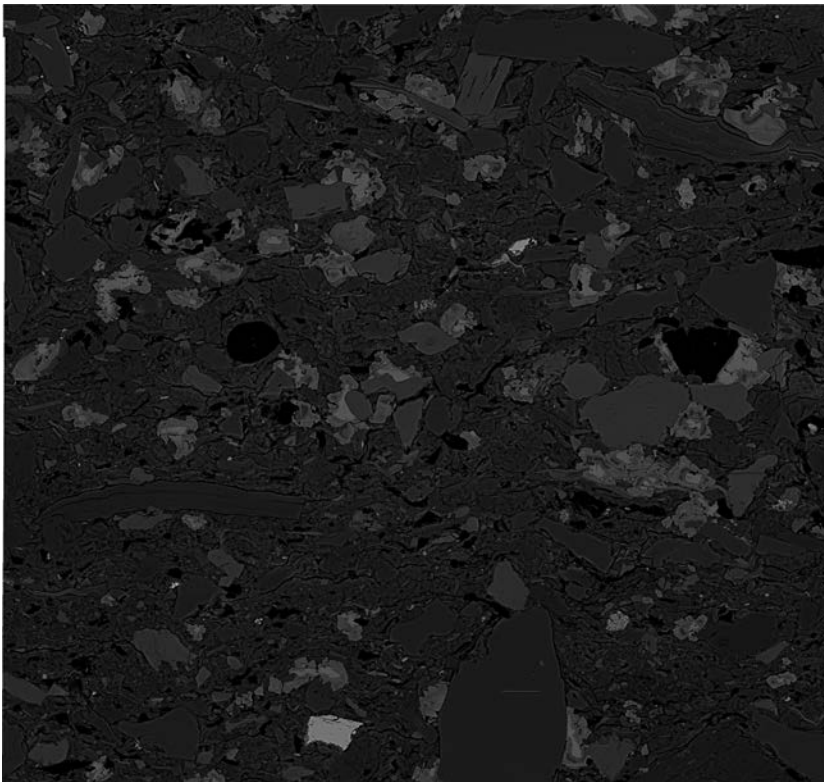


**Fig. 102.** Mineral map and corresponding BSE map of AQM-SEM analysis.

*Silt to fine-sand sized shale with angular quartz, subangular K-feldspar, minor albite, in a matrix of kaolinite with dispersed graphite plus organic fragments. Accessory minerals are kaolinite altered muscovite, Fe-Mg-chlorite altered biotite, rutile, ilmenite, apatite. Matrix in patches replaced by Fe-Mg-carbonates (siderite-ankerite).*

*Image of thin-section, width 23 mm.*

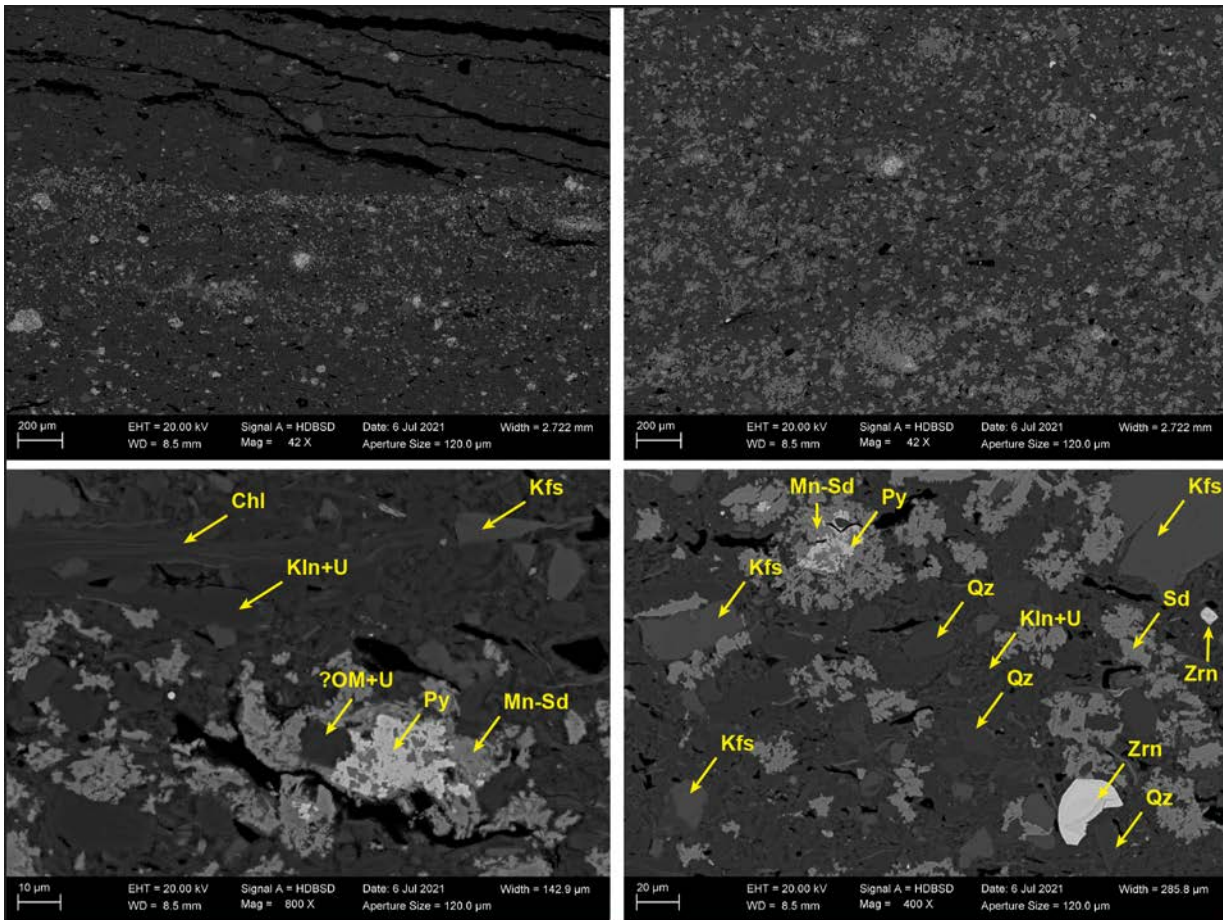
— 50 µm



2.85. FP94-4-5\_200.58 Summary

Laminated silty carbonaceous shale with angular quartz, subangular feldspars, and matrix consisting predominantly of kaolinite. Other minor and accessory minerals are Fe-Mg-chlorite altered biotite, rutile, ilmenite, apatite, zircon, as well as organic matter fragments. Graphite/graphitic carbon is dispersed in matrix. Carbonates of sideritic-ankeritic composition, locally manganoan, replace matrix subparallel to lamination and in patches. Sulphides are a very minor component and predominantly pyrite and in association with manganoan siderite. Clays in matrix with up to 0.7wt% U.

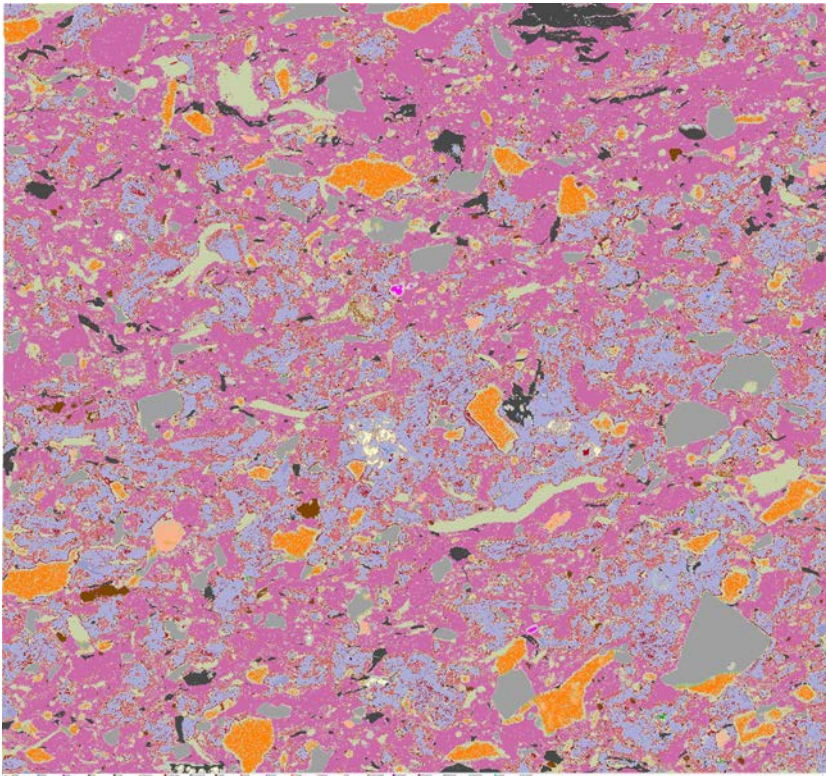
2.86. FP94-4-5\_200.58 SEM-BSE/EDS



**Fig. 103.** Backscatter electron (BSE) micrographs. Silt to locally fine-sand sized angular quartz [Qz] grains and subangular K-feldspar [Kfs] and accessory ilmenite [Ilm] and zircon [Zrc] in kaolinite [Kln]-rich matrix. Locally matrix replaced by Fe-Mg-carbonates (siderite [Sd]-ankerite[Ank]). Graphitic carbon [Gr] and organic matter [OM] fragments dispersed in matrix. Traces of uranium [U] detectable.



2.87. FP94-4-5\_200.58 AQM-SEM

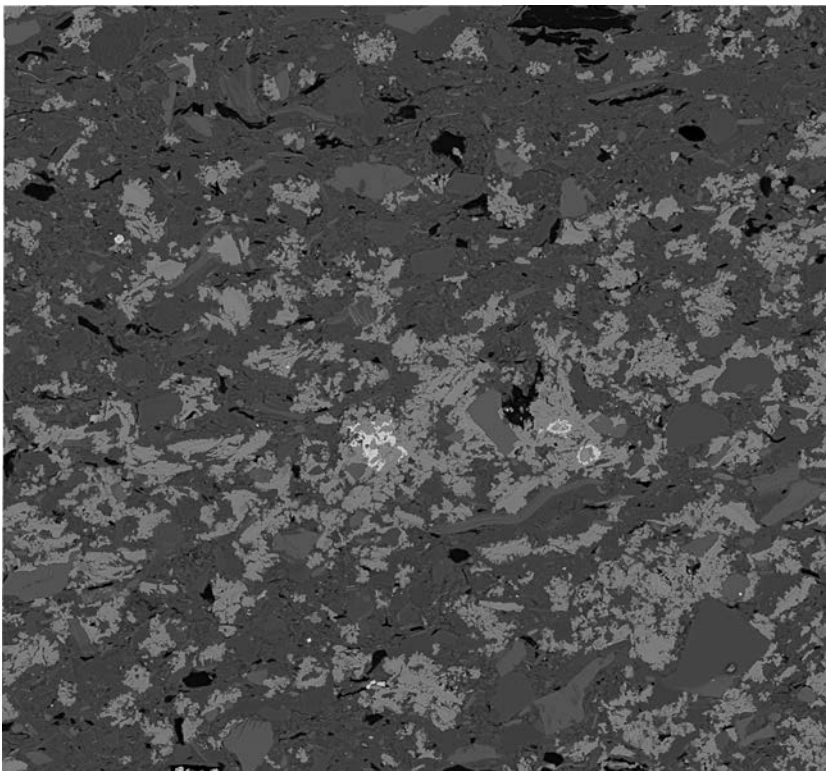
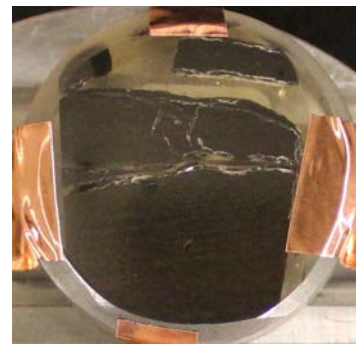


**Fig. 104.** Mineral map and corresponding BSE map of AQM-SEM analysis.

*Silty shale with angular quartz, subangular K-feldspar, minor albite, in a matrix of kaolinite with dispersed graphite plus organic fragments. Accessory minerals are Fe-Mg-chlorite altered biotite, rutile, ilmenite, apatite. Matrix abundantly replaced by Fe-Mg-carbonates (siderite-ankerite), locally manganoan.*

*Image of epoxy puck, width 25.4 mm.*

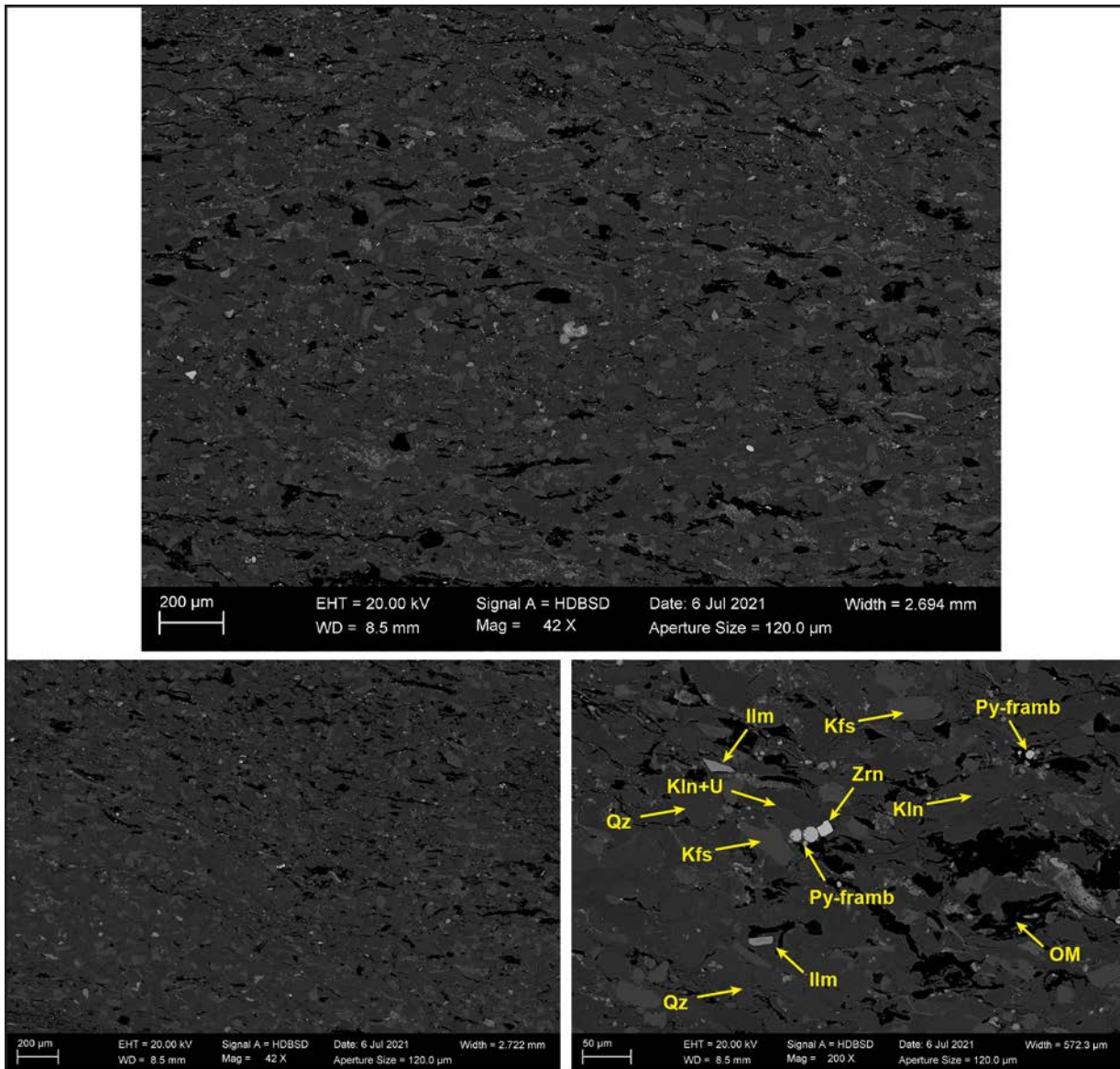
50 µm



2.88. FP94-4-5\_215.70 Summary

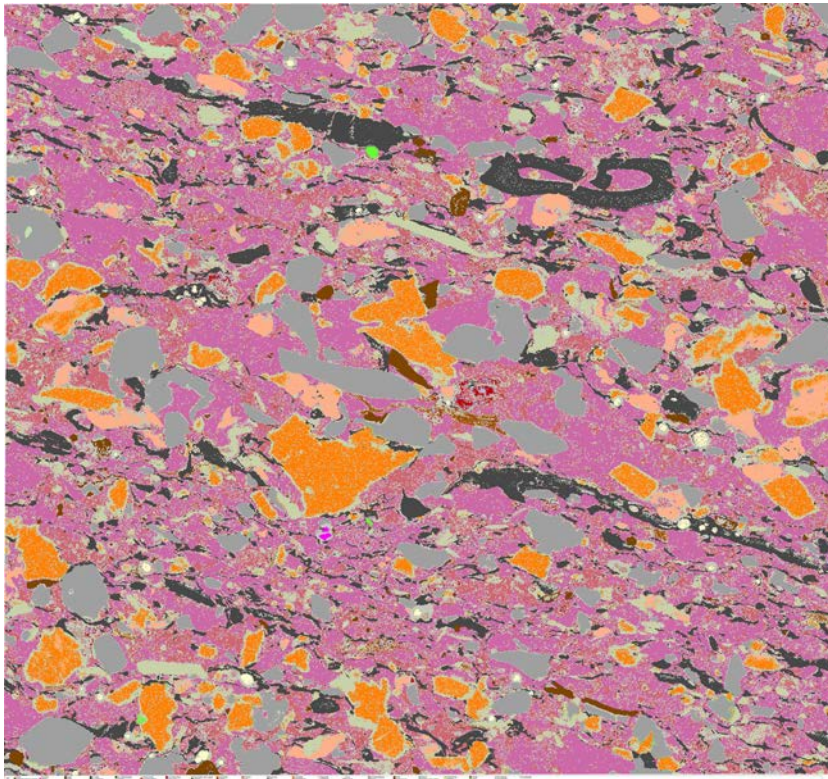
Laminated silty carbonaceous shale with angular quartz, subangular feldspars, and matrix consisting predominantly of kaolinite. Other minor and accessory minerals are Fe-Mg-chlorite altered biotite, rutile, ilmenite, apatite, zircon, as well as organic matter fragments. Graphite/graphitic carbon is dispersed in matrix. Sulphides are a very minor component and predominantly framboidal pyrite and in association with organic matter. Clays in matrix with up to 0.7wt% U.

2.89. FP94-4-5\_215.70 SEM-BSE/EDS



**Fig. 105.** Backscatter electron (BSE) micrographs. Silt sized angular quartz [Qz] grains and subangular K-feldspar [Kfs] and accessory ilmenite [Ilm] and zircon [Zrc] in kaolinite [Kln]-rich matrix. Graphitic carbon and organic matter [OM] fragments dispersed in matrix. Minor framboidal pyrite [Py-framb] associated with organic matter. Traces of uranium [U] detectable.

2.90. FP94-4-5\_215.70 AQM-SEM



**Fig. 106.** Mineral map and corresponding BSE map of AQM-SEM analysis.

*Silty shale with angular quartz, subangular K-feldspar, minor albite, in a matrix of kaolinite with dispersed graphite plus organic fragments. Accessory minerals are Fe-Mg-chlorite altered biotite, rutile, ilmenite, zircon, pyrite.*

*Image of epoxy puck, width 25.4 mm.*



50 μm



### 3. Conclusions

The results of this study show that SEM-based manual and automated mineralogical investigations can complement petrophysical measurements to better define and characterise potential exploration targets. With the presence of magnetic and conductive minerals in the lithological units hosting potential mineral resources, petrophysical/ geophysical measurements alone cannot sufficiently explain the cause for the observed differences in magnetic and electric properties.

The stronger magnetic anomalies observed in the lower basaltic block and initially thought to be caused by the presence of native iron, are in fact a result of the magnetite, whereas higher amounts of native iron and slightly more pyrrhotite occurrences in the upper block, may explain the more conductive behaviour measured in this upper basaltic block.

The role of graphite remains a little enigmatic to a certain extent, as it does not appear to have any significant influence on the electric properties. Interestingly, the graphite in the upper block is always coated in an Fe-bearing amorphous siliceous phase called hisingerite, which is not observed in the lower block. The influence of hisingerite on electric properties, e.g., conductivity, is not known. The presence of hisingerite correlates with higher conductivities observed in the upper block though.

Furthermore, the connectivity of conductive minerals may also be a focus of future research to investigate, why, e.g., the graphite, does not seem to be the driving force for the high conductivities measured in the upper block in this study, as generally assumed.

Based on the mineralogical investigations, the upper basaltic block has more preserved native iron occurrences, whereas the lower block appears to represent a better target for Cu-Ni mineralisation.

Similarly to kimberlite indicator minerals used in diamond exploration, a presence of ulvöspinel, armalcolite, titanomagnetite, and titanite, may represent suite of minerals with potential to be used as indicator minerals for Ni-Cu mineralisation, as those occur in higher quantities in the lower basaltic block.

Future studies may address more detailed mineralogical studies of the pyrrhotite-pentlandite-CuFe-sulphide associations, native Fe-cohenite relations, and hisingerite occurrences, possibly using a combination of high resolution AQM-SEM and microprobe (EPMA) microanalysis.

### 4. Acknowledgements

GEUS is grateful for the financial support from Bluejay Mining Plc. to perform this study. Petrophysical research was also partly funded by the EIT RawMaterials as part of the MULSEDRO (Multi-Sensor-Drone) project (Nr. 16103). We are grateful to Lotte Melchior Larsen and Asger K. Pedersen for their assistance, discussions, and their vast experience regarding the geology and mineralogy of Disko Island and related rocks. Furthermore, we would like to thank Satu Mertanen and Heikki Säävuori from GTK for discussions and the petrophysical measurements and we greatly appreciate the kind support by Jens Gregersen from the GEUS core storage for providing sample material for this study.

## 5. References

Heincke, B. H., Sørensen, E.V., Jackisch, R., Zimmermann, R., Barnes, E., Madriz, Y., Karinen, A., Pirttijärvi, M., Maalimaa, L., and Salmirinne, H. , 2020 Report on the field work activities of the MULSEDRO project on Disko Island, West Greenland, in 2019 (scientific survey license VU-00158-2019). Report for the Mineral Resources Authority, Government of Greenland. 140 pp.

Olshefsky, K. and Jerome, M., 1993, Falconbridge Limited - Report of 1992 Exploration Activities, West Greenland Tertiary Basalt Province for Prospecting License #156 and exploration licenses 02/91, 03/91, 04/91, 25/92. 300 pp.

Olshefsky, K., Jerome, M. and Graves, M., 1995, Falconbridge Greenland A/S, West Greenland Tertiary Basalt Province – Report on 1994 Exploration Activities for Prospecting License 06/94 and Exploration License 02/91 & 03/01. 326 pp.

Pedersen, A.K., Larsen, L.M. and Pedersen, G.K., 2017, Lithostratigraphy, geology and geochemistry of the volcanic rocks of the Vaigat Formation on Disko and Nuussuaq, Paleocene of west Greenland. Geological Survey of Denmark and Greenland Bulletin 39. 248 pp.

Pedersen, A.K., Larsen, L.M. and Pedersen, G.K. ,2018, Lithostratigraphy, geology and geochemistry of the volcanic rocks of the Maligât Formation and associated intrusions on Disko and Nuussuaq, Paleocene of West Greenland. Geological Survey of Denmark and Greenland Bulletin 40, 239 pp.

Ramdohr, P., 1975, Die Erzminerale und ihre Verwachsungen, Akademie-Verlag, Berlin, 1276 pp.

Stensgaard, B.M., Sørensen, L.L., Bernstein, S., and Rosa, D., 2018, Magmatic nickel potential in Greenland. *Geology and Ore: Exploration and Mining in Greenland*, 31, 1-12p.

## 6. Appendices

Data tables: AQM-SEM bulk mineralogy\_summary (Excel file)

AQM-SEM bulk mineralogy\_detailed (Excel file)

Petrophysical data (below)

## Appendix – Petrophysical measurements on the samples of the borehole FB94-4-5

The petrophysical measurements were conducted at the petrophysical laboratory of the Geological Survey of Finland (GTK) in Espoo, Finland, in November 2019. Measurements were financially supported by BlueJay Mining PLC but were collected within the EIT RM upscaling project MULSEDRO (**M**ulti-**S**ensor **D**rones).

The petrophysical measurements were carried out on the same 23 samples from the Qullissat drill core as used for the mineralogical investigations. The used cylindrical core samples were extracted from the drill core of FB-94-4-5 at the GEUS core storage and had a diameter of 3.5 cm. Their lengths typically ranged between 5 and 13 cm. Most samples are basaltic in composition, and they are solid and intact after sampling. However, four samples taken from the sediment units above and below the basalts (samples at depths of 49.50 m, 190.54 m, 200.58 m and 215.73 m) were brittle and had fractures mainly in the horizontal direction such that these samples were shorter. The sample lengths were generally reduced to ~5 cm, when samples were prepared for measurements in GTK's petrological lab (see Fig. A-1).



Figure A-1: The 23 samples that were used for the petrophysical measurements. The samples are ordered by depths from the top left (shallow) to the bottom right (deep).

The aim of the petrophysical measurements was to find explanations for conductance (Olshefsky & M. Jerome, 1993; Data et al., 2005) and magnetic anomalies (Heincke et al., 2020) observed in data from

geophysical surveys acquired for mineral exploration purposes. They comprised determination of the following physical properties:

- (1) (dry) bulk density
- (2) magnetic susceptibility
- (3) magnetic remanence including the magnetization directions (inclination and declination)
- (4) galvanic resistivity in the frequency domain at three frequencies (0.1 Hz, 10 Hz and 500 Hz). In addition, two estimates of the induced polarization (IP) were calculated from these measurements
- (5) Galvanic resistivity and induced polarization in the time domain

## 1. METHODS & MEASURING PROCEDURES

### Density measurements

The dry bulk densities  $\rho_{r,dry}$  (i.e. the pore space is gas filled) were determined in the GTK lab by measuring the sample weights in air and under water. Using Archimedes Principle, the dry density can then be determined by the formula:

$$\rho_{r,dry} = \frac{m_{r,air} \cdot \rho_{water}}{(m_{r,air} - m_{r,water})}$$

with

$m_{r,air}$  := mass of air-filled rock sample

$m_{r,water}$  := apparent mass of rock sample when submerged in water

$\rho_{water}$  := density of water at measuring temperature

Samples with a maximum length of 10 cm can be measured and the accuracy of the density measurements is estimated to be  $\pm 0,1$  % of the absolute values. More details about the measuring setup can be received by the personnel from the GTK petrophysical laboratory.

### Measurements of magnetic properties

The magnetic measurements comprised determination of the magnetic susceptibility ( $k$ ) and the magnitude ( $M_R$ ) as well as the direction (inclination and declination) of the natural remanent magnetization (NRM). However, since the cores in the vertical borehole were unoriented, the declination of the magnetization is not of further use. Also, the measured inclination should be considered with care for two reasons:

- (a) The drill hole is described as vertical in the annual field report from Falconbridge Greenland A/S (Olshefsky et al., 1995). However, it is not reported that the actual inclination of the borehole was measured such that there is a larger uncertainty about the inclination direction of the borehole and, hence, also the inclination of the remanent magnetization.
- (b) Due to some miscommunication between GEUS and GTK, only the magnitude of the remanent magnetization, but not its directional components, were determined in the first measuring cycle. Therefore, the directional components (inclination, declination) were obtained in a second measurement. Since, the samples were saturated in water (for 3 days) for the galvanic resistivity

measurements, which were performed between the two runs, there was some concerns that this might impact the magnetic properties<sup>1</sup>.

To evaluate how far the repeated measurements were consistent, some unused sample material from six depths, where enough of such material was available (see other colored rows in Table A-1), were taken to measure once again the magnetization (magnitude as well as its directions). Comparable inclinations from measurements at the same depths propose that the sample preparation had no major effect onto the remanence.

To measure the magnetic volume susceptibility, a so-called AC susceptibility bridge was used, where the samples were exposed to a low frequency (993 Hz) alternating current in a coil system creating a slowly varying outer magnetic field. The system was first balanced/calibrated without a sample. Then the sample was added and measured inductivity changes in the coil were associated with the susceptibility of the sample. The applied field had about the same magnitude as the Earth magnetic field (20- 50 A/m). The standard error of the susceptibility  $K$  is estimated to be  $20 \times 10^{-6}$  SI and 1 % of the absolute values if  $K$  is smaller and larger than  $10^{-3}$  SI, respectively. More details about the equipment designed and built at GTK is given by Puranen & Puranen (1977).

The remanent magnetization  $M_R$  was measured with a fluxgate magnetometer inside a  $\mu$ -metal shielding, which is used as a shielding against outer Earth magnetic field. The flux density inside the  $\mu$ -metal cylinder is described to be less than 100 nT and the noise level is less than 0.1 nT. The reliability of the remanence measurements is given for weakly magnetic samples as  $\sim 10$  mA/m.

For more details about the used apparatus and measuring devices, the personnel from GTK petrophysical laboratory should be contacted.

#### Measurements of electric properties

Galvanic apparent resistivity measurements, which were carried out both in frequency domain and time domain, were mainly applied to samples having relatively low conductivities (high resistivities). In both domains, induced polarization (IP) parameters reflecting the chargeability of the sample were determined next to resistivity values. Before the measurements, samples were saturated with water for 3 days and the top and bottom surface of the cylindrical samples were polished to be plane and smooth.

Due to heavy fracturing, electric measurements could not be conducted on samples at depths of 49.50 m and 200.58 m and results of the samples at depths of 190.54 m and 215.73 m were considered as not reliable (see Table A-2).

In the frequency domain, measurements were performed with the MAFRIP instrument built by GTK (Puranen et al., 1995). Measurements were conducted at three frequencies of 0.1, 10, and 500 Hz. The samples were placed between two wet electrodes (2-point measurements) connected to a circuit with a known resistance, and both the current density within the sample and the potential difference between the ends of the samples were measured. The measuring results were always  $> \sim 10 \Omega\text{m}$  because the so-called interface resistance was included.

The so-called frequency effect was used to obtain two induced polarization estimates (PL and PT) from the combination of resistivities measured at different frequencies:

---

<sup>1</sup> In addition, the samples were exposed to an external magnetic field during the susceptibility measurements, which can slightly change the remanent magnetization. This should not be ignored, since the remanent magnetization of native iron can be soft and may change at the presence of a changing external field (see Nagata et al., 1970).



$$PL = 100 \cdot \frac{\rho_{0.1} - \rho_{10}}{\rho_{0.1}} [\text{in } \%]$$

and

$$PT = 100 \cdot \frac{\rho_{0.1} - \rho_{500}}{\rho_{0.1}} [\text{in } \%]$$

with  $\rho_x$  := resistivity measured at X Hz.

A SCIP tester (<https://www.gddinstrumentation.com/scip-tester>) was used for measurements in the time-domain. The sample was placed between two sponges that were wet with copper sulphate liquid, which was washed out immediately after the measurements.

The electronic charge of the sample was monitored by making 20 voltage measurements at 80 ms intervals after each voltage pulse. The waveform was an alternating square wave (repetition frequency of 1 Hz), where the voltage first remains constant and positive (+) for a while, then has a value zero and finally is constant and negative (-) (Fig. A-2).

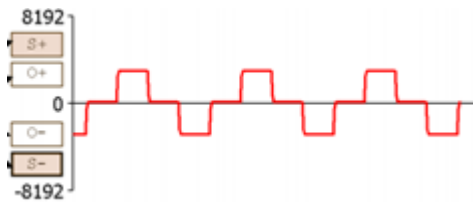


Figure A-2: waveform of the input voltage used for the resistivity and IP measurements in the time-domain.

The IP values were obtained by averaging 20 consecutive (interval 80 ms) voltage measurements (mV/V).

For more details about the used apparatus and measuring devices, the personnel from GTK petrophysical laboratory should be contacted.

## 2. MEASUREMENTS VALUES

The measured petrophysical parameters are listed in the Tables A-1 and A-2.

Table A-1: Measured density and magnetic properties on the rock samples. The ocher coloured rows refer to repeated magnetic measurements performed on unused sample material at six depths.

REAL SAMPLE CODE	SAMPLE CODE	Density and magnetic susceptibility				Magnetic Remanence	
		Mass M	Volume V	Density D	Vol. susceptibility K	Intensity J	Inclination
Units		(g)	(cm <sup>3</sup> )	(kg/m <sup>3</sup> )	(10 <sup>-6</sup> SI)	(10 <sup>-3</sup> A/m)	(°)
FB94-4-5.049.50	1	112,07	52,36	2140	130	117	-
FB94-4-5.049.50	1B		48,57			190	-28
FB94-4-5.054.80	2	119,86	54,37	2205	1.553	1.823	-57
FB94-4-5.066.26	3	154,85	55,60	2785	20.093	405	-39
FB94-4-5.075.90	4	156,30	55,76	2803	23.908	431	65
FB94-4-5.075.90	4B		44,93			292	45
FB94-4-5.087.13	5	156,05	56,11	2781	27.572	217	-28
FB94-4-5.087.13	5B		61,13			175	13
FB94-4-5.095.40	6	152,82	55,10	2774	32.937	367	69
FB94-4-5.095.40	6B		38,56			300	62
FB94-4-5.103.68	7	150,37	54,08	2781	34.296	1.100	81
FB94-4-5.110.90	8	151,40	54,57	2775	34.708	352	-12
FB94-4-5.121.80	9	152,70	54,77	2788	47.537	609	-77
FB94-4-5.126.30	10	153,91	54,95	2801	44.361	272	75
FB94-4-5.127.45	11	150,31	55,16	2725	40.158	2.411	61
FB94-4-5.127.98	12	152,79	55,22	2767	106.589	10.560	-26
FB94-4-5.127.98	12B		64,22			12.263	-37
FB94-4-5.131.60	13	151,65	54,80	2767	129.742	15.244	-40
FB94-4-5.131.60	13B		52,15			13.104	-48
FB94-4-5.142.42	14	152,30	55,14	2762	112.017	13.297	-37
FB94-4-5.153.20	15	152,58	55,27	2761	87.933	6.618	-45
FB94-4-5.159.70	16	152,81	55,23	2767	115.853	7.189	-31
FB94-4-5.170.47	17	154,06	55,15	2794	113.212	7.056	-42
FB94-4-5.177.40	18	152,23	54,42	2797	124.267	10.391	-16
FB94-4-5.183.87	19	96,42	34,75	2775	103.757	5.823	29
FB94-4-5.187.55	20	92,54	33,44	2768	82.729	2.372	-26
FB94-4-5.190.54	21	54,94	22,40	2452	5.126	265	-
FB94-4-5.200.58	22	55,07	21,73	2534	598	289	-
FB94-4-5.215.73	23	77,83	34,12	2281	133	175	-

Table A-2: Measured galvanic resistivity and IP values in frequency domain and time domain.

		Galvanic resistivity and IP measurements						
		Frequency domain					Time domain	
REAL SAMPLE CODE	SAMPLE CODE	Resistivity (0.1 Hz)	Resistivity (10 Hz)	Resistivity (500 Hz)	IP <sub>PL</sub>	IP <sub>PT</sub>	Resisitvity	IP
Units		Ωm	Ωm	Ωm	%	%	Ωm	mV/V
FB94-4-5.049.50	1	-	-	-	-	-	-	-
FB94-4-5.054.80	2	32	31	30	2	6	16	9
FB94-4-5.066.26	3	138	46	29	66	79	8	207
FB94-4-5.075.90	4	86	30	18	65	80	8	221
FB94-4-5.087.13	5	<1	<1	<1	-	-	5	295
FB94-4-5.095.40	6	137	67	46	51	66	5	269
FB94-4-5.103.68	7	120	56	32	54	74	6	249
FB94-4-5.110.90	8	80	35	23	56	71	5	288
FB94-4-5.121.80	9	62	27	18	56	70	7	229
FB94-4-5.126.30	10	100	41	27	59	73	13	141
FB94-4-5.127.45	11	162	88	73	45	55	51	73
FB94-4-5.127.98	12	2.050	1.510	1.220	26	40	1.028	45
FB94-4-5.131.60	13	809	624	538	23	33	496	50
FB94-4-5.142.42	14	13.600	7.830	5.290	42	61	10.269	148
FB94-4-5.153.20	15	7.310	4.590	3.140	37	57	5.667	103
FB94-4-5.159.70	16	23.500	14.800	10.200	37	57	18.723	125
FB94-4-5.170.47	17	7.450	4.630	3.300	38	56	5.601	114
FB94-4-5.177.40	18	12.100	9.080	6.440	25	47	7.949	44
FB94-4-5.183.87	19	45.700	28.500	19.100	38	58	28.690	105
FB94-4-5.187.55	20	10.800	7.350	5.250	32	51	6.653	62
FB94-4-5.190.54	21	75	70	66	6	12	26	13
FB94-4-5.200.58	22	-	-	-	-	-	-	-
FB94-4-5.215.73	23	401	367	339	8	15	124	10

## Literature:

- E. Data, J. Donohue and J. Legault, 2005. Geological report regarding the Quantec TITAN-24 distributed array system Tensor-Magnetotelluric survey over Disko Project, Greenland, during 2004, on behalf of Vismand Exploration Inc. Toronto, On, Canada. Internal report from Quantec Geoscience for Vismand Exploration. 111 pages.
- B. H. Heincke, E.V. Sørensen, R. Jackisch, R. Zimmermann, E. Barnes, Y. Madriz, A. Karinen, M. Pirttijärvi, L. Maalismaa and H. Salmirinne, 2020. Report on the field work activities of the MULSEDRO project on Disko Island, West Greenland, in 2019 (scientific survey license VU-00158-2019). Report for the Mineral Resources Authority, Government of Greenland. 140 pages.
- T. Nagata, Y. Ishikawa, H. Kinoshita, M. Kono, Y. Syono, and R.M. Fisher, 1970. Magnetic properties and natural remanent magnetization of lunar materials: *Geochimica et Cosmochimica Acta Supplement*, v. 1, p. 2325 - 2340.
- K. Olshefsky, M. Jerome and M Graves, 1995. Falconbridge Greenland A/S, West Greenland Tertiary Basalt Province – Report on 1994 Exploration Activities for Prospecting License 06/94 and Exploration License 02/91 & 03/01. 326 pages.
- K. Olshefsky and M. Jerome, 1993. Falconbridge Limited - Report of 1992 Exploration Activities, West Greenland Tertiary Basalt Province for Prospecting License #156 and exploration licenses 02/91, 03/91, 04/91, 25/92. 300 pages.
- M. Puranen and R. Puranen, 1977. Apparatus for the measurements of the magnetic susceptibility and its anisotropy. *Geologinen Tutkimuslaitos – Geological Survey of Finland*. Report of investigation No 28. 46 pages.
- R. Puranen, K. Sulkanen and R. Nissinen, 1995. Galvanic measurements of resistivity and IP effect at computerized petrophysics laboratory. Report of the Geological Survey of Greenland; No 3607. 15 pages.